THE UNIVERSITY OF
WARWICK

Library Declaration and Deposit Agreement

1. STUDENT DETAILS

Please complete the following:

Full name: .....

University ID number: .....

2. THESIS DEPOSIT

2.1 I understand that under my registration at the University, I am required to deposit my thesis with the University in BOTH hard copy and in digital format. The digital version should normally be saved as a single pdf file.

2.2 The hard copy will be housed in the University Library. The digital version will be deposited in the University's Institutional Repository (WRAP). Unless otherwise indicated (see 2.3 below) this will be made openly accessible on the Internet and will be supplied to the British Library to be made available online via its Electronic Theses Online Service (EThOS) service.
[At present, theses submitted for a Master's degree by Research (MA, MSc, LLM, MS or MMedSci) are not being deposited in WRAP and not being made available via EthOS. This may change in future.]

2.3 In exceptional circumstances, the Chair of the Board of Graduate Studies may grant permission for an embargo to be placed on public access to the hard copy thesis for a limited period. It is also possible to apply separately for an embargo on the digital version. (Further information is available in the *Guide to Examinations for Higher Degrees by Research*.)

2.4 ***If you are depositing a thesis for a Master's degree by Research, please complete section (a) below.***
For all other research degrees, please complete both sections (a) and (b) below:

(a) Hard Copy

I hereby deposit a hard copy of my thesis in the University Library to be made publicly available to readers (please delete as appropriate) EITHER immediately OR after an embargo period of ..... months/years as agreed by the Chair of the Board of Graduate Studies.

I agree that my thesis may be photocopied. YES / NO *(Please delete as appropriate)*

(b) Digital Copy

I hereby deposit a digital copy of my thesis to be held in WRAP and made available via EThOS.

Please choose one of the following options:

EITHER My thesis can be made publicly available online. YES / NO *(Please delete as appropriate)*

OR My thesis can be made publicly available only after.....[date] (Please give date)
YES / NO *(Please delete as appropriate)*

OR My full thesis cannot be made publicly available online but I am submitting a separately identified additional, abridged version that can be made available online.
YES / NO *(Please delete as appropriate)*

OR My thesis cannot be made publicly available online. YES / NO *(Please delete as appropriate)*

3. GRANTING OF NON-EXCLUSIVE RIGHTS

Whether I deposit my Work personally or through an assistant or other agent, I agree to the following:

Rights granted to the University of Warwick and the British Library and the user of the thesis through this agreement are non-exclusive. I retain all rights in the thesis in its present version or future versions. I agree that the institutional repository administrators and the British Library or their agents may, without changing content, digitise and migrate the thesis to any medium or format for the purpose of future preservation and accessibility.

4. DECLARATIONS

(a) I DECLARE THAT:

- I am the author and owner of the copyright in the thesis and/or I have the authority of the authors and owners of the copyright in the thesis to make this agreement. Reproduction of any part of this thesis for teaching or in academic or other forms of publication is subject to the normal limitations on the use of copyrighted materials and to the proper and full acknowledgement of its source.
- The digital version of the thesis I am supplying is the same version as the final, hard-bound copy submitted in completion of my degree, once any minor corrections have been completed.
- I have exercised reasonable care to ensure that the thesis is original, and does not to the best of my knowledge break any UK law or other Intellectual Property Right, or contain any confidential material.
- I understand that, through the medium of the Internet, files will be available to automated agents, and may be searched and copied by, for example, text mining and plagiarism detection software.

(b) IF I HAVE AGREED (in Section 2 above) TO MAKE MY THESIS PUBLICLY AVAILABLE DIGITALLY, I ALSO DECLARE THAT:

- I grant the University of Warwick and the British Library a licence to make available on the Internet the thesis in digitised format through the Institutional Repository and through the British Library via the EThOS service.
- If my thesis does include any substantial subsidiary material owned by third-party copyright holders, I have sought and obtained permission to include it in any version of my thesis available in digital format and that this permission encompasses the rights that I have granted to the University of Warwick and to the British Library.

5. LEGAL INFRINGEMENTS

I understand that neither the University of Warwick nor the British Library have any obligation to take legal action on behalf of myself, or other rights holders, in the event of infringement of intellectual property rights, breach of contract or of any other right, in the thesis.

Please sign this agreement and return it to the Graduate School Office when you submit your thesis.

Student's signature: ..... Date: .....

The synthesis, self-assembly and analysis of amphiphilic polymers: Developing microscopy techniques using graphene oxide and building catalytic palladium nanostructures

Submitted for the degree of Doctor of Philosophy

July 2013

Joseph P. Patterson

Department of Chemistry

THE UNIVERSITY OF WARWICK

To my loving Mother, for all her help and support

Contents

Declaration of authorship

This thesis is submitted in partial fulfilment of the requirements for the degree of Doctor of Philosophy. It describes work carried out from October 2009 to July 2013. Unless otherwise indicated, the research described is my own and not the product of a collaboration. No part of this thesis has been submitted to any other university, or as any part of any other submission to the University of Warwick.

Signed,

Date:

Acknowledgements:

Firstly I would like to thank Professor Rachel O'Reilly for providing me with the opportunity to work in her group. Her knowledge, advice and the encouragement to pursue my scientific interests was invaluable. I would like to thank the Department of Chemistry and its entire staff, both scientific and administrative, for providing equipment or assistance whenever I needed it to complete my thesis, and the EPSRC for funding my studies. I am grateful to all the O'Reilly group members who contributed to the effective team work which allowed my research to be conducted efficiently. In particular I would like to thank Adam Moughton, who helped me through the steep learning curve of my first year, Nikos Petzetakis for the collaboration in Chapter 4 and Mathew Robin for the collaboration in Chapters 2 and 4, plus many useful discussions on my thesis as a whole.

My PhD has been a welcome series of collaborations which has broadened my scientific and personal horizons. I would like to thank Neil Wilson and Ana Sanchez (Department of Physics, University of Warwick) for collaboration in Chapter 4 and for teaching me microscopy, Olivier Colombani and Christophe Chassenieux (University of LeMans) for the collaboration in Chapter 3 and for teaching me light scattering and many other aspects of polymer self assembly, Nico Sommerdijk and Paul Bomans (Technical University of Eindhoven) for the collaboration in Chapter 5 and for teaching me that cryo-TEM does not have to be torturous, and finally to Thomas Epps, III and Elizabeth Kelley (University of Delaware) for collaboration in Chapters 2-4, for their general help throughout my PhD, and specifically for their expertise in small angle neutron scattering.

List of Publications

- **J. P. Patterson**, P. Cotanda, E. G. Kelley, A. O. Moughton, A. Lu, T. H. Epps, III and R. K. O'Reilly. "Catalytic Y-tailed amphiphilic homopolymers - aqueous nanoreactors for high activity, low loading SCS pincer catalysts." *Polym. Chem.*, 2013, 4, 2033-2039 (**Chapter 2**)
- **J. P. Patterson,** E. G. Kelley, R. P. Murphy, A. O. Moughton, M. P. Robin, A. Lu, O. Colombani, C. Chassenieux, D. Cheung, M. O. Sullivan, T. H. Epps , III, and R. K. O'Reilly, "Structural Characterization of Amphiphilic Homopolymer Micelles Using Light Scattering, SANS, and Cryo-TEM." *Macromolecules*, 2013. DOI: 10.1021/ma4007544 (**Chapter 3**)
- **J. P. Patterson**, A. M. Sanchez, N. Petzetakis, T.P. Smart, T. H. Epps III, I. Portman, N. R. Wilson, R.K. O'Reilly, "A simple approach to characterizing block copolymer assemblies: graphene oxide supports for high contrast multi-technique imaging," Soft Matter, 2012, 8, 3322-3328 (**Chapter 4**)
- N. Petzetakis, M. P. Robin, **J. P. Patterson**, E. G. Kelley, P. Cotanda, P. H. H. Bomans, N. A. J. M. Sommerdijk, A. P. Dove, T. H. Epps and R. K. O'Reilly. Hollow Block Copolymer Nanoparticles through a Spontaneous One-step Structural Reorganization. *ACS Nano*., 2013, 7, 1120–1128 (**Chapter 4**)
- M. A. Dyson, A. M. Sanchez, **J. P. Patterson**, R. K. O'Reilly, J. Sloan and N. R. Wilson, "A new approach to high resolution, high contrast electron microscopy of macromolecular block copolymer assemblies." *Soft Matter*, 2013, 9, 3741-3749 (**Chapter 4**)
- A..O. Moughton, **J.P. Patterson**, R.K. O'Reilly, "Reversible solution morphology switching nanostructures." *Chem. Commun.*, 2011, 47, 355-357

- P. E. Williams, A. O. Moughton, S. Khodabakhsh, **J. P. Patterson**, R. K. O'Reilly, "Exploring RAFT Polymerization for the Synthesis of Bipolar Diblock Copolymers and their Supramolecular Self-Assembly." *Polym. Chem.*, 2011, *2*, 720-729
- J. Du, H. Willcock, **J.P. Patterson**, R. K. O'Reilly, "Self-assembly of Hydrophilic Homopolymers: A Matter of End Groups". *Small*, 2011, 7, 2070-2080
- P. Cotanda, A. Lu, **J. P. Patterson**, N. Petzetakis, R. K. O'Reilly, Functionalized organocatalytic nanoreactors: hydrophobic pockets for acylation reactions in water. *Macromolecules*, 2012, 45, 2377-2284
- T. O. McDonald, P. Martin, **J. P. Patterson**, D. Smith, M. Giardiello, M. Marcello, V. See, R.K. O'Reilly, A. Owen, S. Rannard, Multi-component Organic Nanoparticles for Fluorescent Studies in Biological Systems. *Adv. Funct. Mater*. 2012, 22, 2469-2478
- R. McHale, **J. P. Patterson**, P.B. Zetterlund, R.K. O'Reilly, *Biomimetic* Radical Polymerization via Cooperative Assembly of Segregating Templates. *Nature Chemistry*, 2012, 491-497
- A. Lu, P. Cotanda, **J. P. Patterson**, D. A. Longbottom & R. K. O'Reilly. Aldol reactions catalyzed by l-proline functionalized polymeric nanoreactors in water. *Chem. Commun.*, 2012, **48**, 9699-9701
- B. W. Greenland, M. B. Bird, S. Burattini, R. Cramer, R. K. O'Reilly, **J. P. Patterson**, W. Hayes, C. J. Cardin and H. M. Colquhoun. Mutual binding of polymer end-groups by complementary π-π-stacking: a molecular "Roman Handshake". *Chem. Commun.*, 2013, **49**, 454-456

Summary

Chapter 1 is an introduction to the solution self assembly of amphiphilic polymers. Initially focusing on the complexity involved in the formation of these structures, followed by a review of the common analysis techniques used to characterise them.

Chapter 2 reports the synthesis of a Pd containing amphiphilic poly(acrylic acid) homopolymer. Its self-assembly in water is studied by SANS and cryo-TEM and its catalytic activity is compared to a small molecule analogue for a literature Suzuki-Mayura coupling reaction.

Chapter 3 uses a similar synthetic strategy to Chapter 2 in order to produce three amphiphilic poly(N-isopropyl acrylamide) homopolymers of different molecular weights. Their self-assembly in water is studied by laser light scattering, small angle neutron scattering and cryo-TEM. The results from each technique are compared in detail and used to asses the effect of polymer molecular weight on the assemblies.

Chapter 4 investigates the use of graphene oxide as a substrate for multiple microscopy techniques in relation to the analysis of polymer aggregates. The images are compared to those by more standard techniques and the benefits of using graphene oxide are demonstrated through the use of advanced imaging techniques.

Chapter 5 shows that graphene oxide supports can be used in conjunction with cryo-transmission electron microscopy. The benefit of having a stable nearly electron transparent support is shown by comparing images to those taken by standard cryo-transmission electron microscopy.

Abbreviations

$\propto$	proportional to
% coverage	the percentage of holes in a TEM grid covered with GO
% S-T	the percentage of GO covered holes in a TEM grid which are covered with single to triple layers of GO
$\langle \boldsymbol{R_{core}} \rangle$	average core radius
α	The angle formed between an object and a lens in a microscope
β	excess scattering length
β_{core}	excess scattering length for the core
β_{corona}	excess scattering length for the corona
γ	surface tension
δ	scaling factor relating R and DP_{corona}
Δt	small change in time
θ	scattering angle
λ	wavelength
μ-EOF	poly(ethylethylene)-b-PEO-b-poly(perfluoropropylene

	oxide) triblock terpolymers
ρ	density
$\rho_{corona}(r)$	radial density for the corona chains
$\widehat{\boldsymbol{\rho}}_{\boldsymbol{corona}}(\boldsymbol{r})$	rescaled radial density corona profile
Σ	the sum of
τ	relaxation time
τ_{fast}	relaxation time for the fast mode
χ	Scaling factor for relating N_{agg} with DP_{corona}
ω	degree of chain stretching
A_2	second virial coefficient
a_o	optimal head group area
ADF	annular dark field
AFM	atomic force microscopy
A_{corona}	amplitude of the corona
A_{core}	amplitude of the core
A_{fast}	amplitude of the fast mode
aq	aqueous

AIBN	2,2'-azo-bis(isobutyronitrile)
b	Scattering length
BCP	block copolymer
br	Broad (NMR, IR)
BTAMA	benzene-1,3,5-tricarboxamide-bearing methacrylate
C	constant
c	concentration
CALB	Candida antarctica lipase B
Calc.	calculated
CCD	charged coupled device
CEVS	controlled environment vitrification system
CFT	contrast transfer function
CRP	controlled radical polymerisation
CMC	critical micelle concentration
Cryo-ET	cryogenic electro tomography
Cryo-TEM	cryogenic transmission electron microscopy
CTA	chain transfer agent

D	translational diffusion coefficient
D_{app}	apparent translational diffusion coefficient
Đ	dispersity
d	Doublet (NMR)
Da	Daltons (g mol^{-1})
DCM	dichloromethane
DDMAT	S-1-dodecyl-S'-(α,α'-dimethyl-α”-acetic acid)trithiocarbonate
DI	deionised
DLS	dynamic light scattering
DMA	N,N-dimethylacrylamide
DMF	dimethyl formamide
DMSO	dimethyl sulfoxide
DP	degree of polymerisation
DRI	differential refractive index
dn/dc	The refractive index increment
E_0	electric field at time zero

eV	electron volts
EELS	electron energy loss spectroscopy
EDCI	*N*-Ethyl-*N*′-(3-dimethylaminopropyl)carbodiimide hydrochloride
EDX	Energy dispersive x-ray spectroscopy
EF-TEM	energy filtered TEM
EPHP	1-Ethylpiperidine hypophosphite
eq	equivalents
ET	electron tomography
EWR	exit wave reconstruction
eV	electron volt
FEG	field emission gun
g_1	electric field auto correlation function
g_2	intensity auto correlation function
GO	graphene oxide
GOX	glucose oxidase
$G(R_{core})$	Schulz distribution for the dispersity of the core radii

HAADF	High angle annular dark field
HHH	hexagonally packed hollow hoops
HPMA	N-(2-hydroxypropyl) methacrylamide
HRP	horseradish peroxidise
ICP-OES	inductively coupled plasma atomic emission spectroscopy
IR	Infra Red
I	average scattered intensity
I_o	incident radiation intensity
I_s	scattered radiation intensity
J	spin-spin coupling constant
l_c	length of hydrophobic tail
k_B	Boltzmann constant
L	length
L_{corona}	length of the corona (nm)
LCM	large compound micelles
LCV	large compound vesicles
LCST	lower critical solution temperature

LLS	laser light scattering
L_{max}	maximum polymer chain length
L_M	Monomer length
m	Multiplet (NMR)
M_n	number average molecular weight
M_w	weight average molecular weight
MW	molecular weight
MWCO	molecular weight cut-off
MW_{core}	molecular weight of the particle core
$MW_{monomer}$	Molecular weight of monomer
$MW_{particle}$	molecular weight of the particle
MW_{pincer}	Molecular weight of the pincer end group
$MW_{polymer}$	molecular weight of the polymer
m/z	mass to charge ratio
n	refractive index
NBS	*N*-bromosuccinimide
NCN	nitrogen-carbon-nitrogen

NCNR	Center for Neutron Research
N_{core}	degree of polymerisation for the core block
N_{corona}	degree of polymerisation for the corona block
N_A	Avogadro's number
NIPAM	*N*-isopropylacrylamide
NIST	National Institute of Standards and Technology
NMR	nuclear magnetic resonance
p	packing parameter
P	form factor
P_{chain}	form factor for a polymer chain
PEGMA	poly(ethylene glycol) methyl ether methacrylate
$P_{micelle}$	form factor for a micelle
ppm	parts per million
ppb	parts per billion
P4VP	poly(4-vinylpyridine)
PVP	Poly(vinyl pyridine)
Pa	Pascals

PAA	Poly(acrylic acid)
PB	poly(1,2-butadiene)
PDEAEMA	poly(N,N-diethylaminoethylmethacrylate)
PCL	Poly(caprolactone)
PEO	Poly(ethylene oxide)
PHEAm	poly(N-hydroxyethylacrylamide)
PI	Poly(isoprene)
PIAT	poly(l-isocyanoalanine(2-thiophen-3-yl-ethyl)amide)
PLLA	poly(L-lactic acid)
PMA	Poly(methyl acrylate)
PMMA	polymethyl methacrylate standards
P*n*BA	poly(*n*-butyl acrylate)
PNIPAM	Poly(*N*-isopropylacrylamide)
PS	poly(styrene)
PTA	phosphotungstic acid
P*t*BuA	poly(*t*-butyl acrylate)
q	scattering vector

RAFT	reversible addition fragmentation chain transfer
r	Absolute resolution
R	radius
R_{core}	radius of the core
R_{corona}	radius of the corona
R_{θ}	Rayeigh Ratio
$R_{\theta,fast}$	Rayeigh Ratio for the fast mode
R_g	radius of gyration
R_H	hydrodynamic radius
RT	room temperature
s	singlet (NMR)
SAED	selected area electron diffraction
SANS	small angle neutron scattering
SAXS	small angle X-ray scattering
SEM	scanning electron microscopy
SET-LRP	single electron transfer living radical polymerization
SEC	size exclusion chromatography

SCS	sulphur-carbon-sulphur
SLS	static light scattering
SLD	scattering length density
STEM	scanning transmission electron microscopy
t	time
t	triplet (NMR)
T	temperature
T_g	glass transition temperature
TEM	Transmission electron microscopy
TFA	trifluoroacetic acid
THF	tetrahydrofuran
TMS	tetramethylsilane
TMV	tobacco mosaic virus
TOF	turnover frequency
TON	turnover number
UA	uranyl acetate
UV	ultraviolet

v	volume
v_{chain}	volume of polymer chains
v_{core}	volume of the core
v_{corona}	volume of the corona
W	Watt
wt	weight
WTF	wave transfer function
Z	atomic number

Chapter 1. Introduction to block copolymer self-assembly: their structural complexity and detailed characterisation

1.1 Soft nanomaterials in solution: inspiration from Nature

There has been much interest in the construction of soft nanomaterials in solution[1] due to a desire to emulate the exquisite structure and function of Nature's equivalents (e.g. enzymes, viruses, proteins and DNA).[2] Nature's soft nanomaterials are capable of selectivity, precision and efficiency in areas such as information storage and replication, transportation and delivery, and synthesis and catalysis. To this end the use of small molecules,[3] amphiphiles,[4] colloids,[1] and polymers[5] have been investigated for the development of advanced materials in myriad fields of biomedicine and synthetic chemistry. Two major challenges are faced in this area of research: the reproducible, scalable and precise synthesis and the reliable, accurate and in-depth analysis of these materials. Chapter 2 of this thesis deals with the synthesis and self-assembly of SCS pincer palladium containing polymeric micelles for catalysis, in order to improve the efficiency and reactivity of Suzuki type reactions. The later chapters focus on the problem of analysing these types of materials. This is done by an in-depth characterisation of a SCS pincer polymer micelle system and by developing new techniques in order to both simplify the performance and increase the value of such analysis. In order to put the work in context it is necessary to review the self-assembly of polymeric materials with a specific focus on metal containing polymers and nanoreactors, as well as the common analysis techniques used for self-assembled polymers in solution.

1.2 Solution self-assembly of polymeric materials

In recent decades, the solution self-assembly of amphiphilic block copolymers (BCP)s has attracted significant attention given their potential utility in a variety of applications, including drug and gene delivery systems,[6, 7] nanoreactors,[8] and in nanoelectronics.[9] Similar to small molecule amphiphiles, amphiphilic BCPs self-assemble into a variety of structures in solution,[10] however, the macromolecular amphiphiles typically have much lower (or non-existent) critical micelle concentrations (CMC)s,[11] greatly improved kinetic stability,[12, 13] and demonstrate ease of structure modification or functionalisation.[14-16] These favourable attributes, along with significant progress in controlled polymerisation techniques,[17-20] have led to amphiphilic BCPs being extensively studied for applications that necessitate aqueous solution self-assembly.[7, 21-24]

Amphiphilic BCPs have been shown to form structures that are more complex than small molecule surfactants, **Figure 1** shows some examples of structures formed from poly(styrene)-*b*-poly(acrylic acid) (PS-*b*-PAA) block copolymers in water. In this case, the hydrophobic PS chains will aggregate together to exclude water molecules. This forces the hydrophilic PAA chains (which are covalently connected to the PS) into close proximity, forming a polymeric corona around the PS core making the particle soluble in the aqueous environment. The terms ‘core’ and ‘corona’ will be used throughout this thesis to refer to the dehydrated hydrophobic polymer blocks or hydrated hydrophilic polymer blocks within self-assembled polymer structures respectively.

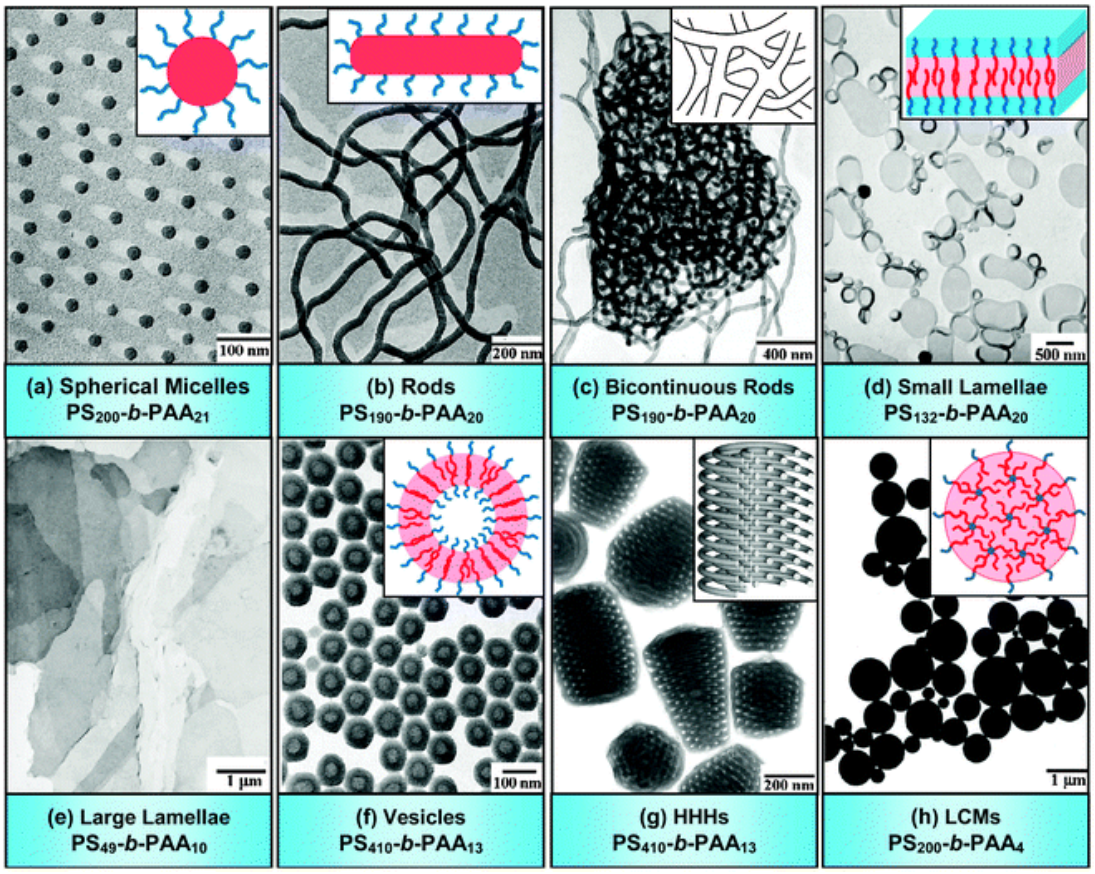

Figure 1. Transmission electron microscopy (TEM) micrographs and corresponding schematic diagrams of various morphologies formed from amphiphilic PS_m-*b*-PAA_n copolymers. In the schematic diagrams, red represents hydrophobic PS parts, while blue denotes hydrophilic PAA segments. HHHs: hexagonally packed hollow hoops; LCMs: large compound micelles, in which inverse micelles consist of a PAA core surrounded by PS coronal chains.[24]

When discussing the self-assembly of polymeric materials it is usual to direct polymer synthesis or to predict final morphology based on the packing parameter 'p': where p is related to the volume of the hydrophobic chains (υ), the optimal area of the head group (a_o) and the length of the hydrophobic tail (l_c) by the equation $p = \upsilon / a_o . l_c$. Subsequently, if $p \leq ⅓$ spherical micelles are favoured, $⅓ \leq p \geq ½$ produces cylinders and $½ \leq p \leq 1$ results in polymersomes (vesicles), **Figure 2** .

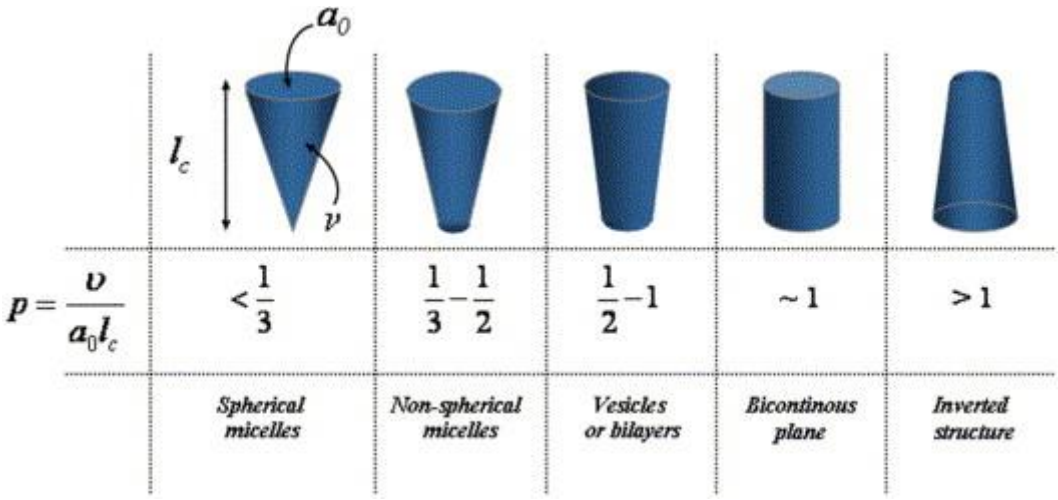

Figure 2. Schematic depicting BCP with different packing parameters (p) and their expected morphology upon self-assembly.[5]

While this can serve as a useful guide, many researchers directly relate this p value to the relative block lengths, weights or volumes of the polymers expecting that one block copolymer should form one predominant structure. However many examples exist of a single block copolymer forming multiple structures based on different preparation conditions.

Eisenberg has shown that PS_{410}-*b*-PAA_{13}, which has a packing parameter indicative of polymersome formation, is capable of forming spheres, polymersomes and multilamella structures (called large compound vesicles, [LCV]) by simply altering the amount of hydrochloric acid added to the solution during self- assembly (**Figure 3**).[25] Furthermore Eisenberg showed that the exact nature of the solvent mixture, polymer concentration, and other additives (e.g. homopolymer or surfactants) can alter the morphology obtained for a single block copolymer.[26]

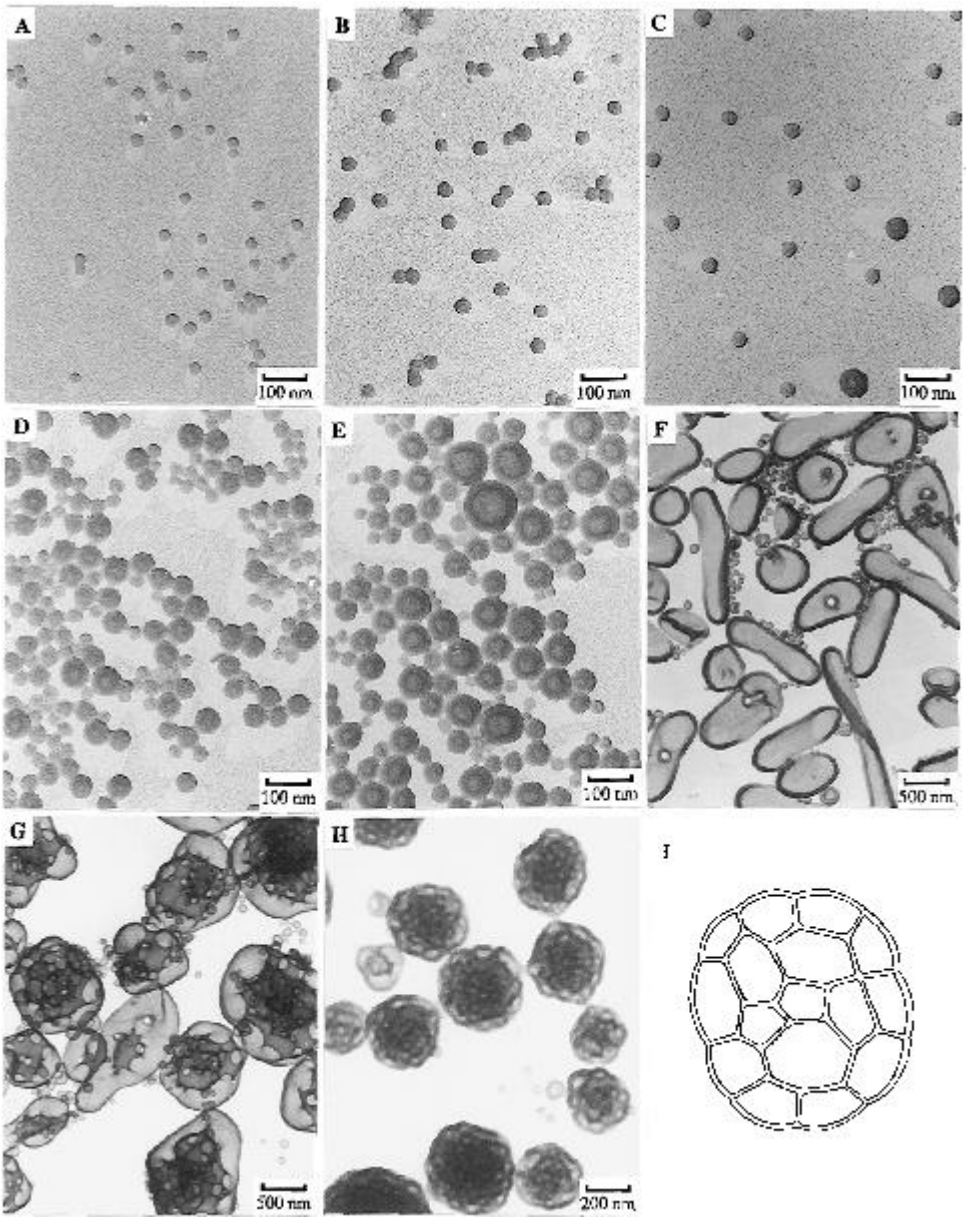

Figure 3. Aggregates from PS_{410}-*b*-PAA_{13} without any additive (A) and with added HCl to different final concentrations: (B) 113 μM; (C) 141 μM; (D) 155 μM; (E) 170 μM; (F) 200 μM; (G) 225 μM; (H) 253 μM. (I) Schematic picture of the cross-section of an LCV in (H).[25]

The reason for this complexity is that a number of factors will affect the morphology of the polymer assemblies, including the degree of stretching in the core block, the interfacial tension between the micelle core and the solvent outside the core and repulsive forces between the corona chains.[27] Furthermore, as many polymeric

micelles can be considered ‘frozen’ (i.e. no exchange of unimers over an appreciable time scale) it is therefore possible to kinetically trap various structures depending on the preparation method.[27, 28] Typically, BCP assemblies are performed by dissolving the copolymer in a good solvent for both blocks, followed by addition of a selective solvent (typically water) in order to induce self-assembly (termed the solvent switch method). Eisenberg also showed that for PS_{310}-*b*-PAA_{52} either spheres, cylinders, or vesicles could be reversibly obtained at concentrations of water, indicating that, in the formation of vesicles by this method, spheres and cylinders are formed as intermediate structures.[26]

Adams and co-workers studied a similar transition (spheres-cylinders-polymersomes) during the assembly of poly(ethylene oxide)-*b*-poly(caprolactone) (PEO-*b*-PCL) BCPs via the solvent switch method.[29] Furthermore they studied the self-assembly mechanism for a polymersome forming pH responsive PEO-*b*-poly(N,N-diethylaminoethylmethacrylate) (PEO-*b*-PDEAEMA) BCP and found that forming the polymersomes by a pH switch method resulted in a different formation mechanism (through some disordered aggregates), which precluded the encapsulation of a hydrophilic guest.[30] These results indicate that not only can final morphology be difficult to predict, but that the mechanism of the self-assembly can impact both the final structure and its performance in the desired application. As mentioned above many BCP systems are considered frozen, but this is not the case for all systems and again this will have an effect on possible applications. Nicolai, Colombani and Chassenieux have discussed the nature of ‘frozen’ vs. ‘dynamic’ polymer assemblies in detail.[28]

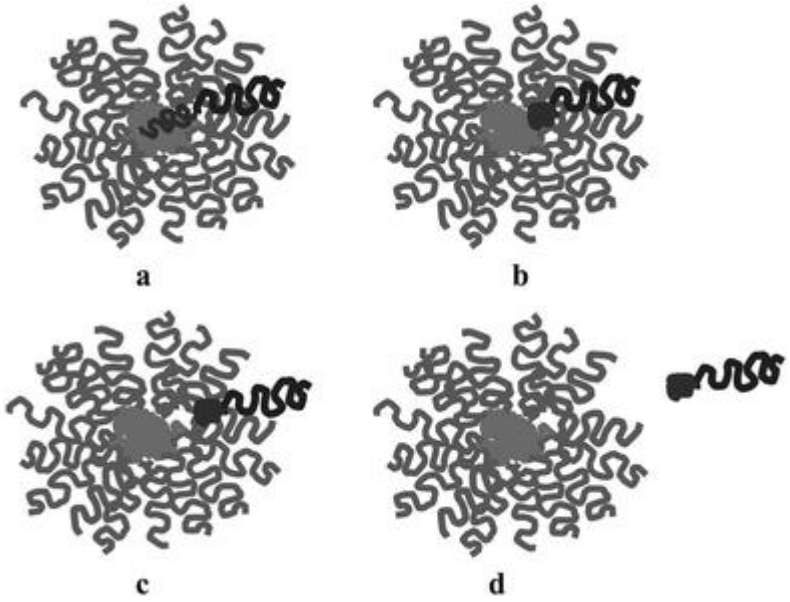

Figure 4. Schematic representation of the escape of a unimer from a polymeric micelle. The solvophobic block, which is somewhat stretched within the core (a), first has to disentangle from the core and form a condensed blob at the core–corona interface (b). Then the polymer has to diffuse through the corona (c) in order to completely liberate itself from the micelle (d).[28]

Figure 4 shows a schematic of a unimer escaping from a polymer micelle and highlights the factors affecting this process. If the polymer core is glassy (i.e. the temperature is below the polymer T_g) then no exchange will occur, however if the polymer core is above its T_g then a number of factors will affect whether or not exchange can occur. This includes the interfacial tension between the core block and the solvent, the temperature, the core block length and the core block architecture. This discussion of dynamics raises an important point on nomenclature; a polymer aggregate (umbrella term) should only be called a 'micelle' if dynamic equilibrium has been reached, whereas 'nanoparticle' is more appropriate for a kinetically trapped (frozen) system. This thesis will try to abide by these rules, however, investigating dynamics is not always simple and for many systems it is unknown whether unimers exchange or not.

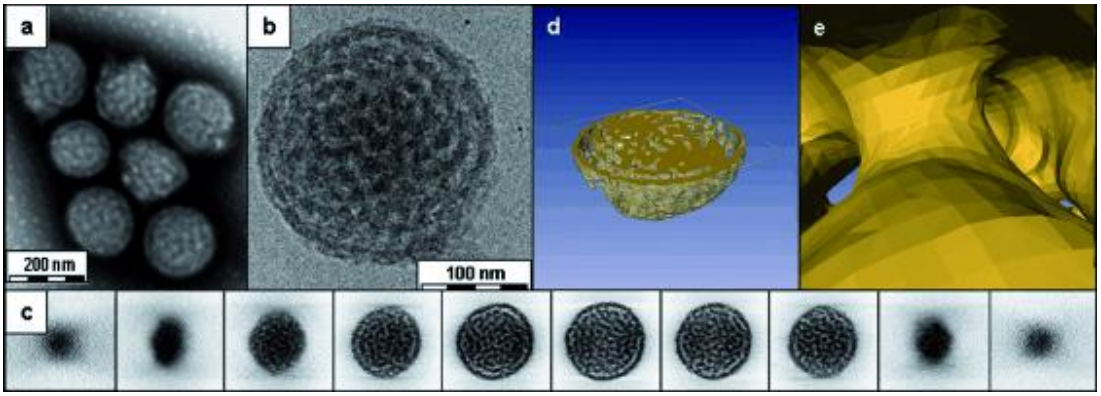

Figure 5. TEM analysis of bicontinuous aggregates. a) Conventional TEM using negative staining; b) cryoTEM image of a vitrified film; c) gallery of *z* slices showing different cross sections of a 3D SIRT (simultaneous iterative reconstruction technique) reconstruction of a tomographic series recorded from the vitrified film in (b); d,e) visualisation of the segmented volume showing d) a cross section of the aggregate and e) a view from within the hydrated channels.[31]

While spheres, cylinders and polymersomes tend to dominate the literature for diblock copolymers, other morphologies are possible. For example, Sommerdik and co-workers showed the formation of some interesting bicontinuous structures from amphiphilic double comb diblock copolymers through the use of cryo-electron tomography, **Figure 5**.[31] If triblock terpolymer systems (e.g. ABC block terpolymers) are used, the formation of many complex morphologies is possible e.g. toroids,[32] discs,[33] Janus,[34] and multicompartmental aggregates.[35] Hillmyer and Lodge have shown the formation of a variety of exquisite and complex multicompartment structures through assembly of poly(ethylethylene)-*b*-PEO-*b*-poly(perfluoropropylene oxide) triblock terpolymers, (μ-EOF),[36] and have recently reviewed the strategies for multicomparmental micelle production which is shown schematically in **Figure 6**. The complexity of self-assembled amphiphilic polymers can be increased even further through the inclusion / encapsulation of a variety of groups such as metal complexes,[37, 38] enzymes,[39] or drugs.[14]

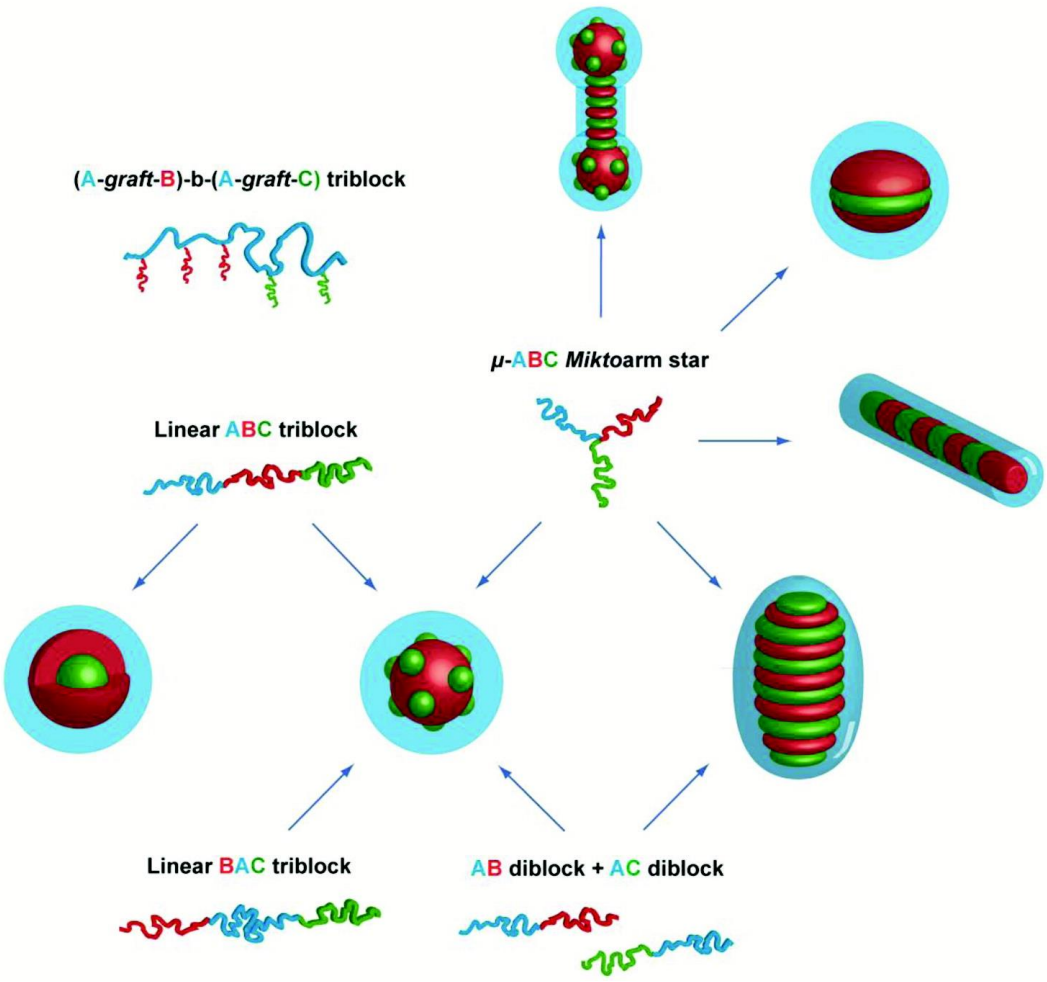

Figure 6. A schematic representation of the five principal strategies adopted for multicompartment micelle production with an illustrative example of the morphology produced.[35]

Wooley and co-workers recently reported an extremely complex system through the hierarchical assembly of cationic shell crosslinked micelles (containing siRNA and decorated with a peptide moiety) with anionic paclitaxel loaded cylinders for dual delivery and tracking of the drug and siRNA.[40] However, the inclusion / encapsulation of materials into self-assembled structures is not solely used for biomedical applications; as mentioned earlier, Nature's soft nanomaterials are capable of synthetic feats which are beyond the reach of organic chemistry.

Synthetic polymer chemists have attempted to emulate this by including catalytically active groups into amphiphilic polymers so that self-assembly can subsequently produce reactors on the nanoscale.

1.3 Reactions within self-assembled systems

There are many examples in the literature of reactions performed within micellar systems, both for small molecule surfactants[41] and amphiphilic polymers.[42] The benefits of such systems are the segregation of reactive components in order to perform cascade reactions,[43] the ability to perform reactions that typically require organic solvents in water,[44] increased local concentration of catalyst,[45] and simple catalyst recovery.[46] One example includes the elegant work of Van Hest in which a cascade reaction was performed by three step enzyme catalysis, facilitated by the incorporation of Candida antarctica lipase B (CALB), horseradish peroxidise (HRP), and glucose oxidase (GOX) to the surface, the membrane and interior water pool of a polymersome (**Figure 7**).[43, 47]

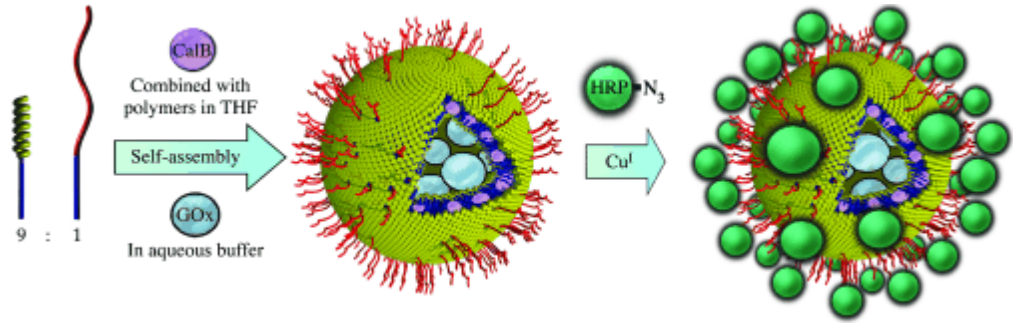

Figure 7. Positional assembly of enzymes in a polymersome. A mixture of Polystyrene-*b*-poly(l-isocyanoalanine(2-thiophen-3-yl-ethyl)amide) (PS-*b*-PIAT) functionalised with enzymes, CalB, GOx and HRP.[47]

They showed that segregation of these enzymes was necessary to perform the cascade reaction, making this not only an example of the complexity achievable in polymer self-assembly, but also an example of how the segregation of catalysts on the nanoscale can allow multiple efficient synthetic steps without the need for purification. The immobilisation of metal catalysts onto polymer supports has been extensively studied and shown to be of great benefit over small molecule analogues.[48, 49] Catalyst separation from products can be achieved by simple filtration or precipitation, enabling recovery and recycling of often expensive / precious / toxic materials. The activity / reactivity of polymer supported catalysts does not always correlate with the solution phase equivalent; an observation which has been related to a change in (possibly a more restricted) catalyst environment.[49, 50] Therefore the inclusion of metal catalysts into amphiphilic BCPs has also seen interest in the literature, as the confinement of catalysts into nanospace may alter activity or reactivity even further.[51, 52] Co(III) (salen) complexes have been incorporated into amphiphilic BCPs and self-assembled into Co containing nanoreactors. They have been shown to effectively catalyse the transformation of epoxides into enantiopure diols.[53] In a very similar study Weck and co-workers synthesised poly(2-oxazoline) based amphiphilic triblock copolymers with Co(III) (salen) functionality which assembled into spherical micelles (**Figure 8**).[54] They explored the kinetic resolution of a range of epoxides of different hydrophobicities and noted that metal leaching occurred upon recycling. They also showed that cross-linking the micelle corona reduces metal leaching in order to improve recovery and reuse over eight cycles. However this also resulted in reduced small molecule permeability and therefore reduced catalytic activity.

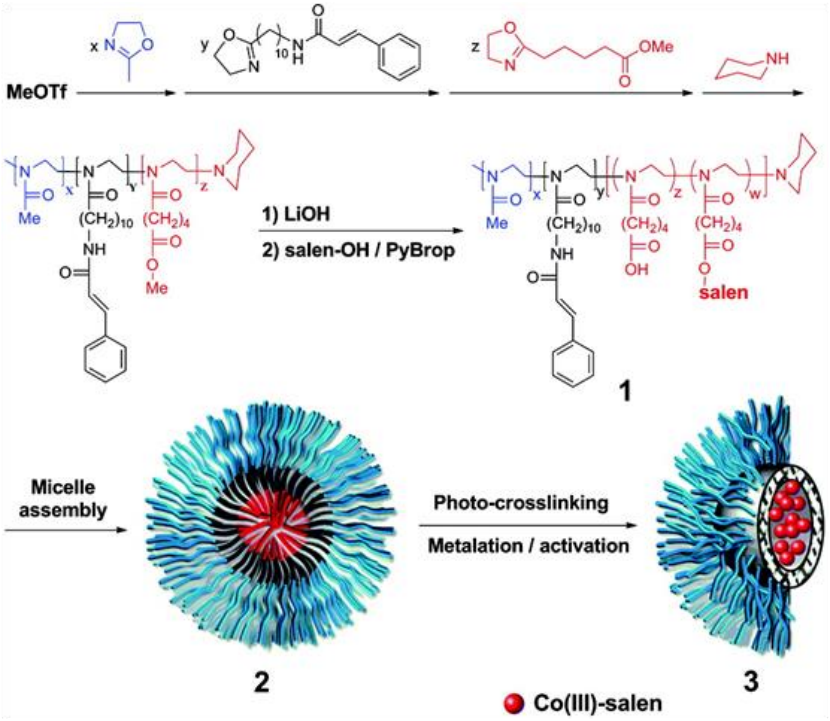

Figure 8. Schematic representation of the synthesis of poly(2-oxazoline) shell crosslinked micelles with Co(III) salen-functionalised cores.[54]

Moughton and O'Reilly created two hollow nanocages functionalised with sulphur-carbon-sulphur (SCS) pincer palladium complexes.[55, 56] They synthesised non-covalently connected block co- and block ter- polymers PS-[Pd]-PAA and PS-[Pd]-poly(methyl acrylate)-*b*-PAA (PS-[Pd]-PMA-*b*-PAA). In both cases the polymers self-assembled into spherical aggregates where the PAA corona could be cross-linked in order to stabilise the structures. They exploited the non-covalent nature of the block copolymers by disconnecting the link between the palladium and the PS block (weakly bound Pd-pyridine complex). This allowed for removal of the PS core by dialysis in THF : H_2O (1 : 4) over 4 days resulting in Pd functionalised nanocages and they proposed their use as nanoreactors for cross-coupling reactions (**Figure 9**).

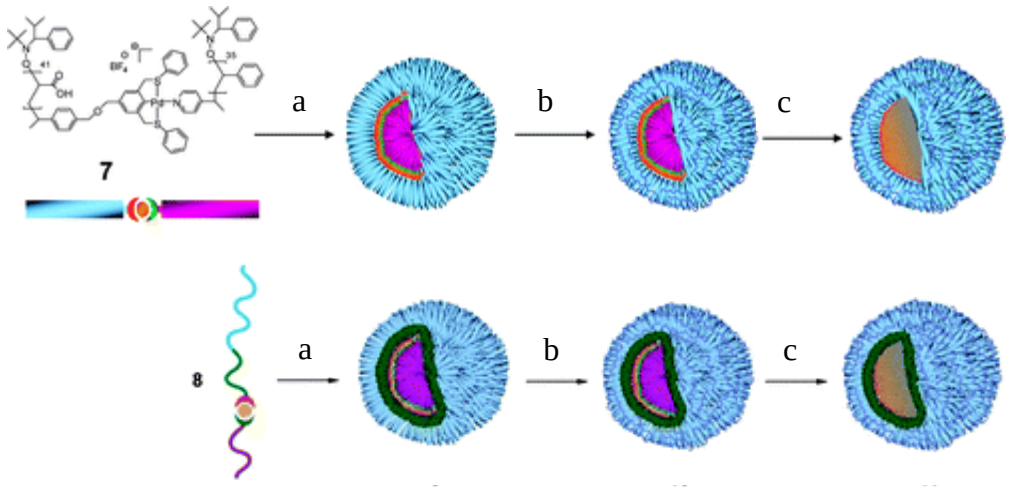

Figure 9. Metallo-block co and terpolymers capable of assembly and modification to form nanocages which are capable of encapsulating hydrophilic and hydrophobic guests.[55, 56] (a) self-assembly by solvent switch, (b) shell cross-linking and (c) core removal by dialysis in THF : H_2O (1 : 4) over 4 days

This example not only demonstrates powerful synthetic methods that can be utilised but raises important issues in analysis when faced with differentiating between similar structures which are altered through a series of modifications. Chapter 2 of this thesis shows how end group induced assembly can be used to produce SCS pincer Pd nanostructures through a synthetically simpler route and the catalytic activity of these nanoreactors is explored in comparison to small molecule pincer analogues.

1.4 Analysis of polymers assemblies in solution

As demonstrated above, the self-assembly of BCPs can be used to produce a vast array of structures with different sizes and morphologies, some of them extremely complex. With the continued improvement of polymerisation techniques,[17-20, 57] and micelle functionalisation strategies,[57-59] it is now possible to synthesise large arrays of functional nanostructures. Of particular interest are the recent developments in single electron transfer living radical polymerisation (SET-LRP) where it has been demonstrated that due to the extremely high end group fidelity and low dispersities, multiblock copolymers and sequence controlled polymers with functional units can be readily synthesised.[60, 61] As polymer synthesis is attempting to attain the precision of Nature's macromolecules, so should we attempt to match the precision and functionality of Nature's solution nanomaterials.

However, in order to take advantage of the vast array of synthetic procedures and complex self-assembly, it is of paramount importance that the structures can be readily and accurately characterised. Furthermore, when these materials are used for specific applications it would be desirable to tailor structural properties with minor alterations to either structure or assembly conditions; again these small differences must be detectable. This is not simple, however, as there are many inherent problems with analysing self-assembled polymers in solution compared to hard bulk nanomaterials, where atomic analysis is routinely applied.

While many of the standard analysis techniques available to chemists (e.g. NMR, IR, UV) can be used to infer information about polymer assemblies in

solution, the most common techniques used for initial analysis are based on microscopy or scattering. Typically a combination of microscopy and scattering techniques will be used as they provide complementary information about the particles. Scattering techniques give good statistics (typically > 10^9 particles),[62] and analysis can be conducted in solution with minimal effect on the sample. However, scattering data gives an average overview of the sample and the data is almost always fitted to a model. This means that analysing samples containing multiple structures or completely unknown structures can be very problematic. Microscopy is complementary in that the sample can be imaged directly, allowing the differences in individual particles to be readily observed. However, analysis of many particles can be time consuming and microscopy is extremely subjective; the user must not only select which areas of the sample to image but must then select which images are 'representative'. Furthermore, almost all microscopy techniques involve removing the sample from its natural state in solution and therefore image interpretation can be difficult. Both the benefits and restrictions of analysis techniques should always be kept in mind, and while the appropriate combination of well performed analysis techniques should allow accurate characterisation of the sample in question, we should always strive to improve analysis and deepen our understanding of such systems. In the subsequent sections the most common analysis techniques based on scattering and microscopy will be reviewed, detailing their various strengths and weaknesses.

1.4.1 Scattering techniques for polymeric aggregates

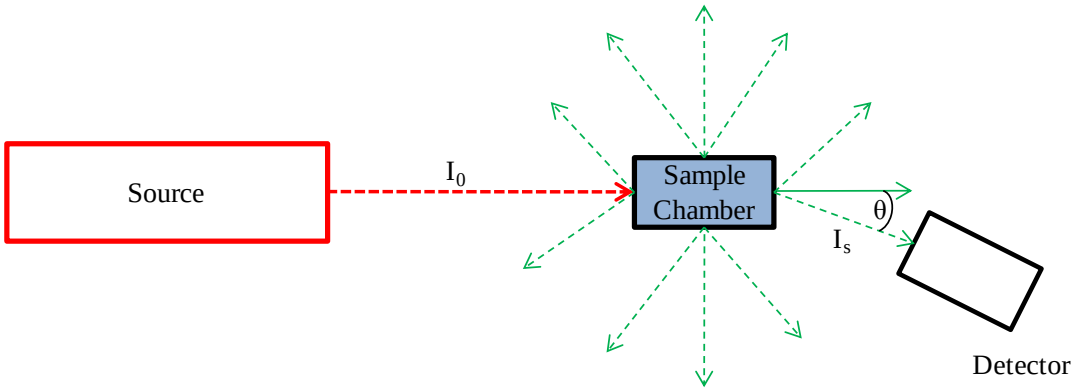

Figure 10. Basic schematic for the experimental setup of scattering experiments

The most common scattering techniques for soft materials in solution are static and dynamic light, small angle X-ray and small angle neutron scattering. A simplified schematic of the general scattering experiment is shown in **Figure 10**. Firstly, radiation of known intensity (I_o) is directed towards a sample chamber; this can be relatively cheap and simple (in the case of light) or extremely expensive and complex (in the case of neutrons). The radiation will then interact with the scattering centres (particles) within the sample which causes a deviation in trajectory (scattering). The intensity of the scattered radiation (I_s) is then detected at some angle (θ). Changing θ allows for the detection of radiation at different scattering vectors (q), where $q = 4\pi \text{ Sin } (\theta)/\lambda$, and λ is wavelength of the radiation.[*] The scattering vector q has units of reciprocal length and can be related to the length scale over which the measured radiation has been scattered. Larger q values

[*] For light scattering the refractive index of the solvent (n) must be accounted for resulting in $q = 4\pi n \text{ Sin } (\theta)/\lambda$

correspond to smaller length scales and consequently the lengths scales being measured can be somewhat tailored by changing both λ or θ. Interpreting scattering data can give information about the particles' size, shape and molecular weight, or if the data is collected as a function of time, particle dynamics can be analysed. Generally for strongly scattering systems (e.g. polymer micelles), the error in parameters obtained by DLS, SLS or SANS is roughly 10-20%,[63] which can be attributed to the accuracies in measuring the standards or backgrounds. As such, in this thesis a general error of 10% is applied to all scattering experiments. However, when comparing values from the same apparatus under the same conditions, the errors can be considered to be significantly smaller and consequently an error of 5% can be applied.[63] While there are many similarities between different scattering techniques, there are some important differences, which generally relate to the difference in λ or how the radiation interacts differently with matter.

1.4.2 Laser Light Scattering (LLS)

The following discussion of LLS highlights some of the uses and limitations of this technique in relation to the analysis of polymeric assemblies. For a more detailed discussion of LLS the reader is directed to these texts,[62, 64, 65] which were used extensively in producing the following information. Light is made up of oscillating electric and magnetic field components. When light interacts with matter (made up of positive and negative charges) it therefore has the effect of altering the spatial charge distribution within the molecules. The magnitude of this interaction is related to how easily these charges can be shifted (the polarisability). This can be determined for each sample by measuring the refractive index increment, dn/dc,

where n is the refractive index of the solution and c is the sample concentration. For BCPs one careful consideration should be the relative contribution of each block to the scattered radiation, for example if one block has a very low dn/dc compared to the other then this block should be considered 'invisible'.[66, 67] Determination of particle MW is still possible either by measuring dn/dc directly or calculating it for the mixed component system,[68,60] but care should be taken when interpreting R_g values.

Small particles (radius, $R < \lambda/20$) obey Rayleigh scattering and emit light isotropically. For larger particles ($R > \lambda/20$) there is sufficient distance between scattering centres within individual particles such that the scattered radiation can be of a sufficiently different phase to cause interference with each other.[62] This leads to anisotropic emission and consequently Mie theory is used to model the scattering.[62] These theories of light scattering are discussed in detail elsewhere,[65] but a few important consequences arise which must be kept in mind when analysing polymer nanoparticles in solution. Firstly, the intensity of light scattered (I_s) is proportional to at least the third power with respect to particle size. This can be explained by considering the relationship between I_s, molecular weight (MW) and size for a 3D object. From the Zimm equation,[62] $I_s \propto MW$, $MW \propto$ volume (equations 1) and volume $\propto L^3$ for a 3D object, where L is some length and N_A is Avogadro's number

$$\frac{\boldsymbol{MW}}{\boldsymbol{N_A}} = \boldsymbol{mass} = \boldsymbol{density} \times \boldsymbol{volume} \qquad (1)$$

Consequently, even the very low concentration impurities (e.g. dust / aggregates of particles), should they be sufficiently large, can cause a significant error in the

measurement. Secondly, for the particles obeying Mie scattering, the larger the particle, the more it scatters in the forward direction. This can have serious consequences when trying to measure highly disperse samples or samples that contain multiple size distributions. Both these issues are encountered in Chapter 3 and are dealt with by the use of multi angle DLS in combination with SLS.

When scattered photons reach the detector the number of photons per unit time is measured. If the time constant is in the range of microseconds then the solution dynamics of the particles play a role in the evolving data set (dynamic light scattering) and if the time constant is in the range of seconds then the solution dynamics are lost and only the average scattered intensity is considered (static light scattering). These two experiments, dynamic light scattering (DLS) and static light scattering (SLS) form the two basic LLS techniques used for analysing assembled polymers in solution using light.

Dynamic light scattering (DLS)

Particles in solution move under Brownian motion and their speed can be related to their (hydrodynamic) size by the Stokes-Einstein equation (equation 2).

$$\boldsymbol{R_H = \frac{k_B T}{6\pi n D}} \qquad (2)$$

Where k_B is the Boltzmann constant, T is the temperature and n in the refractive index of the solvent. The consequence of this is that the hydrodynamic radius (R_H) reported by DLS is the theoretical radius of a perfect hard sphere which moves with the same translational diffusion coefficient (D) as the particle being measured. In order to determine D it is necessary to determine the electric field auto correlation

function, $g_1(q,t)$. This is effectively a measure of how quickly the electric field changes with time. Note: it is the electric field component of light which interacts with the particles and the superpostition of all the scattered electric fields will have some value, E_0. The electric field auto correlation function, $g_1(q,t)$ can therefore be determined by equation 3 (i.e. comparing the E_0 with $E_{0+\Delta t}$, where Δt is a small change in time, for many iterations of Δt).

$$\boldsymbol{g_1(q,t) = \frac{\langle E_0(q,t) E_{0+\Delta t}(q,t)\rangle}{\langle E_o(q,t)\rangle^2}} \qquad (3)$$

However, light scattering detectors do not measure electric fields, they measure light intensity. The Siegert equation,[62] shows that the electric auto correlation function, $g_1(q,t)$ can be related to the intensity auto correlation function ($g_2(q,t)$) by the equation 4.

$$g_2(q,t) = 1 + g_1(q,t)^2 \qquad (4)$$

The intensity auto correlation function ($g_2(q,t)$) can easily be measured by equation 5 which is analogous to equation (3).

$$\boldsymbol{g_2(q,t) = \frac{\langle I_0(q,t) I_{0+\Delta t}(q,t)\rangle}{\langle I_o(q,t)\rangle^2}} \qquad (5)$$

For a single population of monodisperse spheres it has been shown that

$$\boldsymbol{g_1(q,t) = e^{-\frac{t}{\tau}}} \qquad (6)$$

Where τ is the relaxation time. Equation 7 then can be used to determine the apparent diffusion coefficient (D_{app}).

$$\boldsymbol{\tau^{-1} = D_{app} q^2} \qquad (7)$$

The most common DLS instrument is the Zetasizer range from Malvern,[69] the small bench top apparatus is easy to use a provides a quick assessment of particle size distributions. Typically for these setups θ = 173 ° (termed 'back scatter' detectors) in order to avoid scattering larger impurities such as dust. While these instruments are simple to use they are fairly limited in that they can only collect data at one angle. Although it is common to perform DLS experiments at one angle, and while this will give a reasonable indication of particle size, it is more accurate to determine D_{app} from measurements at multiple angles and plot τ^{-1} vs q^2. Furthermore, for systems which are not monodisperse (essentially all polymeric assemblies) and obey Mie scattering, there will be a differing contribution from particles of different sizes at different angles due to the anisotropic scattering behaviour of particles obeying Mie theory. Once an angular independent D_{app} is obtained, measuring this for various concentrations will allow extrapolation of D_{app} to zero concentration. This accounts for interparticle interactions and a true diffusion coefficient D can be obtained. These interactions are related to the second virial coefficient (A_2), which is discussed further in relation to static light scattering. As previously mentioned D can then be used to determine R_H using the Stokes-Einstein equation (equation 2). Due to the scaling of scattering intensity with size, R_H values from DLS can be considered as Z-averages,$\langle R_H \rangle_z$,[62]

$$\boldsymbol{\langle R_H \rangle_z = \frac{\Sigma n_i R_i^6}{\Sigma n_i R_i^5}} \qquad (8)$$

Where, n_i is the number of particles with radius i. This will be particularly important when comparing sizes obtained by different techniques. For spherical aggregates R_H depends on the maximum chain length (L_{max}) of the BCP and the degree of polymer chain stretching (ω). L_{max} can be determined from the degree of polymerisation of both blocks ($N_{core\ +\ corona}$) and the monomer length (L_M) (equation 9) (For vinyl monomers L_M = 0.25 nm).[63] ω can then be determined by equation 10.

$$\boldsymbol{L_{max} = N_{core+corona} L_M} \quad (9)$$

$$\boldsymbol{\omega = \frac{R_H}{L_{max}}} \quad (10)$$

Note: some researchers determine chain stretching by comparing R_H to the length of the unperturbed polymer in dilute solution,[70, 71] while this gives a better indication of how confined and restricted the chains are within the aggregate, the ω values given here are a better representation of whether or not the measured R_H values are realistic. For example, spherical micelles cannot have an ω value > 1. Furthermore, it would be surprising if a micelle radius approached this maximum value as typically the chains are not fully stretched.

Forster and co-workers measured R_H for a library of PS-*b*-poly(4-vinylpyridine) (PS-P4VP) BCPs in toluene which gave ω values between 0.19 and 0.46.[70] Lowe and McCormick studied a series of poly(dimethyl acrylate)-*b*-poly(N-isopropyl acrylamide) (PDMA-*b*-PNIPAM) BCPs which formed micelles upon heating, and gave ω values between 0.18 and 0.27.[72] Comombani and co-workers studied a series of poly(*n*-butyl acrylate)-*b*-PAA (P*n*BA-*b*-PAA) BCP micelles at

different ionisation degrees and salt concentrations which gave ω values between 0.21 and 0.36.[73]

Static light scattering (SLS)

Averaging the scattered light intensity measurements over time scales > 1 second results in loss of solution dynamics and consequently the information is based on particle size and shape. The Zimm equation stated in the form below (equation 11) reveals the information that can be obtained from SLS measurements performed at multiple angles (θ) and concentrations (c). The average scattered intensity of the sample (I_{sample}) is measured in relation to the average scattered intensity of the solvent ($I_{solvent}$) and a standard ($I_{standard}$). This is used to determine the Rayeigh Ratio (R_θ) for the sample, based on the known Rayleigh Ratio of the standard ($R_{\theta,standard}$), equation 11. Kc/R_θ can then be determined using equations (12) and (13) taking into account the wavelength of the laser (λ), the refractive index of the solvent ($n_{solvent}$), the dn/dc of the sample and Avogadro's number (N_A) . Plotting Kc/R_θ vs. q^2 allows for the determination of the radius of gyration (R_g) from the slope and Kc/R_θ at zero angle (zero q) by the intercept.

$$\frac{\boldsymbol{Kc}}{\boldsymbol{R_\theta}} = \frac{\boldsymbol{q^2 R^2 g}}{\boldsymbol{3MW}} + \frac{\boldsymbol{1}}{\boldsymbol{MW}} + \boldsymbol{2A_2 c} \tag{11}$$

$$\boldsymbol{R_\theta} = \frac{\boldsymbol{I_{sample} - I_{solvent}}}{\boldsymbol{I_{standard}}} \boldsymbol{R_{\theta,standard}} \tag{12}$$

$$\boldsymbol{K} = \frac{\boldsymbol{4\pi n_{solvent} \left(\frac{dn}{dc}\right)^2}}{\boldsymbol{N_A \lambda^4}} \tag{13}$$

Plotting Kc/R_θ at zero angle vs. concentration has the result of removing the q^2 term from the equation and therefore

$$\frac{Kc}{R_\theta} = \frac{1}{MW} + 2A_2c \qquad (14)$$

This allows for the determination of the molecular weight (MW), from the intercept and the second virial coefficient (A_2) from the slope. **Figure 11** shows a Zimm plot for PS-*b*-Poly(vinyl benzyl thiamine) (PS-*b*-PVBT) spherical aggregates and indicates how the different parameters can be obtained. Zimm plots are a good way to represent all the collected data on one graph, however an arbitrary constant (c), it typically applied to make the plot aesthetically pleasing.

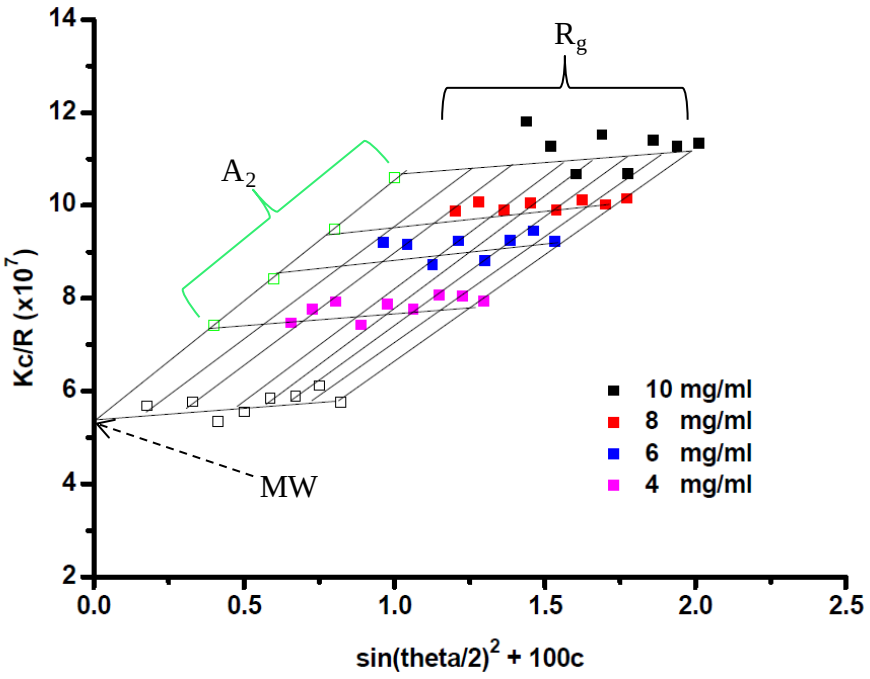

Figure 11. Zimm plot for PS-*b*-PVBT spherical aggregate. The figure indicates how the different parameters can be determined. R_g from the slope of each measured Kc/R_θ values (black, red, blue and pink squares). A_2 from the slope of the zero angle Kc/R_θ values (open green squares). MW from the intercept of the zero concentration Kc/R_θ values (open black squares). Figure adapted from.[74]

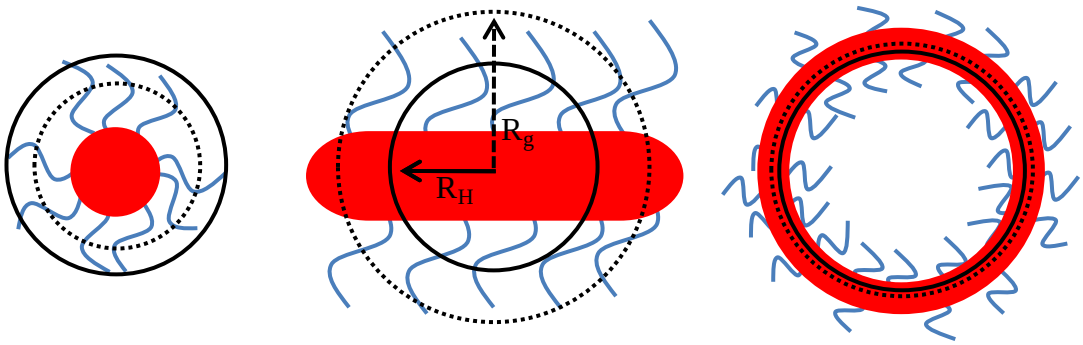

Figure 12. Schematic depicting how different morphologies would display a different R_g/R_h ratio where R_g is the radius indicated by the dashed black line and R_H is the radius indicated by the solid black line.

Static light scattering has been used widely in the investigation of polymer aggregates in solution. R_g values are effectively the mean distance of one scattering centre within the particle, from the centre of the particle as a whole and consequently the ratio of R_g / R_H can be used as a guideline to assess particle morphology.

Table 1. R_g/R_H values and how they can be related to particle morphology

R_g/R_H	Topology	Morphology inferred
0.775	Homogeneous sphere	Spherical aggregate
1	Hollow sphere	Polymersomes
> 1	Extended structure	Cylinders

For polymer assemblies particle MW is almost always used to determine the aggregation number of the assembly by the equation

$$N_{agg} = \frac{MW_{particle}}{MW_{polymer}} \quad (15)$$

As the molecular weight obtained from SLS is a weight average molecular weight, it is more appropriate to use the weight average molecular weight of the polymer (M_w), rather than the number average (M_n).

Table 2 shows typical N_{agg} values for various BCPs and morphologies. The data shows that spheres can have a range of N_{agg} values from less than ten to a few hundred, for cylinders this will of course be related to the length and can either be in the range of spheres or much larger, for polymersomes N_{agg} values are typically very large.

Table 2. Summary of N_{agg} values from SLS for various BCP assemblies

Polymer	Morphology	N_{agg} by SLS
P*n*BA-*b*-PAA[73]	Spheres	270 - 440
DMA-*b*-NIPAM[72]	Spheres	68 - 213
PS-*b*-P4VP[70]	Spheres	6 - 217
PS-*b*-Poly(l-lysine)[75]	Cylinders	60 - 600
PEO-*b*-PCL[29, 76]	Polymersomes	2,200 - 109,00

If the bulk density (ρ) of the core block polymer is known then N_{agg} can also be used to determine micelle core radius (R_{core}) through equation 16, making the assumption the core block is completely dehydrated.

$$\frac{4\pi\rho R_{core}^3}{3} = N_{agg}\frac{MW_{core}}{N_A} \quad (16)$$

Colombani and co-workers used this approach to determine R_{core} for their P*n*BA-*b*-PAA micelles in order to determine the radius of the PAA corona (R_{corona}) by the equation

$$R_{corona} = R_H - R_{core} \quad (17)$$

This allowed for a direct examination of the change in stretching of the PAA corona with changes in ionisation and salt concentrations and showed that ω values of up to 0.9 could be obtained.[63] Charged polymer coronas will have strong repulsive forces therefore ionised PAA chains should be considered extremely extended in relation to other polymer coronas.

The second virial coefficient (A_2) is effectively measuring the change in overall scattering intensity in relation to concentration and therefore gives information about interparticle interactions; these are more dominant at higher concentrations and it is this effect which necessitates extrapolation to zero concentration for the determination of particle MW. If the particles repel each other the overall scattering intensity is reduced and positive A_2 values are seen. If the overall particle-particle interactions are favoured over particle-solvent interactions then negative A_2 values are seen. Most polymer assemblies show positive A_2 values and for micelles these are on the order of 10^4 or 10^5 mL mol g^{-2}.[77, 78]

In summary Laser Light Scattering, if performed thoroughly can be a very useful tool for the investigation of assembled polymers in solution. With the

combination of DLS and SLS it should be possible to obtain the size of the core and corona, aggregation numbers as well as information on particle morphology and interparticle interactions.

1.4.3 Small Angle Neutron and Small Angle X-ray Scattering (SANS and SAXS)

The following discussion of SANS and SAXS highlights some of the uses and limitations of these techniques in relation to the analysis of polymeric assemblies. For a more detailed discussion the reader is directed to these texts,[78, 79] which were used extensively in producing the following information. SANS and SAXS are similar and complementary techniques;[79, 80] in relation to light, both neutrons and X-rays have much smaller wavelengths (typically 0.1 nm) and consequently they can probe much smaller length scales (higher *q* values). One major problem with SANS and SAXS compared to LS is the accessibility of the equipment. LS equipment is relatively cheap and can be contained on the bench top, while neutron and x-ray sources require more complex radiation sorces, e.g. they require reactors or particle accelerators. Although many X-ray experiments can performed using 'bench top' setups, for SAXS measurements of polymer assemblies in solution (i.e. carbon based samples in dilute solutions) these setups do not have high enough intensities to make appreciable measurements on realistic time scales. This is mainly due to the fact that X-rays are scattered by the electron cloud and the intensity of scattering is proportional to atomic number squared (Z^2).[80] SAXS is therefore particularly sensitive to heavier elements and this is possibly why it is less frequently used for the study of polymers assemblies in solution. Neutrons however, are scattered by the

nucleus and the intensity of scattering is dependent on the nuclear scattering length density (SLD). This is more complex than in the case of X-rays and does not scale with atomic number; fortunately SLDs can be readily determined for each sample from the chemical formula and density of the material.[80, 81]

Although not utilised in this thesis one important consequence of the SLD is that hydrogen and deuterium scatter neutrons completely differently. This principle forms the basis of many SANS experiments for polymeric aggregates as deuterating polymers can be used to selectively scatter from certain parts of the assembly.[1, 79, 80, 82] Due to the improved resolution in comparison to LLS experiments, the models for SANS and SAXS can be more complicated and many different models exist.[79, 80] However, this is generally not a problem for inexperienced users as (due to the limited availability of SANS and SAXS equipment) it is essentially impossible to perform the experiments without technical assistance from experts in the field.

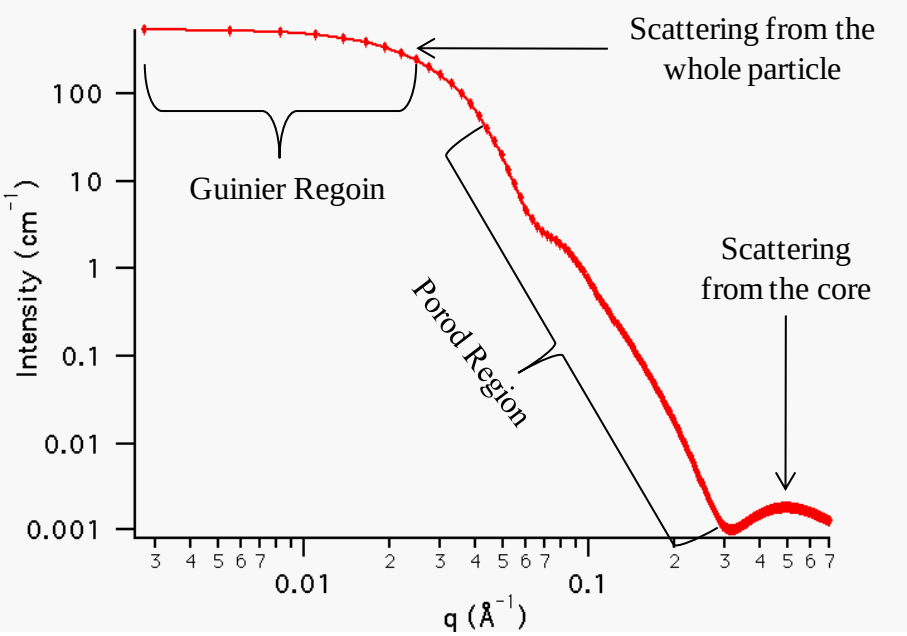

Figure 13. SANS model showing I_s vs q for a disperse spherical particle with a core-shell structure. Adapted from reference.[83]

Figure 13 shows one example of a SANS model which is suitable for spherical micelles in order to demonstrate how some information about the particles can be obtained. The Guinier region of the plot can give information about the overall size of the particle (larger particles will begin to plateau at lower q). Plotting $\ln(I_s)$ vs. q^2 for the points in this region (a Guinier plot) gives a linear fit where the slope = $R_g^{0.66}$. The Porod region corresponds to the scattering from local structure within the particle (i.e. morphology information). Plotting $\log(I_s)$ vs. $\log(q)$ should give a linear plot for this region where the slope of the curve gives information about the morphology of the sample. Hollow structures will give a q^{-2} dependence whereas solid structures will show q^{-4}. Turning points at high q are indicative of scattering from smaller structures. For a core-shell particle (where the core and shell have sufficiently different SLDs) the q value for this 'hump' can give core radius (R) information by equation 18.

$$\frac{2\pi}{q} = 2R \qquad (18)$$

Pedersen and co-workers utilised SANS and SAXS to study spherical micelles of PS-*b*-poly(isoprene) (PS-*b*-PI) in decane. The models used to treat the data assumed a solid spherical core and a corona of semi flexible chains. They were able to determine not only aggregation numbers and micelle diameters, analogous to the information obtainable by light scattering, but also information on the core size and corona profile (size and shape). Epps and Kelley used a similar SANS model to determine the core size and corona profile for poly(1,2-butadiene-*b*-PEO) (PB-*b*-PEO) aggregates in various ratios of D_2O and THF-d_8, **Figure 14**.[84]

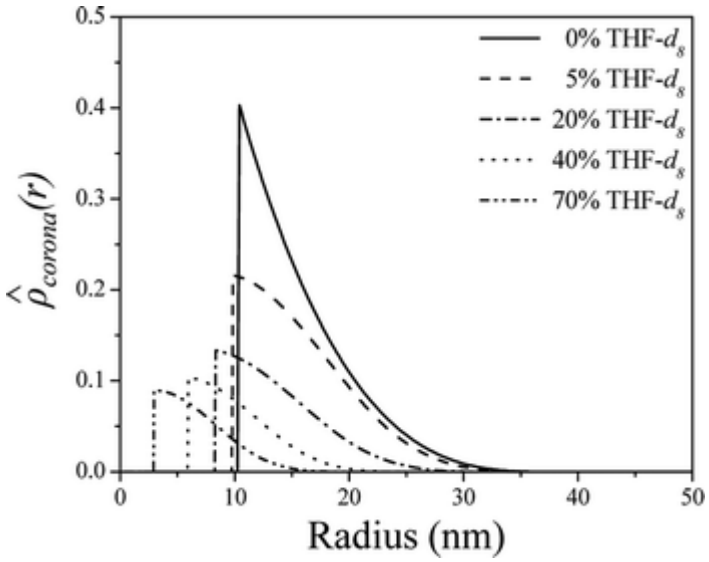

Figure 14. Radial composition profile in PEO corona in PB-PEO micelles in D_2O/THF-d_8 mixtures as determined from SANS data fitting.[84]

They showed that with increasing THF content (good solvent for both blocks) both the core and corona size decreased while the concentration of unimers in solution increased (from effectively zero to about 50 %) making the aggregates dynamic. The same arguments for determining micelle size in relation to polymer block lengths in LLS also apply for SANS and SAXS. Colombani's P*n*BA-*b*-PAA micelles discussed in the LLS section were also analysed by SANS, which allowed for the determination of N_{agg}, R_{core} and R_{corona}, and they showed the data was in rough agreement with that obtained by the LLS experiments.[63] Adams and co-workers utilised SAXS to study their PEO-*b*-PCL polymersomes, and were able to measure the membrane thickness as a function of PCL block length.[29]

In summary SANS and SAXS are extremely valuable tools for the investigation of polymer assemblies in solution. Both techniques have excellent resolutions capable of measuring differences between the core and the corona as well

as inter chain interactions. In the case of SANS the possibility of selectively scattering from different blocks by deuterium labelling allows multiple data sets to be fitted simultaneously which can improve the quality of the models.

1.4.4 Microscopy techniques for polymeric nanoparticles

The following discussion of microscopy techniques highlights some of the uses and limitations of this technique in relation to analysis of polymeric assemblies. For a more detailed discussion the reader is directed to these texts,[85-90] which were used extensively in producing the following information. Microscopy techniques complement scattering data as they directly image individual particles, typically when dried to a substrate or a support. Microscope types are numerous but can be broadly divided into two categories: optical[†] and scanning.[85] Optical microscopes use a beam of radiation (e.g. light or electrons) which is projected onto the object in order to form *an image* of that object. Scanning microscopes use a probe which scans each point of the object serially in order to form *an image* of that object. The use of italics for '*an image*' is meant as a reminder that *an image* is not the object itself, but merely a representation of the object, and furthermore, one object can be represented by many different types of *images*.

The most common types of optical microscopes are the light microscope and the transmission electron microscope, the latter of which is used extensively in this work and will be discussed in detail. Scanning microscopes are extremely numerous,

[†] Technically, optical means using light, however the term is also applied to images formed using electrons.

but for those working with soft nanomaterials, scanning electron microscopy (SEM), scanning transmission electron microscopy (STEM) and atomic force microscopy (AFM) are the most commonly used. As these only feature in Chapter 4 of this thesis, they will be discussed more briefly. The main differences in microscopy techniques come from a difference in how the image is formed. For example, images formed though transmission of radiation (e.g. TEM and STEM) show a projection of the internal structure, whereas many other types of microscopy (e.g. SEM and AFM), are only sensitive to surface (or near surface) structure and give an image which is more akin to that formed by the eye.[85]

Before discussing the various types of microscope used for the analysis of polymer aggregates in solution it is worth briefly discussing absolute resolution (r) of the light microscope and why this technique is not applicable for analysis on the nanoscale. For the light microscope (r) can be determined using equation 19 where λ is the wavelength of light, n is the refractive index of the material and α is the angle formed between the object and the lens (**Figure 15**).

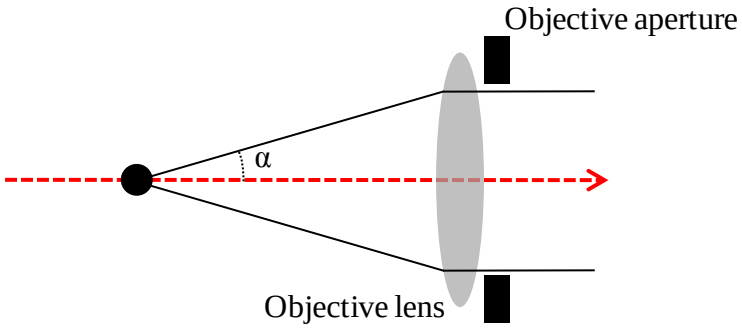

Figure 15. Schematic showing the definition of the angle α, subtended by an aperture.

$$r = \frac{0.61\lambda}{n \sin \alpha} \quad (19)$$

Consequently resolution can be increased by decreasing λ or increasing n or sin α. In practice this limits the resolution of the light microscope (λ = 200 nm for UV light) to about 150 nm and as such renders the technique of little use to those working on the nanoscale.[85] For the electron microscope the equation for absolute resolution is slightly simpler as electromagnetic lenses have a negligible effect on electron speed and α is always very small (a few degrees) such that,[85]

$$r = \frac{0.61\lambda}{\alpha} \quad (20)$$

Of course the major difference between light and electron microscopes is related to λ, which for electrons can be > 100,000 times smaller resulting in an absolute resolution of 0.003 nm (3.3 pm for 200 keV electrons). This is much smaller than the atomic radii of H (0.025 nm). While is it not quite possible to reach this resolution limit, due to aberrations caused by the electromagnetic lenses, imaging on the atomic scale for hard materials is routinely applied and even when using older, less advanced microscopes, researchers working on the nanoscale should not be concerned with the resolution limit of the microscope. The resolution for scanning microscopes varies from technique to technique, but generally they are either directly related to the size of the probe used, or to the degree in which a change in the probe (e.g. position or voltage) can be detected, the latter of which commonly results in atomic resolution.

1.4.5 Transmission Electron Microscopy (TEM)

TEM is one of the most powerful methods for analysing nanomaterials. The extremely high spatial resolution is more than sufficient for anyone working on the nanoscale, and through transmission electron tomography,[91] it is also possible to get 3D images and infer information about internal structure. Furthermore, with the use of analytical TEM techniques such as energy-filtered TEM (EF-TEM), energy-dispersive x-ray spectroscopy (EDX) and electron energy loss spectroscopy (EELS),[85] it is now possible to chemically map out nanomaterials with atomic precision. It would seem then that the transmission electron microscope should be all that is needed to image polymer assemblies in solution. There are however, some complications with TEM which have thus far limited its full potential for analysis in this area.

At ambient pressures an electron beam (200 keV) will only travel a few mm before being completely scattered by gas molecules, therefore in order to operate effectively, the transmission electron microscope must have an internal pressure of $< 10^{-10}$ Pa.[85] Consequently liquid samples cannot be easily imaged by TEM due to evaporation of the solvent, which means one of three approaches must be taken to particles in solution.

1) Samples can be dried to a substrate (dry state TEM)

2) Samples can be imaged at cryogenic temperatures, where evaporation of the solvent is minimised (Cryo-TEM)

3) Samples can be injected into a sealed TEM chamber (liquid-TEM)

There is an increasing complexity from 1 → 3, both in expense / availability of equipment and time taken to perform the analysis. Furthermore there is a decrease (from 1 → 3) in resolution and contrast, which limits the size of structures that can be analysed and the detail that can be obtained. While liquid-TEM is a very exciting method there has currently been only one report for carbon based nanomaterials, where nanolipoprotein disc stacks were imaged,[92] and therefore this technique will not be discussed further. It should also be noted that ionic liquids have been used to image soft nanomaterials at room temperature (due to their lack of vapour pressure),[93] however this is a specific example which, while interesting, is not relevant to the majority of the BCP assemblies in the literature. Dry state TEM and cryo-TEM are however extremely prevalent in the literature, and these are the central focus in Chapters 4 and 5 respectively where new methodologies which improve the imaging of soft nanomaterials are presented and evaluated.

Dry state TEM for polymer aggregates

This approach requires drying samples to a thin substrate (TEM-grid) and imaging them while dehydrated. Clearly all polymer aggregates will be affected by this drying process, which can cause changes in particle size, morphology or even complete destruction of the particles.[94] Any hydrated polymers in solution (e.g. micelle coronas) will completely change their shape upon dehydration, however polymers which are dehydrated in solution, particularly those with high a T_g (e.g. a PS core at room temperature), will be much less affected. The nature and length of the core and corona blocks should always be kept in mind when imaging in the dry state, particularly if the results are being compared to those obtained in solution. For

example, the PS_{410}-*b*-PAA_{13} spheres in **Figure 3** would likely show a very similar size by DLS and TEM as their size will be dominated by the large PS block which will not be greatly distorted upon drying. Conversely if Colombani's P*n*BA_{90}-*b*-PAA_{100} micelles were analysed by dry state TEM, their size would undoubtedly be a lot smaller than the measurements made by DLS, as their R_H will be greatly affected by the long hydrated PAA,[63] which will collapse upon drying.

The substrate to which to particles are dried is the source of another complication. Image contrast in TEM comes from either differences in the number of scattered electrons (termed mass-thickness or z-contrast) or from changes to the phase of the electron waves (termed phase contrast). For mass-thickness contrast the number of electrons scattered depends on sample thickness and electron density (thicker or more electron dense materials will scatter more electrons). To observe particles easily the sample must scatter significantly more electrons than the support; otherwise the scattering from the support will dominate the image. Typical TEM grids contain carbon based films which are roughly 40 nm thick, therefore, any carbon based sample approaching this size will be difficult to image on these grids. Although much thinner grids can be purchased (ca. 5 nm) their higher price and delicate nature has limited their use. Phase contrast mechanisms are much more complex than mass-thickness contrast, but essentially, by adjusting focus, phase contrast can be used to increase the contrast of the particles being imaged. This is discussed in more detail in Chapter 4, and although phase contrast is used widely in cryo-TEM,[95] this approach is generally not sufficient to image carbon nanostructures on conventional TEM grids.

A more common approach has been to apply high atomic number stains (e.g. osmium tetroxide, ruthenium tetroxide, uranyl acetate, and phosphotungstic acid) which will selectively bind to the grid (negative staining) or the particle (positive staining), enhancing the contrast difference between them.[89] As scattering intensity is proportional to Z^2, these stains appear extremely dark in comparison to either the support or the small carbon based particles. **Figure 16** shows polymersomes formed from PEO-*b*-poly(1,2-butylene oxide) (PEO-*b*-PBO) stained with uranyl acetate.[96] As the polymersome membrane appears dark this can be considered positive staining. In this work the authors compared the membrane sizes by staining, cryo-TEM and SAXS finding good agreement in all cases. Although uranyl acetate acted as a positive stain in this case, the nature of staining (positive or negative) will be dependent on the relative affinity for the polymer and the substrate. Generally speaking it has been shown that uranyl acetate interacts strongly with PAA, whereas osmium tetroxide and ruthenium tetroxide are known to interact with unsaturated bonds and aromatics.[89]

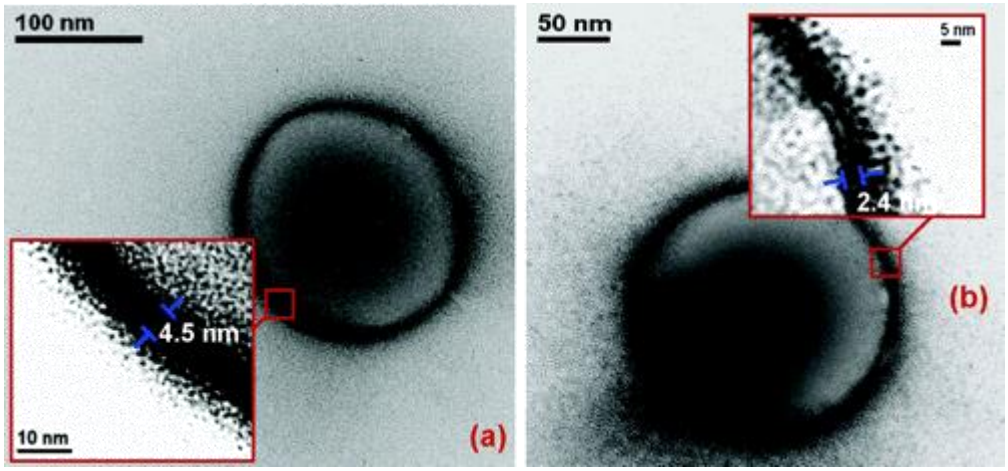

Figure 16. Transmission electron micrograph of PEO_{50}-*b*-PBO_{70} (a) and PEO_{16}-*b*-PBO_{22} (b) polymersomes stained with uranyl acetate.[96]

However, these are only guides as to which stain might be an appropriate choice for the sample in question and not only must stains be selected with care (or screened) but the application of stain to the grid must also be optimised. If too much stain is applied then the electron beam will not be able to penetrate the sample; if too little stain is applied then particle contrast will not be sufficiently enhanced. While, the staining method has proven extremely useful, it has been well known for a long time that these stains can cause artifacts, limit resolution and obscure internal structure information.[94, 95] Furthermore the screening and optimisation processes mentioned above can be very time consuming and frustrating.

With that in mind research has been conducted into creating the thinnest possible supports, so that smaller, more weakly scattering particles can be imaged without the need for staining. The thinnest conceivable support is a single atomically thin sheet of graphene, which at 0.34 nm is almost electron transparent.[97, 98] Meyer and co-workers demonstrated the potential of imaging on graphene by the observation of both carbon and hydrogen adatoms (**Figure 17**).[98] These extraordinary images demonstrated the potential TEM can bring to the analysis of soft materials when low contrast supports are used. Graphene supports have recently been used to image various structures in the dry state including DNA tetrahedra[99] and silicon nanocrystals.[100]

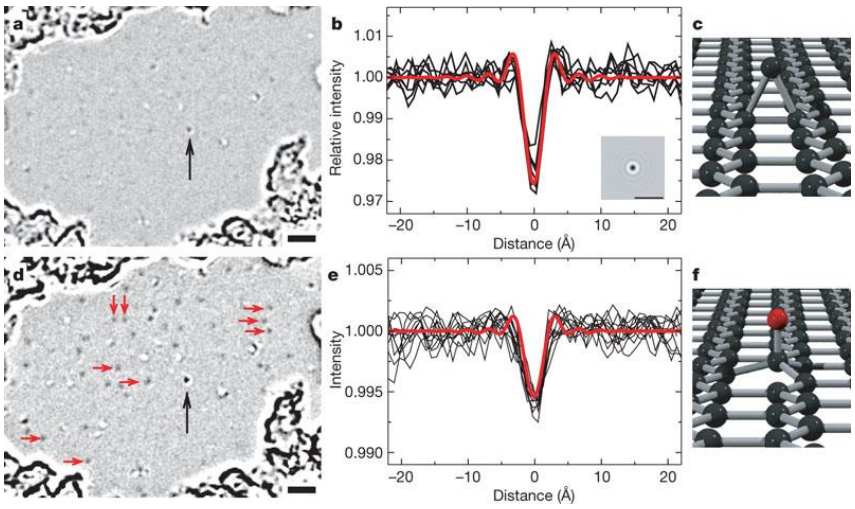

Figure 17. Adatom images. (a) Carbon adatom (indicated by black arrow), (b) Intensity profiles from several images of the carbon adatom (black traces), and a simulated profile (red trace). Inset, simulated image. (c) Carbon adatom configuration, (d) Hydrogen adatoms on the same sample (dark grey spots), a selection of which are indicated by red arrows. Black arrow again indicates the carbon adatom. (e) Profile plots of selected hydrogen adatoms from d (black traces). Red line is the simulated profile for a hydrogen adatom. (f) Hydrogen adatom configuration, All scale bars, 2 nm. [98]

However, graphene TEM-grids can be difficult to prepare and the functionality of graphene means that applying samples from aqueous solution can often be problematic. In comparison, heavily oxidised graphene (or graphene oxide) is readily available in large quantities,[101] it is water dispersible and is also robust and nearly electron transparent. Wilson and co-workers reported the first use of graphene oxide (GO) as a support for TEM in 2009 through analysis of the protein complex ferritin (**Figure 18**).[102] While these examples demonstrate the potential for analysing carbon nanomaterials in the dry state without staining, none of these substrates have been used widely for the analysis of carbon nanomaterials and there have been no reports of the analysis of BCP assemblies.

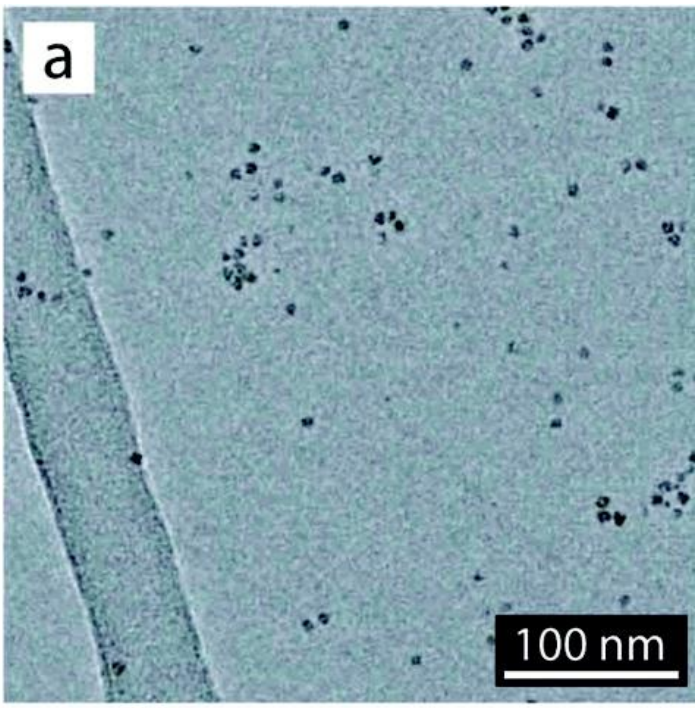

Figure 18. TEM image of ferritin (dark particles) on GO.[102]

Chapter 4 of this thesis shows that using GO-TEM grids allows an unambiguous determination of polymer assemblies in the dry state by the use of multiple TEM techniques. Furthermore it is shown that GO-TEM grids are compatible with other microscopy techniques (e.g. AFM and SEM) which allows for thorough and complementary analysis. Of course, one caveat applies to all dry state microscopy techniques: if the sample cannot survive the drying process, it cannot be analysed in the dry state. In this case imaging must be performed in solution, which is typically achieved through the use of cryo-TEM.

Cryogenic Transmission Electron Microscopy (Cryo-TEM)

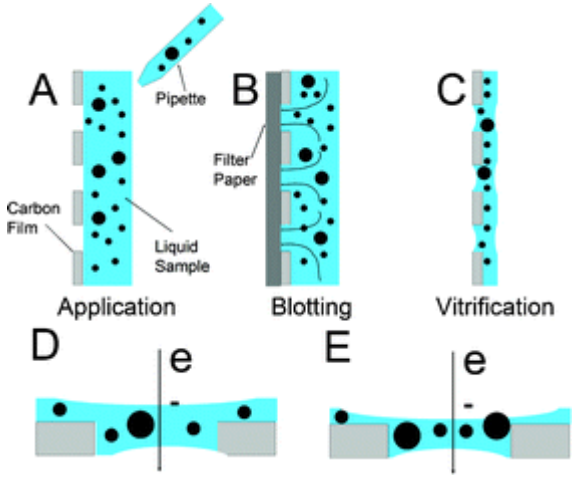

Figure 19. Schematic of cryo-TEM sample preparation: (A) Side view of a liquid containing particles (●) being applied to a perforated carbon TEM grid; (B) removal of excess solution by blotting grid with filter paper; (C) formation of vitrified thin film after rapidly plunging into a suitable cryogen; (D) expanded side view of vitrified grid showing the path of the electron beam when viewed in a TEM column; (E) size segregation may occur during sample preparation, with larger particles at the edges of the holes and smaller particles at the centre of the thin film. Large particles may also protrude from the film.[103]

The primary drawback with dry state TEM analysis is the necessity for sample dehydration before analysis. This can be avoided by the use of cryo-TEM.[95, 104] **Figure 19** shows a schematic for the preparation of cryo-TEM grids. A small volume of sample solution (typically 3 µL) is applied to a perforated TEM grid. The grid is blotted to remove almost all of the solution, creating a thin film (< 300 nm) on the grid.[103] The grid is then rapidly plunged into a vitrification solvent (typically liquid ethane) in order to trap the sample in solution. Once vitrified, the grids are kept at liquid nitrogen temperatures during transfer to the microscope. This ensures that the sample remains frozen in solution and prevents evaporation while in the microscope. With this procedure it should be possible to get a snapshot of the particles in

solution. As such, cryo-TEM has proven to be an extremely powerful technique for the analysis of polymer assemblies in solution.

The work of Adams and co-workers, discussed in section 1.2, which investigated the mechanism of polymersome formation utilised cryo-TEM,[29, 30] as did the work of Epps and Kelley,[84] and that of Colombani and co-workers,[63] discussed in the scattering section. The latter of these is shown in **Figure 20** where it can be seen that the spherical micelles are easily visualised against the background of the vitreous ice, without the need for staining techniques. As the polymer corona (PAA in this case) remains hydrated, it is not typically visible in cryo-TEM and therefore the measured particle radii correspond to the radius of the core. Assuming the core of the assembly is completely spherical, equation 16 can be used to determine N_{agg} of the assemblies and subsequently the MW of the particles. This is essentially the reverse of the calculation discussed in the LLS section. Indeed, this was done by Colombani and co-workers for the P*n*BA-*b*-PAA micelles, and again the core sizes and N_{aggs} were in rough agreement with those from LLS and SANS.[63]

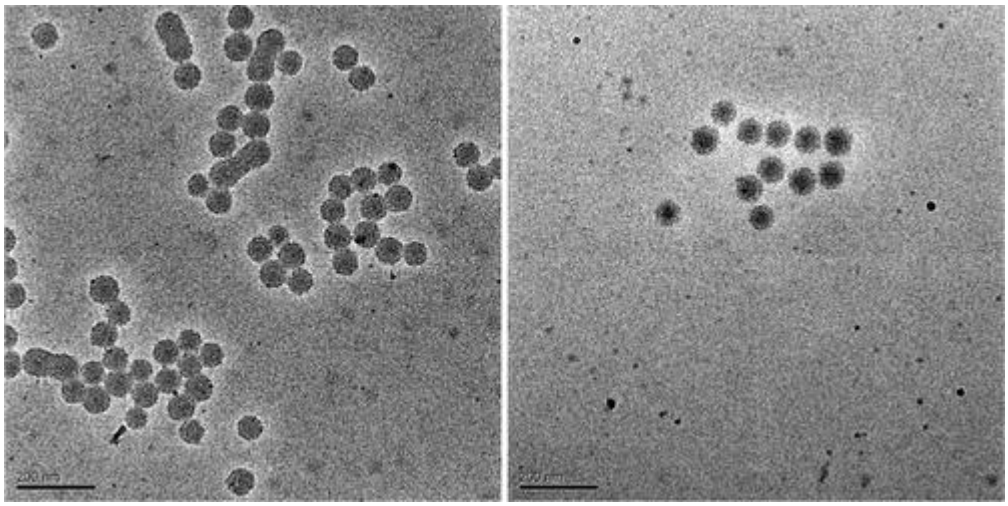

Figure 20. Cryo-TEM of P*n*BA_{90}-*b*-PAA_{300}. The scale bar corresponds to 200 nm.[63]

These examples have been used throughout this introduction, not only because they effectively demonstrate what information can be obtained by the various analysis techniques, but also because they demonstrate the power and confidence gained when using multiple techniques (importantly combining scattering and microscopy) to verify and correlate results. This is the central focus of Chapter 3 in which LS, SANS and cryo-TEM are used for the structural characterisation of amphiphilic homopolymer assemblies, where it is shown for the first time that the corona profiles obtained from cryo-TEM can be correlated to those obtained by SANS.

The disadvantages of cryo-TEM are typically associated with an increase in the time required to analyse samples and the increased cost and skills associated with grid preparation. The blotting and vitrification process mentioned above must take place in a 100 % humidity environment, to ensure that no evaporation will occur before vitrification (so that the sample is not concentrated and no cooling occurs).[95] This can be done manually or by the use of a controlled environment vitrification system (CEVS),[105] which can be particularly useful as incorrect grid preparation can lead to a variety of artifacts.[95, 103] **Figure 21** shows some typical artifacts found on cryo-TEM grids. **Figure 21C** and **D** show the effect of overblotting and unsuccessful vitrification (possibly by not plunging the grid into the vitrification solvent quickly enough) respectively.

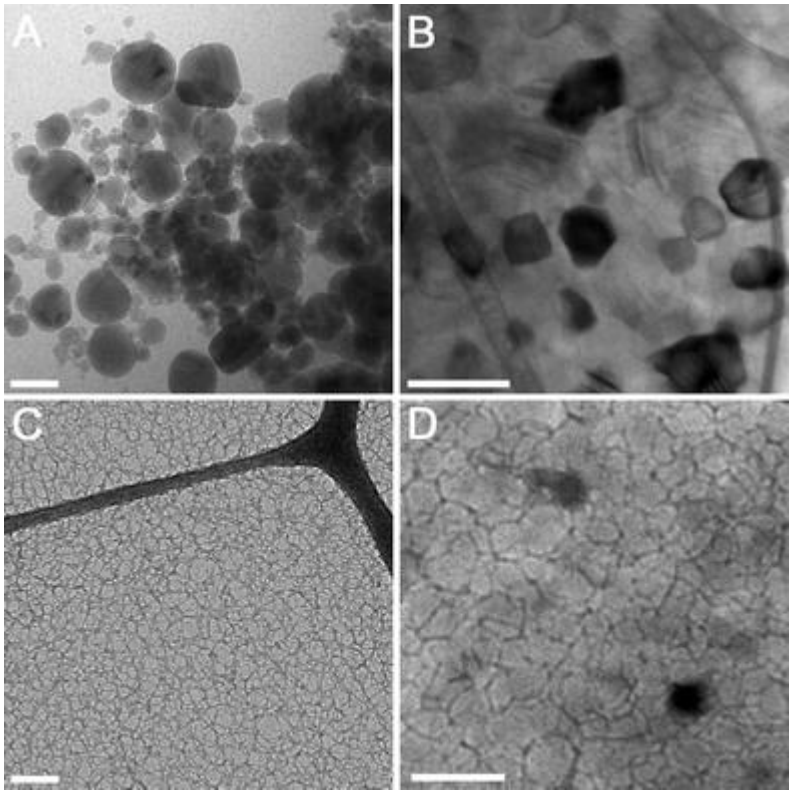

Figure 21. Artifacts of different ice forms: (A) Large ice (frost) crystals; (B) hexagonal and truncated ice crystals. Some crystals seem extremely dark due to Bragg scattering of electrons; (C) porous dry films of vitrified water, most likely due to overblotting. (D) regular polygonal ice-crystal arrangement formed upon unsuccessful vitrification. All scale bars represent 200 nm.[101]

Furthermore any exposure of the grid to air after vitrification (which is essentially unavoidable) will result in moisture from the air forming ice crystals on the cold surface of the grid. **Figure 21A** and **B** show examples of these ice crystals (they can also be seen in **Figure 20**), and demonstrate why this can be problematic while imaging as it can obscure the view of the particles, and in some cases it can be hard to distinguish between ice and particles. Furthermore, when cryo-TEM samples are inserted into the microscope an appropriate amount of time must be left before imaging in order for the beam to stabilise due to temperature fluctuations. This typically limits the number of samples which can be analysed to about six per day

for an experienced user. Extra care must also be taken when imaging as extended beam irradiation can damage both the ice and the particles, and consequently low dose techniques must be applied.[95] Another limitation for cryo-TEM, although rarely discussed, is the size limit for which particles can be detected. As shown in **Figure 21C** if the ice layer becomes too thin then it will be both mechanically and electron beam unstable. Consequently there must be a size limitation for carbon based structures, where particles below this size are not observable due to the comparatively thick ice layer. Furthermore, if the particles are too big, then they will be excluded from the ice layer during blotting and therefore particles > ca. 300 nm will be difficult to analyse by cryo-TEM. This is the central focus of Chapter 5 where it is shown that the use of GO-TEM grids in combination with cryo-TEM (termed GO-cryo-TEM) allows for the creation of 'super-thin' ice layers in order to image particles of a size which is not accessible by conventional cryo-TEM. One further limitation for cryo-TEM is that dedicated cryo-TEM instruments are often not equipped with the additional features that are routinely available on the modern TEM; for example scanning coils, which are used for imaging by STEM.

1.4.6 Scanning Transmission Electron Microscopy (STEM)

If a TEM is equipped with scanning coils, then these microscopes are usually called TEM/STEM microscopes. Instead of forming images by illuminating the object as a whole, in STEM mode images are formed by a raster scan using a small beam of electrons. The spatial resolution in STEM is therefore directly related to the size of this electron beam and for modern STEMs this can be as low as 0.08 nm. The main advantage of STEM over TEM arises from its use as a chemical analysis tool.[85]

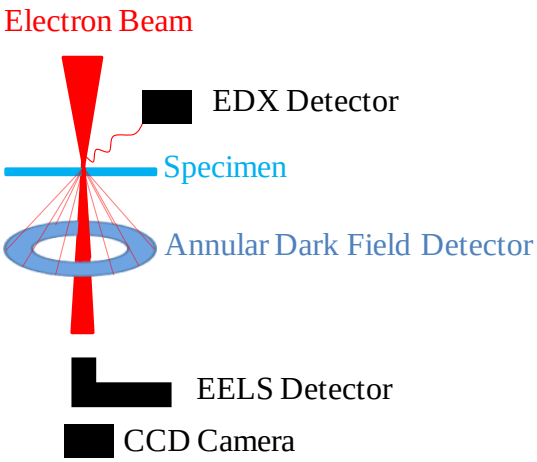

Figure 22. Schematic showing the types of information which can be obtained by STEM

In STEM it is possible to collect chemical information from using an EELS or EDX detector for each pixel in the image (**Figure 22**). EELS and EDX are complementary because X-rays are sensitive to high Z elements and EELS is more sensitive to lower Z elements.[85, 90] Another benefit of STEM is the ability to image using a high angle annular dark field (HAADF) detector (**Figure 22**). This imaging mode is often referred to as mass-thickness contrast imaging as image contrast is directly related to the electron density of the specimen (i.e. no contribution from phase contrast).

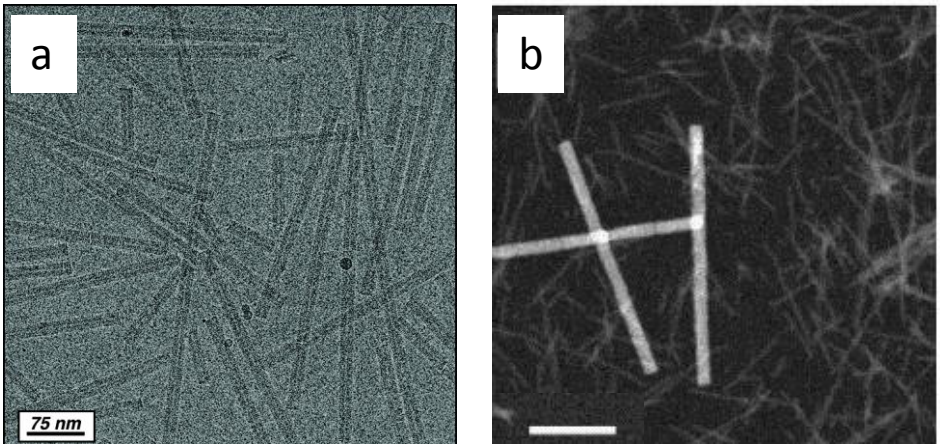

Figure 23. (a) bright field cryo-TEM and (b) HAADF image of the TMV virus, scale bar is 100 nm[90, 106]

Figure 23 shows a comparison between a bright field TEM image and a HAADF image of the tobacco mosaic virus (TMV).[90, 106] Bright field images (**Figure 23a**) are formed by collecting the transmitted electron beam (e.g. using a charge coupled device [CCD] camera, **Figure 22**); consequently areas which scatter more electrons (in this case the TMV) will appear dark. Dark field images (**Figure 23b**) are formed by collecting the scattered electrons (e.g. using an ADF detector, **Figure 22**) and therefore areas which scatter more electrons (again the TMV) will appear bright.

As they are performed in the same instrument, all the complications with sample preparation for TEM also apply to STEM, however, staining techniques are generally not used in conjunction with STEM as the benefits gained from the analytical tools are typically lost.[90] While the analytical tools of STEM can be particularly useful, some of these techniques can be obtained using far less expensive equipment, e.g. a scanning electron microscope.[85]

1.4.7 Scanning Electron Microscopy (SEM)

SEM images are formed by raster scan using a small beam of electrons (similar to STEM), however, the electrons generally have much lower energies (typically 1 - 30 keV) than those used for TEM or STEM (typically 100 – 300 keV). The beam sizes are typically much larger than those in STEM and therefore the spatial resolution is limited to about 5 nm.[85] This low resolution in comparison to TEM / STEM is probably the main reason why SEM has been less widely used for the characterisation of polymer nanostructures.

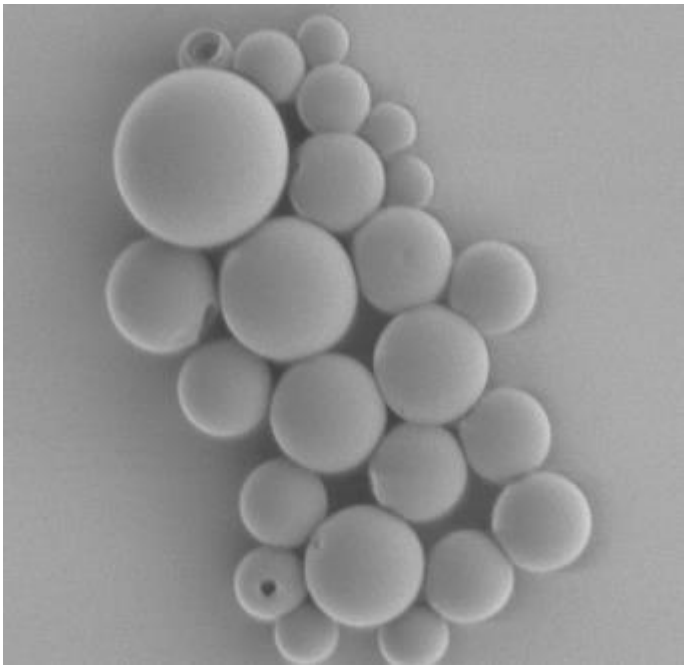

Figure 24. SEM image of PS-*b*-PIAT polymersomes.[107]

SEM is however, complementary to TEM / STEM in that the electrons are collected by a back scatter detector (i.e. not transmission). Therefore rather than giving internal structure information (as in TEM / STEM), the images provide surface (or near surface) information on the particles. SEMs are normally equipped with X-ray

detectors allowing for chemical analysis of the surface.[85] SEM instruments also operate under a vacuum, and the same sample preparation considerations that were discussed for TEM apply to SEM. Typically, carbon based samples are coated with a conducting materials (e.g. Au or Pt), which helps to avoid build-up of charge on the sample, preventing image distortion.[85] SEM has been used to identify polymersomes,[108] micelles,[109, 110] and cylindrical structures.[108] **Figure 24** is an SEM image of PS-*b*-PIAT polymersomes which shows that the internal membrane is not visible due to the surface sensitive nature of SEM. However, it is common for polymersomes to 'burst' (as can be seen at the top of **Figure 24**) during sample preparation which can reveal holes in the structures, and is often seen as evidence of a hollow interior. While SEM images can give 3D information, they cannot accurately determine the height or topology of small particles, for which AFM is a more suitable technique.

1.4.8 Atomic Force Microscopy (AFM)

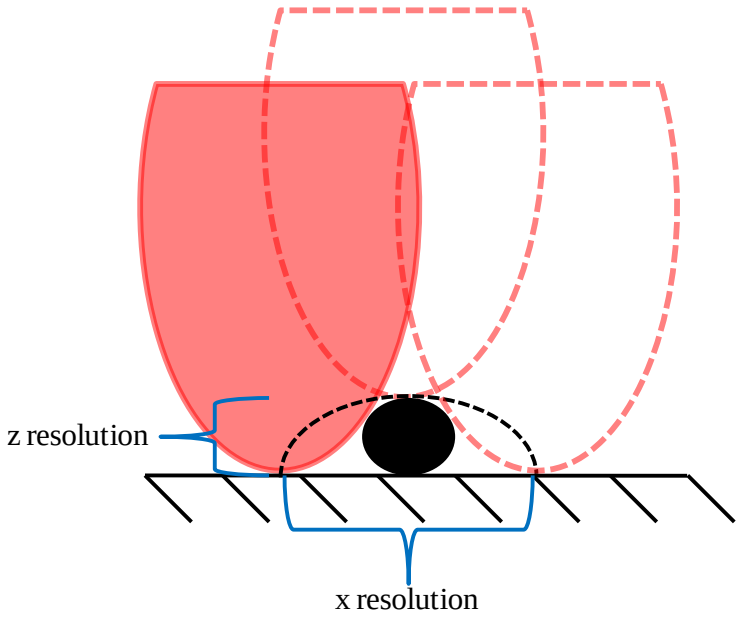

Figure 25. Schematic showing the tip convolution effects which limit the x resolution for AFM. The dashed black line indicates the movement of the tip (red oval) over the particle (black sphere)

AFM images are formed by dragging or tapping a sharp tip across the surface of the sample and, similar to SEM, can provide information about the particle surface. **Figure 25** shows how the x resolution in AFM is limited by the size of the tip due to convolution effects, and while extremely small tips exist (e.g. based on carbon nanotubes),[111] they are generally on the order of 5-10 nm.[87] However, AFM resolution in the z direction is extremely high and most AFMs are easily capable of atomic resolution.[87] This feature has made AFM analysis of extremely small particles, or particles which give weak scattering in TEM, very appealing.[112-114]

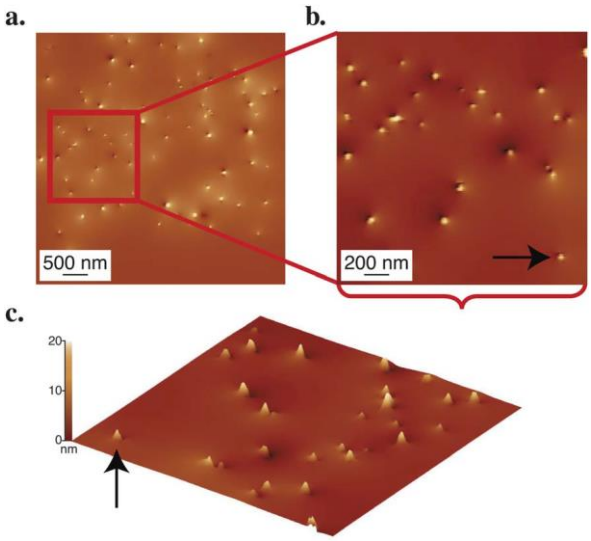

Figure 26. AFM images of single-chain polymer nanoparticles made from PHEAm.[115]

Figure 26 shows AFM images of single chain nanoparticles formed from 168 kDa poly(N-hydroxyethylacrylamide) (PHEAm).[115] The particles were analysed by DLS in water which gave R_H values of 19 nm, indicating that they are hydrated in water and therefore would probably not be visible by cryo-TEM. Once dried to the surface of the AFM substrate (mica) they are extremely flat (a few nm) which would probably make them difficult to image by TEM in the dry-state. Although more beneficial for smaller particles, AFM has still proven useful in identifying the 3D nature of larger polymer structures when dried to a surface.[116-118] Again the drying effects discussed for TEM must also be considered here, however, for AFM it is also possible to image structures while hydrated. This has proven extremely useful in the biological sciences and is therefore often termed biological AFM.[119] However, as AFM is only surface sensitive, measurements can only be made for particles that are surface active (i.e. not in the bulk), which limits its use for polymer aggregates in solution.

1.5 Summary

Although there are many applications for which the self-assembly of polymers in solution could provide utility, and while there is a vast range of synthetic and analytical techniques available, there is a long way to go before many of these applications are realised. Chapter 2 shows how amphiphilic homopolymer micelles could be used to perform coupling reactions with higher rates and lower catalyst loadings. Chapter 3 illustrates the power of complementary analysis through the combination of microscopy and scattering techniques. Generally, the analysis of polymer aggregates seeks to answer two basic questions: What is their size? And what is their morphology? Chapter 4 shows how GO-TEM grids can be used to answer these questions readily and with great confidence through the use of multiple microscopy techniques. But why stop there? Why not ask how each polymer chain is positioned within the assembly? What about the position of each individual atom? The latter of these is clearly beyond our current analysis capabilities, but in Chapter 4 we show how imaging aggregates on GO-TEM grids with the application of exit wave reconstruction, might lead us to the former. Finally, Chapter 5 demonstrates how GO-TEM grids can be used in combination with cryo-TEM to improve image contrast and analyse extremely small particles. To conclude, there is a long way to go before the characterisation of polymer aggregates in solution becomes as thorough and readily accessible as that of the polymers themselves (or even small molecules), however, many exciting advances continue to be presented in the literature to which it is hoped the work in this thesis makes a significant contribution.

1.6 References

1. I. W. Hamley, *Introduction to Soft Matter*, John Wiley & Sons, Ltd, 2007.
2. G. Pasparakis, N. Krasnogor, L. Cronin, B. G. Davis and C. Alexander, *Chem. Soc. Rev.*, 2010, **39**, 286-300.
3. J. A. A. W. Elemans, R. van Hameren, R. J. M. Nolte and A. E. Rowan, *Adv. Mater.*, 2006, **18**, 1251-1266.
4. R. Nagarajan, *Adv. Colloid Interface Sci.*, 1986, **26**, 205-264.
5. J. Rodríguez-Hernández, F. Chécot, Y. Gnanou and S. Lecommandoux, *Prog. Polym. Sci.*, 2005, **30**, 691-724.
6. A. Blanazs, S. P. Armes and A. J. Ryan, *Macromol. Rapid Commun.*, 2009, **30**, 267-277.
7. E. G. Kelley, J. N. L. Albert, M. O. Sullivan and T. H. Epps, *Chem. Soc. Rev.*, 2013. DOI:10.1039/c3cs35512h.
8. K. T. Kim, S. A. Meeuwissen, R. J. M. Nolte and J. C. M. van Hest, *Nanoscale*, 2010, **2**, 844-858.
9. G. L. M. Lazzari, S. Lecommandoux, *Block Copolymers in Nanoscience*, Wiley-VCH, 2006.
10. K. Holmberg, B. Jönsson, B. Kronberg and B. Lindman, in *Surfactants and Polymers in Aqueous Solution*, John Wiley & Sons, Ltd, 2003, pp. 1-66.
11. B. K. Johnson and R. K. Prud'homme, *Phys. Rev. Lett.*, 2003, **91**, 118302.
12. R. Zana, C. Marques and A. Johner, *Adv. Colloid Interface Sci.*, 2006, **123–126**, 345-351.

13. H. Bermudez, A. K. Brannan, D. A. Hammer, F. S. Bates and D. E. Discher, *Macromolecules*, 2002, **35**, 8203-8208.

14. M. Elsabahy and K. L. Wooley, *Chem. Soc. Rev.*, 2012, **41**, 2545-2561.

15. R. K. O'Reilly, C. J. Hawker and K. L. Wooley, *Chem. Soc. Rev.*, 2006, **35**, 1068-1083.

16. R. K. O'Reilly, M. J. Joralemon, K. L. Wooley and C. J. Hawker, *Chem. Mater.*, 2005, **17**, 5976-5988.

17. D. Benoit, V. Chaplinski, R. Braslau and C. J. Hawker, *J. Am. Chem. Soc.*, 1999, **121**, 3904-3920.

18. M. Kamigaito, T. Ando and M. Sawamoto, *Chem. Rec.*, 2004, **4**, 159-175.

19. C.-U. Lee, T. P. Smart, L. Guo, T. H. Epps and D. Zhang, *Macromolecules*, 2011, **44**, 9574-9585.

20. G. Moad, E. Rizzardo and S. H. Thang, *Polymer*, 2008, **49**, 1079-1131.

21. S. H. Choi, F. S. Bates and T. P. Lodge, *Macromolecules*, 2011, **44**, 3594-3604.

22. D. E. Discher and A. Eisenberg, *Science*, 2002, **297**, 967-973.

23. S. Jain and F. S. Bates, *Science*, 2003, **300**, 460-464.

24. Y. Mai and A. Eisenberg, *Chem. Soc. Rev.*, 2012, **41**, 5969-5985.

25. L. Zhang and A. Eisenberg, *Macromolecules*, 1996, **29**, 8805-8815.

26. A. Choucair and A. Eisenberg, *Eur. Phys. J. E.*, 2003, **10**, 37-44.

27. D. J. Adams and P. D. Topham, in *Supramoecular Chemistry*, / editors-in-chief, Philip A. Gale, Jonathan W. Steed, John Wiley & Sons, Ltd, 2012.

28. T. Nicolai, O. Colombani and C. Chassenieux, *Soft Matter*, 2010, **6**, 3111-3118.

29. D. J. Adams, C. Kitchen, S. Adams, S. Furzeland, D. Atkins, P. Schuetz, C. M. Fernyhough, N. Tzokova, A. J. Ryan and M. F. Butler, *Soft Matter*, 2009, **5**, 3086-3096.

30. D. J. Adams, S. Adams, D. Atkins, M. F. Butler and S. Furzeland, *J. Control. Release*, 2008, **128**, 165-170.

31. A. L. Parry, P. H. H. Bomans, S. J. Holder, N. A. J. M. Sommerdijk and S. C. G. Biagini, *Angew. Chem. Int. Ed.*, 2008, **47**, 8859-8862.

32. Z. Y. Chen, H. G. Cui, K. Hales, Z. B. Li, K. Qi, D. J. Pochan and K. L. Wooley, *J. Am. Chem. Soc.*, 2005, **127**, 8592-8593.

33. Z. Li, Z. Chen, H. Cui, K. Hales, K. Qi, K. L. Wooley and D. J. Pochan, *Langmuir*, 2005, **21**, 7533-7539.

34. H. Mori and A. H. E. Muller, *Prog. Polym. Sci.*, 2003, **28**, 1403-1439.

35. A. O. Moughton, M. A. Hillmyer and T. P. Lodge, *Macromolecules*, 2011, **45**, 2-19.

36. Z. Li, M. A. Hillmyer and T. P. Lodge, *Langmuir*, 2006, **22**, 9409-9417.

37. A. O. Moughton and R. K. O'Reilly, *Macromol. Rapid Commun.*, 2010, **31**, 37-52.

38. J. F. Gohy, *Coord. Chem. Rev.*, 2009, **253**, 2214-2225.

39. S. F. M. van Dongen, M. Nallani, J. J. L. M. Cornelissen, R. J. M. Nolte and J. C. M. van Hest, *Chem. Eur. J.*, 2009, **15**, 1107-1114.

40. M. Elsabahy, R. Shrestha, C. Clark, S. Taylor, J. Leonard and K. L. Wooley, *Nano Lett.*, 2013, **13**, 2172-2181.

41. T. Dwars, E. Paetzold and G. Oehme, *Angew. Chem. Int. Ed.*, 2005, **44**, 7174-7199.

42. K. T. Kim, S. A. Meeuwissen, R. J. M. Nolte and J. C. M. v. Hest, *Nanoscale*, 2010, **2**, 844-858.

43. D. M. Vriezema, P. M. L. Garcia, O. N. Sancho, N. S. Hatzakis, S. M. Kuiper, R. J. M. Nolte, A. E. Rowan and J. C. M. van Hest, *Angew. Chem. Int. Ed.*, 2007, **46**, 7378-7382.

44. G. Hamasaka, T. Muto and Y. Uozumi, *Angew. Chem. Int. Ed.*, 2011, n/a-n/a.

45. Y. Liu, Y. Wang, J. Lu, V. Pinon, 3rd and M. Weck, *J. Am. Chem. Soc.*, 2011, **133**, 14260-14263.

46. P. Cotanda, A. Lu, J. P. Patterson, N. Petzetakis and R. K. O'Reilly, *Macromolecules*, 2012, **45**, 2377-2384.

47. Stijn F. M. van Dongen, M. Nallani, Jeroen J. L. M. Cornelissen, Roeland J. M. Nolte and Jan C. M. van Hest, *Chem. Eur. J*, 2009, **15**, 1107-1114.

48. B. Clapham, T. S. Reger and K. D. Janda, *Tetrahedron*, 2001, **57**, 4637-4662.

49. N. Madhavan, C. W. Jones and M. Weck, *Acc. Chem. Res.*, 2008, **41**, 1153-1165.

50. D. C. Sherrington, *J. Polym. Sci. Part A: Polym. Chem.*, 2001, **39**, 2364-2377.

51. K. T. Kim, S. A. Meeuwissen, R. J. Nolte and J. C. van Hest, *Nanoscale*, 2010, **2**, 844-858.

52. P. Cotanda and R. K. O'Reilly, *Chem. Commun.*, 2012, **48**, 10280-10282.

53. B. M. Rossbach, K. Leopold and R. Weberskirch, *Angew. Chem. Int. Ed.*, 2006, **45**, 1309-1312.

54. Y. Liu, Y. Wang, Y. Wang, J. Lu, V. Piñón and M. Weck, *J. Am. Chem. Soc.*, 2011, **133**, 14260-14263.

55. A. O. Moughton and R. K. O'Reilly, *J. Am. Chem. Soc.*, 2008, **130**, 8714-8725.

56. A. O. Moughton, K. Stubenrauch and R. K. O'Reilly, *Soft Matter*, 2009, **5**, 2361-2370.

57. R. Fu and G.-D. Fu, *Polym. Chem.*, 2011, **2**, 465-475.

58. N. Li and W. H. Binder, *J. Mater. Chem.*, 2011, **21**, 16717-16734.

59. C. F. Hansell and R. K. O'Reilly, *ACS Macro Letters*, 2012, **1**, 896-901.

60. Q. Zhang, J. Collins, A. Anastasaki, R. Wallis, D. A. Mitchell, C. R. Becer and D. M. Haddleton, *Angew. Chem. Int. Ed.*, 2013, **52**, 4435-4439.

61. A. H. Soeriyadi, C. Boyer, F. Nyström, P. B. Zetterlund and M. R. Whittaker, *J. Am. Chem. Soc.*, 2011, **133**, 11128-11131.

62. W. Schärtl, *Light Scattering from Polymer Solutions and Nanoparticle Dispersions*, Springer Berlin Heidelberg, Verlag Berlin Heidelberg, 2007.

63. O. Colombani, M. Ruppel, M. Burkhardt, M. Drechsler, M. Schumacher, M. Gradzielski, R. Schweins and A. H. E. Müller, *Macromolecules*, 2007, **40**, 4351-4362.

64. N. C. Santos and M. A. Castanho, *Biophys. J.*, 1996, **71**, 1641-1650.

65. M. Jonasz and G. R. Fournier, in *Light Scattering by Particles in Water*, Academic Press, Amsterdam, 2007, pp. 87-143.

66. Y. Tsunashima and Y. Kawamata, *Macromolecules*, 1993, **26**, 4899-4909.

67. G. Guérin, J. Raez, I. Manners and M. A. Winnik, *Macromolecules*, 2005, **38**, 7819-7827.

68. W. Bushuk and H. Benoit, *Can. J. Chem.*, 1958, **36**, 1616-1626.

69. http://www.malvern.com (April 2013).

70. S. Forster, M. Zisenis, E. Wenz and M. Antonietti, *J. Chem. Phys.*, 1996, **104**, 9956-9970.

71. L. Zhang and A. Eisenberg, *Polym. Adv. Technol.*, 1998, **9**, 677-699.

72. A. J. Convertine, B. S. Lokitz, Y. Vasileva, L. J. Myrick, C. W. Scales, A. B. Lowe and C. L. McCormick, *Macromolecules*, 2006, **39**, 1724-1730.

73. O. Colombani, M. Ruppel, F. Schubert, H. Zettl, D. V. Pergushov and A. H. E. Müller, *Macromolecules*, 2007, **40**, 4338-4350.

74. R. McHale, J. P. Patterson, P. B. Zetterlund and R. K. O'Reilly, *Nature Chem.*, 2012, **4**, 491-497.

75. A. Lübbert, V. Castelletto, I. W. Hamley, H. Nuhn, M. Scholl, L. Bourdillon, C. Wandrey and H.-A. Klok, *Langmuir*, 2005, **21**, 6582-6589.

76. R. Šachl, M. Uchman, P. Matějíček, K. Procházka, M. Štěpánek and M. Špírková, *Langmuir*, 2007, **23**, 3395-3400.

77. K. Khougaz, I. Astafieva and A. Eisenberg, *Macromolecules*, 1995, **28**, 7135-7147.

78. L. J. M. Vagberg, K. A. Cogan and A. P. Gast, *Macromolecules*, 1991, **24**, 1670-1677.

79. J. S. Higgins and H. Benoît, *Polymers and neutron scattering*, Clarendon Press Oxford, 1994.

80. R.-J. Roe and R. Roe, *Methods of X-ray and neutron scattering in polymer science*, Oxford University Press New York, 2000.

81. http://www.ncnr.nist.gov/resources/sldcalc.html (March 2013).

82. J. S. Pedersen, I. W. Hamley, C. Y. Ryu and T. P. Lodge, *Macromolecules*, 2000, **33**, 542-550.

83. V. Degiorgio and M. Corti, *Physics Of Amphiphiles: Micelles, Vesicles And Microemulsions: Proceedings Of The International School Of Physics*, Elsevier Science Ltd, 1985.

84. E. G. Kelley, T. P. Smart, A. J. Jackson, M. O. Sullivan and T. H. Epps, *Soft Matter*, 2011, **7**, 7094-7102.

85. P. J. Goodhew, F. J. Humphreys and R. Beanland, *Electron microscopy and analysis*, Taylor & Francis Group, 2001.

86. D. B. Williams and C. B. Carter, *The Transmission Electron Microscope*, Springer, 1996.

87. F. J. Giessibl, *Reviews of Modern Physics*, 2003, **75**, 949-983.

88. J. Loos, E. Sourty, K. B. Lu, G. de With and S. van Bavel, *Macromolecules*, 2009, **42**, 2581-2586.

89. M. R. Libera and R. F. Egerton, *Polym. Rev.*, 2010, **50**, 321-339.

90. A. A. Sousa and R. D. Leapman, *Ultramicroscopy*, 2012, **123**, 38-49.

91. A. J. Koster, R. Grimm, D. Typke, R. Hegerl, A. Stoschek, J. Walz and W. Baumeister, *J. Struct. Biol.*, 1997, **120**, 276-308.

92. J. E. Evans, K. L. Jungjohann, P. C. K. Wong, P.-L. Chiu, G. H. Dutrow, I. Arslan and N. D. Browning, *Micron*, 2012, **43**, 1085-1090.

93. R. R. Maddikeri, S. Colak, S. P. Gido and G. N. Tew, *Biomacromolecules*, 2011, null-null.

94. Y. Talmon, *J. Colloid Interface Sci.*, 1983, **93**, 366-382.

95. H. Friedrich, P. M. Frederik, G. de With and N. A. J. M. Sommerdijk, *Angew. Chem. Int. Ed.*, 2010, **49**, 7850-7858.

96. G. Battaglia and A. J. Ryan, *J. Am. Chem. Soc.*, 2005, **127**, 8757-8764.

97. G. Eda, G. Fanchini and M. Chhowalla, *Nature Nano.*, 2008, **3**, 270-274.

98. J. C. Meyer, C. O. Girit, M. F. Crommie and A. Zettl, *Nature*, 2008, **454**, 319-322.

99. S. Buckhout-White, J. T. Robinson, N. D. Bassim, E. R. Goldman, I. L. Medintz and M. G. Ancona, *Soft Matter*, 2013.

100. M. G. Panthani, C. M. Hessel, D. Reid, G. Casillas, M. José-Yacamán and B. A. Korgel, *J.Phys. Chem. Part C*, 2012, **116**, 22463-22468.

101. D. R. Dreyer, S. Park, C. W. Bielawski and R. S. Ruoff, *Chem. Soc. Rev.*, 2010, **39**, 228-240.

102. N. R. Wilson, P. A. Pandey, R. Beanland, R. J. Young, I. A. Kinloch, L. Gong, Z. Liu, K. Suenaga, J. P. Rourke, S. J. York and J. Sloan, *ACS Nano*, 2009, **3**, 2547-2556.

103. H. Cui, T. K. Hodgdon, E. W. Kaler, L. Abezgauz, D. Danino, M. Lubovsky, Y. Talmon and D. J. Pochan, *Soft Matter*, 2007, **3**, 945-955.

104. S. Zhong and D. J. Pochan, *Polym. Rev.*, 2010, **50**, 287-320.

105. J. R. Bellare, H. T. Davis, L. E. Scriven and Y. Talmon, *J. Electron. Microsc. Technique*, 1988, **10**, 87-111.

106. R. S. Pantelic, J. W. Suk, Y. Hao, R. S. Ruoff and H. Stahlberg, *Nano Lett.*, 2011, **11**, 4319-4323.

107. D. M. Vriezema, J. Hoogboom, K. Velonia, K. Takazawa, P. C. M. Christianen, J. C. Maan, A. E. Rowan and R. J. M. Nolte, *Angew. Chem. Int. Ed.*, 2003, **42**, 772-776.

108. J. T. Xu, L. Tao, C. Boyer, A. B. Lowe and T. P. Davis, *Macromolecules*, 2011, **44**, 299-312.

109. Y. Q. Yang, L. S. Zheng, X. D. Guo, Y. Qian and L. J. Zhang, *Biomacromolecules*, 2011, **12**, 116-122.

110. M. D. Hossain, L. T. B. Tran, J. M. Park and K. T. Lim, *J. Polym. Sci. Part A: Polym. Chem.*, 2010, **48**, 4958-4964.

111. N. R. Wilson and J. V. Macpherson, *Nat Nano*, 2009, **4**, 483-491.

112. N. Ormategui, I. Garcia, D. Padro, G. Cabanero, H. J. Grande and I. Loinaz, *Soft Matter*, 2012, **8**, 734-740.

113. P. Wang, H. Pu and M. Jin, *J. Polym. Sci. Part A: Polym. Chem.*, 2011, **49**, 5133-5141.

114. C. T. Adkins, H. Muchalski and E. Harth, *Macromolecules*, 2009, **42**, 5786-5792.

115. E. A. Appel, J. d. Barrio, J. Dyson, L. Isaacs and O. A. Scherman, *Chem. Sci.*, 2012, **3**, 2278-2281.

116. Z. Li, J. Ma, N. S. Lee and K. L. Wooley, *J. Am. Chem. Soc.*, 2011, **133**, 1228-1231.

117. A. Presa Soto, J. B. Gilroy, M. A. Winnik and I. Manners, *Angew. Chem. Int. Ed.*, 2010, **49**, 8220-8223.

118. G. Hamasaka, T. Muto and Y. Uozumi, *Angew. Chem. Int. Ed.*, 2011, **50**, 4876-4878.

119. I. Casuso, F. Rico and S. Scheuring, *J. Mol. Recognit.*, 2011, **24**, 406-413.

Chapter 2. Catalytic Y-tailed amphiphilic homopolymers: aqueous nanoreactors for high activity, low loading SCS pincer catalysts

2.0 Abstract

A new amphiphilic homopolymer bearing an SCS pincer palladium complex has been synthesised by reversible addition fragmentation chain transfer polymerization. The amphiphile has been shown to form spherical and worm-like micelles in water by cryogenic transmission electron microscopy and small angle neutron scattering. Segregation of reactive components within the palladium containing core results in increased catalytic activity of the pincer complex compared to a small molecule analogue. This allows carbon-carbon bond forming reactions to be performed in water with reduced catalyst loadings and enhanced activity.

2.1 Introduction

In recent decades, the solution self-assembly of amphiphiles has attracted significant attention in the field of catalysis. Both small molecular surfactant[1-5] and amphiphilic BCP[6-8] systems have been investigated and shown to increase catalyst efficiency. The advantages of these self-assembled structures over non-supported systems include the segregation of reactive components in order to perform cascade reactions,[9, 10] the ability to react hydrophobic substrates in water,[6] increased local concentration of substrates[11-15] and simple catalyst recovery.[8]

Reports can also be found for the solution self-assembly of another class of amphiphiles, so-called 'associative polymers' or 'amphiphilic homopolymers'.[16-35] Examples of these systems include homopolymers where the monomer units contain both hydrophilic and hydrophobic moieties[17, 19, 20] or homopolymers

end-functionalised with ionic head groups,[18] enzymes,[16] or small hydrophobic groups, such as alkyl chains.[20, 22-24, 26-30, 36] Much of the work on end-functionalised homopolymers focuses on telechelic polymers, where both chain ends are functionalised with small hydrophobic groups.[22, 23, 25-28] Telechelic polymers with hydrophobic contents as low as 2 wt % have been shown to self-assemble into flower-like micelles,[23, 25] as well as other complex structures in aqueous solutions.[22] The self-assembly of mono-functionalised amphiphilic homopolymers, poly(ethylene oxide)[27-30] and poly(*N*-isopropylacrylamide)[31, 36] end-functionalised with single alkyl chains have been shown to self-assemble into star-like micelles in aqueous solutions. Additionally, amphiphilic homopolymers end-functionalised with two-tailed or 'Y-tailed' hydrophobic groups are reported in the literature.[21, 31-38] Many of these examples are lipid-functionalised polymers used to sterically stabilise liposomes,[21, 33, 34] with only a few examples demonstrating the self-assembly of Y-tailed amphiphilic homopolymers in aqueous solutions.[21, 35, 37] The use of end functionalised amphiphilic homopolymers for the formation of nanoreactors presents a potentially simple route in comparison to BCP assembly in order to investigate the catalytic activity of these systems. Palladium is one of the most widely used metals for the catalysis of organic reactions and it is often employed in combination with different ligands for a variety of highly selective chemical transformations.[39]

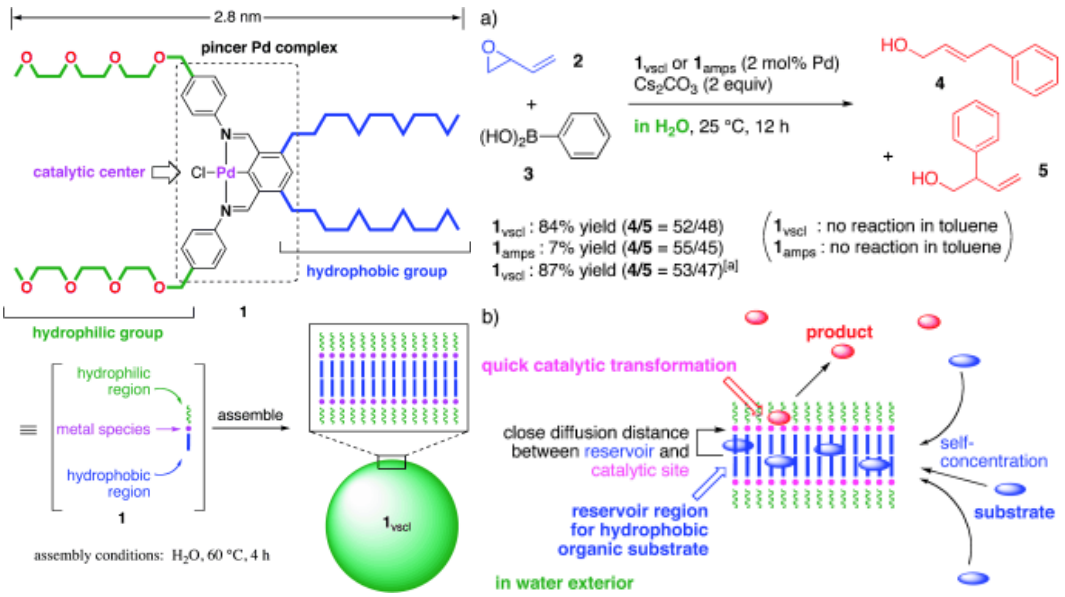

Figure 27. (left) Formation of vesicle by self-assembly of the pincer palladium complex 1, (right) (a) Palladium-catalyzed oxirane ring opening with $PhB(OH)_2$ and (b) Schematic image of the concept of catalysis within the bilayer membrane of the vesicle.[40]

Like many other catalysts, it would be desirable to obtain a general protocol in order to perform reactions at low catalyst loadings with easy recovery, and under ambient conditions (i.e. low temperatures, in air and / or water). In this direction, extensive research has been conducted on supported Pd using silica, polymers, carbon etc., to allow simple catalyst recovery and recyclability.[41] Uozumi and co-workers recently synthesised a nitrogen-carbon-nitrogen (NCN) pincer Pd-amphiphile which, after heating in water at 60 °C for 4 hours, assembled into vesicles with an average diameter of 500 nm (**Figure 27**). The vesicles were capable of sequestering hydrophobic substrates into the membrane where the palladium complex could catalyse the Suzuki-Miyaura reaction. This allowed for the catalysis of non-water-soluble materials to take place in an overall aqueous medium.[42] Unfortunately, neither recyclability nor increased activity (compared to reactions in organic

solvents) was shown in this work. In this chapter the synthesis and self-assembly of a novel sulfur-carbon-sulfur (SCS) pincer Pd nanoreactor is reported and the rates are compared to a small molecule analogue, molecularly dissolved in organic solvents. Rate increases of > 100 times are observed over the small molecule non-self-assembled analogue, allowing for effective catalysis of a model cross-coupling reaction at significantly reduced catalyst loadings.

2.2 Results and discussion

2.2.1 Chain Transfer Agent design

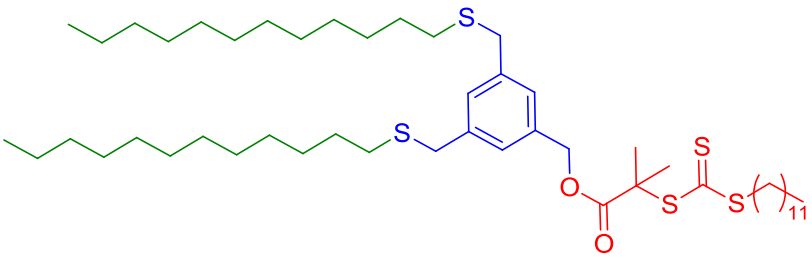

Figure 28. Chain transfer agent structure highlighting the three key features: the trithiocarbonate (red), the SCS pincer (blue) and the dodecyl chains (green)

The chain transfer agent (CTA) in **Figure 28** consists of three important moieties: 1) the trithiocarbonate (red), which is based on a CTA capable of polymerising a wide range of vinyl monomers (e.g. styrenes, acrylates, acrylamides);[43] 2) the SCS pincer moiety (blue) which is capable of complexation to Pd making it catalytically active;[44] and 3) the dodecyl chains (green) attached to sulfur groups which make the pincer moiety hydrophobic and should cause aggregation in an aqueous environment. Therefore, upon polymerisation of a hydrophilic monomer and

complexation with palladium, the resulting polymer should be able to form catalytically active nanostructures in water. This should provide, in comparison to the Pd functionalised nanocages previously reported by Moughton and O'Reilly,[44, 45] a relatively simple route to these types of structures.

2.2.2 Synthesis of SCS Pincer CTA 2.06

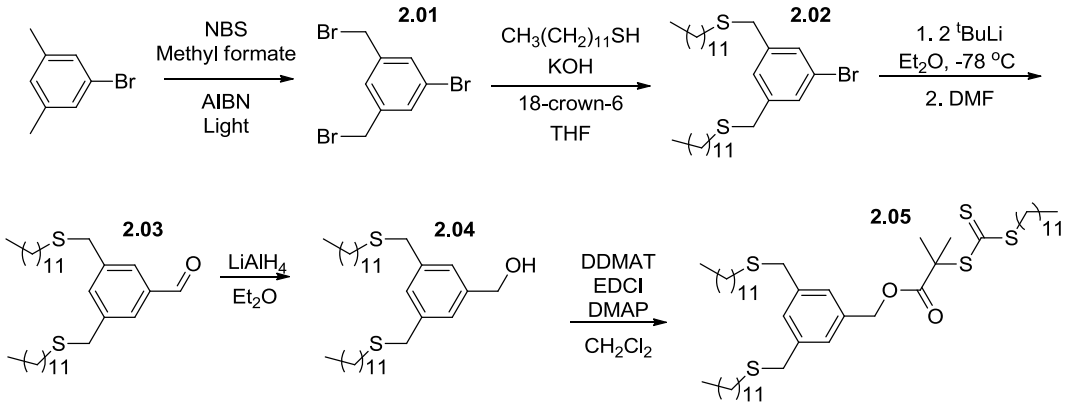

Scheme 1. Overall synthesis of SCS pincer functionalised RAFT CTA, **2.05** overall yield of 5%.

Scheme 1 shows the synthesis of the SCS pincer CTA. As the procedure is nearly identical to a previously published synthesis by Moughton and O'Reilly (where thiophenol was used in place of dodecane thiol),[44, 45] only the characterization of the final compound (**2.05**) will be given here, however, the full synthesis is reported in the experimental section.

,

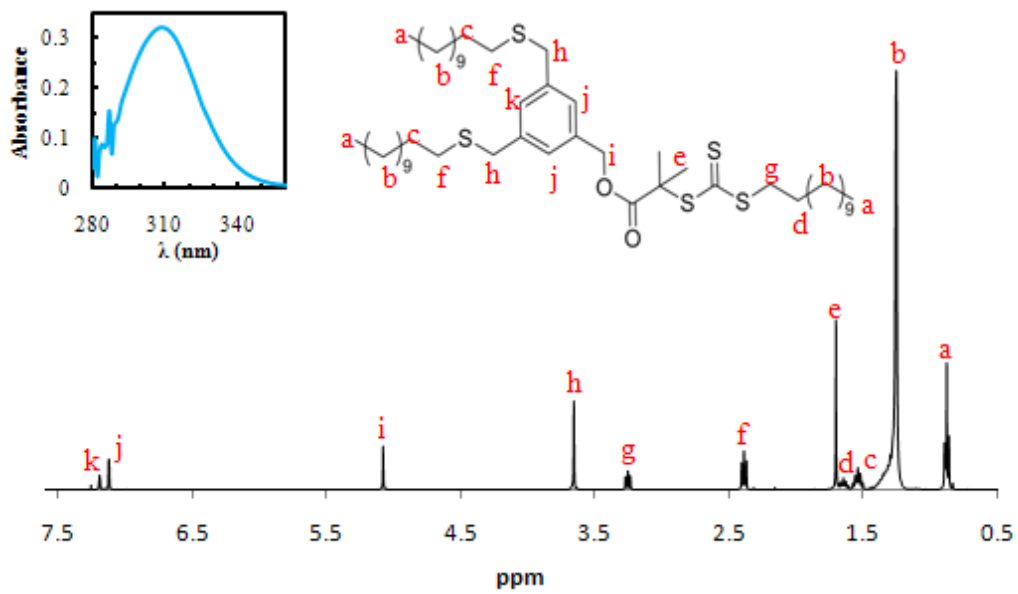

Figure 29. ^{1}H NMR and UV/Vis (inset) spectrum for Pincer CTA, **2.05** in $CDCl_3$ and THF respectively.

Figure 29 shows the ^{1}H NMR spectrum for the SCS pincer CTA. Peaks (H_f) and (H_g) are particularly useful for determining polymer M_n from ^{1}H NMR spectroscopy and, as they reside on both the R and Z group of the CTA respectively, they are useful for evaluating polymer end group fidelity. The UV-Vis spectrum shows a large absorbance at 309 nm which is also useful for evaluating end group fidelity by size exclusion chromatography coupled with a UV detector. Elemental analysis for C, H and S were all within 0.3 % of the calculated values confirming a high level of purity.

2.2.3 Preparation of SCS-pincer compounds

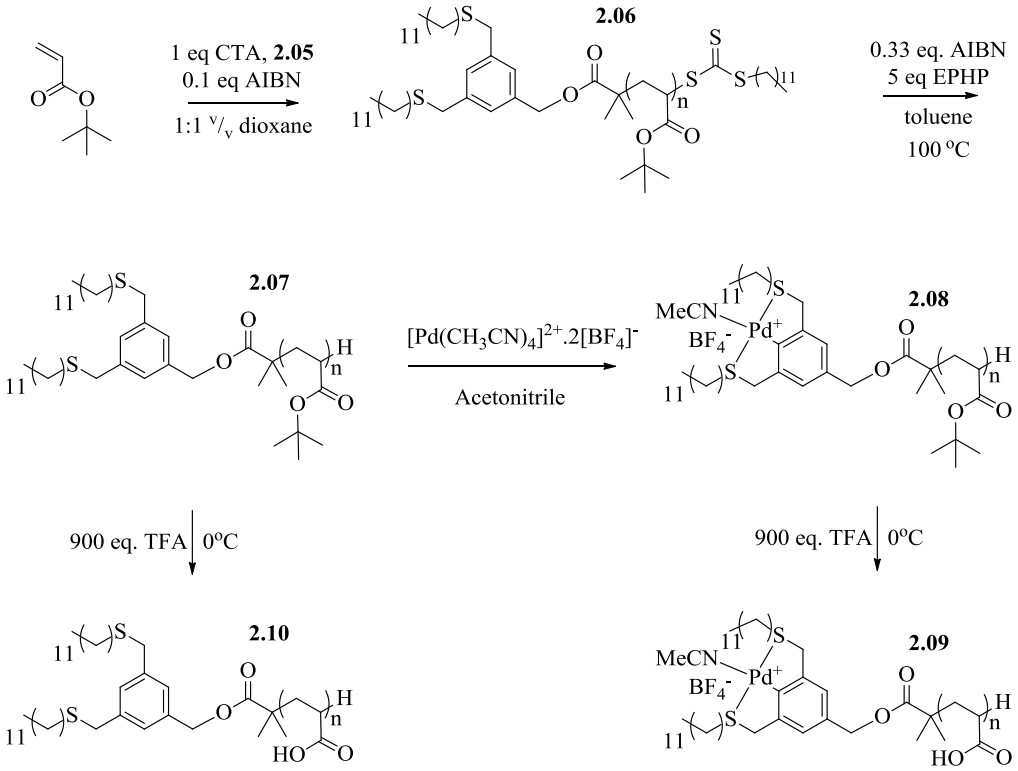

Scheme 2. Synthesis of Pd SCS pincer functionalised PAA, **2.09** and non Pd functionalised SCS pincer PAA, **2.10**

Polymerisation of *t*butyl acrylate, 2.06

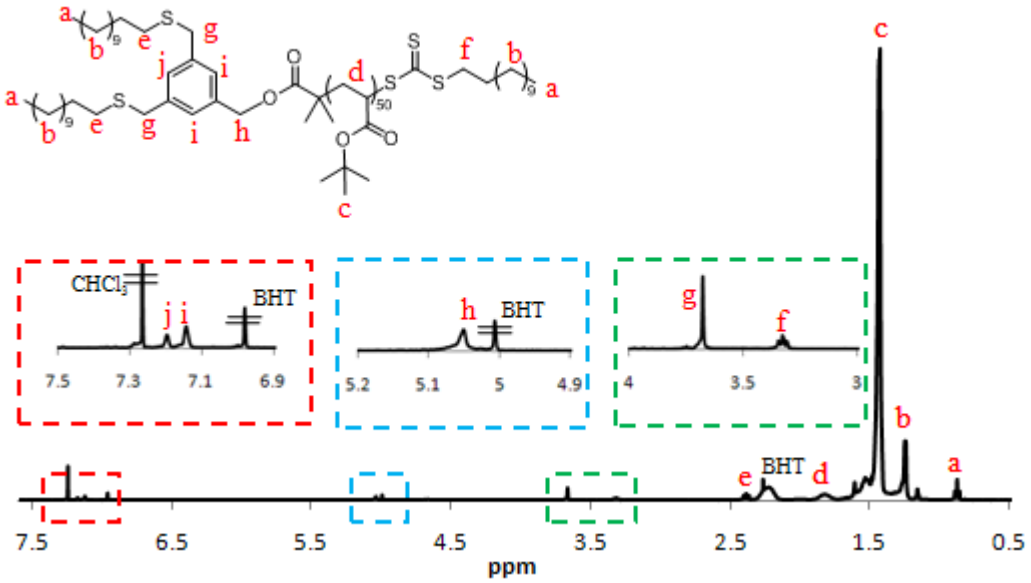

Figure 30. ^{1}H NMR spectrum for **2.06** in $CDCl_3$. Butylated hydroxyltoluene (BHT) is a stabiliser added to THF. Note: the last step in the polymer synthesis is removal of THF under vacuum, consequently BHT appears throughout the synthesis until it is removed in the last step by dialysis. BHT peaks appear at 6.98, 5.0, 2.27 and 1.43 ppm.

Polymerisation of *t*butyl acrylate (*t*BuA) at 65 °C in dioxane, followed by precipitation into MeOH:H_2O 9:1 v/v resulted in a well-defined P*t*BuA homopolymer with high end group fidelity. **Figure 30** shows the ^{1}H NMR spectrum for **2.06**, the peaks for the pincer end group (H_g, H_h, H_i and H_j) and the RAFT end group (H_f) integrated well with respect to each other, indicating good end group fidelity. This is backed up by an overlay of the differential refractive index (DRI) and UV (at 309 nm) trace form SEC analysis of the polymer. As shown in **Figure 29**, the trithiocarbonate group absorbs strongly at 309 nm and therefore overlaying this with the DRI trace indicates that the trithiocarbonate end group is present throughout the molecular weight distribution of polymer chains.

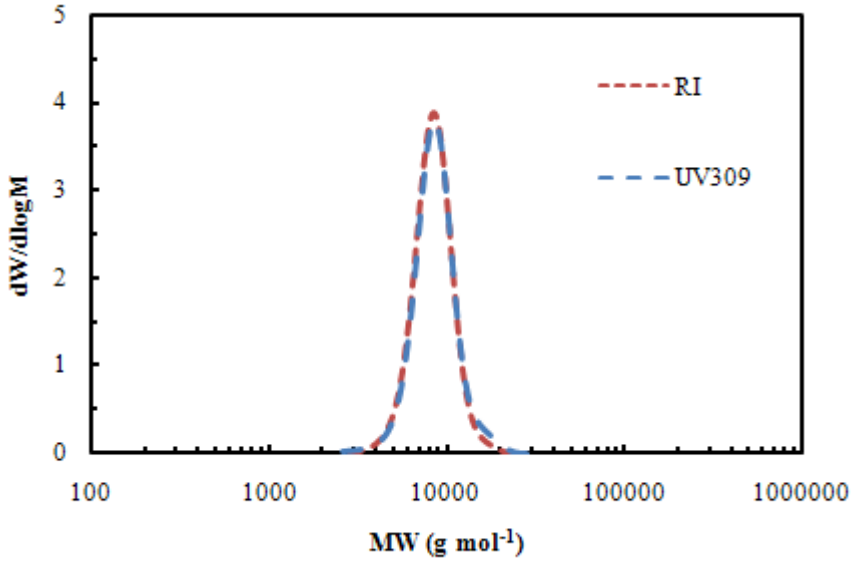

Figure 31. SEC traces using DRI (red) and UV (at 309 nm) (blue) detectors for the **2.06** in THF.

SEC was performed in tetrahydrofuran (THF), and calibrated against narrow poly(methyl methacrylate) standards (PMMA). Analysis gave M_n = 8.1 kDa and $Đ$ = 1.07. End group analysis by ^{1}H NMR spectroscopy gives DP = 50.

End group removal of P*t*BuA, 2.07

It has been previously shown that the trithiocarbonate group is a competitive binder to palladium and therefore it is necessary to remove it prior to complexation of the pincer ligand.[45] This was achieved by heating the polymer to 100 °C for ca. 12 hours in the presence of AIBN and ethylpiperidine hypophosphite (EPHP).[46] End group removal could be seen in both the ^{1}H NMR spectrum and by SEC analysis. **Figure 32** shows the ^{1}H NMR spectrum for **2.07**, complete disappearance of the peak H_f can be seen while the peaks H_h, H_i and H_j still integrate well with respect to each other and the backbone.

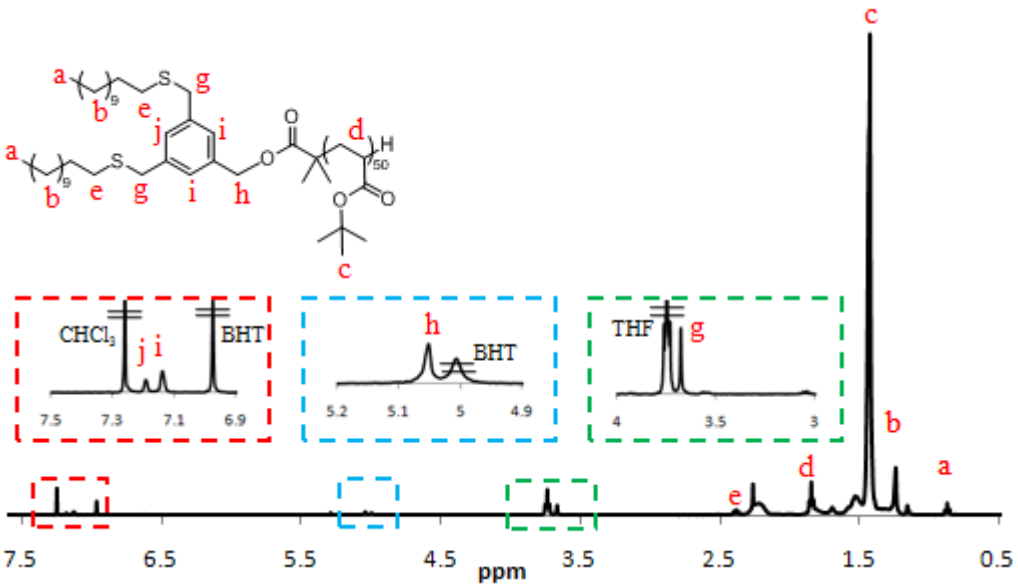

Figure 32. ^{1}H NMR spectrum for **2.07** in $CDCl_3$.

A comparison of the UV309 traces before and after end group removal (normalised with respect to the DRI traces to account for concentration differences in the samples) shows complete end group removal of the trithiocarbonate group.

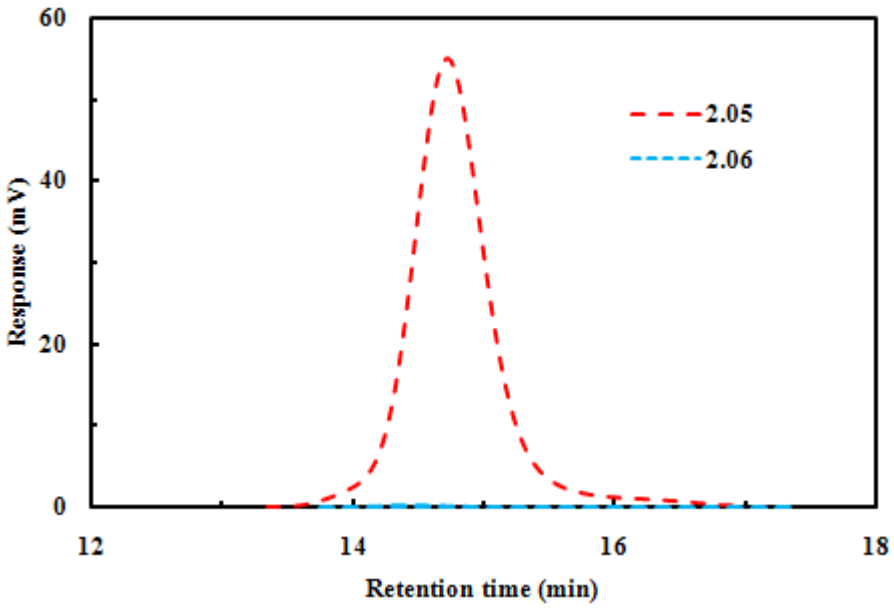

Figure 33. SEC traces using a UV detector for (at 309 nm) **2.06** (red) and **2.07** (blue).

Complexation of P*t*BuA, 2.08

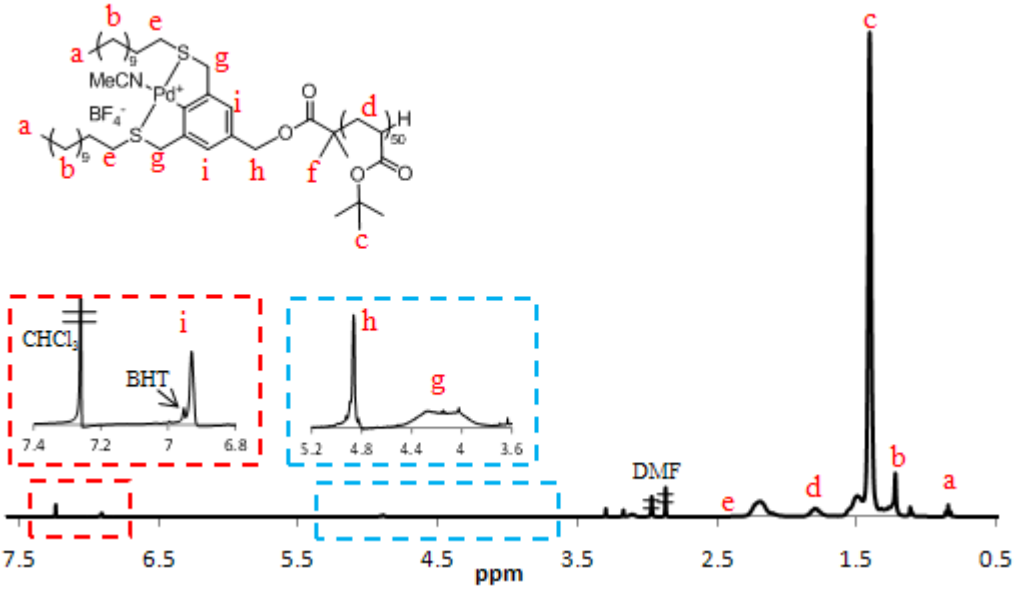

Figure 34. crude ^{1}H NMR spectrum for **2.08** in $CDCl_3$.

Polymer **2.07**, was then stirred in acetonitrile under N_2 (g) and at room temperature with the palladium precursor complex, $[Pd(NCMe)_4]2[BF_4]$, for two days. Removal of the acetonitrile *in vacuo* resulted in an orange solid which was used without further purification. The crude ^{1}H NMR spectrum shows complete disappearance of the aromatic proton (H_j) where Pd insertion has taken place. The spectrum also shows a shift and broadening for the methylene bridge protons (H_g) on complexation which has previously been observed for similar pincer complexes.[47, 48]

Deprotection of P*t*BuA to form PAA-Pd, 2.09

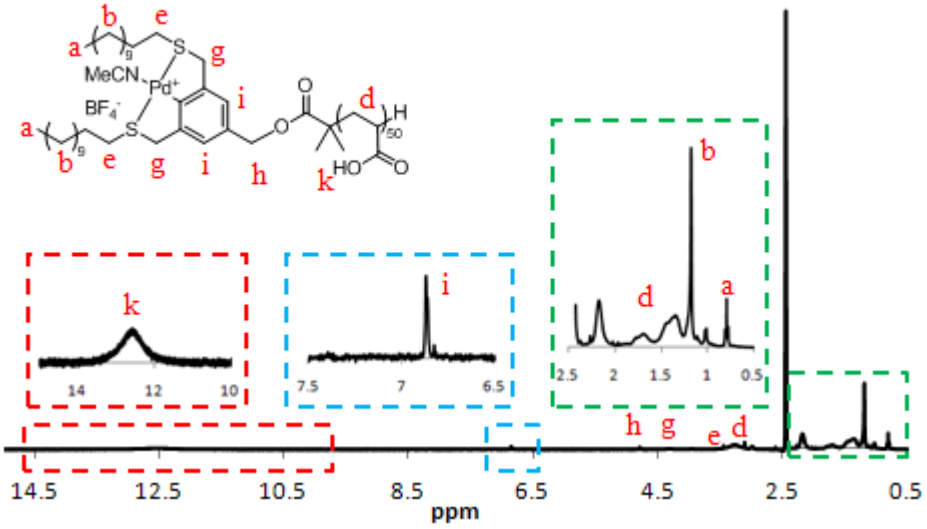

Figure 35. ^{1}H NMR spectrum for **2.09** in d^{6}-DMSO

Deprotection of the hydrophobic P*t*BuA with trifluoroacetic acid (TFA) afforded a hydrophilic poly(acrylic acid) (PAA). After purification by dialysis the complexed homopolymer was analysed by ^{1}H NMR and IR spectroscopy. The NMR spectrum shows the complete loss of the protons H_c (at 1.43 ppm) and the appearance of the acidic H_k protons. The pincer end groups discussed in the previous section are still present and integrate well with respect to each other indicating that the palladium pincer end group is still present. The IR spectra (**Figure 36**) shows a carbonyl peak shift from 1724 cm^{-1} to 1698 cm^{-1} upon deprotection; the latter peak being much broader and indicative of acidic functionality. Acidic functionality can also be inferred from the broad peak at ca. 3000 cm^{-1} (OH stretch). There is also a loss of the peak at 1143 cm^{-1} associated with the C-O stretching of the ester. All assignments match those found in the literature.[44, 49, 50]

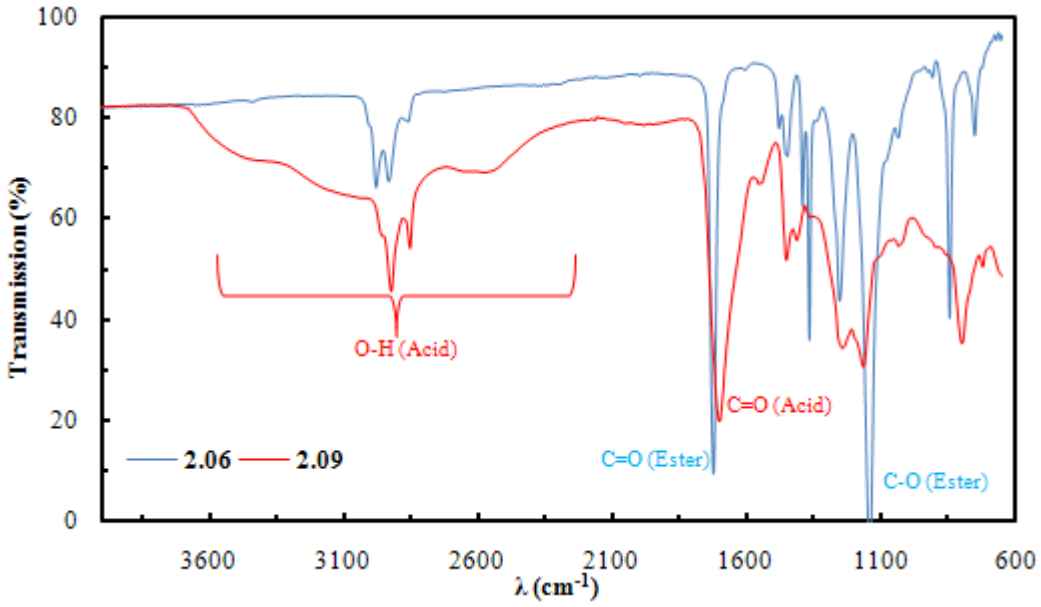

Figure 36. IR spectrum for **2.06** and **2.09** showing the conversion from *t*butyl acrylate to acrylic acid.

Deprotection of non-pallidated P*t*BuA to form PAA, 2.10

The deprotection step was performed analogous to above, but using polymer **2.07**. **2.10** was then analysed by ^{1}H NMR and IR spectroscopy to confirm the loss of *t*butyl groups and appearance of acid functionality analogous to **2.09** (see experimental section for details).

Synthesis of alkyl pincer complex, 2.12

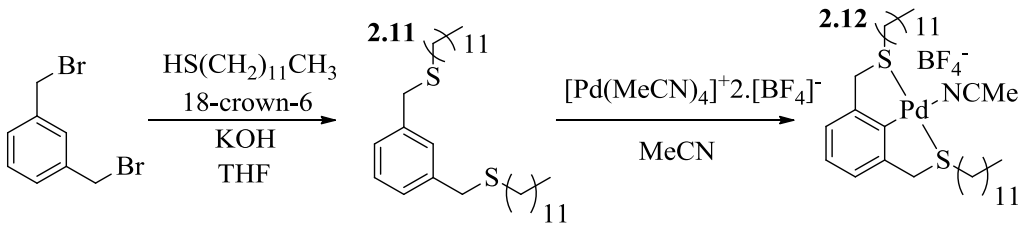

Scheme 3. Synthesis of alkyl pincer complex, **2.12**.

In order to compare the activity and reactivity of the Pd functionalised amphiphiles to a small molecule analogue, it was necessary to synthesise the small molecule equivalent. Dibromo-*m*-xylene was converted to the alkyl SCS pincer ligand by reaction with dodecane thiol in THF. The SCS pincer ligand was then complexed using the same conditions as the polymer complexation in the previous section. The ^{1}H NMR spectrum (**Figure 37**) shows the loss of the aromatic proton, the shift (from 3.68 – 4.22 ppm) and broadening of H_g protons and the appearance of the acetonitrile protons H_e. High resolution mass spectrometry gave *m/z* = 611.2945, which matches the molecular ion minus the acetonitrile ligand (expected *m/z* = 611.2936) and the expected palladium isotope pattern was observed.

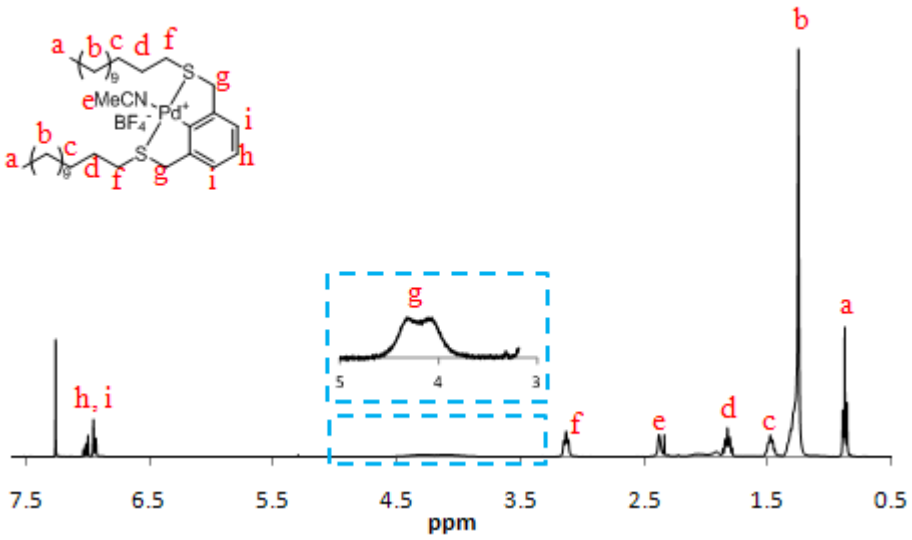

Figure 37. ^{1}H NMR spectrum for **2.09** in $CDCl_3$

2.2.4 Analysis of self-assembled structure in water

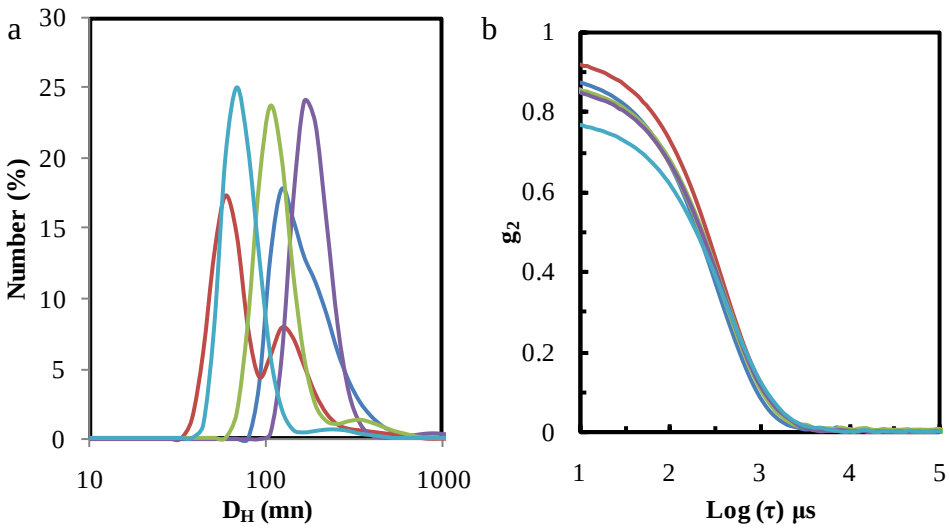

Figure 38. (a) DLS traces and (b) corresponding auto correlation functions for consecutive runs of **2.09** in water at 2 mg mL^{-1}. The data indicates that the DLS results were not consistent or reliable.

Polymers **2.09** and **2.10** were directly dissolved in water at 2 mg mL^{-1} and analysed by DLS. Typically, DLS traces are averaged over a number of runs; however, in this case consecutive runs were not consistent and showed structures ranging from 20-200 nm in size which were either narrowly distributed or highly disperse depending on the individual run (**Figure 38**). This behaviour was noted for **2.09** and **2.10** at a range of concentrations (0.25 - 10 mg mL^{-1}), with the additions of salts and by various preparation methods (direct dissolution or solvent switch). Similar behaviour has been previously reported and identified as spurious aggregation due to columbic interactions between the PAA chains (known as the polyelectrolyte effect.).[51, 52] For this reason it was not appropriate to analyse these samples by light scattering methods.

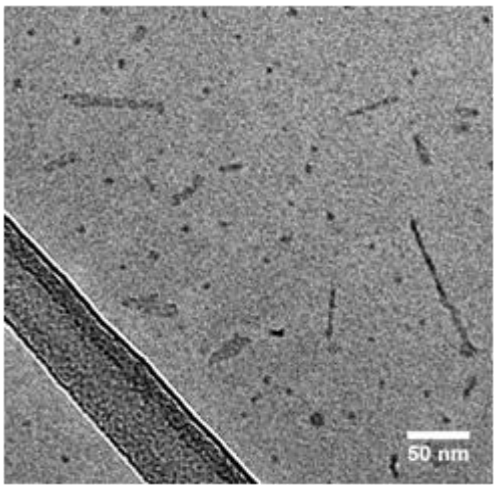

Figure 39. Cryo-TEM image of **2.09** in D_2O at 2 mg mL^{-1}.

Polymers **2.09** and **2.10** spontaneously self-assembled in water at 2 mg mL^{-1} as indicated by cryo-TEM, **Figure 39** and SANS, **Figure 40** and **Figure 41**. The cryo-TEM image shows the presence of both spherical and worm-like assemblies, both with a diameter of ca. 5 nm. In the cryo-TEM image, it is likely that all contrast comes from the Pd-containing core, and the size-scale is consistent with the theoretical core diameter based on the volume of the aromatic ring and the alkyl chain length. Cryo-TEM analysis of polymer **2.10** in water was unsuccessful, which is likely to be due to poor contrast obtained between the very small weakly scattering core (containing only carbon and no higher Z elements) and the relatively thick layer of vitreous ice.

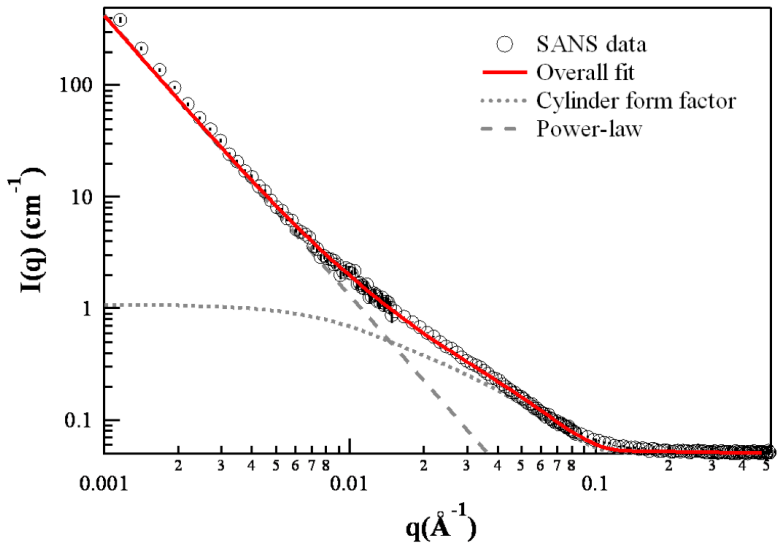

Figure 40. SANS data for **2.09** with overall model fit and the respective micelle and aggregate contributions

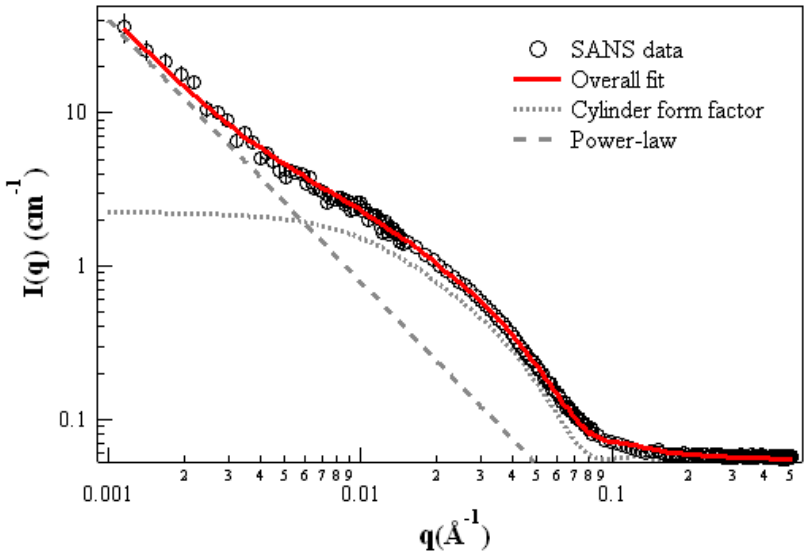

Figure 41. SANS data for **2.10** with overall model fit and respective micelle and aggregate contributions.

The SANS data for **2.09** and **2.10** suggested both cylindrical micelles and aggregates of micelles. The modelling for both **2.09** and **2.10** suggested that the cylinder core radius and lengths were ca. 3-4 nm and 35-40 nm respectively. The scattering

contributions from these aggregates can be seen in the upturn at low-*q* (**Figure 40** and **Figure 41**), and the SANS data suggest the aggregates are on the order of microns in size. To account for the presence of the micelles and aggregates, the SANS intensity was fitted with a linear combination of models,

$$I(q) = I_{micelle}(q) + I_{aggregate}(q) + B \quad (1)$$

where $I_{micelle}(q)$ and $I_{aggregate}(q)$ are the scattering contributions from the micelles and aggregates, respectively, and B is the incoherent scattering background.

The scattering contributions from the micelles were modelled with a form factor for cylinders with a uniform SLD and a Schulz distribution of cylinder lengths.[53] The SLD of the cylinders was calculated using the density of PAA, while also accounting for the effects of exchangeable hydrogens (calculated SLD = 3.4×10^{-6} Å^{-2}).[54] The cylinder scale factor, radius, and length were fit during the data analysis. The dispersity in lengths was fixed at 0.3, which gave a similar length distribution to that seen in the TEM micrographs for **2.09**, however, the dispersity value had little effect on the overall fit. Note that modelling the micelles as cylinders with a uniform scattering length density does not account for any radial dependence of the micelle profile,[55] and the deviations of the fit values from the experimental data at higher-*q* may be due to this simplifying assumption. Also, the fit values for the cylinder radii may not represent the overall micelle radius due to this assumption.

The scattering from the aggregates was described by a power-law,

$$I_{aggregate}(q) = I_0 q^{-\varepsilon} \quad (2)$$

where I_0 and ε were constants and fit during the analysis. The incoherent background scattering was fixed at a constant value. All fitting procedures were performed using

the NIST SANS package in Igor Pro, and the calculated scattered intensity was corrected for instrument resolution.[53] The modelling results for **2.09** and **2.10** are summarized in **Table 3**. Due to the strong scattering contributions from the aggregates at low- and intermediate-*q*, it was difficult to accurately determine the length of the cylinders. However, using an approximate cylinder length from the cryo-TEM micrographs resulted in satisfactory fits to the data. As seen in **Figure 41**, sample **2.10** also contained cylindrical micelles and aggregates. The fit value for the cylinder length was more reliable for **2.10** because scattering from the aggregates did not dominate at intermediate-*q*, and the fit values for the cylindrical micelle lengths for **2.09** and **2.10** were comparable.

Table 3. Summary of SANS data modelling results

Sample	cylinder radius (nm)	cylinder length (nm)	I_0	ε
2.09	3 ± 1	40 ± 4	$2 \times 10^{-5} \pm 2 \times 10^{-6}$	2.51 ± 0.02
2.10	4 ± 1	34 ± 3	$3 \times 10^{-4} \pm 3 \times 10^{-5}$	1.71 ± 0.01

2.2.5 Evaluation of critical micelle concentration

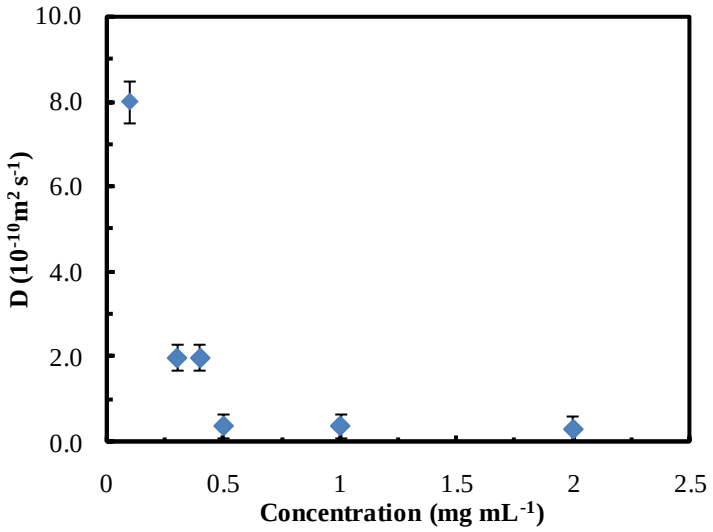

Figure 42. Diffusion coefficient (D) measured by DOSY NMR for **2.09** in D_2O as a function of concentration. Error bars obtained from D values measured from four different peaks.

The CMC of **2.09** was evaluated by diffusion ordered NMR spectroscopy (DOSY NMR).[56] The data show a constant D between 2.0 and 0.5 mg mL^{-1}, indicating that micelles are present in solution between these values (SANS and cryo-TEM analysis confirm structures in solution at 2.0 mg mL^{-1}). Below 0.5 mg mL^{-1}, D increases which indicates the possible dissociation of the micelles into unimers. Note: the NMR spectrum at 0.1 mg mL^{-1} was quite noisy due to poor signal at such a low concentrations and therefore it was not possible to measure any lower concentrations. In conclusion the CMC of **2.09** appears to be roughly 0.5 mg mL^{-1}. An example DOSY spectra in shown in **Figure 43**.

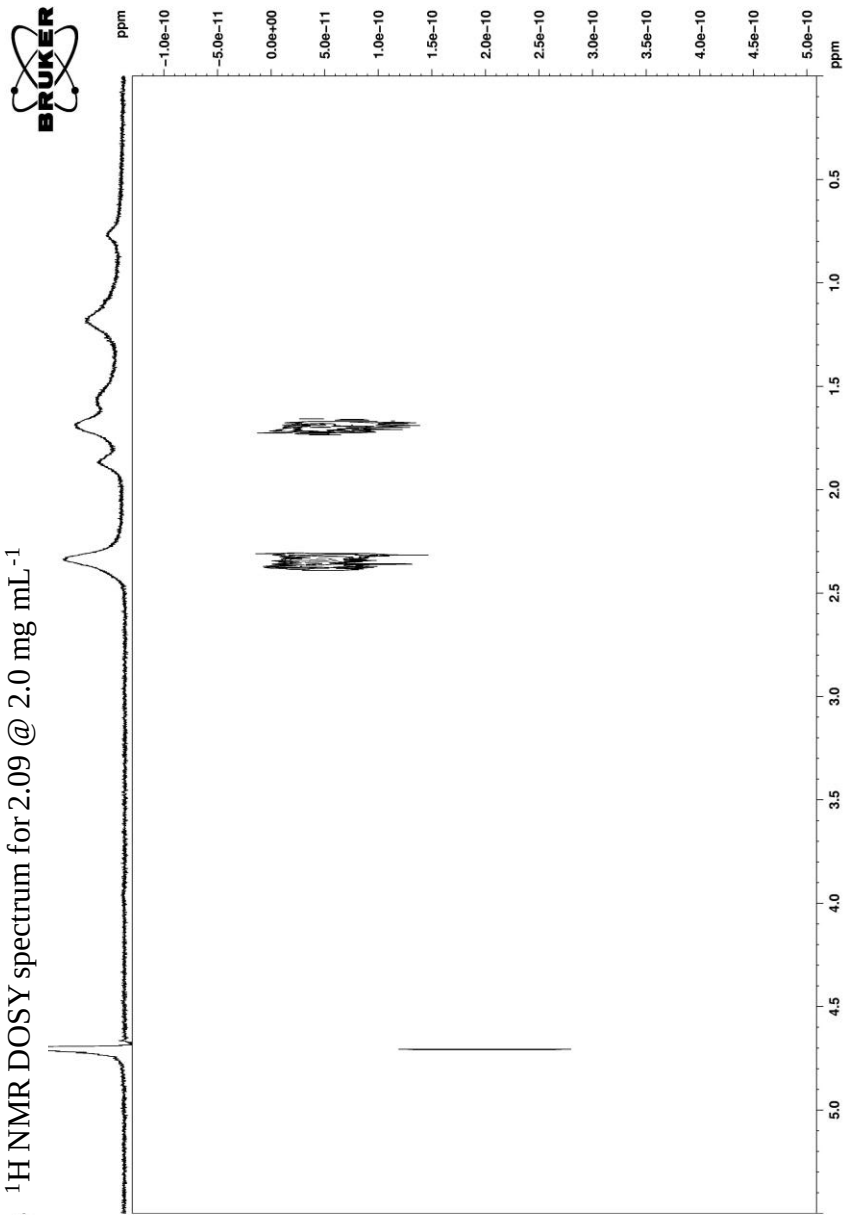

Figure 43. ^{1}H NMR DOSY spectrum for **2.09** @ 2.0 mg mL^{-1}.

2.2.6 Catalytic activity of polymer 2.09 vs. small molecule 2.12 at 2 mol%

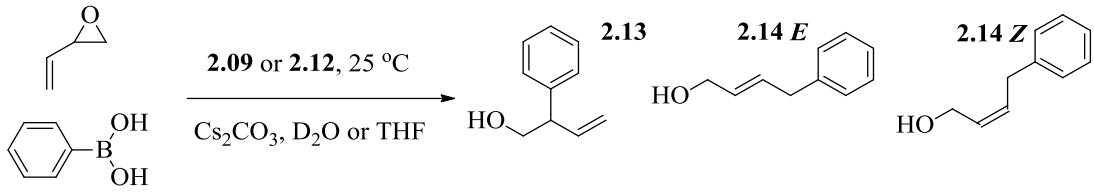

Scheme 4. SCS Pd-pincer catalysed cross-coupling of vinyl epoxide with phenylboronic acid to afford branched (**2.13**) and linear (**2.14**) alcohols.

The palladium catalysed cross-coupling of boronic acids with unsaturated substitutes (Sizuki-Miyuara coupling) is an extremely important synthetic tool,[57] with specific examples of coupling to vinyl epoxides using Pd(II) having been previously reported.[58] To evaluate the effect of creating a catalytically active nanostructure, a small molecule analogue of **2.09** was also synthesised, **2.12**.[57, 58] The catalytic activity of **2.09** and **2.12** were compared for the coupling reaction described in **Scheme 4**. Reagents were added simultaneously to the catalyst solution at 2 mol% and the mixture was agitated at 25 °C (Note: for the micellar system it was not necessary to pre-form the micelles in water and the order of reagent addition did not affect the catalysis significantly). Samples from both reactions were removed at set times and analysed by ^{1}H NMR spectroscopy in D_2O and $CDCl_3$ for **2.09** and **2.12** respectively in order to follow the reaction kinetics (an example ^{1}H NMR spectrum showing how conversion was determined is discussed later, **Figure 49**).

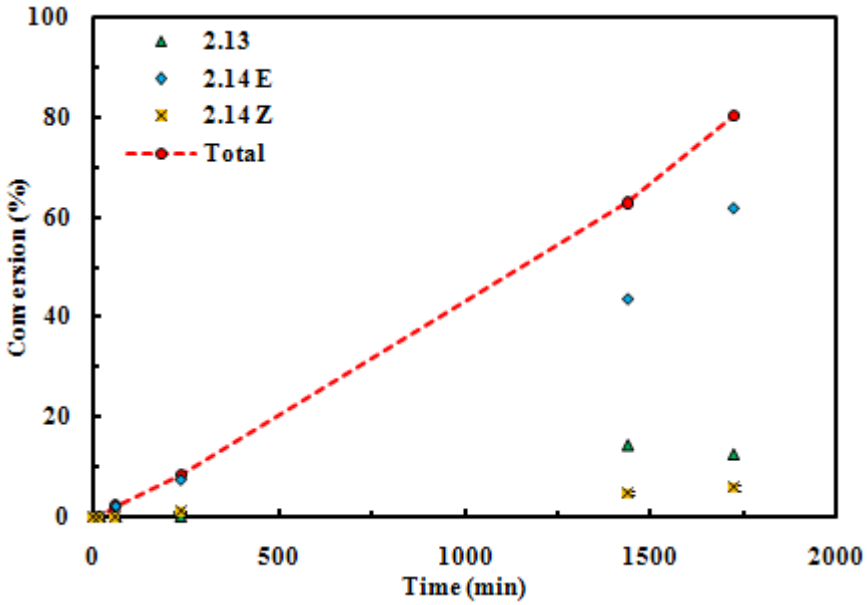

Figure 44. Conversion vs. time data for catalysis by **2.12** at 2 mol %, showing the distribution of products and the total conversion.

The reaction times of the benchmark catalyst, **2.12** (at 2 mol %) in THF (**Figure 44**), were similar to previous literature, where 16 hours in THF gave 84 % yield.[58] **Figure 44** also shows that the product distribution remains constant throughout the reaction 1 : 2 : 11 (**2.14*Z*** : **2.13** : **2.14*E***), with the linear *E* alkene (**2.14*E***) being the most favoured. Again this is similar to the previous literature which showed a 11 : 1 ratio of linear to branched for a similar pincer ligand.[58] The data indicated the new SCS pincer complex **2.12** catalyses this Suzuki–Miyaura effectively and performs comparably to other pincer catalysts.

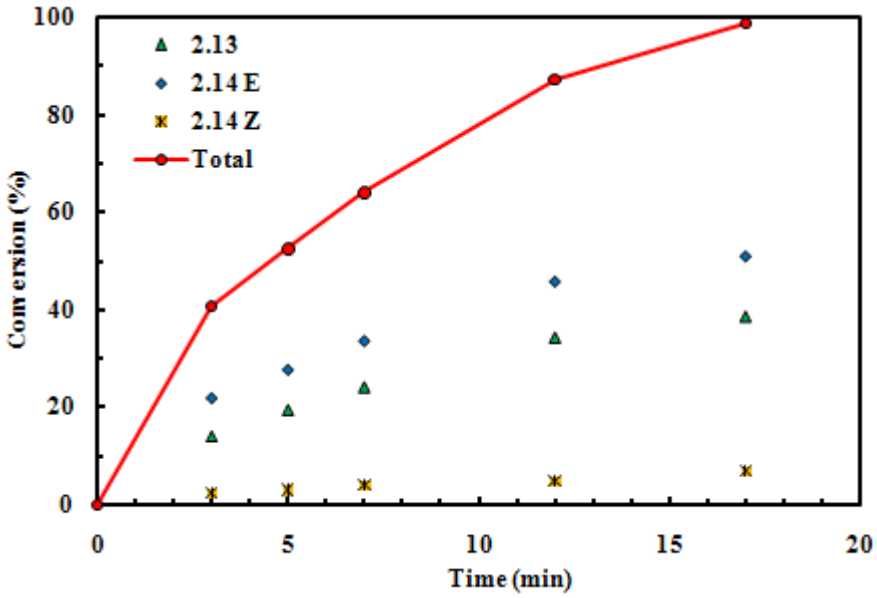

Figure 45. Conversion vs. time data for catalysis by **2.09** at 2 mol %, showing the distribution of products and the total conversion (**2.13** + **2.14*E*** + **2.14*Z*)**.

The self-assembled structures of polymer **2.09** in water (also at 2 mol%) catalysed the reaction approximately 100 times quicker than **2.12** in organic solvents (**Figure 45** and **Figure 44**). **Figure 45** also shows that the ratio of product distribution remains constant throughout the reaction (1 : 6 : 7) (**2.14*Z*** : **2.13** : **2.14*E***), for catalysis by **2.09** but that the selectivity toward the linear **2.14*E*** is diminished. This was also seen for Uozumi's nanoreactors which had a selectivity of 1 : 1 for the linear vs. branched products (the *E/Z* selectivity was not mentioned). This suggests that the product distribution can possibly be altered by performing the reaction in a confined environment. However, for a similar coupling reaction using allylic alcohol and boronic esters, it has been shown that more protic environments lead to enhanced selectivity towards branched alcohols over the linear product,[59] therefore the difference here could also be due to the reaction environment (aqueous vs. organic). Another interesting comparison between the kinetics of **2.09** and **2.10** is

related to the reaction profile. By simple inspection **2.09** appears to show a first order kinetic profile whereas **2.10** appears to be zero order (with respect to reactant concentration). Typically, zero order reactions occur when the rate limiting step is during the catalytic cycle (i.e. the catalyst is effectively saturated with reactants). In the case of **2.09** this rate limiting step must have changed which causes both an increase in overall reaction rate and a shift to first order kinetics. Further investigation is needed for a more detailed understanding of the change in kinetic profiles and this is discussed later in relation to the recycling experiments. Due to the poor solubility of PAA in chloroform separation of reactants and polymer supported catalyst was achieved by simple extraction with $CDCl_3$. After 3 extractions with $CDCl_3$ no product could be observed in the water phase by ^1H NMR spectroscopy, indicating complete extraction. For the reaction with **2.09** at 2 mol % 100 % conversion was reached in less than 20 minutes, isolated yields were quantitative (measured by ^1H NMR using DMF as an internal standard) and the products could be characterised after extraction without the need for further purification (**Figure 46**).

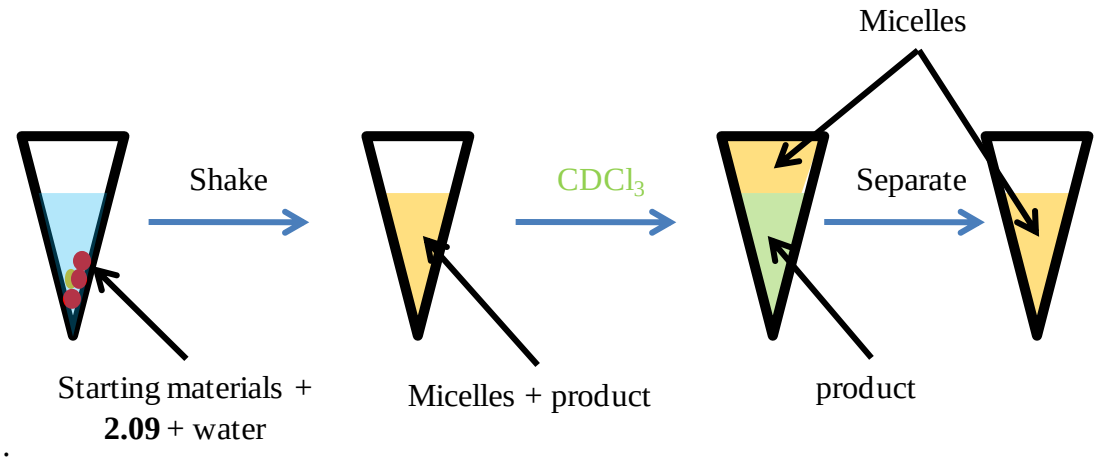

.

Scheme 5. Reaction protocol for catalysis by **2.09** in water.

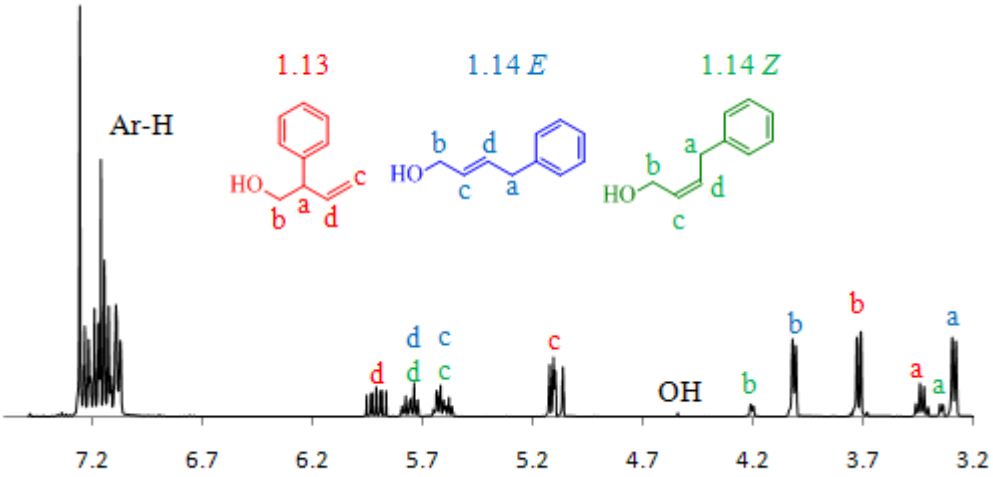

Figure 46. ^{1}H NMR spectrum of the crude products **2.13** and **2.14** after extraction with $CDCl_3$.

Control reactions in water using **2.10** (a PAA-pincer amphiphile which self-assembled but without Pd complexation) or **2.12** (which was insoluble in water) under the same conditions showed no product formation after 24 hours. This result indicates that the nanostructures must be capable of sequestering the hydrophobic substrates and also have the active Pd-pincer complex to promote effective catalysis in water. The dramatic rate increase observed in the self-assembled system **2.09** compared to the small molecule reactions in organic solvents can be attributed to an increase in local concentration around the catalyst, driven by the hydrophobic concentrator effect.[6, 11-13] This increase of rate compared to the previously reported nanoreactor vesicle system,[60] is attributed to an increase in nanoreactor surface area due to a reduced particle radius of the spherical or cylindrical micelles compared to vesicles, as well as the orientation in active site location; here the active site is facing inward towards the hydrophobic domain which creates a more hydrophobic local

environment (**Figure 27**). The dramatic rate increase for catalysis by **2.09** in water allows for this coupling reaction to be performed in minutes rather than hours. However, as Pd is expensive and the synthesis of pincer ligands is often time consuming it might be more desirable to perform the reactions at lower loadings rather than in shorter time scales.

2.2.6 Catalytic activity at different polymer concentrations (and Pd loadings)

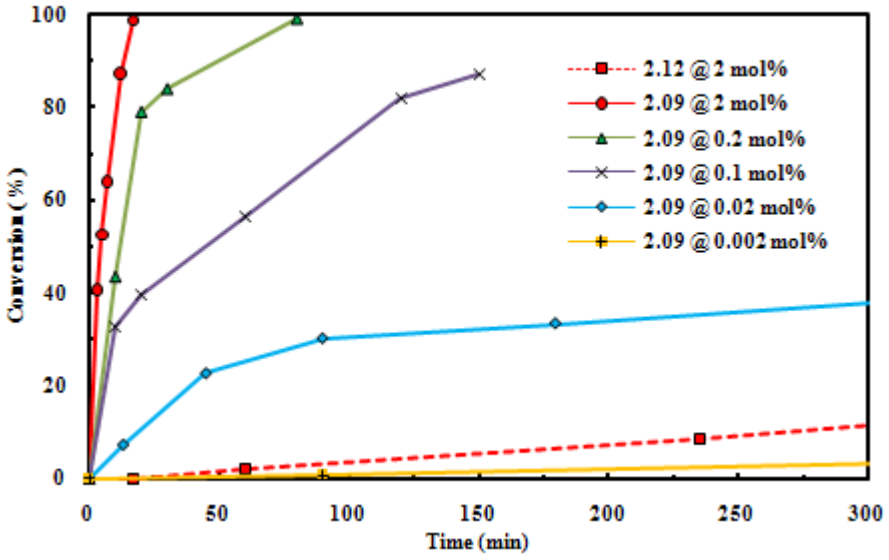

Figure 47. Conversion against time data for catalysis by **2.09** (solid lines) at different loadings and **2.12** (dashed line) at 2 mol %, showing the total conversion.

The kinetics of the self-assembled catalytic system, **2.09**, were investigated as a function of catalyst loading by reducing the polymer concentration in solution (and hence micelle concentration). **Figure 46** shows that even with 100 times less catalyst (0.02 mol %) the reaction is faster than **2.12** in organic solvents.

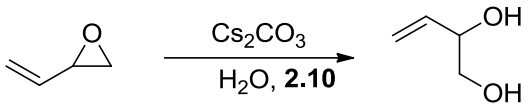

Scheme 6. Reaction of epoxy starting materials with water in the presence of **2.10** to aid solubility. Note: **2.10** was used to solubilise the starting materials in water.

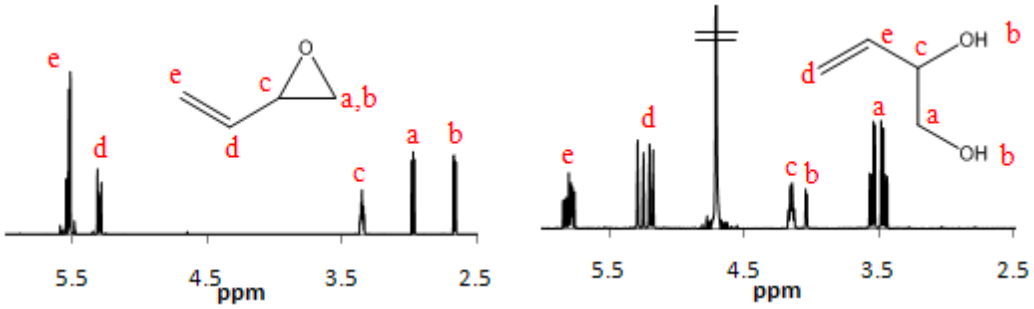

Figure 48. ^{1}H NMR spectrum of epoxy starting material in $CDCl_3$ and of the diol formed from reaction of the epoxy starting material with water in D_2O after 24 hours.

However, under basic aqueous conditions the epoxide is prone to attack by hydroxide nucleophiles and forms a diol. While Pd is known to catalyse this ring opening,[61] the diol product was also observed in basic aqueous conditions in the absence of Pd. This side reaction is negligible for short reaction times but becomes significant at < 0.2 mol % catalysis. The side reaction can be monitored by ^{1}H NMR spectroscopy and the conversion adjusted accordingly, so that at < 0.2 mol % the reaction never reaches 100 %.

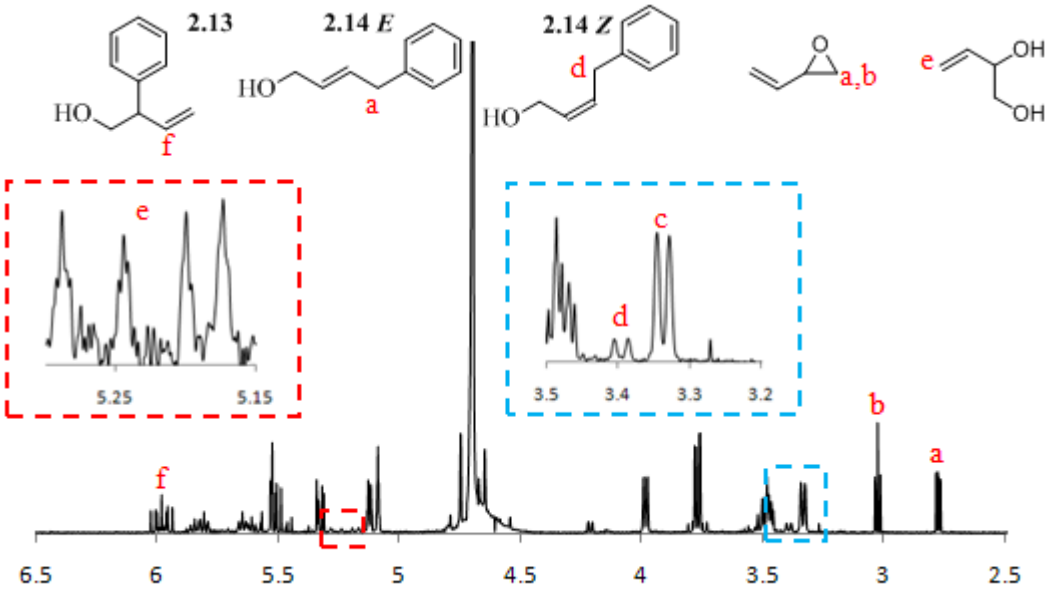

Figure 49. ^{1}H NMR spectrum for catalysis by **2.09** at 0.1 mol % after 60 min. The labelled peaks show those which were used for determining conversion and the amount of epoxy starting material which had degraded.

Despite the competing decomposition, turnover numbers (TON) of 872 (0.1 mol %) and 3500 (0.02 mol %) can be achieved. At 0.002 mol % (0.01 mg mL^{-1} of polymer) the reaction rate is significantly reduced which is likely to be due to the break-up of the assembled structures due to the low concentration (well below the CMC as indicated by DOSY NMR, **Figure 42**) and hence the hydrophobic starting materials could not be sequestered (this could also been seen visually as the starting materials were not solubilised in the reaction media). At catalyst loadings of 2, 0.2 and 0.1 mol % turn over frequencies (TOF) (at 30 % conversion) of 7, 22 and 32 min^{-1} respectively were achieved. The latter is ca. 1500 times greater than that of **2.12** at 2 mol % (the small molecule catalyst) where the TOF (at 30 %) was 0.022 min^{-1}. The increase of TOF with decreasing catalyst loading indicates that the initial rate of reaction is limited by the rate of substrate encapsulation into the core. For high

concentrations, there is an excess of active catalyst sites in the core with respect to substrates and therefore not all catalytic sites are continuously turning over substrates. At lower concentrations there are less active sites, therefore, each individual Pd centre is working more efficiently.

2.2.7 Decoupling polymer concentration with Pd loading

In the previous section the catalyst loading (mol %) was reduced by decreasing the amount of polymer added to the reaction mixture. This changes two parameters for the catalytic system: the catalyst loading (mol %); and the concentration of micelles (mg mL^{-1} of polymer). In order to further reduce catalyst loadings while retaining high activity it would be desirable to decouple these two parameters, i.e. to be able to reduce the mol % while retaining the same concentration of micelle forming polymer. In an attempt to decouple the micelle concentration from catalyst loading, reactions were performed with mixtures of **2.09** and **2.10**. It was hoped that by mixing these two polymers, mixed micelles (micelles containing both **2.09** and **2.10, Figure 50**) would form. Using the same conditions as 0.1 mol % catalysis by **2.09**, the mass of **2.10** was added to give an equivalent polymer concentration to that in the 0.2 mol % experiment (i.e. the mass of each polymer added was roughly the same). **Figure 51** shows kinetic data for reactions performed at 0.1 mol % by **2.09** and by **2.09** with unfunctionalised polymer **2.10**. The kinetics show that when polymer **2.10** is added to the reaction mixture the rate decreases. This could indicate that two discrete micellar aggregates are forming in solution: micelles made from **2.09** (catalytically active); and micelles made from **2.10** (not catalytically active).

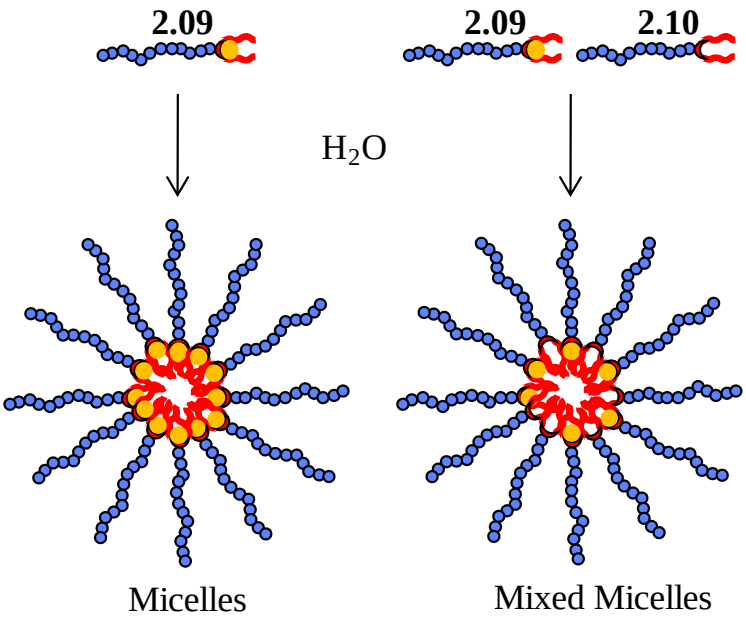

Figure 50. Schematic of micelles formation from polymer **2.09** and mixed micelle formation from polymers **2.09** and **2.10**.

Both types of micelles are capable of sequestering starting material but only the micelles formed from **2.09** are able to promote catalysis. This theory was corroborated by a second experiment performed with an excess of **2.10** compared to **2.09** (90 % by weight) which showed no conversion after 120 min, which is to be expected as they will be sequestering ca. 90 % of the starting materials.

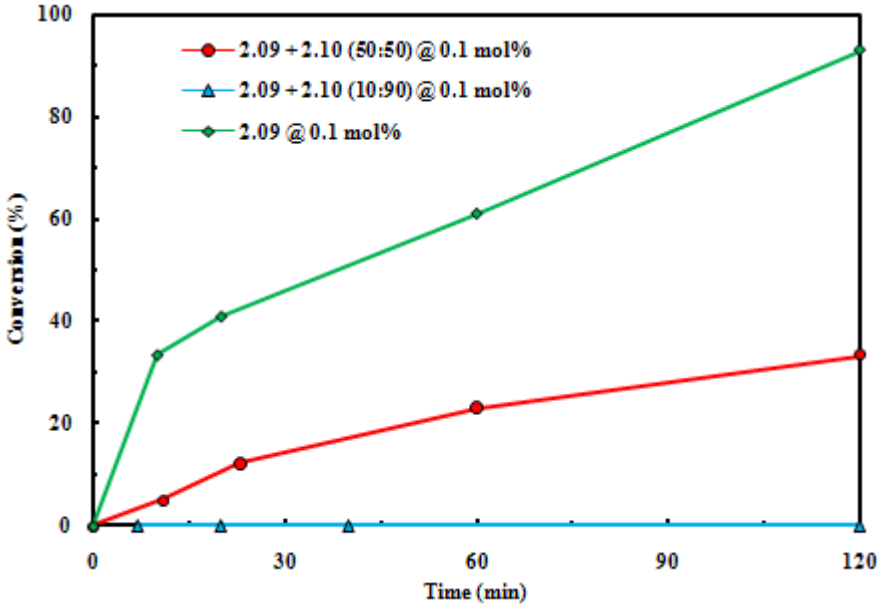

Figure 51. Conversion vs. time data for catalysis by **2.09** and **2.09** + **2.10** at 0.1 mol % showing the total conversion.

2.2.8 Recycling and degradation experiments

One major benefit for supported catalysis is the ability to recover and reuse expensive or precious materials. As demonstrated in **Scheme 5** the reaction protocol allows for easy recycling of the micelles via extraction of the products by chloroform and simple separation of the organic and aqueous layers. However, once recycled **2.09** shows a significant decrease in activity compared to the initial run (**Figure 52**), furthermore the kinetics show a reaction profile similar to the small molecule catalysts (zero order with respect to starting materials). It is well known that these Pd-pincer complexes can degrade and leach out from the support, forming highly catalytically active Pd(0).

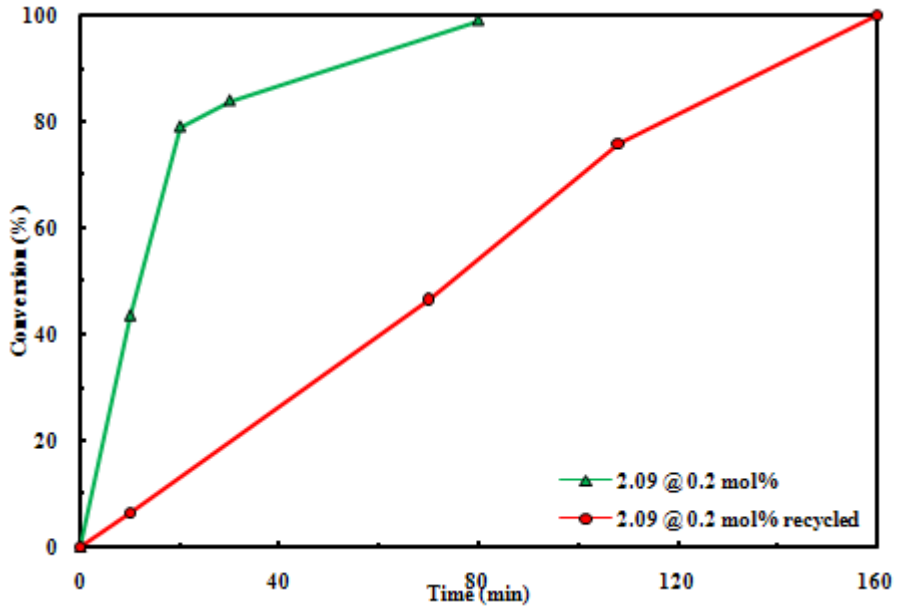

Figure 52. Conversion vs. time data for catalysis by **2.09** at 0.2 mol % showing the total conversion for the initial run and the recycled polymer.

Weck[62-64] and co-workers have studied this extensively and several reviews have been published on the subject;[65, 66] they showed that during early stages in the reaction, polymer tethered Pd(II) is converted into free Pd(0) and that it is this free Pd(0) that is the true catalyst in the reaction. One obvious downside of this is that the free Pd(0) cannot be easily recycled. Typically these degradation reactions were observed for Heck coupling, where pincer compounds were subject to high temperatures (> 100°C).[65] However, Gebbink and van Koten[67] recently reported the first example of SCS-pincer Pd degradation under extremely mild reaction conditions (e.g. low temperature, non-acidic, non-basic conditions) for the stannylation of cinnamyl chloride with hexamethylditin. This work suggests that the decomposition of such complexes is inherent to the catalytic cycle and not a result of harsh or inappropriate reaction conditions. The drop on reactivity upon recycling indicates that degradation is taking place during the catalytic cycle and the switch

from first to zero order kinetics indicates that this degradation to Pd(0) is somehow linked to the kinetic profile. Two common tests for evaluating Pd leaching and its effect on the catalytic activity of the supported system are to add Hg(0) or poly(vinyl pyridine) (PVP) to the reaction mixture. Both PVP and Hg(0) are strong Pd binders and capable of shutting down its catalysis and have been used previously to test the leaching of tethered Pd to free Pd in solution.[63, 64, 67, 68] **Figure 53** shows that the addition of Hg(0) (250 eq) or PVP (200 eq) to the reaction mixture results in retardation of the reaction kinetics which again indicates that free Pd is forming during the reaction and is at least partially responsible for catalysis. Inductively coupled plasma atomic emission spectroscopy (ICP-OES) was used to confirm the degree of degradation after one cycle at 0.2 mol %. ICP-OES measurements of **2.09** before the reaction found 867 parts per billion (ppb) of Pd (expected 837 ppb, reaction solution diluted 30x water). After 2 h PVP was added to the reaction mixture (34 mg) to bind any free Pd(0). The PVP was then removed by centrifugation, a small portion of the supernatant was then removed (diluted 30x with water) and analysed by ICP-OES which showed 521 ppb of Pd remained (40% loss). The recycling and degradation experiments clearly indicate Pd leaching occurs during the reaction, which is consistent with previous literature and provides another example of leaching occurring under mild reaction conditions (room temperature).

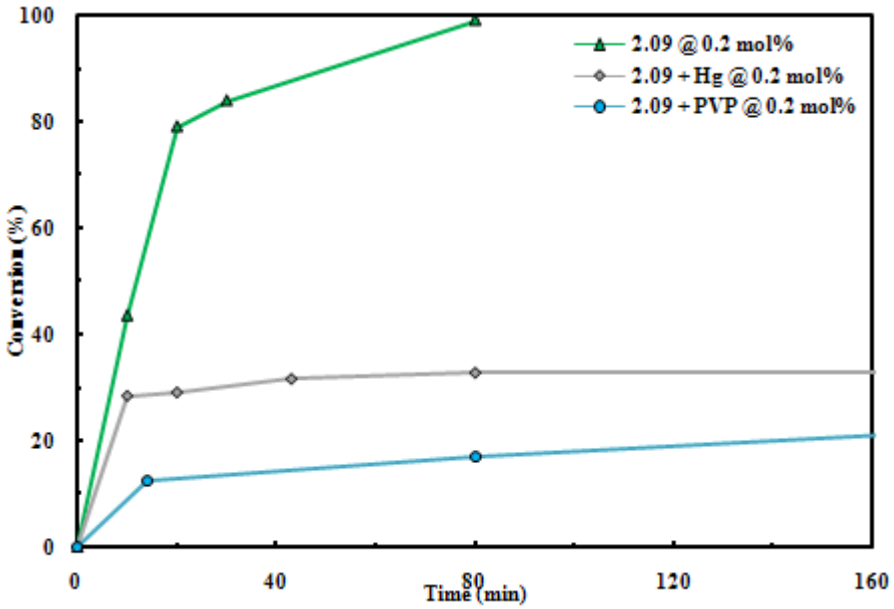

Figure 53. Conversion vs. time data for catalysis by **2.09** at 0.2 mol % and **2.09** with added Hg(0) or PVP

2.3 Conclusions

The ability of palladium containing polymeric nanoreactors to sequester substrates due to the hydrophobic effect provides an opportunity to lower catalyst loadings while maintaining high catalytic activity. For this system, TONs were increased significantly upon decrease in catalyst loading and this resulted in high efficiency reactions where TOFs of 32 min^{-1} were achieved. Higher TONs were also achieved by further decreasing the catalyst concentration. It has been confirmed that SCS-pincer ligands are not suitable for recycling experiments due to the formation of free Pd(0). Given these limitations, the incorporation of pincer ligands into hydrophobic nanopockets to significantly reduce the loadings of otherwise relatively poor performing pincer catalysts becomes much more important. While the analysis of the self-assembled structures **2.09** and **2.10** is convincing, more in-depth analysis was

not possible due to the mixed morphology. In order to study the effect of catalytic activity vs. changes in particle architecture it would be desirable to have a well-defined, more thoroughly analysed system. This analysis problem will be the addressed in the next chapter.

2.4 Experimental Section

2.4.1 Materials

All chemicals were used as received from Aldrich, Fluka, or Acros unless otherwise stated. *t*Butyl acrylate were distilled over CaH_2 prior to use and stored at 5 °C. AIBN [azobisisobutyronitrile] was recrystallized twice from methanol and stored in the dark at 5 °C. DDMAT [S-dodecyl-S'-(α',α'-dimethyl-α''-acetic acid)] was synthesised as previously reported.[43]

2.4.2 Instrumentation

^{1}H NMR spectra were recorded on a Bruker DPX-400 spectrometer in $CDCl_3$. Chemical shifts are given in parts per million (ppm) downfield from tetramethylsilane (TMS). For the DOSY experiments, D values were extracted from the spectra using the SCORE algorithm and the DOSY Toolbox, with the D value taken as the average of four peaks arising from the polymer. A 500W halogen lamp was purchased from a local hardware store. from a Size exclusion chromatography (SEC) measurements were conducted on a system comprised of a Varian 390-LC-Multi detector suite fitted with differential refractive index (DRI) and ultra-violet (UV) detectors and equipped with a guard column (Varian Polymer Laboratories

PLGel 5 µM, 50 × 7.5 mm) and two mixed D columns (Varian Polymer Laboratories PLGel 5 µM, 300 × 7.5 mm). The mobile phase was tetrahydrofuran with 5% triethylamine operating at a flow rate of 1.0 $mL.min^{-1}$, and samples were calibrated against Varian Polymer laboratories Easi-Vials linear poly(styrene) standards (162 - 2.4×10^5 $g.mol^{-1}$) using Cirrus v3.3 software. Cryo-TEM samples (2 mg mL^{-1} in D_2O) were examined using a Jeol 2010F TEM operated at 200 kV and imaged using a GatanUltrascan 4000 camera. Images were captured using Digital Micrograph software (Gatan). A 3 µL droplet of the sample solution at ambient temperature was added to a holey carbon-coated copper grid, and the grid was blotted to remove excess solution. Subsequently, the grid was plunged into liquid ethane to vitrify the sample. The temperature of the cryo stage was maintained below -170 °C, using liquid nitrogen, during imaging. Small Angle Neutron Scattering (SANS) experiments were conducted at ambient temperatures on the NG-7 30 m SANS instrument at the National Institute of Standards and Technology (NIST) Center for Neutron Research (NCNR) (Gaithersburg, MD, United States). Measurements were made using an incident neutron wavelength of 6.0 Å with a wavelength spread ($\Delta\lambda/\lambda$) of 0.12 and sample to detector distances of 1.0 m, 4.0 m, and 13.5 m. Additional low-q data were collected at a detector distance of 15.3 m using an incident neutron wavelength of 8.09 Å with $\Delta\lambda/\lambda = 0.12$ and focusing lenses. The total q-range used for these experiments was 0.001 Å-1 < q < 0.6 Å-1, where the scattering vector is defined as $q = 4\pi/\lambda \sin(\theta/2)$, and θ is the scattering angle. SANS data were reduced using the standard procedure provided by NIST. Samples were prepared at 2 mg mL^{-1} in D_2O.[53]

2.4.3 Synthetic Procedures

Synthesis of 2.01

5-bromo-m-xylene (25.0 g, 0.135 mol), *N*-bromosuccinimide (NBS) (57.6 g, 0.324 mol) azobisisobutyronitrile (AIBN) (0.125 g, 0.761 mmol) and methyl formate (300 mL) were added to a 1 L round bottom flask fitted with a reflux condenser. The reaction mixture was stirred and illuminated with a 500 W incandescent lamp at a distance of ca. 30 cm for 18 h. Next, the methyl formate was removed *in vacuo* leaving a yellow solid. The solid was dissolved in dichloromethane and washed with saturated brine until the solution was virtually colourless. Removal of the solvent *in vacuo* resulted in an off-white solid. Then, the solid was recrystallized from diethyl ether to afford 17.5 g of white needles (38% yield). ^{1}H NMR ($CDCl_3$): δ (ppm) 7.48 (s, 2H, Ar-*H*), 7.34 (s, 1H, Ar-*H*), 4.40 (s, 4H, C*H*$_2$Br). ^{13}C {^{1}H} NMR ($CDCl_3$): δ (ppm) 140.3, 132.0, 128.3, 122.7. 31.5. $C_8H_7Br_3$ Calc. C, 28.03; H, 2.06; Br, 69.92, Found C, 28.00; H, 1.95; Br, 69.97.

Synthesis of 2.02

2.01 (6.00 g, 17.5 mmol), potassium hydroxide (4.90 g, 87.5 mmol) and 18-crown-6 (0.462 g, 1.75 mmol) were added to a round bottom flask (500 mL) with tetrahydrofuran (*ca.* 200 mL) at 0 °C under N_2. Dodecanethiol (16.0 ml, 70.0 mmol) was added dropwise over 30 min. The reaction mixture was stirred at room temperature overnight. Then, the reaction mixture was dried to remove any remaining dodecanethiol. The crude mixture was purified by column chromatography (petroleum ether) and recrystallized twice from hexane. 3.24 g of a

light yellow solid was recovered (31% yield). ^{1}H NMR ($CDCl_3$): δ (ppm) 7.34 (s, 2H, Ar-*H*), 7.18 (s, 1H, Ar-*H*), 3.63 (s, 4H, S*CH*$_2$-Ar), 2.40 (t, J = 7.4 Hz, 4H, SC*H*$_2$CH$_2$), 1.50-1.60 (m, 4H, SCH$_2$C*H*$_2$), 1.35-1.18 (br m, 36H, (C*H*$_2$)$_9$CH$_3$), 0.88 (t, J = 6.8 Hz, 6H, CH$_2$C*H*$_3$). ^{13}C {^{1}H} NMR ($CDCl_3$): δ (ppm) 141.1, 130.3, 128.0, 122.4, 35.7, 31.9, 31.5, 29.7, 29.6, 29.4, 29.3, 29.2, 28.9, 22.7, 14.1. $C_{32}H_{57}Br_1S_2$ Calc. C, 65.61; H, 9.81; Br, 13.64; S, 10.95, Found C, 65.67; H, 9.87; Br, 13.72; S, 10.94.

Synthesis of 2.03

A clean, dry ampoule containing a magnetic stirrer bar was evacuated and back-filled with N_2 three times. **2.02** (3.46 g, 5.91 mmol) was added to the ampoule, and the evacuation/back-filling process was repeated three times. Dry diethyl ether (*ca.* 80 mL) was added *via* cannula transfer, and the solution was cooled to -78 °C. *t*-butyl lithium (1.7 M in pentane, *ca.* 8 mL, 13 mmol), was added dropwise *via* cannula transfer, with stirring. The reaction mixture was stirred for 2 h at -78 °C. Dimethyl formamide (*ca.* 1 mL, 13 mmol) was added *via* a syringe, and the reaction mixture was allowed to warm to room temperature and stirred overnight. The crude product was washed with water, NaOH (1 M) and brine. The aqueous layers were extracted with diethyl ether. All organic layers were combined and dried under vacuum overnight. The crude product was recrystallized twice from hexane. 2.16 g of a white solid was recovered (68 % yield). ^{1}H NMR ($CDCl_3$): δ (ppm) 10.00 (s, 1H, C*H*O), 7.70 (s, 2H, Ar-*H*), 7.56 (s, 1H, Ar-*H*), 3.75 (s, 4H, SC*H*$_2$-Ar), 2.40 (t, J = 7.4 Hz, 4H, SC*H*$_2$CH$_2$), 1.50-1.60 (m, 4H, SCH$_2$C*H*$_2$), 1.35-1.18 (m, 36H, (C*H*$_2$)$_9$CH$_3$), 0.88 (t, J = 6.8 Hz, 6H, CH$_2$C*H*$_3$). ^{13}C {^{1}H} NMR ($CDCl_3$): δ (ppm)

191.9, 140.3, 136.9, 135.2, 128.6, 35.8, 31.9, 31.6, 29.7 29.6, 29.5, 29.4, 29.3, 29.2, 28.9, 22.7, 14.1. $C_{33}H_{58}OS_2$ Calc. C, 74.09; H, 10.93; O, 2.99; S, 11.99, Found C, 74.10; H, 10.95; O, 2.98; S, 11.97.

Synthesis of 2.04

Lithium aluminium hydride (0.834 g, 21.95 mmol) was weighed into a clean dry Schlenk flask. The flask was evacuated and back-filled with N_2 three times. Then, dry diethyl ether (*ca.* 75 mL) was added *via* cannula transfer forming a green suspension. **2.03** (1.728 g, 2.20 mmol), dissolved in dry diethyl ether (*ca.* 25 mL), was added *via* cannula transfer to the Schlenk flask under nitrogen at 0 °C with stirring. The reaction mixture was allowed to warm to room temperature and stirred under nitrogen for 3 days. A saturated brine solution (*ca.* 20 mL) was carefully added to the reaction mixture. The solution was filtered, and the organic layer was repeatedly washed with brine. All volatiles were removed under vacuum, and 0.92 g of white solid was recovered (78 % yield). ^{1}H NMR ($CDCl_3$): δ (ppm) 7.19 (s, 2H, Ar-*H*), 7.18 (s, 1H, Ar-*H*), 4.68 (d, J = 6.0 Hz, 2H, C*H*$_2$OH), 3.69 (s, 4H, SC*H*$_2$-Ar), 2.40 (t, J = 7.4 Hz, 4H, SC*H*$_2$CH$_2$), 1.63 (t, J = 6.0 Hz, 1H, CH$_2$O*H*), 1.50-1.60 (m, 4H, SCH$_2$C*H*$_2$), 1.35-1.18 (m, 36H, (C*H*$_2$)$_9$CH$_3$), 0.88 (t, J = 6.8 Hz, 6H, CH$_2$C*H*$_3$). ^{13}C {^{1}H} NMR ($CDCl_3$): δ (ppm) 141.5, 139.2, 128.6, 126.0, 65.0, 36.2, 31.9, 31.6, 29.7, 29.6, 29.4, 29.3, 29.0, 22.7, 14.1. $C_{33}H_{60}OS_2$ Calc. C, 73.81; H, 11.26; O, 2.98; S, 11.94, Found C, 73.81; H, 11.32, O, 3.00; S, 11.87.

Synthesis of 2.05

S-dodecyl-S'-(α',α'-dimethyl-α''-acetic acid) (DDMAT) (0.580 g, 1.59 mmol) was dissolved in dichloromethane (*ca.* 20 mL) at 0 °C, under N_2. Then, *N*-(3-dimethyl-aminopropyl)-*N*-ethylcarbodiimide hydrochloride (0.308 g, 1.59 mmol) and 4-(dimethyl amino)pyridine (0.032 g, 0.27 mmol) were added, and the reaction mixture was stirred for 1 h. Next, **2.04** (0.712 g, 1.33 mmol) was added, and the reaction mixture was stirred at room temperature for 3 days. Finally, *N*-(3-dimethyl-aminopropyl)-*N*-ethylcarbodiimide hydrochloride (0.308 g, 1.59 mmol) and 4-(dimethyl amino)pyridine (0.032 g, 0.27 mmol) were added to drive the reaction to completion, and the mixture was stirred for an additional 2 days. The reaction mixture was extracted three times with a saturated brine solution, dried over magnesium sulphate, and filtered. The organic solution was removed *in vacuo*, and the crude product was purified *via* column chromatography using 40:1 petroleum ether:ethyl acetate. 1.17 g of **2.05** (yellow solid) was recovered (78 % yield). ^{1}H NMR ($CDCl_3$): δ (ppm) 7.20 (s, 1H, Ar-*H*), 7.13 (s, 2H, Ar-*H*) 5.01 (s, 2H, Ar-C*H*$_2$O), 3.69 (s, 4H, SC*H*$_2$-Ar), 3.26 (t, J= 7.6 Hz, 2H, SCSC*H*$_2$), 2.40 (t, J = 7.4 Hz, 4H, SC*H*$_2$CH$_2$) 1.70 (s, 6H, C(C*H*$_3$)$_2$) 1.64 (tt, J = 7.6, 7.2 Hz, 2H, SCSCH$_2$C*H*$_2$), 1.50-1.60 (m, 4H, SCH$_2$C*H*$_2$), 1.35-1.18 (br m, 54H, (C*H*$_2$)$_9$CH$_3$), 0.88 (t, J = 6.8 Hz, 9H, CH$_2$C*H*$_3$). ^{13}C {^{1}H} NMR ($CDCl_3$): δ (ppm) 221.2, 172.7, 139.2, 136.1, 129.1, 127.0, 67.4, 55.9, 37.0, 36.1, 32.0, 31.5, 29.7, 29.7, 29.6, 29.5, 29.4, 29.3, 29.3, 29.2, 29.0, 28.9, 27.9, 25.4, 22.7, 14.2. $C_{50}H_{90}O_2S_5$, Calc. C, 67.97; H, 10.27; O, 3.62; S, 18.15, Found C, 68.03; H, 10.39; O, 3.65; S, 17.93.

Polymerization of *tert*-butyl acrylate, 2.06

2.05 (0.094 g, 0.11 mmol), *t*-butyl acrylate (0.776 mL, 5.30 mmol), AIBN (1.7 mg, 0.011 mmol) and dioxane (0.776 mL) were added to a clean dry ampoule under N_2 (g). The solution was degassed *via* 3 freeze-pump-thaw cycles and heated to 65 °C for 2 hours under N_2 (g) with stirring. The viscous solution was dissolved in the minimum amount of THF, and the polymer was precipitated into 9:1 cold MeOH:H_2O. The MeOH:H_2O solution was decanted, and the polymer was dissolved in THF. Then, the solution was dried over $MgSO_4$ and filtered, and the solvent removed *in vacuo*. 0.369 g of yellow polymer, **2.06** was recovered. M_n^{NMR} = 6.9 kDa, M_n^{SEC}= 8.1 kDa, $Đ^{SEC}$ = 1.07. ^{1}H NMR ($CDCl_3$): δ (ppm) 7.20 (s, 1H, Ar-*H*), 7.14 (s, 2H, Ar-*H*), 5.05 (s, 2H, Ar-CH_2O), 3.68 (s, 4H, SCH_2-Ar), 3.33 (t, J = 7.6 Hz, 2H, SCSCH_2), 1.20-1.50 (br, $C(CH_3)_3$ polymer backbone), 1.30-2.30 (br, CH and CH_2 polymer backbone).

End group removal of poly(*tert*-butyl acrylate), 2.07

Polymer **2.06** (0.36 g, 0.052 mmol), AIBN (0.003 g, 0.02 mmol), 1-ethylpiperidine hypophosphite (EPHP) (0.046 g, 0.26 mmol) and toluene (*ca* 5 mL) were added to a clean dry ampoule under N_2 (g). The reaction vessel was degassed *via* 5 freeze-pump-thaw cycles. The ampoule was filled with N_2 (g) and heated to *ca.* 100 °C for 12 hours. All volatiles were removed *in vacuo*, and the white solid was dissolved in a minimum volume of THF. The polymer was precipitated into MeOH:H_2O 9:1 (*ca.* 100 mL). The solution was decanted from the solid polymer, and the polymer was re-dissolved in THF. Then, the solution was dried over $MgSO_4$ and filtered, and the solvent removed *in vacuo* to afford 0.26 g of a white polymer, **2.07**. M_n^{SEC} = 7.1 kDa

kDa, M_n/M_w^{SEC} = 1.07. ^{1}H NMR ($CDCl_3$): δ (ppm) 7.20 (s, 1H, Ar-*H*), 7.14 (s, 2H, Ar-*H*), 5.05 (s, 2H, Ar-C*H*$_2$O), 3.68 (s, 4H, SC*H*$_2$-Ar), 1.20-1.50 (br, C(C*H*$_3$)$_3$ polymer backbone), 1.30-2.30 (br, CH and CH_2 polymer backbone).

Complexation of poly(*t*-butyl acrylate), 2.08

Polymer **2.07** (0.250 g, 0.038 mmol), tetrakis(acetonitrile)palladium(II) tetrafluoroborate (50 mg, 0.11 mmol) and acetonitrile (*ca.* 15 mL) were added to a clean dry ampoule. The reaction vessel was degassed *via* 5 freeze-pump-thaw cycles. The ampoule was filled with N_2 (g) and stirred at room temperature for 2 days. The acetonitrile was removed *in vacuo,* and the polymer was re-dissolved in THF. After stirring for *ca.* 10 min, activated charcoal was added to remove the excess palladium. The solution was filtered, and the THF removed *in vacuo* affording a light orange solid, **2.08** that was used without further purification.

Deprotection of poly(*tert*-butyl acrylate) to form poly(acrylic acid), 2.09

2.08 (0.25 g, 0.038 mmol) and trifluoroacetic acid (TFA) (4.3 g, 37 mmol) were dissolved in CH_2Cl_2 (*ca*. 10 mL) at 0 °C. The solution was stirred at 0 °C for 60 min then allowed to warm to room temperature overnight. All volatiles were removed under N_2 (g), and the remaining white solid was dissolved in THF:H_2O 1:1, transferred to a dialysis membrane tube (molecular weight cut-off [MWCO] 1.0 kDa), and dialyzed against deionized water (3 L) with 7 water changes. Lyophilization resulted in 0.15 g of yellow solid, **2.09**. ^{1}H NMR (DMSO): δ (ppm) 12.50 (br, OH polymer backbone), 6.93 (s, 2H, Ar-*H*), 4.86 (br, 2H, Ar-C*H*$_2$O), 4.34 (br, 4H, SC*H*$_2$-Ar), 2.49-1.00 (br, CH and CH_2 polymer backbone).

Synthesis of poly(acrylic acid) polymer, 2.10

Synthesis was repeated as for **2.09** but without the complexation step **2.08**. ^{1}H NMR (DMSO): δ (ppm) 12.50 (br, OH polymer backbone), 7.18 (s, 1H, Ar-*H*), 7.13 (s, 2H, Ar-*H*), 4.99 (s, 2H, Ar-C*H*$_2$O), 4.34 (br, 4H, SC*H*$_2$-Ar), 2.49-1.00 (br, CH and CH_2 polymer backbone).

Synthesis of 2.11

Dibromo-*m*-xylene (3.0 g, 11 mmol), 18-crown-6 (0.30, 1.4 g) and KOH (3.2 g, 57 mmol) were added to a Schlenk tube with THF (*ca.* 100 mL) at 0 °C under N_2 (g). Dodecanethiol (14 mL, 57 mmol) was added dropwise over 10 min. The reaction mixture was stirred at room temperature for 24 hours. The white precipitate that formed during the reaction was removed *via* filtration, and the reaction mixture was dried *in vacuo*. The product was dissolved in dichloromethane, and the organic solution was washed twice with sodium hydroxide (150 mL, 1M) and once with a saturated brine solution. The crude mixture was purified by column chromatography using 4:1 hexane:dichloromethane to afford 2.8 g of an off-white solid, **2.11** (49% yield). ^{1}H NMR ($CDCl_3$): δ (ppm) 7.25-7.17 (m, 4H, Ar-*H*), 3.68 (s, 4H, SC*H*$_2$-Ar) 2.40 (t, 4H, J = 7.2 Hz, SC*H*$_2$CH$_2$) 1.55 (m, 4H, SCH$_2$C*H*$_2$) 1.25 (m, 36H, (C*H*$_2$)$_9$CH$_3$), 0.88 (t, 6H, J = 6.8 Hz, CH$_2$C*H*$_3$). ^{13}C {^{1}H} NMR ($CDCl_3$): δ (ppm) 138.9, 129.3, 128.6, 127.4, 36.2, 31.9, 31.4, 29.7, 29.6, 29.6, 29.4, 29.3, 28.9, 22.7, 14.1. $C_{32}H_{58}S_2$ Calc. C, 75.82; H, 11.53; S, 12.65, Found C, 75.92; H, 11.49; S, 12.65.

Synthesis of 2.12

2.11 (0.10 g, 0.20 mmol) and tetrakis(acetonitrile)palladium(II) tetrafluoroborate (0.105 g, 0.24 mmol) were dissolved in acetonitrile (*ca*. 10 mL). The stirred solution was purged with N_2 (g) for *ca.* 2 hours, sealed, and stirred for *ca.* 24 hours. Then, the solvent was removed *in vacuo* leaving a yellow precipitate. The solid was dissolved in the minimum amount of acetonitrile, to which ether was added dropwise forming a black precipitate. The solution was filtered, and the solvent removed *in vacuo*, affording 0.072 g of light brown flaky solid, **2.12** (50% yield). ^{1}H NMR ($CDCl_3$): δ (ppm) 7.04-6.94 (m, 3H, Ar-*H*), 4.22 (br, 4H, SC*H*$_2$-Ar) 3.13 (t, 4H, J = 7.2 Hz, SC*H*$_2$CH$_2$), 2.38 (s, br, 3H, PdNCC*H*$_3$), 1.83 (tt, 4H, J = 7.6, 7.6 Hz, SCH$_2$C*H*$_2$), 1.25 (m, 36H, (C*H*$_2$)$_9$CH$_3$), 0.88, (6H, t, J = 6.8 Hz, CH$_2$C*H*$_3$). ^{13}C {^{1}H} NMR ($CDCl_3$): δ (ppm) 149.1, 124.3, 122.3, 37.6, 30.9, 28.6, 28.6, 28.5, 28.3, 28.2, 27.6, 21.7, 13.1. $C_{32}H_{57}PdS_2$ HRMS: *m/z* 611.2945, [M-MeCN].[70]

2.4.4 Catalysis Procedures

2 mol% catalyst loading using pincer compound 2.09

3,4-Epoxy-1-butene (5.53 mg, 78.9 µmol), phenyl boronic acid (12.0 mg, 98.6 µmol) and caesium carbonate (55.7 mg, 157.8 µmol) were added to 0.7 mL of a D_2O stock solution of **2.09** (at a concentration of 10 mg mL^{-1}). Then, the solution was agitated at 25 °C. For kinetics experiments, samples were removed at predetermined times for analysis by ^{1}H NMR spectroscopy. Products were extracted twice with 1 mL $CDCl_3$ and analysed by ^{1}H NMR spectroscopy. Dimethyl formamide was used as an

internal standard to determine the reaction yield. For lower mol % experiments, the stock solutions of the assemblies were diluted accordingly.

2.14 E ^{1}H NMR ($CDCl_3$): δ (ppm) 7.24-7.08 (5H, m, Ar-*H*), 5.75-5.84 (m, 1H, $OHCH_2HC{=}CH$), 5.70 (m, 1H, $OHCH_2CH$), 4.02 (d J = 5.6 Hz, 2H, $OHCH_2$), 3.28 (d J = 2.8 Hz, 2H, Ar-CH_2)

2.14 Z ^{1}H NMR ($CDCl_3$): δ (ppm) 7.24-7.08 (m, 5H, Ar-*H*), 5.75-5.84 (m, 1H, $OHCH_2HC{=}CH$), 5.70 (m, 1H, $OHCH_2CH$), 4.21 (d J = 5.2 Hz, 2H, $OHCH_2$), 3.34 (d J = 5.59 Hz, 2H, Ar-CH_2)

2.13 ^{1}H NMR ($CDCl_3$): δ (ppm) 7.24-7.08 (m, 5H, Ar-*H*), 5.96-5.87 (ddd J = 10.4, 7.6, 6.8 Hz, 1H, $H_2C{=}CHC$), 5.13-5.06 (m, 2H, $HC{=}CH_2$), 3.72 (d, J = 7.2 Hz, 2H, CH_2OH), 3.44 (dt, J = 7.2, 7.2 Hz, 1H, Ar-*CH*).

2 mol% catalyst loading using pincer compound 2.12 in THF

3,4-Epoxy-1-butene (22.4 mg, 0.32 mmol), phenyl boronic acid (46.8 mg, 0.38 mmol) and caesium carbonate (226 mg, 0.64 mmol) were added to 0.66 mL of 10:1 THF:D_2O. Then, the solution was agitated at 25 °C. For kinetics experiments, samples were removed at predetermined times for analysis by ^{1}H NMR spectroscopy.

2.4.5 Recycling and Degradation Experiments

Reaction of the starting materials with water:

3,4-Epoxy-1-butene (5.53 mg, 78.9 μmol) was added to 0.7 ml of a D_2O stock solution of **2.10** (at a concentration of 10 mg mL^{-1}). The solution was agitated for 24 h at 25 °C.

Recycling experiment

After the products were extracted from the initial reaction with $CDCl_3$, the aqueous polymer solution of **2.09** was dried under vacuum to remove any residual $CDCl_3$. Then, the catalysis reaction was repeated as described in the experimental section.

Inductively Coupled Plasma Optical Emission Spectrometry (ICP-OES) Study

After performing the catalysis at 0.1 mol% and extraction of the products by $CDCl_3$, the aqueous solution was analysed by ICP-OES and showed a Pd concentration of 867 ppb (expected concentration was 837 ppb). Then, poly(vinyl pyridine) (PVP) (34.3 mg) particles were added to the solution to bind any free palladium that leached out of the micelles during the reaction. The solution was stirred for 2 h and then left to stand for 1 h to allow the PVP particles to settle. Next, the solution was analysed by ICP-OES, which gave a Pd concentration of 521 ppb, indicating that approximately 40% of the Pd had been removed by the PVP particles.

Poisoning Experiments[63, 65, 66]

Hg drop test: The catalysis was performed as described earlier, but with the addition of Hg (80 mg) to the solution.

PVP Test: The catalysis was performed as described earlier, but with added PVP (10 mg) to the catalysis reaction mixture.

2.5 References

1. T. Dwars, E. Paetzold and G. Oehme, *Angew. Chem.*, 2005, **44**, 7174-7199.
2. F. Trentin, A. Scarso and G. Strukul, *Tetrahedron Lett.*, 2011, **52**, 6978-6981.
3. S. Ta§cioğlu, *Tetrahedron*, 1996, **52**, 11113-11152.
4. K. Manabe, S. Iimura, X.-M. Sun and S. Kobayashi, *J. Am. Chem. Soc.*, 2002, **124**, 11971-11978.
5. M. Kunishima, K. Kikuchi, Y. Kawai and K. Hioki, *Angew. Chem. Int. Ed.*, 2012, **51**, 2080-2083.
6. P. Cotanda, A. Lu, J. P. Patterson, N. Petzetakis and R. K. O'Reilly, *Macromolecules*, 2012, **45**, 2377-2384.
7. K. T. Kim, S. A. Meeuwissen, R. J. Nolte and J. C. van Hest, *Nanoscale*, 2010, **2**, 844-858.
8. Y. Liu, Y. Wang, Y. Wang, J. Lu, V. Piñón and M. Weck, *J. Am. Chem. Soc.*, 2011, **133**, 14260-14263.
9. D. M. Vriezema, P. M. L. Garcia, O. N. Sancho, N. S. Hatzakis, S. M. Kuiper, R. J. M. Nolte, A. E. Rowan and J. C. M. van Hest, *Angew. Chem. Int. Ed.*, 2007, **46**, 7378-7382.
10. S. F. M. van Dongen, M. Nallani, J. J. L. M. Cornelissen, R. J. M. Nolte and J. C. M. van Hest, *Chem. Eur. J.*, 2009, **15**, 1107-1114.
11. B. Helms, C. O. Liang, C. J. Hawker and J. M. J. Fréchet, *Macromolecules*, 2005, **38**, 5411-5415.
12. K. Manabe, S. Iimura, X. M. Sun and S. Kobayashi, *J. Am. Chem. Soc.*, 2002, **124**, 11971-11978.

13. K. Manabe, X. M. Sun and S. Kobayashi, *J. Am. Chem. Soc.*, 2001, **123**, 10101-10102.

14. A. Lu, P. Cotanda, J. P. Patterson, D. A. Longbottom and R. K. O'Reilly, *Chem. Commun.*, 2012, **48**, 9699-9701.

15. P. Cotanda and R. K. O'Reilly, *Chem. Commun.*, 2012, **48**, 10280-10282.

16. M. J. Boerakker, J. M. Hannink, P. H. H. Bomans, P. M. Frederik, R. J. M. Nolte, E. M. Meijer and N. A. J. M. Sommerdijk, *Angew. Chem. Int. Ed.*, 2002, **41**, 4239-4241.

17. M. Changez, N.-G. Kang and J.-S. Lee, *Small*, 2012, **8**, 1173-1179.

18. N. Hadjichristidis, S. Pispas and M. Pitsikalis, *Prog. Polym. Sci.*, 1999, **24**, 875-915.

19. T. S. Kale, A. Klaikherd, B. Popere and S. Thayumanavan, *Langmuir*, 2009, **25**, 9660-9670.

20. H. Ringsdorf, J. Venzmer and F. M. Winnik, *Macromolecules*, 1991, **24**, 1678-1686.

21. M. l. Bathfield, D. Daviot, F. D'Agosto, R. Spitz, C. Ladavière, M.-T. r. s. Charreyre and T. Delair, *Macromolecules*, 2008, **41**, 8346-8353.

22. J. Du, H. Willcock, J. P. Patterson, I. Portman and R. K. O'Reilly, *Small*, 2011, **7**, 2070-2080.

23. T. Koga, F. Tanaka, R. Motokawa, S. Koizumi and F. M. Winnik, *Macromolecules*, 2008, **41**, 9413-9422.

24. P. Kujawa, F. Segui, S. Shaban, C. Diab, Y. Okada, F. Tanaka and F. M. Winnik, *Macromolecules*, 2006, **39**, 341-348.

25. P. Kujawa, F. Tanaka and F. M. Winnik, *Macromolecules*, 2006, **39**, 3048-3055.

26. P. Kujawa, H. Watanabe, F. Tanaka and F. M. Winnik, *Eur. Phys. J. E*, 2005, **17**, 129-137.

27. F. Laflèche, D. Durand and T. Nicolai, *Macromolecules*, 2003, **36**, 1331-1340.

28. F. Laflèche, T. Nicolai, D. Durand, Y. Gnanou and D. Taton, *Macromolecules*, 2003, **36**, 1341-1348.

29. T. Nicolai, F. Laflèche and A. Gibaud, *Macromolecules*, 2004, **37**, 8066-8071.

30. F. Renou, T. Nicolai, E. Nicol and L. Benyahia, *Langmuir*, 2009, **25**, 515-521.

31. A. Yamazaki, J. M. Song, F. M. Winnik and J. L. Brash, *Macromolecules*, 1998, **31**, 109-115.

32. H. Götz, E. Harth, S. M. Schiller, C. W. Frank, W. Knoll and C. J. Hawker, *J. Polym. Sci. Part A: Polym. Chem.*, 2002, **40**, 3379-3391.

33. N. Heldt, M. Gauger, J. Zhao, G. Slack, J. Pietryka and Y. Li, *Reactive and Functional Polymers*, 2001, **48**, 181-191.

34. H. Kitano, Y. Akatsuka and N. Ise, *Macromolecules*, 1991, **24**, 42-46.

35. J. T. Xu, L. Tao, C. Boyer, A. B. Lowe and T. P. Davis, *Macromolecules*, 2011, **44**, 299-312.

36. K. Akiyoshi, E.-C. Kang, S. Kurumada, J. Sunamoto, T. Principi and F. M. Winnik, *Macromolecules*, 2000, **33**, 3244-3249.

37. C. Li, J. Hu, J. Yin and S. Liu, *Macromolecules*, 2009, **42**, 5007-5016.

38. P. Théato, E. Preis, M. Brehmer and R. Zentel, *Macromol. Symp.*, 2001, **164**, 257-268.

39. C. C. Johansson Seechurn, M. O. Kitching, T. J. Colacot and V. Snieckus, *Angew. Chem.*, 2012, **51**, 5062-5085.

40. G. Hamasaka, T. Muto and Y. Uozumi, *Angew. Chem.*, 2011, n/a-n/a.

41. A. Molnar, *Chem Rev*, 2011, **111**, 2251-2320.

42. G. Hamasaka, T. Muto and Y. Uozumi, *Dalton Trans.*, 2011, **40**, 8859-8868.

43. J. Skey and R. K. O'Reilly, *Chem. Commun.*, 2008, 4183-4185.

44. A. O. Moughton and R. K. O'Reilly, *J. Am. Chem. Soc.*, 2008, **130**, 8714-8725.

45. A. O. Moughton, K. Stubenrauch and R. K. O'Reilly, *Soft Matter*, 2009, **5**, 2361-2370.

46. Y. K. Chong, G. Moad, E. Rizzardo and S. H. Thang, *Macromolecules*, 2007, **40**, 4446-4455.

47. D. E. Bergbreiter and S. Furyk, *Green Chem.*, 2004, **6**, 280-285.

48. C. A. Kruithof, H. P. Dijkstra, M. Lutz, A. L. Spek, R. Gebbink and G. van Koten, *Organometallics*, 2008, **27**, 4928-4937.

49. Q. G. Ma and K. L. Wooley, *J. Polym. Sci. Part A: Polym. Chem.*, 2000, **38**, 4805-4820.

50. A. Kawasaki, J. Furukawa, T. Tsuruta, G. Wasai and T. Makimoto, *Die Makromolekulare Chemie*, 1961, **49**, 76-111.

51. W. Schärtl, *Light Scattering from Polymer Solutions and Nanoparticle Dispersions*, Springer Berlin Heidelberg, Verlag Berlin Heidelberg, 2007.

52. J. Li, T. Ngai and C. Wu, *Polym J*, 2010, **42**, 609-625.

53. S. R. Kline, *J. Appl. Crystallogr.*, 2006, **39**, 895-900.

54. W. Groenewegen, S. U. Egelhaaf, A. Lapp and J. R. C. van der Maarel, *Macromolecules*, 2000, **33**, 3283-3293.

55. R. Lund, V. Pipich, L. Willner, A. Radulescu, J. Colmenero and D. Richter, *Soft Matter*, 2011, **7**, 1491-1500.

56. Y. Bakkour, V. Darcos, S. Li and J. Coudane, *Polym. Chem.*, 2012, **3**, 2006-2010.

57. N. Miyaura and A. Suzuki, *Chem. Rev. (Washington, DC, U. S.)*, 1995, **95**, 2457-2483.

58. J. Kjellgren, J. Aydin, O. A. Wallner, I. V. Saltanova and K. J. Szabó, *Chem. Eur. J.*, 2005, **11**, 5260-5268.

59. N. Selander and K. l. n. J. Szabó, *The J. Org. Chem.*, 2009, **74**, 5695-5698.

60. G. Hamasaka, T. Muto and Y. Uozumi, *Angew. Chem.*, 2011, **50**, 4876-4878.

61. B. M. Trost and E. J. McEachern, *J. Am. Chem. Soc.*, 1999, **121**, 8649-8650.

62. W. J. Sommer, K. Yu, J. S. Sears, Y. Ji, X. Zheng, R. J. Davis, C. D. Sherrill, C. W. Jones and M. Weck, *Organometallics*, 2005, **24**, 4351-4361.

63. K. Yu, W. Sommer, J. M. Richardson, M. Weck and C. W. Jones, *Adv. Synth. Catal.*, 2005, **347**, 161-171.

64. K. Yu, W. Sommer, M. Weck and C. W. Jones, *J. Catal.*, 2004, **226**, 101-110.

65. M. Weck and C. W. Jones, *Inorg. Chem.*, 2007, **46**, 1865-1875.

66. N. T. S. Phan, M. Van Der Sluys and C. W. Jones, *Adv. Synth. Catal.*, 2006, **348**, 609-679.

67. N. J. M. Pijnenburg, H. P. Dijkstra, G. van Koten and R. J. M. K. Gebbink, *Dalton Trans.*, 2011, **40**, 8896-8905.

68. N. Selander and K. J. Szabo, *Chem Rev*, 2011, **111**, 2048-2076.

69. M.-P. Chien, M. P. Thompson and N. C. Gianneschi, *Chem. Commun.*, 2011, **47**, 167-169.

70. *The expected mass for compound 3 minus the acetonitrile ligand*.

Chapter 3. In-depth structural characterisation of Y-tailed amphiphilic homopolymer micelles by Cryo-TEM, SANS and LLS

3.1 Abstract

The aqueous self-assembly of Y-tailed SCS pincer amphiphilic PNIPAM homopolymers has been studied in detail by NMR, Cryo-TEM, DLS, SLS, SANS and spectrophotometry. Although the hydrophobic ligand accounted for <5 wt % of the overall homopolymer mass, these polymers self-assembled into well-defined spherical micelles in aqueous solution. The data obtained from the scattering and microscopy techniques are compared in relation to scaling parameters and the factors which effect micelle size, and the shape of the NIPAM chains. Radial density profiles extracted from both the cryo-TEM micrographs and SANS models suggested that the PNIPAM chains formed a diffuse corona with a radially decreasing corona density profile, characteristic of star-like micelles. The similarity between the SANS and cryo-TEM results indicated that detailed information about the micelle density profile can be obtained directly from cryo-TEM and highlighted the utility of cryo-TEM in the structural characterisation of solution-assemblies. In addition to the structural profiles, the thermo-responsive properties of these micelles were investigated. Changes in the micelle size or aggregation number did not affect the micelle cloud point upon heating; however, a hysteresis upon cooling was noted which dependent on the molecular weight of the polymer.

3.2 Introduction

PNIPAM is widely used in the self-assembly of BCPs into various nanostructures. Perhaps its most attractive feature is its thermoresponsive nature, whereby at low temperatures (typically < 32 °C) the polymer is soluble in water, but upon heating (typically > 32 °C) the polymer becomes water insoluble due to intra- or inter- chain H-bonding being more favourable than polymer-water H-bonding.[1, 2] The thermoresponsivity of PNIPAM has been exploited for self-assembled polymer systems by use in nanoreactor recovery,[3] morphology switching systems[4, 5] and drug delivery.[6] Winnik has studied amphiphilic homopolymers based on PNIPAM in detail, with an early focus on telechelic polymers and their thermoresponsive properties[7-9] as well as a more recent neutron scattering study on flower-like micelles.[10] Amphiphilic homopolymers often self-assemble into spherical micelles at low concentrations due to their low hydrophobic content. However, Lowe and Davis recently reported vesicles and cylinders formed from Y-tailed amphiphilic homopolymers of *N*,*N*-dimethylacrylamide (DMA) and *N*-(2-hydroxypropyl) methacrylamide (HPMA) with hydrophobic contents as low as 6 wt%, as characterised by SEM, DLS, and fluorescence spectroscopy (**Figure 54**).[11] By changing the structure of the Y-shaped hydrophobic group, they determined that polymers end-functionalised with two rigid pyrene rings self-assembled into vesicles, while polymers functionalised with two flexible octadecyl chains formed spherical micelles at comparable weight fractions.

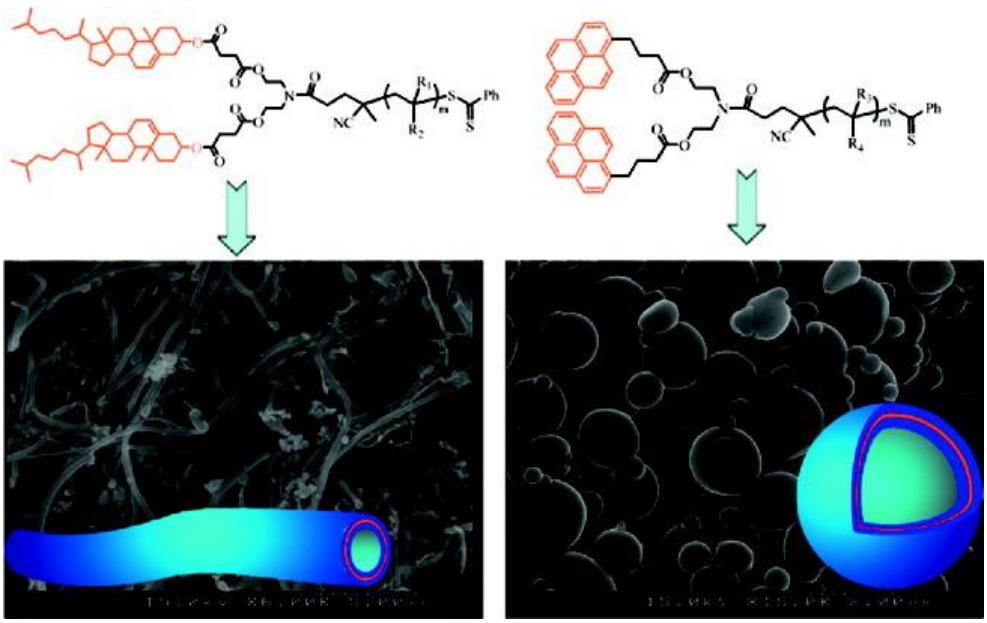

Figure 54. Cylinders (left) and vesicles (right) formed from Y-tailed amphiphilic homopolymers by changing the nature of the 'Y' group.

Lowe and Davis' report further demonstrates the importance of end groups in homopolymer solution-assembly and shows that amphiphiles, even with small hydrophobic components (< 10 wt %), can form a variety of well-defined nanoscale structures. In this chapter a series of Y-tailed amphiphilic PNIPAM homopolymers are synthesised and their solution assembly is studied in detail. The work focuses on characterising the assemblies in water and understanding how changes in polymer length affect the nanostructures. The three different molecular weight PNIPAMs are analysed by tensiometry, fluorescence spectroscopy, NMR, Cryo-TEM, DLS, SLS, SANS and spectrophotometry.

3.3 Results and discussion

3.3.1 Synthesis of SCS functionalised PNIPAMS, 3.04-3.06 and unfunctionalised PNIPAM 3.08

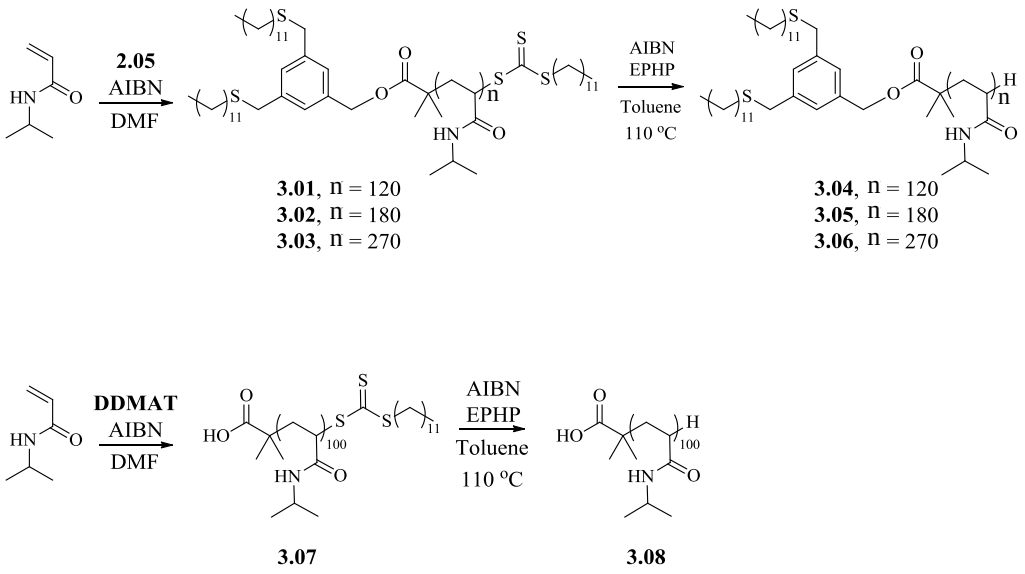

Scheme 1. Synthesis of end-functionalised PNIPAM polymers **3.04-3.06** and non functionalised PNIPAM **3.08**.

In order to build well defined SCS pincer assemblies which could be accurately characterised, Y-tailed amphiphilic homopolymers of PNIPAM were synthesised. In relation to the Y-tailed PAA polymers synthesised in Chapter 2 (**2.09** and **2.10**) the degree of polymerisation (DP) was extended (from 50 to > 100) in an attempt to obtain a single population of spheres. Three different molecular weight (MW) PNIPAMs were synthesised using **2.05** in order to assess the effect of MW on the assemblies.

Table 4. Polymer characterisation data for **3.04-3.06**

Sample	M_n[a] (kDa)	M_n[b] (kDa)	M_w[c] (kDa)	DP_{PNIPAM}[d]	$Đ$[a]	$f_{hydrophobic}$[e]
3.04	11.8	14.2	15.8	120	1.12	0.04
3.05	20.3	21.0	25.3	180	1.21	0.03
3.06	23.8	30.6	38.5	270	1.24	0.02

[a]From SEC based on PMMA standards in DMF. [b]Based on end-group analysis from ^{1}H NMR. [c]Calculated from ^{1}H NMR and SEC according to $M_w = DP_{PNIPAM} MW_o * Đ + MW_{pincer}$. [d]determined from ^{1}H NMR end-group analysis. [e]Hydrophobic weight fraction calculated from ^{1}H NMR.

A non end-functionalised PNIPAM was also synthesised using the RAFT agent DDMAT (precursor to **2.05**) in order to perform control CMC experiments. The synthesis of the SCS pincer end functionalised polymers was performed using an analogous method to the PAA polymer in Chapter 2. The data for each polymer **3.04**-**3.06** is summarised in Table 1 and example polymerisations are detailed in the experimental section. As in Chapter 2, the polymer degree of polymerisation was determined by ^{1}H NMR end group analysis (H_a, **Figure 55**) which was subsequently used to determine M_n. For the light scattering analysis it is more appropriate to use M_w and this was subsequently determined by the equation $M_w = DP_{PNIPAM} MW_{monomer} * Đ + MW_{pincer}$ where DP is the degree of polymerisation, $MW_{monomer}$ is the MW of the monomer, $Đ$ is the dispersity (measured by SEC) and MW_{pincer} is the MW of the end group.

3.3.2 ^{1}H NMR spectroscopy analysis

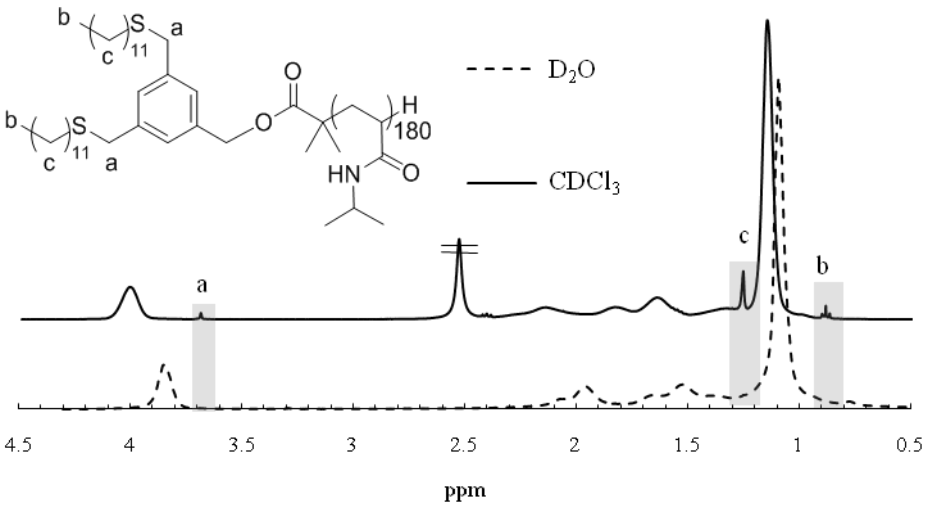

Figure 55. ^{1}H NMR spectra of **3.05** in $CDCl_3$ and D_2O, where boxed regions highlight the peaks associated with hydrophobic pincer end-group.

Peaks associated with the hydrophobic pincer end-group were seen clearly in the ^{1}H NMR spectra (at δ = 3.7, 1.2, and 0.8 ppm) in deuterated chloroform, a good solvent for both the end-group and the polymer (**Figure 55**). However in D_2O, a selective solvent for PNIPAM, the end-group peaks were attenuated. The attenuation of these peaks indicated that the end-groups have become dehydrated / confined to a less mobile environment (consequently the nuclear spins have a longer relaxation time), which is indicative of either self-assembly or single chain nanoparticle formation. The PAA Y-tailed amphiphilic homopolymers in Chapter 2 formed a mixtures of spherical and cylindrical micelles, this combined with the difficulties in performing light scattering on samples due to the polyelectrolyte effect resulted in only a basic understanding of the size and morphology of the structures. Detailed analysis of the PNIPAM Y-tailed amphiphilic homopolymers should allow a much better

understanding of the assemblies formed from these types of structures and how the system can be altered by changing the length of the NIPAM chain.

3.3.3 Evaluation of CMC by tensiometry‡ and fluorescence spectroscopy

The CMCs could not be evaluated using DOSY NMR as used previously for the PAA **2.09** as the detection level of the technique is not sensitive enough, therefore CMCs were studied using surface tensiometry,[12] and fluorescence spectroscopy.[13] Plots of surface tension (γ) vs. the log of surfactant concentration (c) can be used to determine the critical micelle concentration. For pure water, γ = 72 nN m^{-1}, which decreases upon addition of surfactants because they adsorb preferentially at the air-water interface. Upon micelle formation the surface tension becomes independent of surfactant concentration and this point can be defined as the CMC.[14]

The surface tension measurements (**Figure 56**) indicate a trend in the CMC, **3.04** < **3.05** < **3.06**. This is in stark contrast to previous studies for BCPs and surfactants where the more hydrophobic amphiphiles have a lower CMC.[15-19] However, surface tension analysis of the unfunctionalised PNIPAM **(3.08**, DP = 100) (**Figure 56**) shows an almost identical result to that of **3.04** (DP = 120) which indicates that PNIPAM itself is surface active (due to the hydrophobic backbone and hydrophilic side chains, **Figure 57**).

‡ Tensiometry experiments were performed by Dave Adams and Lin Chen, University of Liverpool

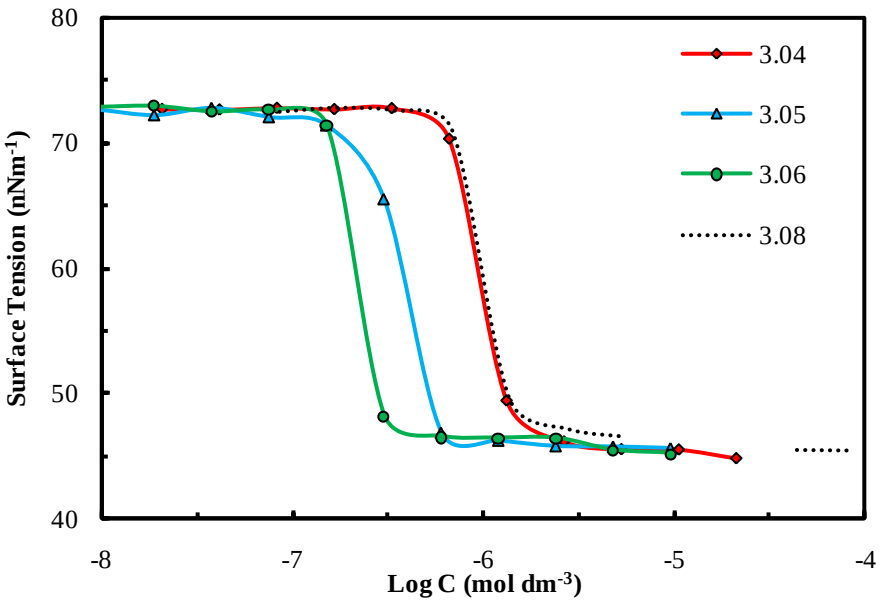

Figure 56. Plot of surface tension as a function of polymer concentration for **3.04-3.06** and **3.08**

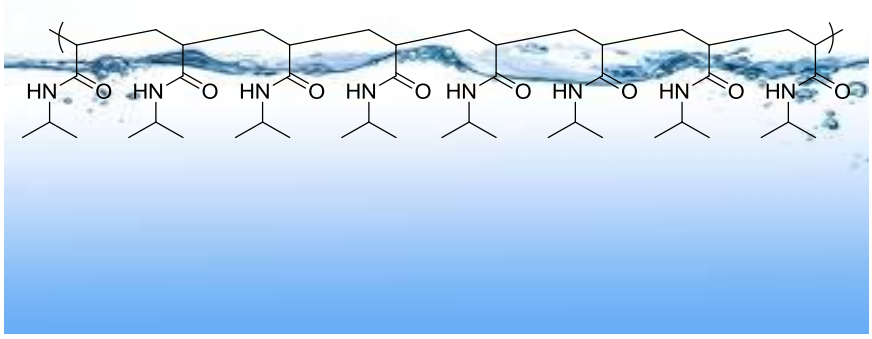

Figure 57. Schematic of the proposed surface activity of PNIPAM.

While CMC measurements using surface tensiometry are not common for PNIPAM or other vinyl polymers, there are examples in the literature and care should be taken to perform appropriate control experiments.[20-22] With this in mind the trend of surface saturation with increasing NIPAM MW can easily be explained as the longer polymer chains will saturate the surface at lower molar concentrations because they cover a greater surface area.

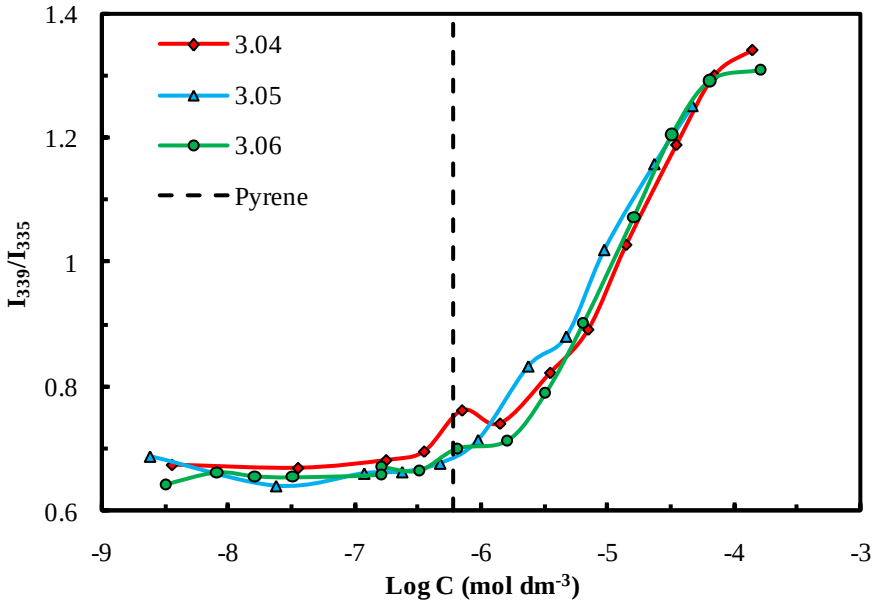

Figure 58. Plot of the intensity ratio I_{339}/I_{335} from the pyrene excitation spectra as a function of polymer concentration for **3.04-3.06,** the dashed black line indicated the pyrene concentration in each solution.

Winnik showed how the CMC of PS-b-PEO aggregates can be determined using pyrene and fluorescence spectroscopy.[13] Encapsulation of pyrene into a hydrophobic domain results in changes to the absorption / emission spectra and consequently can be used to determine the onset of micelle formation. Specifically, there is a slight red shift in the excitation maximum (ca. 335 - 339 nm) upon encapsulation into a hydrophobic domain. Therefore plotting the change in the I_{335}/I_{339} ratio vs. the log of polymer concentration shows the onset of micelle formation at the intersection between the slope and the flat line. The fluorescence measurements in **Figure 58** show apparent CMC values of ca. 1 µM, however as indicated by the dashed black line, the pyrene concentration in this experiment was 0.6 µM. As the molar concentration of pyrene is equivalent to the polymer molar concentration the change in pyrene environment (from hydrophobic to hydrophilic) is likely to be due to a

partitioning between micelles and the aqueous environment, due to an excess of pyrene, rather than a breakup of the micelles. Therefore it can be concluded that the CMC is ≤ 0.6 µM (ca. 10^{-2} mg ml^{-1}). Note: the unfunctionalised PNIPAM (**3.08**) did not show a shift in excitation spectra showing that **3.08** is not capable of encapsulating a hydrophobe (**Figure 59**).

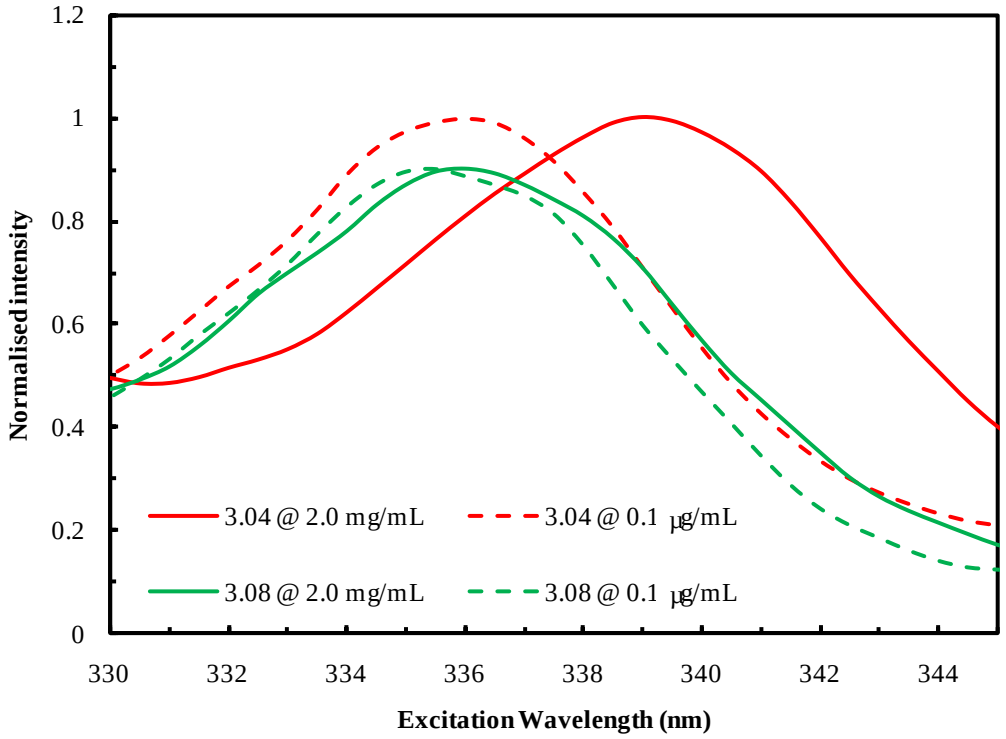

Figure 59. Excitation spectra (λ_{em} = 390 nm) for **3.04** and **3.08**.

3.3.4 Analysis of self-assembled structures by cryo-TEM

The solution assembly of samples **3.04**-**3.06** was also investigated using cryo-TEM (2 mg mL^{-1} in D_2O). **Figure 60** shows all samples form spherical micelles of ca. 20-40 nm in diameter. As the polymers **3.04**-**3.06** have the same hydrophobic end group as the polymers **2.09** and **2.10**, the core sizes should be the same. The cryo-TEM and SANS analysis in Chapter 2 indicated the core of these SCS pincer structures should be on the order of a few nm, which means there must be significant scattering from the PNIPAM chains and that the corona is visible in addition to the core. While polymeric coronas often are not visible in cryo-TEM due to their hydrated nature, the direct visualisation of micelle coronas (including PNIPAM) has been reported previously.[23-27] Being able to visualise the NIPAM corona makes determining an accurate size difficult as the particles do not have a well-defined edge. The polymer chain density should decrease from the core of the micelle to the ends of the polymer chains. As this density decreases the contrast against the vitrified water layer will be reduced making it difficult to define the particle edge.

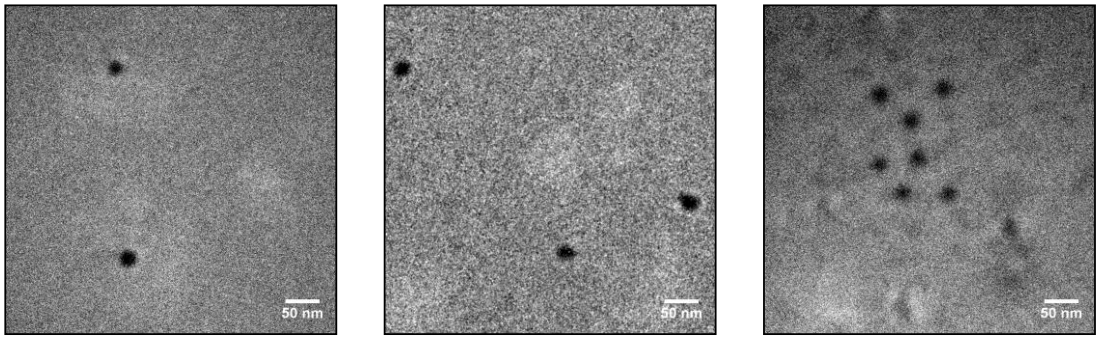

Figure 60. Cryo-TEM micrographs for **3.04** (left), **3.05** (center), and **3.06** (right) in D_2O showing that the polymers self-assemble into spherical micelles. Scale bars are 50 nm.

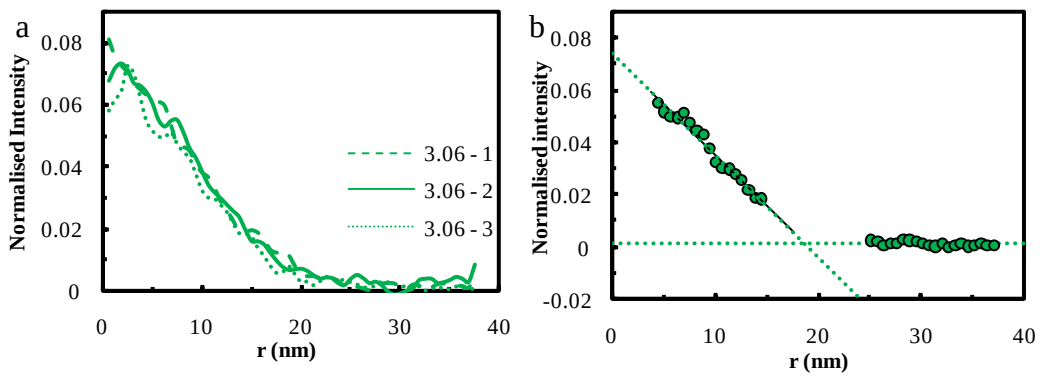

Figure 61. Radial plot profiles from cryo-TEM image **Figure 60c** for **3.06**. (a) shows an overlay of three plot profiles and (b) shows how micelle radius was determined for each micelle by extrapolating the slope of the radial profile to the background.

Therefore circularly averaged plot profiles, starting from the centre of the micelle, were taken for each of the micelles in **Figure 60**, the intensity values were then normalised, giving the background intensity as zero. **Figure 61a** shows an overlay for three of the micelles formed from **3.06**, indicating that the micelles are well defined, as they all overlay well. **Figure 61b** gives an example of how the sizes were determined by extrapolating the slope to the scattering of the background. Micelle radius (R) was determined to be 15 (± 1.0), 16 (± 0.5) and 19 (± 0.3) nm for **3.04**, **3.05** and **3.06** respectively. An increasing radius with DP_{corona} is expected from previous experimental literature and scaling theories for small molecule surfactants[15, 17] and BCP assemblies.[16, 18, 19, 28]

Cryo-TEM is widely used to obtain quantitative structural information about biological molecules such as the radial density distribution of the tobacco mosaic virus[29] and the 3D structure of many viruses.[30]

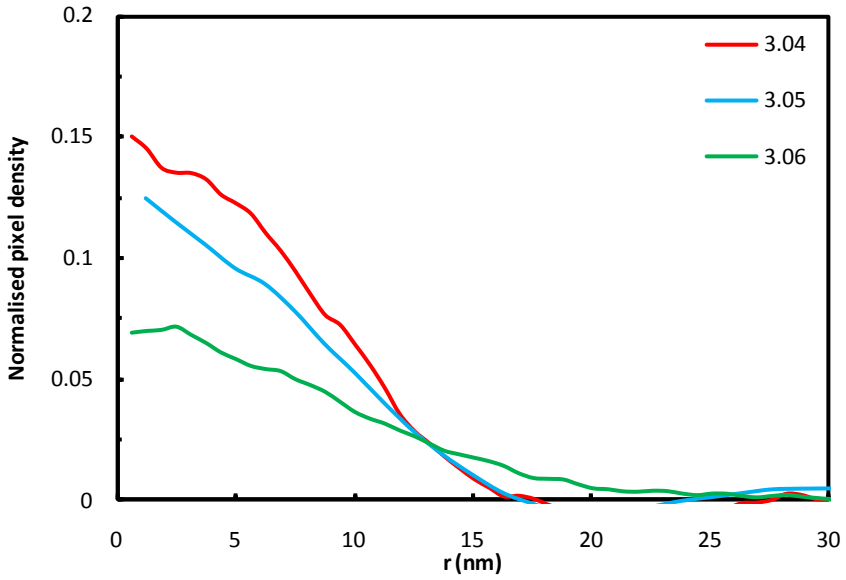

Figure 62. Average Radial plot profiles from the micelles in cryo-TEM images in **Figure 60** for **3.04**-**3.06.**

Using a similar approach and assuming mass-thickness contrast dominates (i.e. small contribution from the phase contrast),[24, 29] radial profiles from the cryo-TEM images should correspond to an average micelle density distribution. The radial plot profiles for each system (**3.04**-**3.06**) were averaged and overlaid to compare the effect on increasing DP on the assemblies (**Figure 62**). While the data set for these samples is small, there seems to be a clear difference between the corona profiles for each sample; this is discussed in more detail later in relation to the SANS data. It should be noted that these images were recorded keeping imaging parameters (beam intensity, focus, magnification, ice thickness) as constant as possible. This, combined with the general difficulties in performing cryo-TEM, and the difficulties associated with imaging very weakly contrasting samples, recording data for a large number of micelles was not possible and therefore validating this data further with scattering techniques was crucial.

3.3.5 Analysis of Self-assembled Structures by Laser Light Scattering

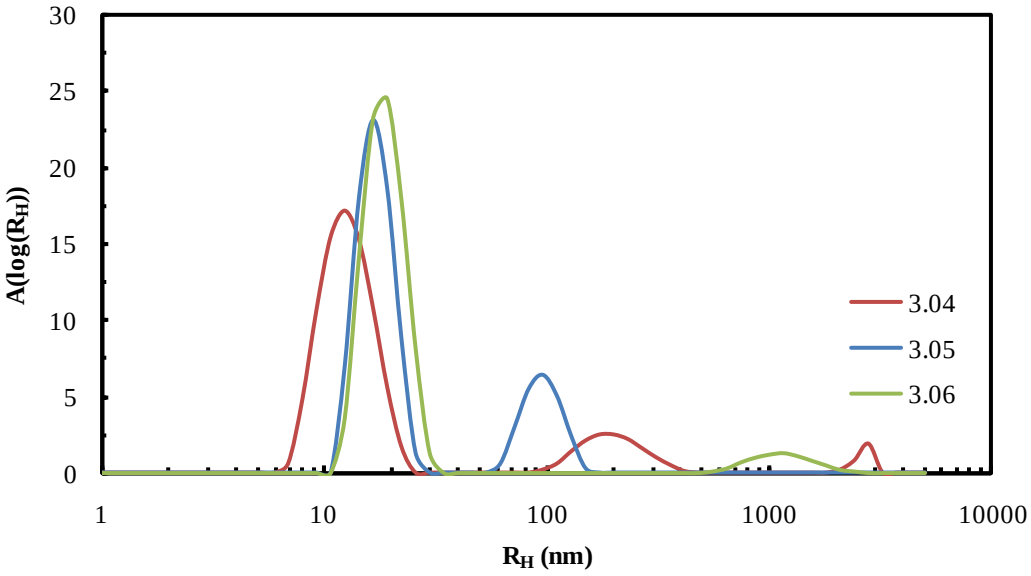

Figure 63. Representative size distributions from DLS for **3.04**-**3.06** in H_2O at a concentration of 2.0 mg mL^{-1}. The size distributions show a major population of small micelles, R_H ~ 10 to 20 nm, and a minor population of large, spurious aggregates, R_H ~ 200 nm.

All scattering experiments were performed at concentrations much greater than the CMC (ca. 10^{-2} mg ml^{-1}) in order to keep the concentration of unimers negligible. The aqueous solution assembly of these polymers was further investigated by DLS and SLS. Representative size distributions from DLS for **3.04**-**3.06** at 2.0 mg mL^{-1} are shown in **Figure 63**. At all concentrations, the DLS results showed a major population of small micelles with hydrodynamic radii (R_H) of 10 - 20 nm, and a minor population of larger aggregates, R_H ~ 200 nm. These larger aggregates could not be removed by the addition of salts, filtration, changes in concentration or by a variety of different preparation methods. However, considering that the intensity-weighted population of the larger aggregates is the minority population and that the intensity of scattered light is proportional to at least the square of the radius, R^3, the

weight concentration of the larger aggregates could be considered negligible.[31] Similar populations of large aggregates were reported for poly(ethylene oxide) (PEO) end-capped with dodecyl groups and were identified as spurious aggregates.[31] While the weight concentration of these larger aggregates is negligible, their contribution to the overall scattering intensity is not. To account for the presence of the larger aggregates in the SLS experiments, DLS and SLS data were collected simultaneously, allowing the following procedure to be applied in order to eliminate the effect of the larger particles on the total scattering.[31-33] Measurements were made at 4 different concentrations (c) ranging from 1.0 mg mL^{-1} to 5.0 mg mL^{-1} and 7 different angles (θ) ranging from 30° to 140°. The scattered intensity was measured over a period of 100 s and measurements were made in duplicate to determine both the intensity auto correlation function, $g_2(t)$ (equation 1), for DLS and the mean scattered intensity, *I*, for SLS.

$$\boldsymbol{g_2(q,t) = \frac{\langle I(q,t) I(q,t+\tau)\rangle}{\langle I(q,t)\rangle^2}} \qquad (1)$$

For DLS data, the measured $g_2(t)$ was related to the electric field auto correlation function, $g_1(t)$, using the Siegert relation, equation (2).[34] The resulting functions were analysed using the REPES routine[35] assuming a continuous distribution of relaxation times, $A(\log(\tau))$, according to equation 3.

$$g_2(q,t) = 1 + g_1(q,t)^2 \qquad (2)$$

$$\boldsymbol{g_1(\log(t)) = \int_0^\infty \tau A(\tau)\, exp\left(-\frac{t}{\tau}\right) d\log\tau} \qquad (3)$$

The resulting distribution of relaxation times were bimodal and were consequently separated into the fast (τ_{fast}, from the dominant population of micelles) and slow (τ_{slow}, from the spurious aggregates) modes of relaxation. τ_{fast} (micelles) was dependant on the scattering vector q^2. The scattering vector was defined as $q = 4\pi n/\lambda \sin(\theta/2)$, where n is the refractive index of the solvent. The apparent diffusion coefficient (D_{app}) was determined for each concentration by taking the slope of $(\tau_{fast})^{-1}$ vs. q^2 (equation 4, **Figure 64**a). The apparent diffusion coefficients were extrapolated to zero concentration (**Figure 64b**) in order to determine a true diffusion coefficient D. D was used to calculate the hydrodynamic radii (R_H) according to the Stokes-Einstein equation using the Boltzmann constant (k_B) at a known temperature (T), equation 5.

$$\boldsymbol{\tau_{fast}^{-1} = D_{app} q^2} \qquad (4)$$

$$\boldsymbol{R_H = \frac{k_B T}{6\pi n D}} \qquad (5)$$

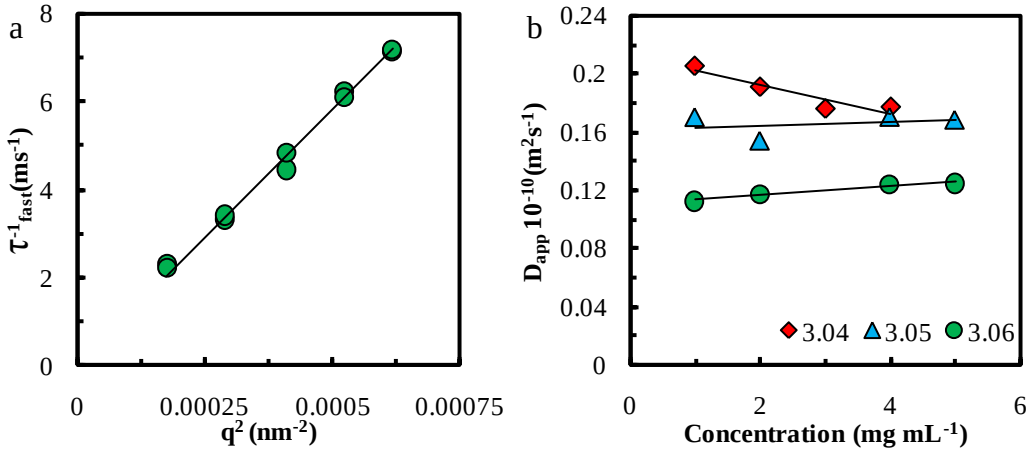

Figure 64. (a) Example plot of τ^{-1} vs. q^2 in order to determine D_{app} from the slope according to equation (4) for **3.06** at 2 mg mL^{-1}, showing both runs for each angle and (b) Plot of D_{app} vs. concentration for **3.04**-**3.06** in order to determine micelle M_w and A_2 from equation (6).

For SLS experiments the particle M_w and second virial (A_2) coefficient were determined according to the Zimm equation (equation 6). However, both the slow and fast modes of relaxation contributed to the total scattered intensity. The relative scattered intensity contributions from the micelles (fast mode of relaxation) and larger spurious aggregates (slow mode of relaxation) were determined from DLS analysis of the data (as described above), for each scattering angle and concentration. This allowed for the calculation of the Rayleigh ratio for the micelles only ($R_{\theta, fast}$) according to Equation 10.

$$\frac{Kc}{R_\theta} = \frac{q^2 R^2 g}{3MW} + \frac{1}{MW} + 2A_2 c \tag{6}$$

$$K = \frac{4\pi n_0 \left(\frac{dn}{dc}\right)^2}{N_A \lambda^4} \tag{7}$$

$$R_\theta = \frac{I_{sample} - I_{solvent}}{I_{Toluene}} R_{\theta,Toluene} \tag{9}$$

$$R_{\theta,fast} = A_{fast} R_\theta \tag{10}$$

Where R_g is radius of gyration, n is the refractive index of the solvent (1.33), dn/dc is the refractive index increment of the polymer in water (0.12), determined using a refractometer with the same wavelength laser used for light scattering), N_A is Avogadro's number (6.022 x10^{23}), λ is the wavelength of the laser, 632.8 nm, R_θ is the Rayleigh Ratio and I is the average scattered intensity.

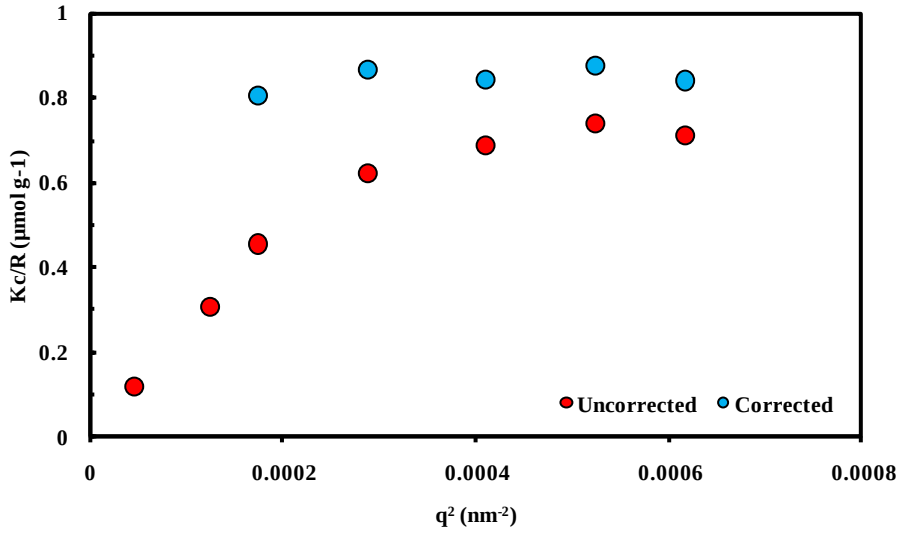

Figure 65. Plot of Kc/R_θ vs. q^2 for sample **3.04** at 4.0 mg mL^{-1} showing the uncorrected (raw) and corrected (for the fast mode of relaxation only) data.

Figure 65 shows the effect of separating the two distributions by plotting the total Kc/R_θ values (uncorrected) and $Kc/R_{\theta,fast}$ (corrected) against q^2. The uncorrected values all indicate a higher MW species (lower Kc/R_θ values) and the values do not show a linear fit (expected for spherical micelles). The data at lower q^2 values (more forward angles) shows even more deviation from the corrected values as the spurious aggregates contribute even more to the total scattering intensity (as larger particles scatter more in the forward direction),[36] and for the two lowest q^2 values it was not possible to accurately separate out the two modes. The corrected values show a linear fit and can therefore be used to determine $Kc/R_{\theta,fast}$ at zero angle. Because the micelle radius of gyration (R_g) is less than 20 nm, $Kc/R_{\theta,fast}$ was effectively independent of q^2 (due to the assumption of 10% error in the measurements), and therefore it is more appropriate to determine $Kc/R_{\theta,fast}$ at zero angle by averaging the values in **Figure 65**, than by extrapolation.

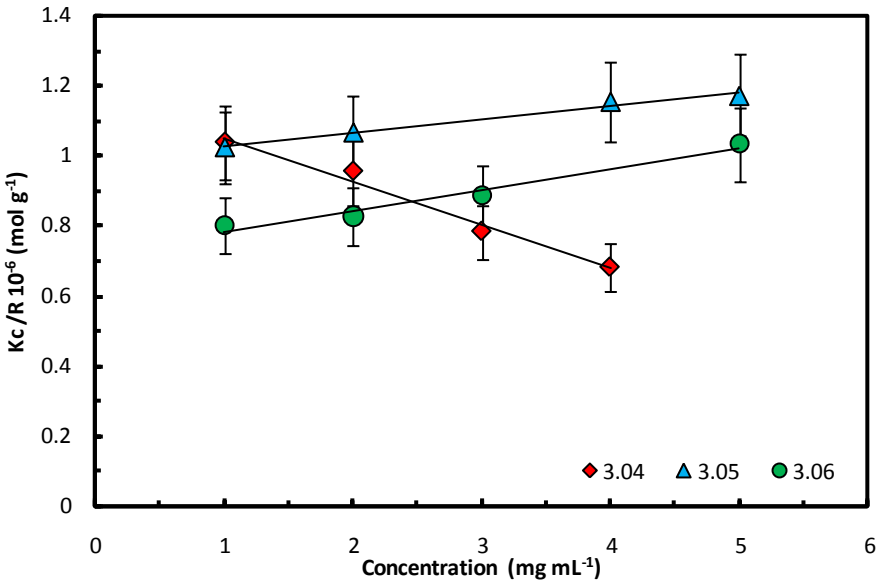

Figure 66. Plot of $Kc/R_{\theta,fast}$ versus concentration for **3.04**-**3.06** in H_2O. The M_w and A_2 values for the micelles were determined from the intercept and slope, respectively, of linear fits to the SLS data. Error bars are 10 % as standard for all the LLS experiments

The second consequence of this is that accurate R_g could not be determined using light scattering methods as it comes from the slope of this plot. The averaged $Kc/R_{\theta,fast}$ values were plotted against concentration to determine the true micelle molecular weight (M_w, at zero concentration) and second virial coefficient (A_2) (**Figure 66**, **Table 5**). As shown in **Table 5**, micelle sizes from DLS increase and micelle aggregation numbers decrease with increasing DP_{corona}, which is also consistent with surfactant and block copolymer scaling theories. Values for A_2 were determined to be -6.2 x 10^{-4}, 1.9 x 10^{-5}, 6.0 x 10^{-5} mL mol g^{-2} for **3.04**, **3.05** and **3.06** respectively. One interesting feature is that A_2 for **3.04** and **3.05** are positive, while **3.06** shows a negative value. A_2 values represent the relationship between particle-solvent and particle-particle interactions, where a positive A_2 values means the former is dominant and a negative A_2 value the latter. As previously mentioned A_2

values for BCP assemblies are typically on the order of 10^4 or 10^5,[5, 37, 38] and therefore these A_2 values can be considered very small, which could indicate that water is approaching the theta solvent for these systems and that the negative value relates to a small preference of particle-particle interactions. Savin and co-workers,[39] and Gast and co-workers,[40] also noted negative A_2 values for the assembly of polymer aggregates and in both these cases A_2 values were also very small, $\pm 10^{-4}$ and $\pm 10^{-6}$ mL mol g^{-2} respectively.

3.3.6 Analysis of self-assembled structures by SANS[§]

To further investigate the structural profile of the micelles, SANS experiments were performed on micelle solutions prepared in D_2O. The SANS data was fit with a form factor model for spherical polymer micelles with a homogenous core and radially decreasing corona density profile, modelled as a linear combination of 2 *b* splines.[41-43] The form factor (*P*) model considers four terms: the self-correlation of the core, the self-correlation of the corona chains, the cross-term between the core and corona, and the cross-term between different corona chains (equation 11). [41-43]

$$\begin{aligned} \boldsymbol{P_{micelle}}(\boldsymbol{q}) = {} & \boldsymbol{N_{agg}^2 \beta_{core}^2 A_{core}^2}(\boldsymbol{q}) + \boldsymbol{N_{agg} \beta_{corona}^2 P_{chain}}(\boldsymbol{q}) \\ & + \boldsymbol{2 N_{agg}^2 \beta_{core} \beta_{corona} A_{core}}(\boldsymbol{q}) \boldsymbol{A_{corona}}(\boldsymbol{q}) \\ & + \boldsymbol{N_{agg}}(\boldsymbol{N_{agg}} - \boldsymbol{1}) \boldsymbol{\beta_{corona}^2 A_{corona}^2}(\mathrm{q}) \end{aligned} \qquad (11)$$

Where *q* is the scattering wave vector, N_{agg} is the aggregation number, and β_{core} and β_{corona} are the total excess scattering lengths of the core and corona, respectively. The total excess scattering lengths were defined as $\beta_{core} = v_{core}(SLD_{core} - SLD_{solvent})$

[§] SANS data collection and analysis was performed by Elizabeth Kelley and Thomas H Epps, III

and $\beta_{corona} = v_{corona}(SLD_{corona} - SLD_{solvent})$, where v_{core} and v_{corona} are the volumes of the core and corona blocks, and SLD_{core}, SLD_{corona}, and $SLD_{solvent}$ are the scattering length densities of the core, corona, and solvent, respectively. The SLDs were calculated using the density of PNIPAM,[44] and the molecular volume (v) and scattering length (Σb) for the pincer end group, where SLD = Σb/v.[45, 46] Because of the small contribution of the pincer end group to the overall scattered intensity, the fits were not affected by slight changes in the SLD of the end group, (i.e. whether or not the aromatic group was included in the calculation). The scattering amplitude of the core with radius, R_{core}, was described by the hard sphere form factor

$$\boldsymbol{A_{core}(q) = 3[\sin(qR_{core}) - qR_{core}\cos(qR_{core})]/(qR_{core})^3} \quad (12)$$

The self-correlation of the corona chains was described by a Debye function, where the chains are assumed to be Gaussian with a radius of gyration, R_g.

$$\boldsymbol{P_{chain}(q) = 2[\exp(-q^2R_g^2) - 1 + q^2R_g^2]/(q^2R_g^2)^2} \quad (13)$$

The form factor for the corona chains was calculated as the normalized Fourier transform of the radial density distribution of corona chains, $\rho_{corona}(R)$,

$$\boldsymbol{A_{corona}(q) = \frac{4\pi \int \rho_{corona}(R)[sin(qR)/qR]R^2 dR}{4\pi \int \rho_{corona}(R)R^2 dR}} \quad (14)$$

$\rho_{corona}(R)$ was modelled as a linear combination of two cubic *b* splines, as originally developed by Pedersen and co-workers.[43]

A Schulz distribution of core radii was included to account for dispersity in micelle size,

$$G(R_{core}) = \frac{R_{core}^{\phi}}{\Gamma(\phi+1)}\left(\frac{\phi+1}{\langle R_{core}\rangle}\right)^{Z+1} \exp\left[-\frac{(\phi+1)R_{core}}{\langle R_{core}\rangle}\right] \quad (5)$$

$\langle R_{core}\rangle$ is the average core radius and ϕ is related to the dispersity, Đ, by Đ = 1/(Đ+1). The distribution was truncated at R_{core} = 0. The fit quality was not significantly affected by the dispersity; therefore, the value was fixed at 0.2.

The coherent scattered intensity was then given by,

$$I(q) = \frac{c}{M_{n,micelle}} \int P_{micelle}(q)\, G(R_c) dR_c \quad (6)$$

c is the polymer concentration and $M_{n,micelle}$ is the number average mass of the micelles. Scattering contributions from a structure factor were not included in the SANS data model. The calculated scattered intensity was corrected for instrument resolution and all data were fit using the procedures provided by NIST.[47] Five parameters were fit during the data analysis: N_{agg}, R_{core}, R_g, the width of the corona profile, and the weighting of the *b* splines. The corona profiles obtained from the SANS data modelling were rescaled using Equation 5,

$$\int 4\pi\hat{\rho}_{corona}(R)R^2 dr = N_{agg} v_{corona} \quad (5)$$

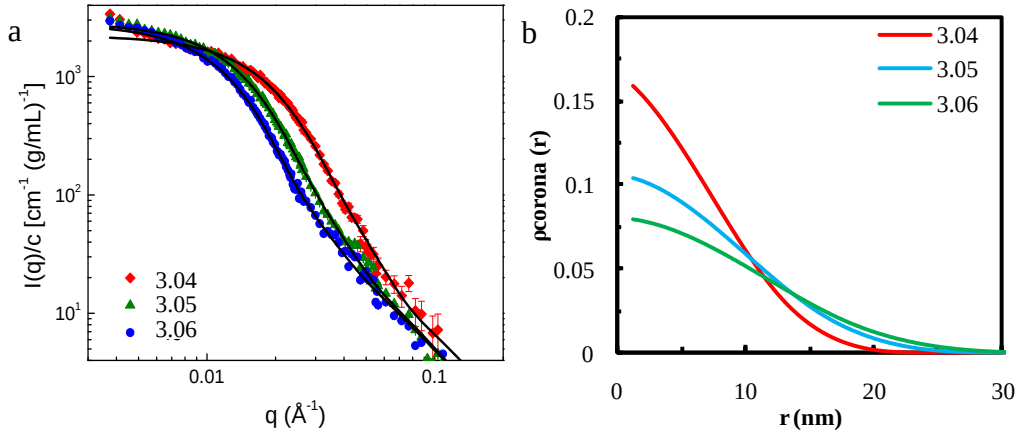

Figure 67 (a) SANS data (symbols) and fits with a spherical micelle form factor (lines) for **3.04-3.06** in D_2O and (b) micelle corona profiles from the SANS data fits.

in which $\hat{\rho}_{corona}(R)$ is the rescaled corona profile and represents the volume fraction of the corona chains, R is the distance from the centre of the micelles, N_{agg} is the aggregation number, and v_{corona} is the volume of the PNIPAM block.[42] The micelle radius was defined as the radius at which the volume fraction of PNIPAM in the corona profile was less than 0.02.[42, 48] The results of the SANS data modelling are summarised in **Table 5** and **Figure 67b**. The analysis suggested that the micelle core radius was between 1 and 2 nm, which was consistent with the results presented in Chapter 2.[49, 50] The micelle cores were surrounded by a diffuse, hydrated corona characteristic of star-like micelles, as seen in the corona profiles in **Figure 67b**.

3.3.7 Comparison of data obtained from cryo-TEM, LLS and SANS

Table 5. Summary of micelle characterization data

Polymer	R* (nm) TEM	R_H (nm) DLS	R (nm) SANS	N_{agg} SLS	N_{agg} SANS
3.04	15 ± 1.0	11	15	54	48
3.05	16 ± 0.5	15	17	40	43
3.06	19 ± 0.3	22	18	36	34

*errors are given as ± on standard deviation

As mentioned in Chapter 1 the standard error applied to scattering experiments is 10 %, however, when comparing values obtained from the same apparatus under the same conditions, the errors can be considered to be significantly smaller and consequently an error of 5 % is applied.[38] The collective results show that polymers **3.04-3.06** self-assemble into well-defined micelles despite having a very low hydrophobic wt % (< 5 wt %). As seen in Table 2, all of the characterisation results were in good agreement and indicated that the micelle radius increased with increasing DP_{corona}, consistent with small molecule surfactants[15, 17] and block copolymer assemblies.[16, 18, 19, 28] Furthermore, the data shows that N_{agg} decreases with increasing DP_{corona}, which is also consistent with the literature where $N_{agg} \propto DP_{corona}^{-\chi}$, where χ ranges from 0.0 to 0.51.[18] Both SLS and SANS data show that χ values for these systems are similar and at the top end of the normal range (0.5 and 0.4 from the SLS and SANS respectively). The overall size of star-like micelles, particularly with small cores, depends on length and degree of stretching of the hydrophilic block. Previous literature states micelle radius, R, should scale with the

DP of the hydrophilic block, as $R \propto DP_{corona}^{\delta}$ where $0.5 < \delta < 1.0$.[9, 28, 51, 52] For this system $\delta = 0.9$, 0.3 and 0.3 from the DLS, SANS and cryo-TEM results respectively. While it is difficult to determine exact δ values from only three results, it appears there is a significant scaling difference between the measurements made by DLS compared to SANS and cryo-TEM. As stated above, the degree of stretching will also be important in determining the overall size of the micelle. The degree of stretching (ω) can be determined form the ratio of the calculated NIPAM chain length (L_{corona}) and the maximum possible chain extension (L_{max}) so that $\omega = L_{corona} / L_{max}$, where $L_{corona} = R - R_{core}$, and $L_{max} = DP \times 0.25$, with 0.25 nm being the length of one vinyl monomer unit.[53]

Table 6. Summary of degree of stretching (ω) values for **3.04-3.06**

Polymer	L_{max} (nm)	ω DLS	ω SANS	ω TEM
3.04	30.0	0.3	0.5	0.5
3.05	45.0	0.3	0.3	0.3
3.06	67.5	0.3	0.3	0.3

Table 6 shows the ω values from DLS, SANS and cryo-TEM. The data shows the source of the difference in δ values is that **3.04** is less stretched when measured by DLS compared to SANS and cryo-TEM. The degree of stretching for polymer coronas can generally be related to two factors: the aggregation number, (where higher N_{agg} will favour more stretching) and the solvent quality (where better solvents favour more stretching). Note: DLS and SLS were performed in H_2O whereas SANS and cryo-TEM were performed in D_2O. **3.04** has a higher N_{agg} compared to **3.05** and **3.06** which explains the increase in stretching for **3.04**

measured by SANS and cryo-TEM, as higher N_{agg} assemblies will have a higher density of polymer chains, forcing them to be more extended. The situation is more complicated for the stretching of **3.04** when measured by DLS (in water) as not only has N_{agg} changed, between **3.04** compared to **3.05** and **3.06** (measured in water by SLS) but so has the solvent quality. This is indicated by a change in sign of the A_2 value from positive for **3.05** and **3.06**, to negative for **3.04** (measured by SLS in water). It appears that in this case the poorer solvent quality has resulted in less chain stretching for **3.04**. Although A_2 values cannot be determined from the SANS experiment (performed at one concentration), previous literature reports by Wu and Wang,[54] and Winnik,[32 55] have noted a preference of PNIPAM for D_2O over H_2O. This is a good indication that this sign change may not occur for the systems when in D_2O. Perhaps the most interesting conclusion from this discussion is that the chain stretching can be determined from the cryo-TEM data and compares well to SANS results. **Figure 68** compares the corona profiles obtained from the SANS and cryo-TEM results.

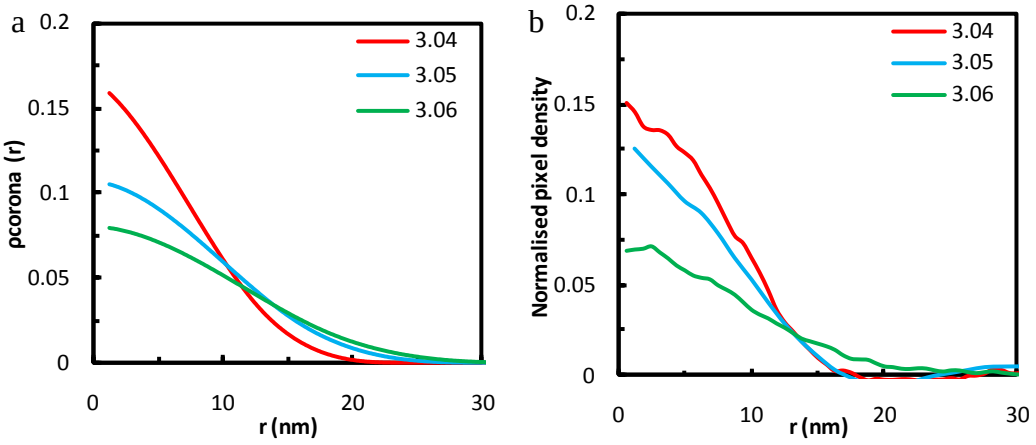

Figure 68. Radial composition profiles from (a) SANS data modelling and (b) cryo-TEM analysis.

Despite the small sample size from cryo-TEM the data compares remarkably well indicating that corona profiles can be obtained correctly from cryo-TEM. Not only are the sizes comparable but the shape of the corona profiles and the relative core densities at the core are also similar. The shape of the profile is again related to corona stretching (as previously discussed) and the relative densities at the core should be related to micelle N_{agg} where higher N_{aggs} result in an increased density at the core and consequently more scattering. Gianneschi and co-workers demonstrated the utility of cryo-TEM for analysing the radial density distribution of polymeric particles.[56] However the author can only find one report of radial profiling from cryo-TEM being directly compared to scattering data where Ballauff and co-workers used small angle X-ray scattering (SAXS) and cryo-TEM to analyse PS-b-PNIPAM aggregates.[24] They compared both the overall size of the particles are the radial profile fopr the PS core and the PNIPAM shell finding good agreement in both cases.

3.3.8 Analysis of self-assembled structures by temperature controlled spectrophotometry

There have been many studies on the thermoresponsive nature of PNIPAM, including free PNIPAM,[57] BCP[58, 59] and amphiphilic homopolymer micelles,[9] branched polymer nanoparticles,[60] and microgels.[61] Literature reports of free PNIPAM homopolymers indicate that the cloud point (measured upon heating) approaches ~ 32 °C for molecular weights ≥ 20,000 g mol^{-1}.[62-64] It has also been shown that this temperature can be increased or decreased by the attachment of hydrophilic,[60] or hydrophobic,[9, 65] groups respectively. The thermo-responsive

properties of the micelles were studied by turbidity experiments. The micelle solutions became turbid upon heating as shown by the sharp decrease in transmission in **Figure 69**, indicative of the cloud point. Within experimental error, the cloud point (determined as the mid-point of the slope of the red heating curve, **Figure 69**) for all of micelle samples was 32 °C. Although all the micelle MWs were >> 20,000 g mol^{-1}, it appears that the cloud point is not depressed by the pincer end groups which could be due to the relatively low wt % of the end group and consequently low aggregation number micelles formed. Although the heating curves are very similar the blue cooling curve for **3.04** is very different from that of **3.05** or **3.06**, as it shows much less hysteresis. Wu and Wang first reported hysteresis upon cooling PNIPAM homopolymer solutions,[66] and subsequently hysteresis has been reported for PNIPAM-based microgels[61] and BCP micelles.[58, 67] The hysteresis upon cooling is hypothesised to be from intra- and inter- chain hydrogen bonds that form in the collapsed state and dissociate at temperatures much lower than the cloud point.[66, 68, 69]

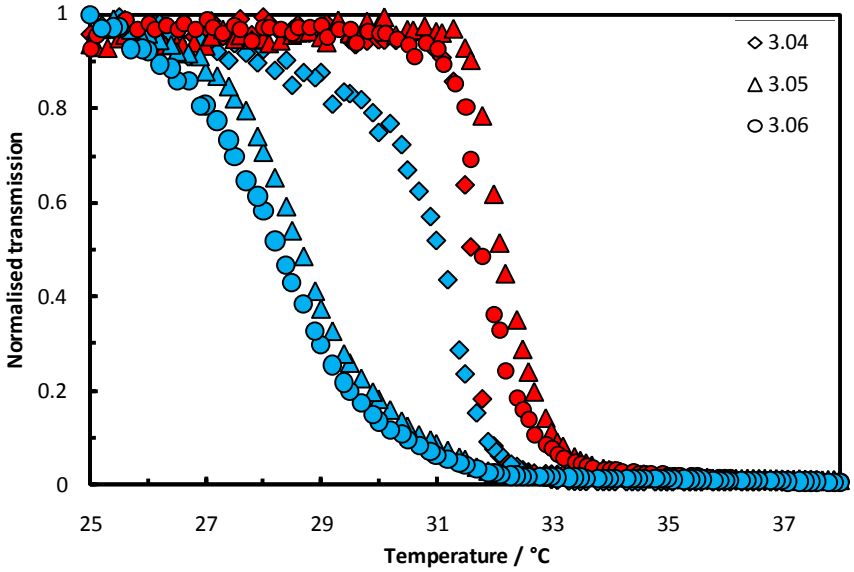

Figure 69. Temperature-dependent light transmission for solutions of **3.04**-**3.06** at 2 mg mL^{-1} in H_2O upon heating (red) and cooling (blue). Data were normalised such that the transmission values were between 0 and 1.

While there are several studies on the structural evolution of PNIPAM micelles upon heating,[10, 67] and more recently the kinetics of this evolution,[70, 71] few studies have investigated the structural changes on cooling. Winnik and co-workers demonstrated that upon heating, telechelic-PNIPAM micelles form stable aggregates and it was suggested the individual micelle structures may not be maintained within these aggregates.[10] If this applies to the micelles of **3.04**-**3.06**, individual polymer chains should be solubilised upon cooling, before re-forming micelles in solution. As the solutions are cooled and individual chains start to become solubilised, it is the properties of the individual chains which will control the evolution of the cooling curve (and the amount of hysteresis). Comparing the MW of the free chains shows that **3.04** (15.8 kDa) should have a higher cloud point than **3.05** or **3.06** (> 20 kDa). Consequently the resolubilisation of **3.04** should occur at a fast rate resulting in less hysteresis. Also, a recent study demonstrated that molecular weight greatly affects

the kinetics of PNIPAM phase transitions,[71] and it is possible that entanglement of the higher molecular weight chains may also play a part.

3.4 Conclusions

An SCS-pincer functionalised RAFT agent was used to synthesise a series of hydrophobically end-functionalised PNIPAM polymers. The self-assembly of these polymers was studied by ^{1}H NMR, DLS, SLS, cryo-TEM, SANS and spectrophotometry to fully understand the micelle structure. Importantly, detailed information about the micelle density profiles was extracted from the cryo-TEM micrographs and was comparable to the SANS results, highlighting the immense potential of the complementary use of these two techniques. Additionally, micelle properties such as size, aggregation number, and corona density profile were dependent on the DP of the PNIPAM block. However, these changes in size and structure did not significantly alter the micelle cloud point upon heating. Finally, the thermo-responsive studies presented here suggest that while the micelle molecular weight dictates the cloud point upon heating, the amphiphilic homopolymer molecular weight may influence the hysteresis upon cooling. One issue that arises from both Chapters 2 and 3 is that due to the small size and largely hydrated nature of the particles, the non-pallidated PAA in Chapter 1 and the PNIPAMS in Chapter 2 were extremely difficult to analyse by cryo-TEM. The subsequent chapters in this thesis will deal with improving the analysis of self-assembled polymers by the development of new electron microscopy methods.

3.5 Experimental Section

3.5.1 Materials.

All chemicals were used as received from Aldrich, Fluka, or Acros unless otherwise stated. NIPAM (N-isopropylacrylamide) was recrystallised from a 9:1 mixture of hexane/acetone. AIBN (azobisisobutyronitrile) was recrystallized twice from methanol and stored in the dark at 5 °C.

3.5.2 General procedure for RAFT polymerisation of NIPAM

2.05 (0.050 g, 57 µmol), NIPAM (1.3 g, 12 mmol), AIBN (2.8 mg, 17 µmol), and dimethylformamide (DMF) (2.7 mL) were added to a clean, dry ampoule under N_2 (g). The solution was degassed via 3 freeze-pump-thaw cycles and heated to 65 °C for 5 h under N_2 (g). The viscous crude reaction medium was dissolved in the minimum amount of tetrahydrofuran (THF), and the polymer was precipitated into diethyl ether and filtered. The precipitation process was repeated, and 1.35 g of yellow polymer was recovered. M_n^{NMR} (21.3 kDa), M_n^{SEC} (20.2 kDa), $Đ^{SEC}$ (1.22). ^{1}H NMR 400MHz ($CDCl_3$): δ (ppm) 7.19 (s, 1H, Ar-*H*), 7.14 (s, 2H, Ar-*H*), 5.70-7.50 (br, N*H*, polymer), 5.05 (s, 2H, Ar-CH_2O), 4.00 (s, br, N$(CH_3)_2$C*H*, 180H, polymer), 3.68 (s, 4H, SCH_2-Ar), 3.33 (t, J = 7.6 Hz, 2H, SCSCH_2C), 2.39 (t, J = 7.4 Hz, 4H, $CH_2SCH_2CH_2$), 1.2-2.5 (br, CH, CH_2, CH_3 polymer).

3.5.3 General procedure for end group removal.

PNIPAM (1.1 g, 72 µmol), AIBN (5.0 mg, 29 µmol), 1-ethylpiperidine hypophosphite (EPHP) (0.065 g, 0.36 mmol), and toluene (ca 10 mL) were added to

a clean, dry ampoule under N_2 (g). The reaction vessel was degassed via 5 freeze-pump-thaw cycles. The ampoule was filled with N_2 (g) and heated to ~100 °C for 12 h. All volatiles were removed *in vacuo*, the white solid was dissolved in the minimum volume of THF, and the polymer was precipitated into hexanes. 0.79 g of white polymer was recovered. For additional purification, the polymer was dialyzed against deionized water. M_n^{NMR} (21.0 kDa), M_n^{SEC} (20.3 kDa), $Đ^{SEC}$ (1.22). ^{1}H NMR 400MHz ($CDCl_3$): δ (ppm) 7.19 (s, 1H, Ar H), 7.14 (s, 2H, Ar H), 5.70-7.50 (br, NH, polymer), 5.05 (s, 2H, $PhCH_2O$), 4.00 ($N(CH_3)_2CH$, 180H, polymer), 3.68 (s, 4H, SCH_2Ph), 2.39 (t, J = 7.4 Hz, 4H, $CH_2SCH_2CH_2$), 1.2-2.5 (br, CH, CH_2, CH_3 polymer).

3.5.4 Polymer characterization.

^{1}H NMR spectra were recorded on a Bruker DPX-400 spectrometer in $CDCl_3$. Chemical shifts are given in ppm downfield from tetramethylsilane (TMS). The degree of polymerisation (N_{PNIPAM}) was determined by comparing the integration of the end group peaks (δ 5.05, 3.68 and 3.33) to the C*H* peak (δ 4.00) of the polymer backbone. The number average molecular weight from NMR was calculated according to $M_n = DP_{PNIPAM} * M_o + MW_{pincer}$, where M_o is the repeat unit molecular weight of PNIPAM, and MW_{pincer} is the end-group molecular weight.

Size exclusion chromatography (SEC). SEC measurements were conducted on a system comprised of a Varian 390-LC-Multi detector suite fitted with differential refractive index (DRI), and ultra-violet (UV) detectors, and equipped with a guard column (Varian Polymer Laboratories PLGel 3 μM, 50 × 7.5 mm) and two mixed D columns (Varian Polymer Laboratories PLGel 5 μM, 300 × 7.5 mm). The mobile

phase was DMF (1 mg.mL^{-1} LiBr) at a flow rate of 1.0 mL min^{-1}, and samples were calibrated against Varian Polymer laboratories Easi-Vials linear poly(methyl methacrylate) standards using Cirrus v3.3 software.

Fourier Transform Infrared Spectroscopy (FT-IR). FT-IR spectra were recorded using a Perkin-Elmer Spectrum 100 FT-IR spectrometer.

3.5.5 Micelle preparation.

Micelle solutions were prepared by adding H_2O to the dried polymer powder and stirring overnight. The resulting solutions were filtered through a 0.45 μm nylon filter.

3.5.6 Micelle characterization.

Fluorescence Measurements. Fluorescence spectra were collected on a PerkinElmer LS 55 Fluorescence Spectrometer. Pyrene (12.0 mg) was dissolved in acetone (1 mL) and diluted to a concentration of 6.0 x10^{-5} M. Then, 10 μL of the pyrene solution was added to a glass vial and left overnight to evaporate the acetone. Solutions of **3.04-3.06** were added to the vials at various concentrations ranging from 1.0 x10^{-5} to 2.0 x10^{0} mg mL^{-1} and stirred for 5 h. The excitation spectra (300-400 nm) were recorded using an emission wavelength of 390 nm. The λ_{max} for the highest concentration of polymer (339 nm) and the λ_{max} for the lowest concentration of polymer (335 nm) were selected to measure the change in pyrene environment by the ratio of I_{339}/I_{335}.

Tensiometry: The surface tension measurements were performed on the high throughput Delta-8 system (Kibron Inc.), and the data were analyzed by the Delta-8 Manger software. The samples were transferred onto the first column of a standard Nunclon 96 well plate and three measurements were made for each sample.

Light Scattering (LS). Static light scattering (SLS) and dynamic light scattering (DLS) measurements were performed on a ALV CGS3 spectrometer operating at λ = 632.8 nm, except as mentioned below. All LLS data were collected at 25 °C. The DLS population distribution data were recorded using a Zetasizer Nano series instrument (Malvern Instruments) at a fixed scattering angle of 173°. The experimental correlation functions from the Zetasizer Nano were analysed using the Non-negative least squares (NNLS) algorithm.

Cryogenic transmission electron microscopy (cryo-TEM). Micelle solutions for cryo-TEM experiments were prepared at concentrations ranging from 2.0 mg mL^{-1} to 5.0 mg mL^{-1}. Samples for cryo-TEM were prepared at 25 °C in a constant humidity environment using a FEI 110 Vitrobot. A 2 - 10 μL droplet of micelle solution was applied to a holey carbon-coated copper grid, and the grid was blotted to remove excess solution. Subsequently, the sample was vitrified by plunging the grid into liquid ethane. Grids were transferred to a Gatan cryo stage and imaged using a Tecnai G2 12 Twin TEM at an accelerating voltage of 120 kV. The temperature of the cryo stage was maintained below -170 °C.

Small angle neutron scattering (SANS). Solutions for SANS experiments were prepared at a concentration of 2.0 mg mL^{-1} by direct dissolution of the polymer powder in D_2O and then filtered using a 0.2 μm nylon filter. SANS experiments

were performed at the National Institute of Standards and Technology (NIST) Center for Neutron Research (NCNR, Gaithersburg, MD) on the NG-7 30 m SANS beamline. An incident wavelength of 6.0 Å with a wavelength spread ($\Delta\lambda/\lambda$) of 0.12 was used with sample to detector distances of 1.0 m, 4.0 m, and 13.5 m to access a scattering vector modulus (q) range of 0.004 $Å^{-1} < q < 0.6$ $Å^{-1}$. Here, the scattering vector is defined as $q = 4\pi/\lambda \sin(\theta/2)$, where θ is the scattering angle. All measurements were performed at ambient temperature (20 ± 1 °C). SANS data were reduced using standard procedures provided by NIST,[72] and background scattering from D_2O was subtracted from the data.

Spectrophotometry studies. Turbidity experiments were performed on a Perkin Elmer Lambda 35 UV/Vis spectrometer at λ = 500 nm using a PTP-1+1 Peltier temperature programmer and stirring system and a PCB 1500 water system. All samples were studied upon heating from 25 ^{o}C to 50 ^{o}C, followed by cooling to 25 ^{o}C. Temperature ramp rates were 1 ^{o}C/min in all cases. The transmission values were normalized between 0 and 1, and the reported values are the average of three consistent runs.

3.6 References

1. H. G. Schild, *Prog. Polym. Sci.*, 1992, **17**, 163-249.
2. A. Housni and R. Narain, *Eur. Polym. J.*, 2007, **43**, 4344-4354.
3. P. Cotanda, A. Lu, J. P. Patterson, N. Petzetakis and R. K. O'Reilly, *Macromolecules*, 2012, **45**, 2377-2384.
4. A. O. Moughton and R. K. O'Reilly, *Chem. Commun.*, 2010, **46**, 1091-1093.

5. K. Wei, L. Su, G. Chen and M. Jiang, *Polymer*, 2011, **52**, 3647-3654.

6. G. Li, S. Song, L. Guo and S. Ma, *J. Polym. Sci. Part A: Polym. Chem.*, 2008, **46**, 5028-5035.

7. H. Ringsdorf, J. Venzmer and F. M. Winnik, *Macromolecules*, 1991, **24**, 1678-1686.

8. J. M. Song, F. M. Winnik and J. L. Brash, *Macromolecules*, 1998, **31**, 109-115.

9. P. Kujawa, F. Tanaka and F. M. Winnik, *Macromolecules*, 2006, **39**, 3048-3055.

10. T. Koga, F. Tanaka, R. Motokawa, S. Koizumi and F. M. Winnik, *Macromolecules*, 2008, **41**, 9413-9422.

11. J. T. Xu, L. Tao, C. Boyer, A. B. Lowe and T. P. Davis, *Macromolecules*, 2011, **44**, 299-312.

12. I. Mukherjee, S. P. Moulik and A. K. Rakshit, *J. Colloid Interface Sci.*, 2013, **394**, 329-336.

13. M. Wilhelm, C. L. Zhao, Y. C. Wang, R. L. Xu, M. A. Winnik, J. L. Mura, G. Riess and M. D. Croucher, *Macromolecules*, 1991, **24**, 1033-1040.

14. I. W. Hamley, *Introduction to Soft Matter*, John Wiley & Sons, Ltd, 2007.

15. R. Nagarajan, *Adv. Colloid Interface Sci.*, 1986, **26**, 205-264.

16. R. Nagarajan and K. Ganesh, *J. Chem. Phys.*, 1989, **90**, 5843-5856.

17. C. Tanford, Y. Nozaki and M. F. Rohde, *J. Phys. Chem.*, 1977, **81**, 1555-1560.

18. S. Forster, M. Zisenis, E. Wenz and M. Antonietti, *J. Chem. Phys.*, 1996, **104**, 9956-9970.

19. S. Pioge, L. Fontaine, C. Gaillard, E. Nicol and S. Pascual, *Macromolecules*, 2009, **42**, 4262-4272.

20. Z. Ge, S. Luo and S. Liu, *J. Polym. Sci. Part A: Polym. Chem.*, 2006, **44**, 1357-1371.

21. T. Liu, X. Li, Y. Qian, X. Hu and S. Liu, *Biomaterials*, 2012, **33**, 2521-2531.

22. A. Kelarakis, T. Tang, V. Havredaki, K. Viras and I. W. Hamley, *J. Colloid Interface Sci.*, 2008, **320**, 70-73.

23. E. Betthausen, M. Drechsler, M. Fortsch, F. H. Schacher and A. H. E. Muller, *Soft Matter*, 2011, **7**, 8880-8891.

24. J. J. Crassous, C. N. Rochette, A. Wittemann, M. Schrinner, M. Ballauff and M. Drechsler, *Langmuir*, 2009, **25**, 7862-7871.

25. C. V. Synatschke, F. H. Schacher, M. Fortsch, M. Drechsler and A. H. E. Muller, *Soft Matter*, 2011, **7**, 1714-1725.

26. A. Wolf, A. Walther and A. H. E. Müller, *Macromolecules*, 2011, **44**, 9221-9229.

27. Y. Zheng, Y.-Y. Won, F. S. Bates, H. T. Davis, L. E. Scriven and Y. Talmon, *J. Phys. Chem. B*, 1999, **103**, 10331-10334.

28. E. B. Zhulina, M. Adam, I. LaRue, S. S. Sheiko and M. Rubinstein, *Macromolecules*, 2005, **38**, 5330-5351.

29. J. P. Langmore and M. F. Smith, *Ultramicroscopy*, 1992, **46**, 349-373.

30. T. S. Baker, N. H. Olson and S. D. Fuller, *Microbiol. Mol. Biol. Rev.*, 1999, **63**, 862-922.

31. C. Chassenieux, T. Nicolai and D. Durand, *Macromolecules*, 1997, **30**, 4952-4958.

32. C. Lefay, B. Charleux, M. Save, C. Chassenieux, O. Guerret and S. Magnet, *Polymer*, 2006, **47**, 1935-1945.

33. E. Lejeune, C. Chassenieux and O. Colombani, *Prog. Colloid Polym. Sci.*, 2011, **138**, 7-16.

34. B. Berne, J. and R. Pecora, *Dynamic light scattering, with application to chemistry, biology, and physics*, Wiley, New York, 1976.

35. J. Jakes, *Collect. Czech. Chem. Commun.*, 1995, **60**, 1781-1797.

36. W. Schärtl, *Light Scattering from Polymer Solutions and Nanoparticle Dispersions*, Springer Berlin Heidelberg, Verlag Berlin Heidelberg, 2007.

37. K. Khougaz, I. Astafieva and A. Eisenberg, *Macromolecules*, 1995, **28**, 7135-7147.

38. O. Colombani, M. Ruppel, M. Burkhardt, M. Drechsler, M. Schumacher, M. Gradzielski, R. Schweins and A. H. E. Müller, *Macromolecules*, 2007, **40**, 4351-4362.

39. S. S. Naik, J. G. Ray and D. A. Savin, *Langmuir*, 2011, **27**, 7231-7240.

40. L. J. M. Vagberg, K. A. Cogan and A. P. Gast, *Macromolecules*, 1991, **24**, 1670-1677.

41. S. Y. Choi, F. S. Bates and T. P. Lodge, *J. Phys. Chem. B*, 2009, **113**, 13840-13848.

42. E. G. Kelley, T. P. Smart, A. J. Jackson, M. O. Sullivan and T. H. Epps, III., *Soft Matter*, 2011, **7**, 7094-7102.

43. J. S. Pedersen, C. Svaneborg, K. Almdal, I. W. Hamley and R. N. Young, *Macromolecules*, 2003, **36**, 416-433.

44. L. Zhang, E. S. Daniels, V. L. Dimonie and A. Klein, *J. Appl. Polym. Sci.*, 2010, **118**, 2502-2511.

45. E. Beaudoin, O. Borisov, A. Lapp, L. Billon, R. C. Hiorns and J. Francois, *Macromolecules*, 2002, **35**, 7436-7447.

46. E. Caponetti, R. Triolo, P. C. Ho, J. S. Johnson, L. J. Magid, P. Butler and K. A. Payne, *J. Colloid Interface Sci.*, 1987, **116**, 200-210.

47. S. Kline, in *J. Appl. Cryst.*, 2006, vol. 39, pp. 895-900.

48. J. S. Pedersen and M. C. Gerstenberg, *Colloids Surf., A*, 2003, **213**, 175-187.

49. J. Israelachvili, *Intermolecular & Surface Forces*, Elsevier, 1991.

50. C. Sommer, J. S. Pedersen and V. M. Garamus, *Langmuir*, 2005, **21**, 2137-2149.

51. A. Halperin, *Macromolecules*, 1987, **20**, 2943-2946.

52. A. N. Semenov, J. F. Joanny and A. R. Khokhlov, *Macromolecules*, 1995, **28**, 1066-1075.

53. O. Colombani, M. Ruppel, F. Schubert, H. Zettl, D. V. Pergushov and A. H. E. Müller, *Macromolecules*, 2007, **40**, 4338-4350.

54. X. H. Wang and C. Wu, *Macromolecules*, 1999, **32**, 4299-4301.

55. P. Kujawa and F. M. Winnik, *Macromolecules*, 2001, **34**, 4130-4135.

56. T.-H. Ku, M.-P. Chien, M. P. Thompson, R. S. Sinkovits, N. H. Olson, T. S. Baker and N. C. Gianneschi, *J. Am. Chem. Soc.*, 2011, **133**, 8392-8395.

57. K. Kubota, S. Fujishige and I. Ando, *J. Phys. Chem.*, 1990, **94**, 5154-5158.

58. P. Cotanda, A. Lu, J. P. Patterson, N. Petzetakis and R. K. O'Reilly, *Macromolecules*, 2012, **45**, 2377-2384.

59. J. J. Crassous, M. Ballauff, M. Drechsler, J. Schmidt and Y. Talmon, *Langmuir*, 2006, **22**, 2403-2406.

60. P. Chambon, L. Chen, S. Furzeland, D. Atkins, J. V. M. Weaver and D. J. Adams, *Polym. Chem.*, 2011, **2**, 941-949.

61. H. Shirota, N. Kuwabara, K. Ohkawa and K. Horie, *J. Phys. Chem. B*, 1999, **103**, 10400-10408.

62. R. Plummer, D. J. T. Hill and A. K. Whittaker, *Macromolecules*, 2006, **39**, 8379-8388.

63. Y. Xia, N. A. D. Burke and H. D. H. Stover, *Macromolecules*, 2006, **39**, 2275-2283.

64. Y. Xia, X. C. Yin, N. A. D. Burke and H. D. H. Stover, *Macromolecules*, 2005, **38**, 5937-5943.

65. P. Kujawa, F. Segui, S. Shaban, C. Diab, Y. Okada, F. Tanaka and F. M. Winnik, *Macromolecules*, 2006, **39**, 341-348.

66. X. Wang, X. Qiu and C. Wu, *Macromolecules*, 1998, **31**, 2972-2976.

67. J. Adelsberger, A. Kulkarni, A. Jain, W. N. Wang, A. M. Bivigou-Koumba, P. Busch, V. Pipich, O. Holderer, T. Hellweg, A. Laschewsky, P. Muller-Buschbaum and C. M. Papadakis, *Macromolecules*, 2010, **43**, 2490-2501.

68. H. Cheng, L. Shen and C. Wu, *Macromolecules*, 2006, **39**, 2325-2329.

69. B. J. Sun, Y. N. Lin, P. Y. Wu and H. W. Siesler, *Macromolecules*, 2008, **41**, 1512-1520.

70. J. Adelsberger, E. Metwalli, A. Diethert, I. Grillo, A. M. Bivigou-Koumba, A. Laschewsky, P. Muller-Buschbaum and C. M. Papadakis, *Macromol. Rapid Commun.*, 2012, **33**, 254-259.

71. Y. Tsuboi, T. Tada, T. Shoji and N. Kitamura, *Macromol. Chem. Phys.*, 2012, **213**, 1879-1884.

72. S. Kline, *J. Appl. Crystallogr.*, 2006, **39**, 895-900.

Chapter 4 – Graphene oxide supports for high contrast multi-technique imaging

4.1 Abstract

Transmission electron microscopy (TEM) is a powerful technique for characterising polymer aggregates formed in solution, but chemical fixing / staining techniques are usually required to increase image contrast and protect specimens from electron beam damage. Graphene oxide (GO) is a robust, water-dispersible, and nearly electron transparent material: an ideal support for TEM. Here it is shown that when using GO supports, no stains are required to acquire high contrast TEM images and that the specimens remain stable under the electron beam for long periods, allowing sample analysis by a range of other microscopy techniques (e.g. STEM, SEM and AFM). The benefit of increased contrast is exploited through the use of exit wave reconstruction, which can increase image resolution to the point where individual polymer chains can be observed. The simplicity of sample preparation and analysis, as well as the potential for significantly increased contrast, make GO supports an attractive alternative for the analysis of polymer aggregates.

4.2 Introduction

With the increasing popularity and commercial availability of controlled radical polymerisation initiators / chain transfer agents, the synthesis of amphiphilic polymers has become synthetically simple and hence widely accessible.[1, 2] Furthermore, a wide range of pre-made amphiphilic polymers are commercially available requiring simple dissolution in a suitable solvent for self-assembly to occur. Such amphiphiles have been proposed to find utility in a range of nanoscale

applications,[3-5] however to achieve this, the characterisation of their size and morphology must be accurately and readily determined. The wide ranging applications mean that these systems are used by researchers in a variety of fields with different skills and backgrounds, consequently the analysis techniques should be widely accessible and the interpretation of results should be relatively simple.

In Chapter 1 the relative benefits and limitations of various analysis techniques were discussed in relation to polymer aggregates in solution. The transmission electron microscope was shown to be an essential tool for this analysis and the two common methods of sample preparation (dry-state and cryo-TEM) were reviewed. Typically, analysis in the dry state is combined with staining techniques to increase image contrast, however these have been shown to cause artifacts and the applications of stains can be a time consuming and subjective process.[6] Cryo-TEM can negate the use for stains, however, as demonstrated in Chapters 2 and 3, there are problems associated with imaging weakly scattering materials. Furthermore the increased expense and complications associated with cryo-TEM have resulted in the continued and prevalent use of dry state staining techniques.

Recent advances in low background contrast TEM specimen supports (e.g. graphene and graphene oxide) provide the opportunity to develop a simple alternative to staining, with some complementary advantages to cryo-TEM. Wilson and co-workers reported the first use of graphene oxide (GO) as a support for TEM. [7] They showed that GO supports are cheap and easy to make; a drop of GO solution is placed on a holey carbon TEM grid and allowed to dry. The hydrophilic functionalities of GO promote the adhesion of many species, and the low

background contrast facilitates high-resolution imaging. GO supports have recently been used for imaging atomically resolved small molecules in motion,[8] and vitrified biological molecules,[9] however the use of GO (or graphene) as a TEM substrate has not become standard practice and there have been no examples for the analysis of polymer aggregates. Wilson and co-workers showed by electron diffraction experiments that GO sheets are crystalline (analogous to graphene) and that single layers of GO create a six fold diffraction pattern, with additional layers giving multiples of this pattern (**Figure 70**). While two perfectly overlapping layers would create one 6 fold diffraction pattern, single layers can still be proven by comparing the relative intensities of the 1100-type and 2110-type reflections (**Figure 70c**) and it was observed that stacks of GO layers have no preference for this type of overlapping.[7]

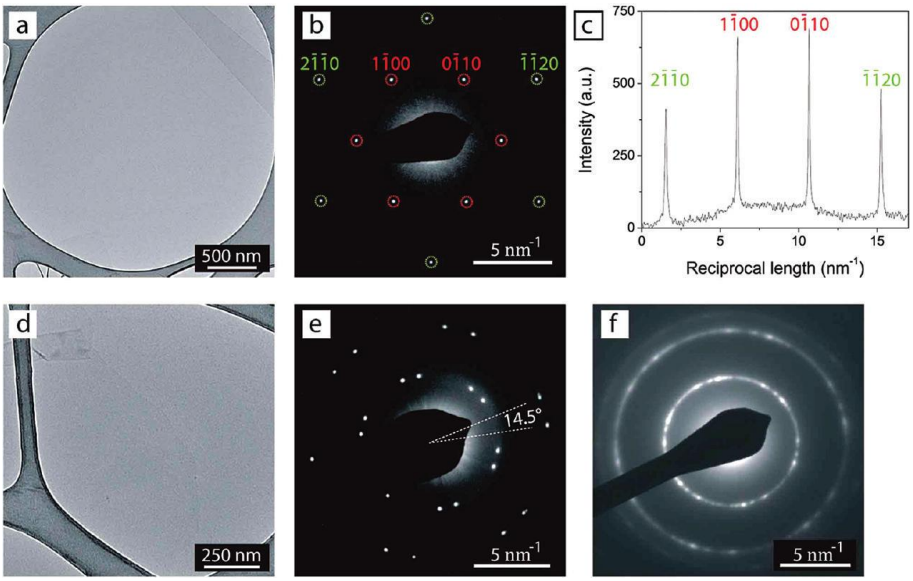

Figure 70. (a) TEM image of a single GO sheet on a lacey carbon support, (b) SAED of the centre of the region shown in (a), the diffraction spots are labelled with Miller-Bravais indices, (c) Intensity profile through the diffraction spots labelled in panel (b), (d) TEM image with two overlapping GO sheets, (e) an SAED pattern from the double sheet region (d) and (f) electron diffraction pattern from a thin film of GO ca. 15-20 layers thick.[7]

Furthermore, it has been shown that the mechanical strength of GO, despite being only one atom thick, allows monolayer GO supports to be used for sample imaging by AFM,[10] and they are equally robust to exposure in SEM.[7]

In this chapter the exploration of GO as a support for analysis of BCP assemblies by multiple microscopy techniques is demonstrated through analysis of the three most common types of assemblies (polymersomes, spheres, and cylinders). The data obtained using GO-grids without staining is compared to data obtained using conventional staining techniques and cryo-TEM; a schematic for each grid type is shown in **Figure 71**. Complementary data from AFM and SEM is also presented, including analysis of the same individual polymersomes on a GO substrate using all three techniques. This is not possible using stained samples or cryo-TEM and presents a significant advance in the detailed characterisation of polymeric nanostructures. In addition the low background of GO readily enables the use other electron microscopy techniques such as tomography, STEM and exit wave reconstruction.

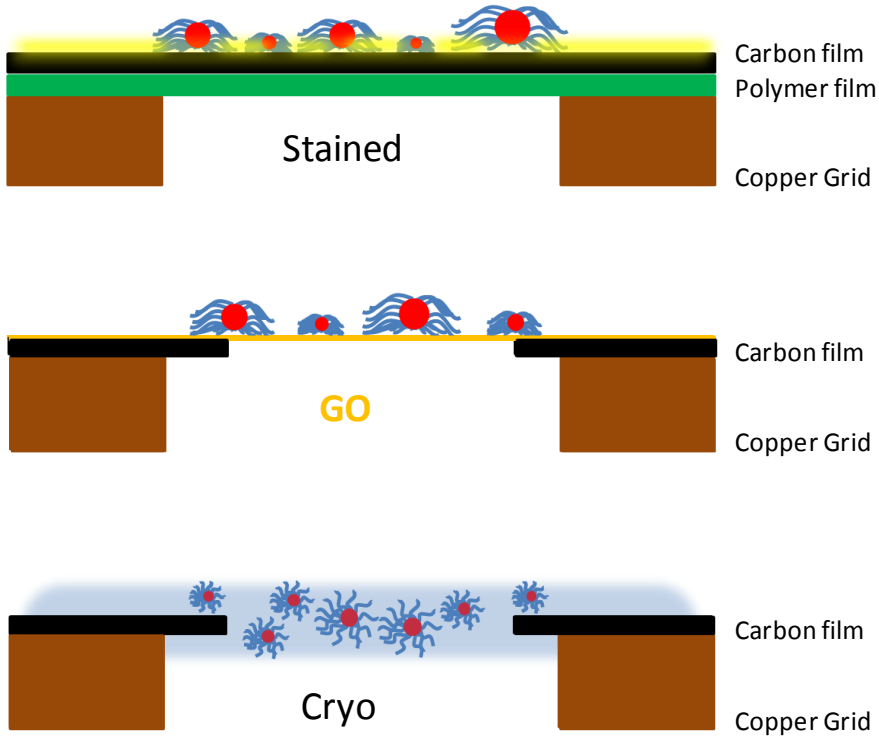

Figure 71. Schematic representation of a stained, GO and cryo TEM grid.

4.2 Results and discussion

4.2.1 Preparation of GO-TEM grids

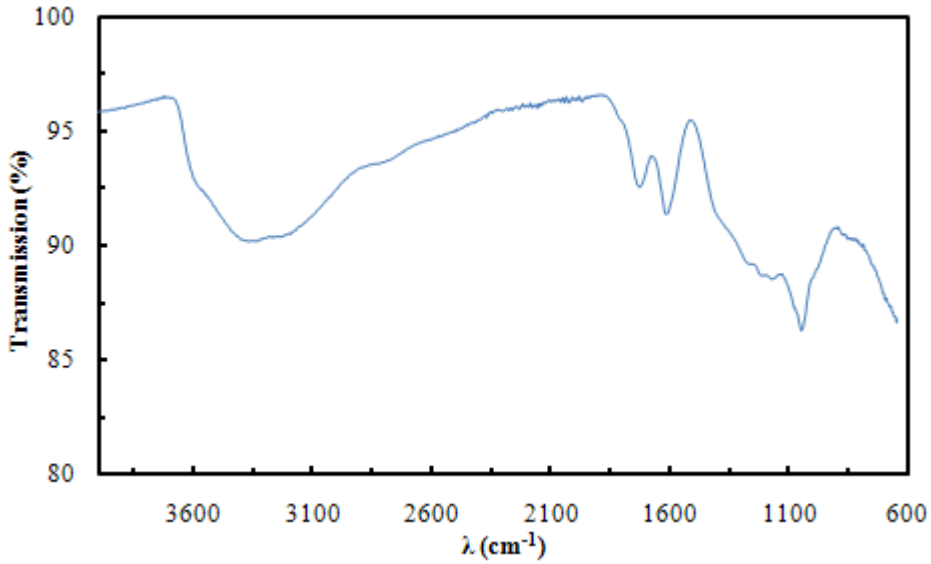

Figure 72. IR spectrum of GO flakes.

Graphene oxide was synthesised from graphite via a modified Hummers method,[11] as previously reported.[25] Graphite flakes were oxidised by stirring in mixtures of conc. H_2SO_4, $KMnO_3$ and H_2O_2, before being washed with DI water and freeze dried resulting in GO flakes. The GO flakes were characterised by IR spectrocopy (**Figure 72**) which shows a broad absorbance from 2500-3600 cm^{-1}, which can be assigned to the alcohol, acid and water groups and some sharp peaks around 1000 and 1800 cm^{-1}, which can be assigned to epoxide, hydroxy, carboxy, and ketone groups.[12]

Figure 73. Photograph of aqueous graphene oxide suspensions of decreasing concentration from left to right as marked.[7]

GO flakes can be dispersed in water by stirring overnight to form orange-brown solutions (**Figure 73**), which are stable after mild sonication in order to exfoliate the sheets. Previously GO-TEM grids have been made by placing a holey carbon TEM grid onto a filter paper and adding one drop of a sonicated GO solution (ca. 0.1 mg mL^{-1}) onto the grid.[7, 10] The result is a partial covering of the holes with GO sheets which range from single to multiple (> 3) to many (>10) layers of GO. Once made GO-TEM grids can be stored in air for many months with no sign of deterioration and are extremely stable under the electron beam. Clearly the best contrast for particles will be provided by single layer GO, therefore the coverage and thickness of GO-sheets were investigated with respect to changes in solution concentration and sonication time in order to optimise GO-TEM grid preparation.

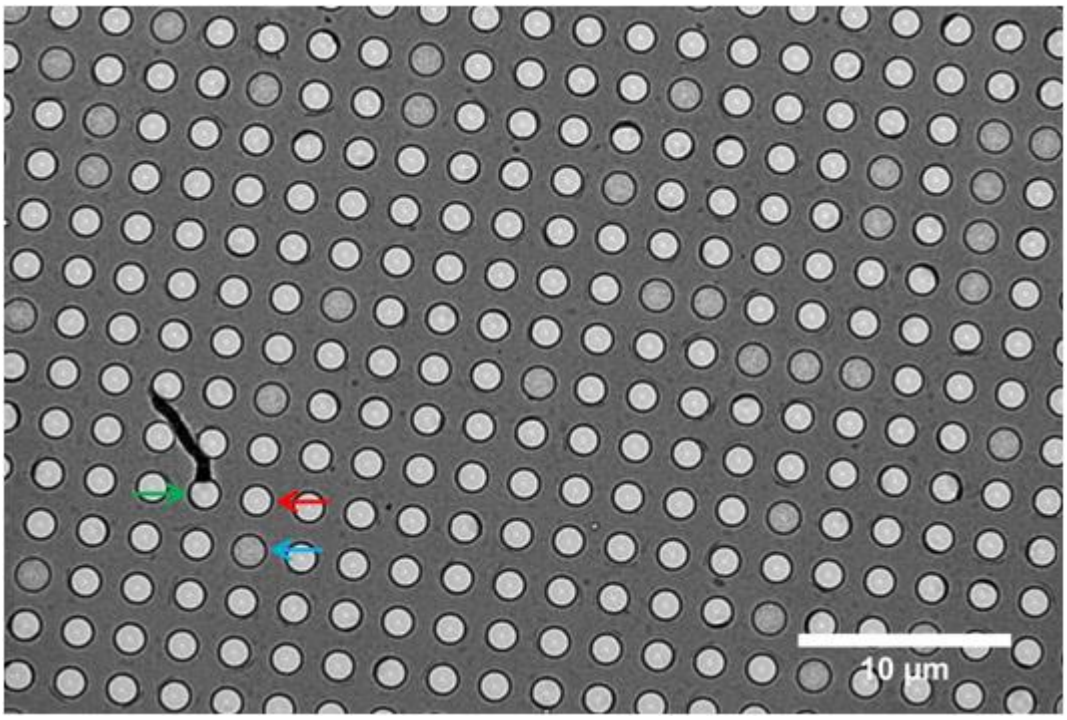

Figure 74. TEM image for GO-TEM grid at 0.01 mg mL^{-1} and 300 seconds sonication at low magnification and extreme defocus. The dark holes indicate the hole is covered by GO and light holes indicate an empty hole. The coloured arrows indicate the holes which were used to prove a single layer of GO can be seen under these conditions (**Figure 75**). The green arrow shows the empty hole next to the bacteria, the blue and red arrows show the holes where the diffraction patterns in **Figure 75c** and **d** were recorded respectively.

Quantifoil TEM grids that contain regular arrays of holes with a diameter of ca. 2 µm were used (**Figure 74**), however, any holey carbon grids will be suitable, provided the GO sheets are large enough to cover the holes. Initial experiments revealed that glow discharging the TEM grids (to impart negative charge on the surface) prior to drop deposition of GO solutions gives a much better coverage of GO and consequently lower concentrations are needed.

GO flakes were dispersed in nanopure water at 0.1 mg mL^{-1} by stirring overnight. Solutions were diluted to concentrations of 0.010, 0.015, 0.020 and 0.025 mg mL^{-1} and each solution was sonicated for 30, 300 or 600 seconds.

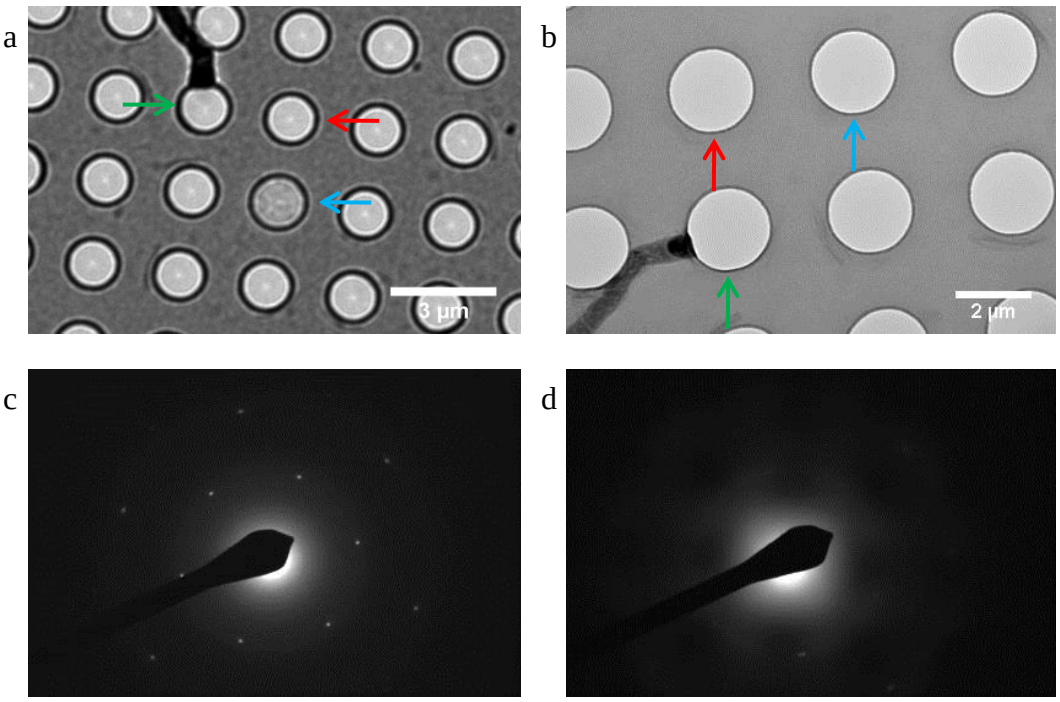

Figure 75. TEM images for GO-TEM grid formed from GO 0.01 mg mL^{-1} with 300 seconds sonication (a) low magnification and extreme defocus (enlargement of **Figure 74**), (b) higher magnification, (c) diffraction pattern at 400 mm camera length for the hole indicated by the blue arrow showing a single sheet of GO and (d) diffraction pattern at 400 mm camera length for the hole indicated by the red arrow showing no GO layers.

The grids were then characterised by 2 parameters: 1) the % of holes which were covered by GO (% coverage) and 2) for the holes which were covered, the % of these holes which were covered by either a single, double or triple layer of GO (% S-T). Single layered GO provides the best contrast and is therefore the ideal substrate for imaging, however double and triple layers are still thin enough to provide excellent contrast. The % coverage of the grids was determined by taking images at low magnification and extreme defocus (ca. 3 mm) (**Figure 74** and **Figure 75a**). The extreme defocus is needed to observe the difference between filled (covered with GO) and empty holes. Four images were taken, starting from the centre of the grid and moving towards the edge, which allowed > 600 holes to be counted for each

grid. The % S-T was determined by taking images at higher magnification (**Figure 75b**) and then recording a selected area electron diffraction pattern (SAED) of each hole in that image, using a selected area aperture of 2 μm (i.e. covering one entire hole, **Figure 75c** and **d**). Areas for % S-T analysis were selected at random from the previous low magnification images until approximately 40 diffraction patterns were recorded for each grid. **Figure 75** provides direct evidence that under the low magnification imaging conditions used there is sufficient contrast to differentiate between a hole covered by one single layer of GO and an empty hole. The large bacteria (indicated by the green arrow), provides a marker for imaging the same holes at low and high magnification. At low magnification and extreme defocus there is a clear contrast difference between the two holes indicated by the red and blue arrows in **Figure 74** and **Figure 75a**. At higher magnification with much less defocus the holes cannot be differentiated by contrast (due to the weakly scattering atomically thin layer) but they can be located using the large bacteria (**Figure 75b**). Recording SAED patterns of the areas indicated by the blue and red arrows reveals that the former contains a single layer of GO and the latter is empty. The results for the GO-TEM grid preparation study are summarised in **Table 1** and **Figure 76**. For solutions sonicated for 30 and 300 seconds there is a linear trend of increasing % coverage with increasing solution concentration. For solutions sonicated for 600 seconds this trend is not so obvious and it is possible that extended sonication times are breaking down the size of the GO sheets. If the sheets become too small they will therefore not cover the holes in the TEM grid. This is supported by the significant drop in coverage after 600 seconds sonication for 0.010 and 0.020 mg mL^{-1} solutions. To further support this, a 0.01 mg mL^{-1} solution was sonicated for 900

seconds which resulted in only 5% of coverage. **Figure 76b** shows a linear decrease in % S-T sheets with increase in GO solution concentration. This is expected as higher concentration solutions will result in greater stacking of sheets. **Figure 76b** also shows an increase in % S-T sheets after 300 seconds sonication compared to 30 seconds, which indicates that short sonication times can help to exfoliate the sheets.

Table 7. Summary of GO sheet coverage and thickness for different preparations of GO-TEM grids

Concentration (mg mL^{-1})	Sonication time (s)	% Coverage	% S-T
0.01	30	29	75
0.01	300	34	93
0.01	600	15	*
0.015	30	36	61
0.015	300	31	69
0.015	600	43	*
0.02	30	59	53
0.02	300	59	78
0.02	600	26	*
0.025	30	65	29
0.025	300	83	51
0.025	600	75	20

*not analysed by SAED

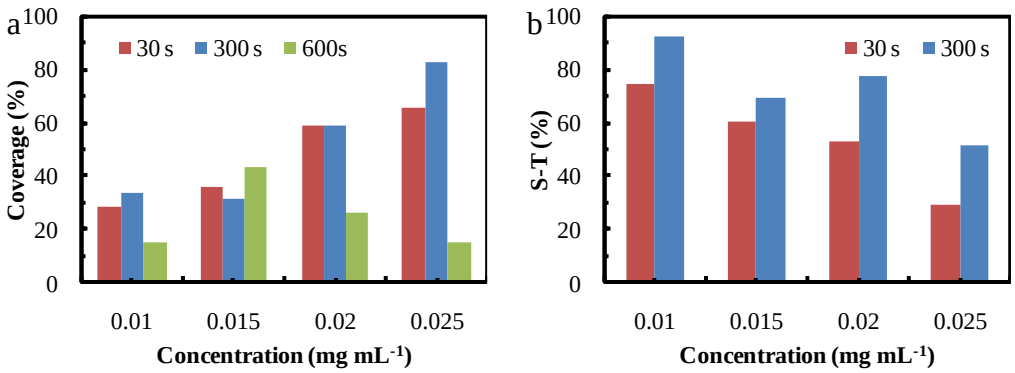

Figure 76. Bar charts displaying (a) % Coverage against GO solution concentration data for sonication times of 30, 300 and 600 seconds and (b) % Single-Triple layered GO against GO solution concentration.

The ideal situation would of course be 100 % coverage with 100 % single sheet GO, but this is not possible with the current preparation method. However, due to the simple nature of this method (which allows for a large number of grids to be prepared quickly) and the fact that only a small portion of a TEM grid is ever imaged, the current levels of coverage and sheet thickness are acceptable. Furthermore, the data shows that with this method it is possible to a certain degree to tailor both the % coverage and % S-T layers depending on the sample or analysis requirements. From the above data it is recommended that GO solutions are sonicated for 300 seconds prior to drop deposition as this will increase sheet separation in all cases. It is recommended that concentration of GO should then be selected based on the desired coverage (discussed in more detail later).

4.2.2 Modification of GO hydrophilicity

Figure 77. Photographs showing the increasing contact angles of GO thin films after heating for 1 hour with respect to increasing heating temperature. (a) No heating, (b) 50 °C, (c) 75 °C, (d) 100 °C and (e) 200 °C

It has been previously reported that hydrophobicity GO can be controlled by sonication in different ratios of water / acetone .[13] However, as the grid preparation has already been optimised, modification of the GO hydrophilicity after deposition onto the grid would be more desirable. Wilson and Rourke reported that the oxygen content in GO is largely due to so called 'oxidative debris' attached to the graphene like sheets and that this content can be removed by heating GO layers in air.[12] Therefore it may be possible to tailor the hydrophilicity by heating the GO-TEM grids.

GO solutions (1.5 mg mL^{-1}) were spin cast onto SiO_2 chips in order to create thin films of GO on the surface. The GO covered SiO_2 chips were then heated on a hot plate for 1 hour at various temperatures (50, 75, 100 and 200 °C). **Figure 77** shows contact angle measurements for water (10 µL) on each of the GO covered SiO_2 chips. The images show a gradual increase of contact angle (from about ~ 12° to ~ 90°) with increasing heating temperature. Note: the original SiO_2 contact angle was ca. 65°. This shows that the hydrophilicity of GO thin films can be tailored by heating the substrates on a hot plate. These heating experiments were repeated using the GO-TEM grids and no noticeable damage to the GO sheets was observed.

4.2.3 Application of samples to GO-TEM grids

Figure 78. Photograph of a GO-TEM grid held with tweezers with 4 µL of water applied.

Applying samples to GO-TEM grids is relatively simple and most methods used for preparation of stained grids will be suitable. One caveat however is that GO-TEM grids cannot be plasma cleaned or glow discharged prior to use as this process will destroy the GO layers. Three methods were used apply samples to GO-TEM grids as detailed below.

Method 1: Apply a small volume (typically 4 µL) of sample to a GO-TEM grid held with a pair of tweezers (**Figure 78**), leave for a set time period (typically 2 min) to allow the structures to adsorb to the GO, wick the water away with a piece of filter paper and leave until the water has completely evaporated.

Method 2: Apply a small volume (typically 4 µL) of sample to a GO-TEM grid held with a pair of tweezers (**Figure 78**) and leave until the water has completely evaporated.

Method 3: Apply a small volume (typically 4 µL) of sample to a GO-TEM grid held with a pair of tweezers (**Figure 78**), leave for a set time period (typically 2 min) to allow the structures to adsorb to the GO, submerge the grid in liquid nitrogen in order to freeze the sample, place the grid under vacuum in order to sublime water from the grid.

Typically method 1 is the most appropriate for aqueous assemblies. Method 2 is suitable for extremely low concentrations or if the sample does not readily adhere to the GO. Method 3 is used for more delicate assemblies in an attempt to avoid distortion / destruction upon drying.

4.2.4 Analysis of 2.09 by TEM on GO-TEM grids

The non-pallidated SCS pincer functionalised PAA, **2.10** (Chapter 1) is an ideal candidate for TEM analysis using GO-TEM grids. As previously discussed the assemblies are very small (ca. 5 nm) and weakly contrasting, furthermore their cylindrical nature should make them easy to identify. **Figure 79** shows a typical image of **2.10** on GO-TEM grids. The increased contrast and texture of the GO sheets indicates that they are covered with a non-structured thin film of polymer. This indicates that the assembled structures cannot survive the drying process, despite numerous grid preparations by each of the three methods. This is perhaps not surprising considering the core forming moiety, dodecane thiol, is a small molecule liquid, and will therefore have weak aggregation forces and no entanglement.

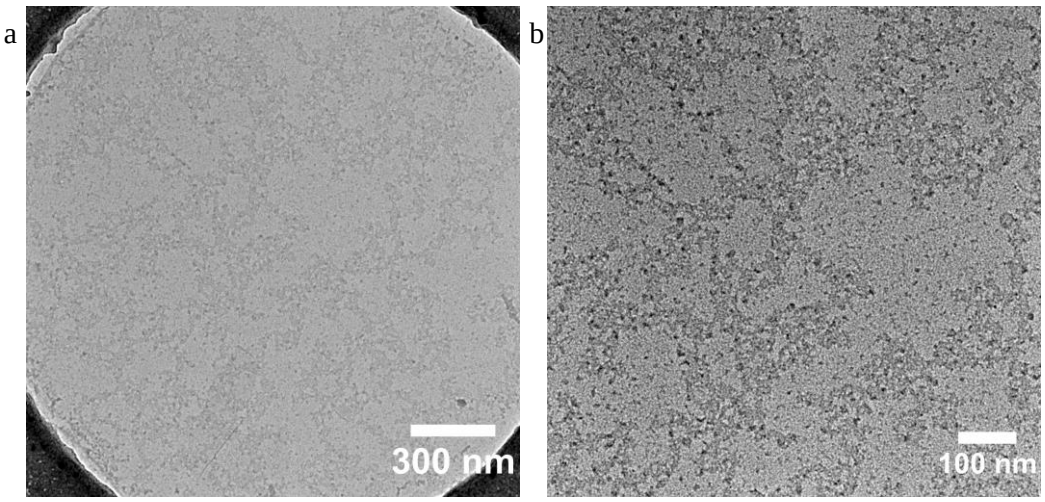

Figure 79. Representative TEM images of **2.10** on a GO-TEM grid.

4.2.5 Analysis of PB-*b*-PEO spherical micelles on GO-TEM grids

The next level up in rigidity would be a low T_g polymeric core, therefore spherical micelles composed of poly(1,3-butadiene$_{57}$-*b*-ethylene oxide$_{183}$) (PB_{57}-PEO_{183}) [**] were analysed. Note the T_g of PB is ca. -50 °C. Aqueous solutions of PB_{57}-PEO_{183} have been extensively studied by SANS and cryo-TEM and shown to form spherical micelles with a core diameter of 24 nm and an overall diameter of 54 nm.[14] **Figure 80a** shows a representative TEM image of the PB_{57}-PEO_{183} on a GO-TEM grid. It can be seen that these micelles have also collapsed upon drying forming a lamella / cylindrical type phase in the bulk, which, although potentially interesting for thin films studies of this polymer, provides no information about the polymer nanostructures in solution.

[**] poly(butadiene-*b*-ethylene oxide micelles were provided by Thomas Epps, III and Elizabeth Kelley

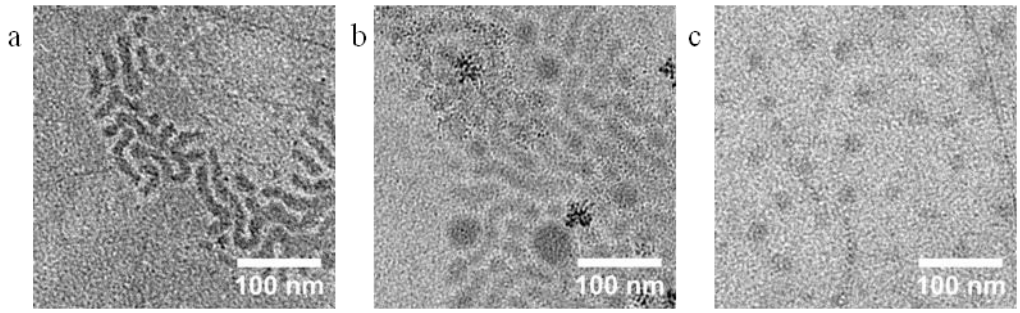

Figure 80. TEM images of PB_{57}-PEO_{183} on GO-TEM grids (a) as made (b) heated for one hour at 65 °C and (c) heated for one hour at 90 °C prior to sample deposition.

This collapse / rearrangement was also observed when freeze drying the sample to the grid (method 3, **Figure 81b**). While the hydrophilicity of the GO grids is useful for adsorbing functional polymers, it is possible that it could be contributing to the deformation of the particles on the surface. As the particles dry, a more hydrophobic surface might help retain the spherical structure of the micelle corona in the water droplet when almost dehydrated, and consequently help retain the micelle structure when completely dehydrated. **Figure 80b** shows an image of the PB_{57}-*b*-PEO_{183} on a GO-TEM grid heated at 65 °C for one hour, the lamella type phase is still present, however, some spherical objects are present which are more indicative of the solution structure. **Figure 80c** shows an image of the PB_{57}-*b*-PEO_{183} on a GO-TEM grid heated at 90 °C for one hour which shows spherical micelles of ca. 25 nm, in much better agreement with the cryo-TEM and SANS analysis. While this data indicates that the hydrophobicity of the GO-TEM grids can help to prevent collapse of the particles, it should be noted that the heated grids did not contain uniform structures and many areas showed collapsed particles and the lamella type phases (**Figure 81a**).

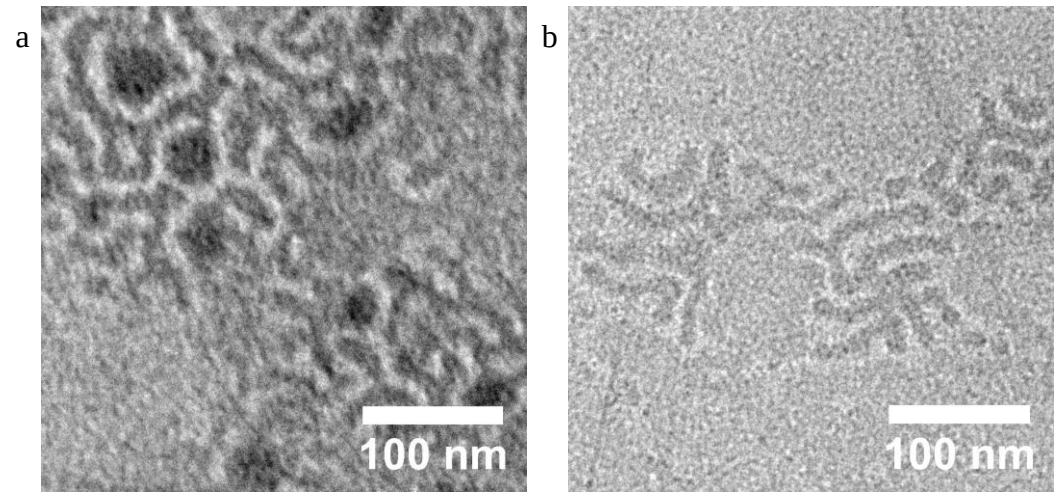

Figure 81. TEM images of PB_{57}-PEO_{183} on GO-TEM grids (a) heated to 90 °C (b) sample prepared by method 3.

When analysing self-assembled structures in the dry state if the core is a high T_g polymer or if the particle is sufficiently cross-linking, minimal distortions will occur upon drying. For most other cases it is unlikely that the structure will be retained in the absence of water. Therefore, the ideal structure for analysis in the dry state is one with a high T_g polymer core and a small corona. Since the seminal work of Eisenberg and co-workers,[15, 16-19] PS-*b*-PAA has become an archetypal amphiphilic BCP for self-assembly into higher ordered structures. As discussed in Chapter 1, using a range of block ratios and assembly conditions it has been shown that these BCPs can form spheres, cylinders, polymersomes, multilamellar structures, and compound micelles. With this in mind PS-*b*-PAA BCPs were synthesised, assembled into polymersomes and spheres, and analysed using the GO-TEM grids.

4.2.6 Synthesis of PS-*b*-PAA BCPs, 4.05 and 4.06

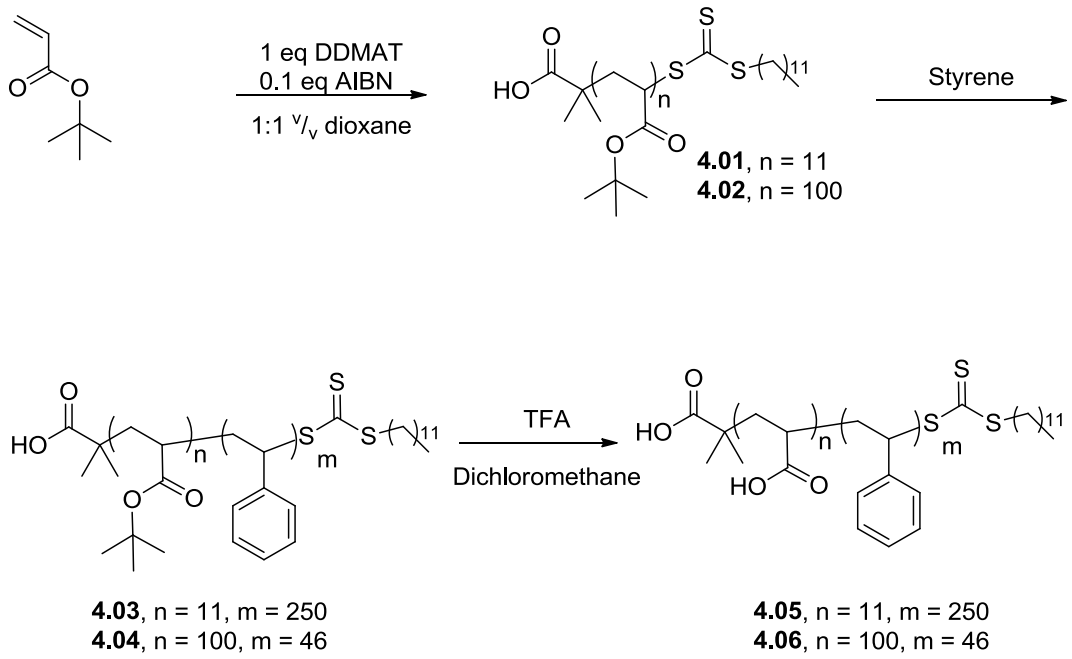

Scheme 7. Synthesis of poly(styrene)-*b*-poly(acrylic acid) block copolymers, **4.05** and **4.06**

Polymerisation of *t*BuA at 65 °C in dioxane, followed by precipitation into MeOH:H_2O 9:1 resulted in a well-defined P*t*BuA homopolymers **4.01** and **4.02.** ^{1}H NMR spectroscopy (**Figure 82**) shows that the end group peaks H_f are clearly visible and can be used to determine M_n by NMR. Good end group fidelity can be inferred from an overlay of the DRI and UV (at 309 nm) trace for SEC analysis of the polymer (**Figure 83**).

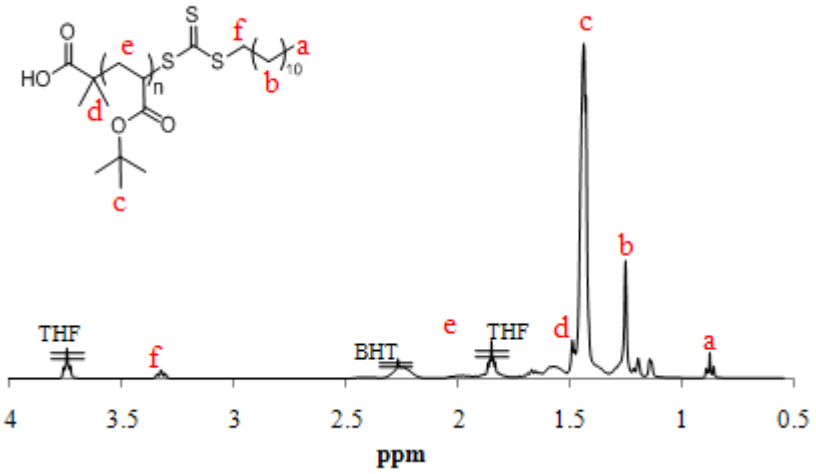

Figure 82. ^{1}H NMR spectrum for **4.01** in $CDCl_3$.

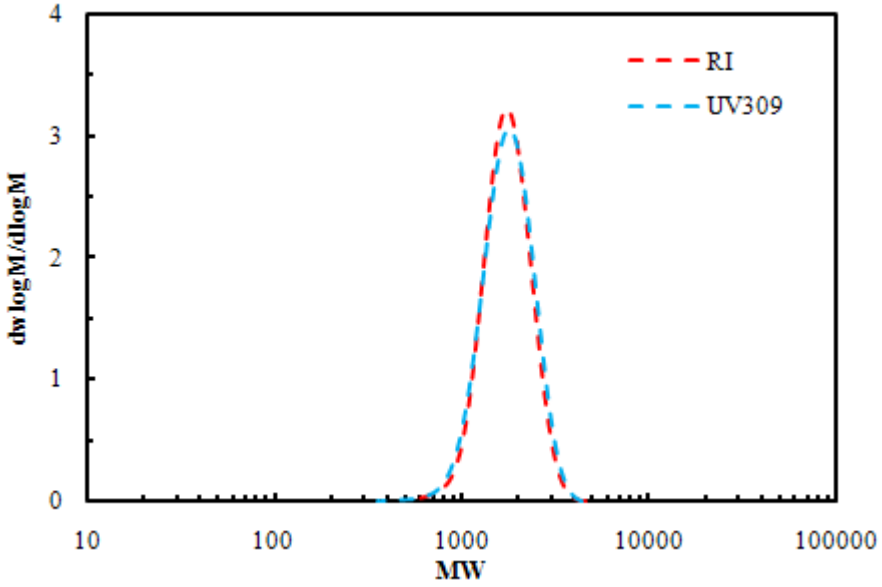

Figure 83. SEC traces using an DRI (red) and UV (at 309 nm) (blue) detectors for the *t*butyl acrylate **4.01** in THF.

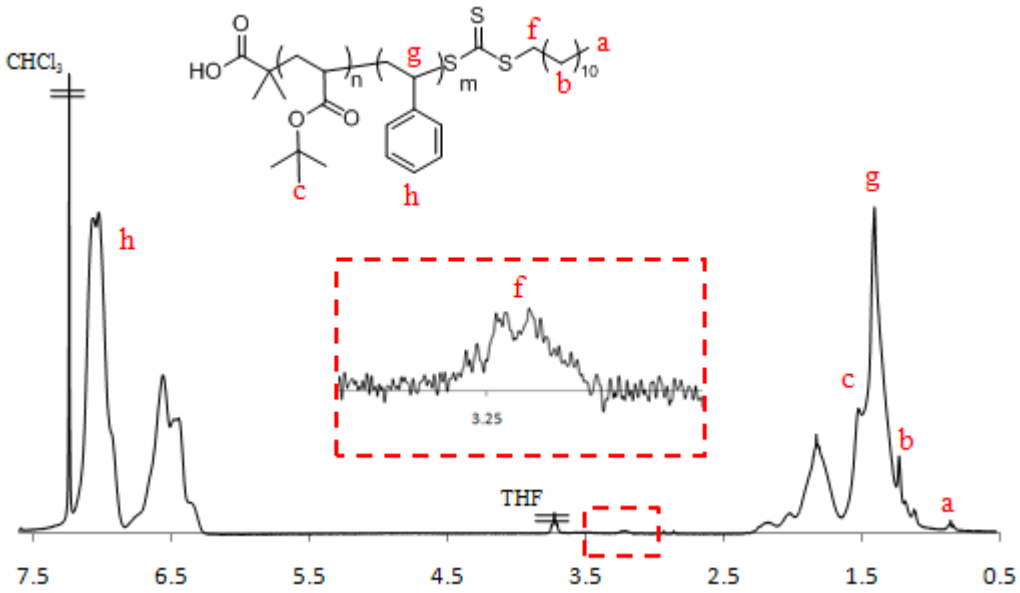

Figure 84. ^{1}H NMR spectrum for **4.03** in $CDCl_3$.

Chain extension of P*t*BuA homopolymers with styrene in bulk at 110 °C resulted in well-defined BCPs **4.03** and **4.04**. Block formation can be seen in both the ^{1}H NMR spectrum (**Figure 84**) by the appearance of aromatic protons H_h, and retention of protons H_f and by the large shift in MW by SEC (**Figure 85**). The lack of residual P*t*BuA also indicates the high end group fidelity of the homopolymer **4.01**.

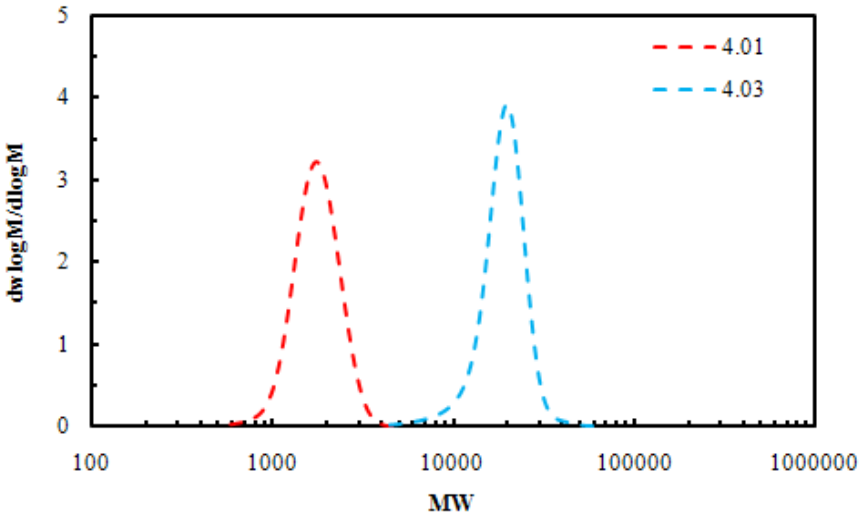

Figure 85. SEC traces using an RI detector for **4.01** (red) and **4.03** (blue) in THF.

Deprotection of the hydrophobic P*t*BuA with trifluoroacetic acid (TFA) afforded amphiphilic PS-*b*-PAA BCPs **4.05** and **4.06**. As in Chapter 2 IR spectroscopy gives good evidence for removal of the *t*BuA groups showing a carbonyl shift from 1730 cm^{-1} to 1700 cm^{-1} (sharp → broad) as well as the loss of the peak at 1153 cm^{-1} associated with the C-O stretching of the ester.[20-22]

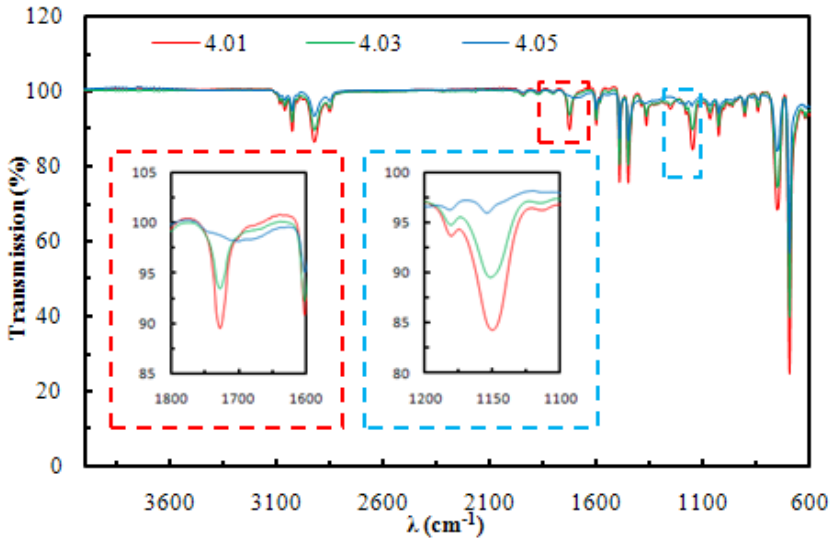

Figure 86. IR spectrum for **4.01**, **4.03** and **4.05.** Insets show the peaks indicative of *t*butyl loss from **4.03** to **4.05**.

4.2.7 Self-assembly of 4.05 and 4.06

Polymers **4.05** and **4.06** were self-assembled by the solvent switch method. Water was added drop wise to DMF solutions of **4.05** (2 mg mL^{-1}) and **4.06** (1 mg mL^{-1}). The first evidence of self-assembly appears after the addition of ca. 1-5wt % of water when the solutions became turbid. The DMF:Water solutions were extensively dialysed against nanopure water, filtered (0.45 micron nylon filters) and analysed by dynamic light scattering (DLS). **Figure 87** shows the DLS intensity, number and volume traces for **4.05** in water. As might be expected from the block ratios, **4.05** (PS_{250}-*b*-PAA_{11}) has formed large structures of ca. 290 nm (indicative of polymersomes). **Figure 88** shows the DLS intensity, number and volume traces for **4.06** (PS_{46}-*b*-PAA_{100}). The data indicates that **4.06** has formed predominantly small structures of ca. 38 nm (indicative of spherical aggregates).

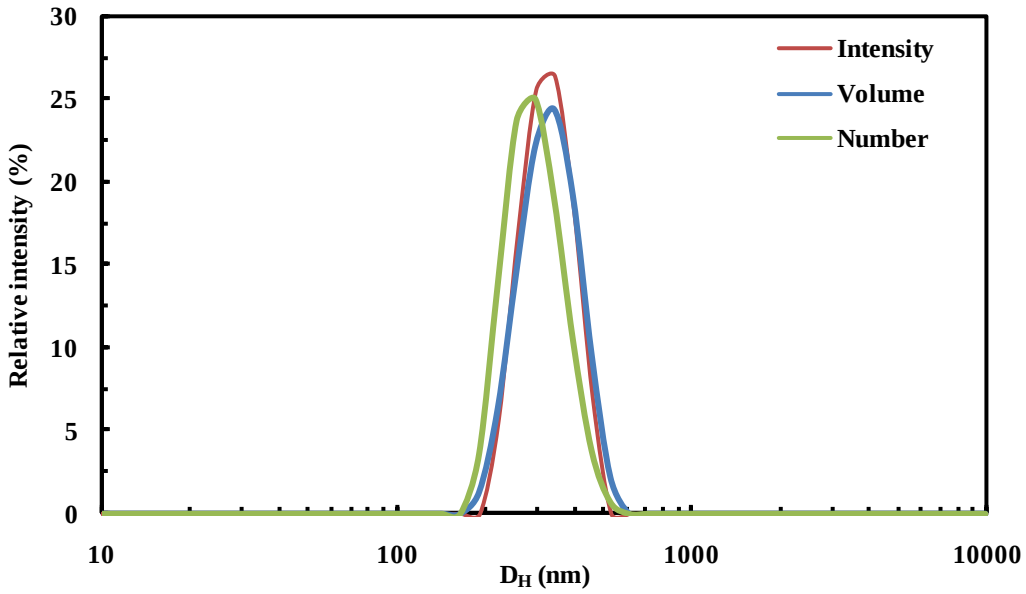

Figure 87. DLS traces showing the intensity, volume and number distributions for **4.05** in water at 0.65 mg mL^{-1}. D_H = 290 nm (z-average), $Đ$ = 0.13.

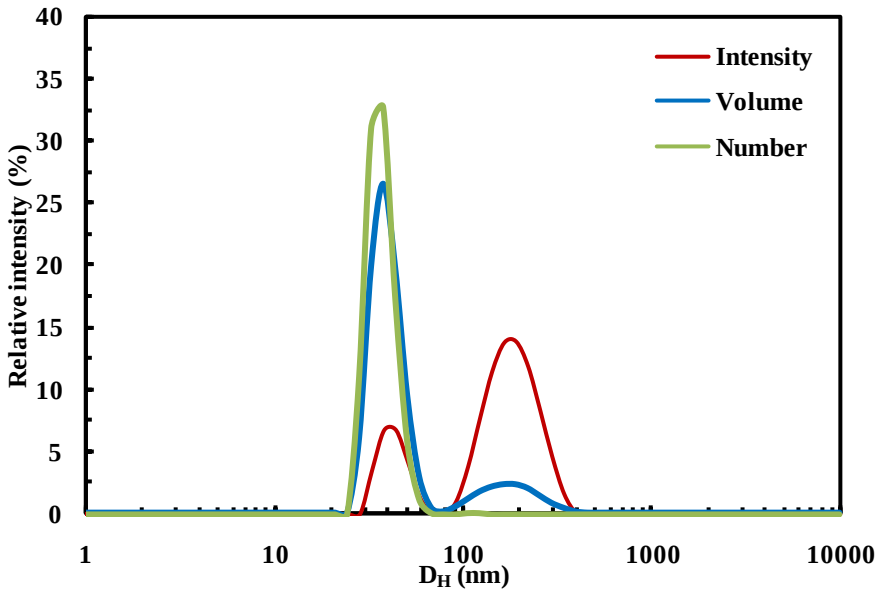

Figure 88. DLS traces showing the intensity, volume and number distributions for **4.06** in water at 0.30 mg mL^{-1}. D_H = 38 nm (by number), $Đ$ = 0.30.

As discussed in Chapter 3 the larger structures present in **4.06** will make up a negligible concentration in solution and therefore are not likely to be observed by TEM analysis. DLS was used only to provide preliminary evidence for particle formation and as the aim of this work is the detailed analysis by microscopy, it was only necessary to perform DLS at one angle and concentration.

4.2.8 Analysis of 4.05 and 4.06 by TEM on stained, GO and cryo TEM grids

The formation of polymersomes has attracted particular interest for nanoreactor[23-25] and biomedical[26, 27] applications as the hydrophobic membrane and hydrophilic interior allow for the incorporation and segregation of various reactive / active groups.[28, 29] Imaging of these structures requires the membrane to be resolved, and often the thickness of this membrane is integral to their application.

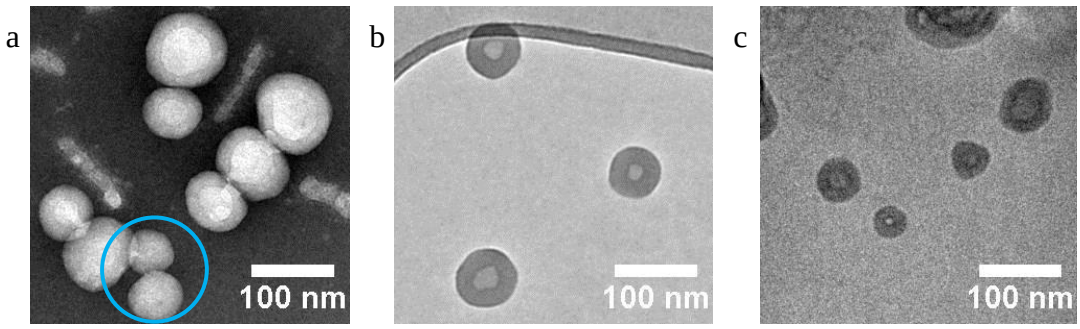

Figure 89. Representative TEM images of **4.05** polymersomes using (a) a carbon formvar grid and UA staining (b) imaged on a GO grid and (c) imaged using cryo-TEM.

Figure 89 (**a-c**) shows TEM images of the self-assembled structures obtained from **4.05** using a formvar carbon grid stained with uranyl acetate (UA), a GO-TEM grid (with no staining), and cryo-TEM (**a-c** respectively). It should be noted that in addition to polymersomes this sample also contained some multilamellar structures, in agreement with previous reports,[17] which are discussed later. **Figure 89a-c** shows the membrane structure which is indicative of polymersome formation. The contrast in the stained image (**Figure 89a**) is due to increased electron scattering where the stain is present, and, as in this case the stain has been adsorbed to the grid and not to the polymersomes (negative staining), the polymersomes appear bright (see **Figure 71** for a schematic representation). However, the stained image also shows artifacts such as rod-like features, which are not found when analysing the same sample by cryo-TEM or on a GO support (a common feature of using a negative staining technique). In addition the fine structure of the polymersomes can be obscured by the UA stain: looking at the particles in the blue circle of **Figure 89a**, in some cases the bilayer is difficult to distinguish. By comparison the polymersome structure is clearly and unambiguously resolved in **Figure 89b** without the application of a stain

through, the utilisation of GO as a low contrast support. The contrast in this GO image is mainly due to electrons scattered by the polymersomes, and hence reflects their actual structure. A comparison of the polymersome images taken by cryo-TEM (**Figure 89c**) and on GO supports (**Figure 89b**) indicates that the background scattering is significantly lower on GO than from the vitrified water support (cryo-TEM), permitting clearer resolution of the particle structures. This is expected as the vitrified water layer must be at least as thick as the particles (**Figure 71**) and is typically about 100 nm.[30] Combined with the inherent difficulties in performing cryo-TEM, this makes statistical analysis of a large number of particles considerably easier using GO as a substrate. Average membrane thicknesses for the polymersomes were measured using each imaging technique. The data obtained for GO (21 ± 2 nm), UA staining (21 ± 2 nm) and cryo-TEM (17 ± 3 nm) were comparable as the averages are within one standard deviation (used to define the error), which indicates a negligible amount of membrane distortion upon drying.

The distinction between image contrast in stained and unstained samples is reinforced by analysis of the spherical aggregates formed from **4.06** (**Figure 90a-c**).[31] When a UA stain is applied (**Figure 90a**) it selectively binds to the acrylic acid corona so that a ring-like feature is noted, perhaps suggesting a membrane like structure. Imaging the same sample unstained on a GO support (**Figure 90b**) showed solid spherical aggregates; the true nature of the structures. **Figure 90c** shows that applying the UA stain to the GO grid gives a similar artificial ring-like contrast indicating that if stains are required, e.g. to identify the location of a particular polymer block within a particle, they can be used on GO grids.[32]

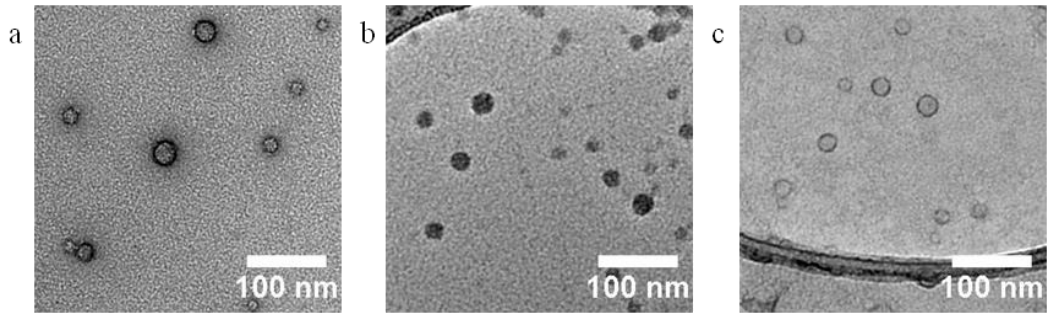

Figure 90. Representative TEM images of **4.06** spherical aggregates imaged using (a) a carbon formvar grid and UA staining, (b) a GO-TEM grid and (c) a GO-TEM grid with UA staining

4.2.9 Analysis of 4.05 by AFM on GO-TEM grids

A significant advantage of the GO-TEM grids over staining and cryo-TEM is that they allow for the direct comparison by TEM and AFM on the same support. This is important as conventional TEM (dry-state or cryo) gives images that are 2D projections of 3D objects from which it is impossible to infer the overall 3D morphology, however AFM analysis can provide information on the 3D structure of the materials. **Figure 91** shows an AFM image of a large polymersome (ca. 125 nm in diameter); in this particle the centre appears collapsed, as expected when drying a large hollow structure to a substrate. Typically, when TEM / AFM are used in combination to study polymer assemblies, individual samples are prepared for each technique on different substrates and therefore drying effects are likely to be different in each case. Performing both analysis techniques for the same sample on the same substrate allows more accurate correlation of the results and hence more robust analysis of polymeric nanostructures.

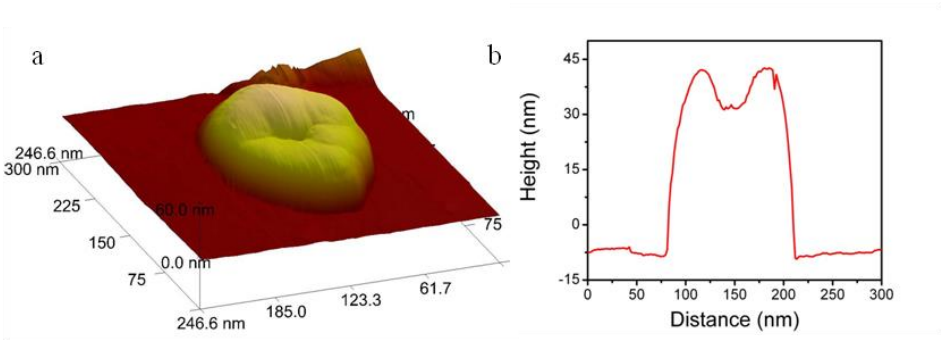

Figure 91. (a) an AFM image and (b) corresponding line profile of a polymersome of **4.05** on the same GO grid that was used for TEM analysis.

One practical consideration arises when performing TEM and AFM on the same GO-TEM grid; having a high % coverage of GO, while not essential, is useful as it can be difficult to optimise the feedback loop (a key operational setting related to how the microscope deals with changes in sample height) when trying to record images in an area of the grid with many holes. 3D imaging can also be performed using electron tomography (discussed below), however collection of data for many particles will be much more time consuming and requires more complex treatment of the collected images.

4.2.10 Analysis of 4.05 by electron tomography

Resolving the full 3D morphology of polymeric assemblies, including the internal structure, can be achieved through electron tomography (ET) analysis. Significant advances have been made in cryo-electron tomography (cryo-ET), but despite the beautiful work by Sommerdijk and co-workers[33, 34] cryo-ET is not yet widely used to study self-assembled polymeric nanostructures.

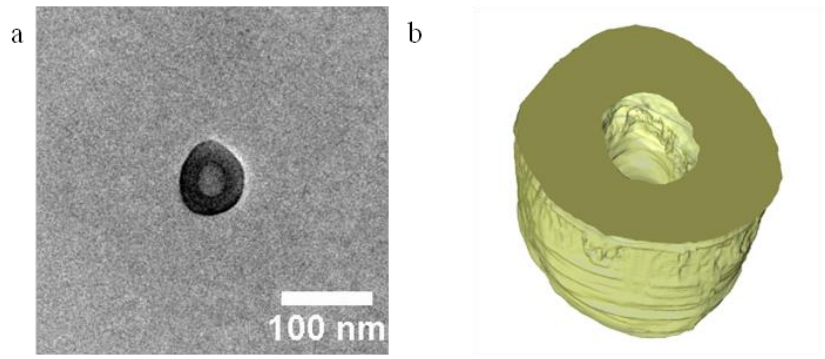

Figure 92. (a) 2D Bright field TEM image of a polymersome 3, (b) cross section of the 3D reconstruction of the polymersome showing the hollow core.

This is due in part to the relatively high background contrast of the vitreous support, and as a result of beam damage during the prolonged exposure required for cryo-ET. However, the extremely low contrast background and stability of the GO support make ET and higher resolution images more accessible. **Figure 92a** shows the bright field TEM image of a **4.05** polymersome, acquired at 0° tilt and **Figure 92b** shows the surface-rendered tomographic reconstruction of the polymersome. The cross section of the 3D reconstruction clearly shows the hollow core of the polymersome. **Figure 93** shows bright field TEM images and 3D reconstructions for the multilamella structures formed by **4.05**. The 3D reconstructions here show channels through the structures indicating a bicontinuous phase. The particle in **Figure 93**(**a** and **b**) show large channels which are clearly visible in the 2D image, whereas the particle in **Figure 93**(**c** and **d**) shows much smaller channels in the 3D reconstruction which are not visible in the 2D image. Therefore, imaging and tomography analysis on GO for more complex structures, e.g. multi-compartmental or Janus micelles, could prove invaluable and the availability of high contrast dry-state tomography should encourage the wider use of this technique.

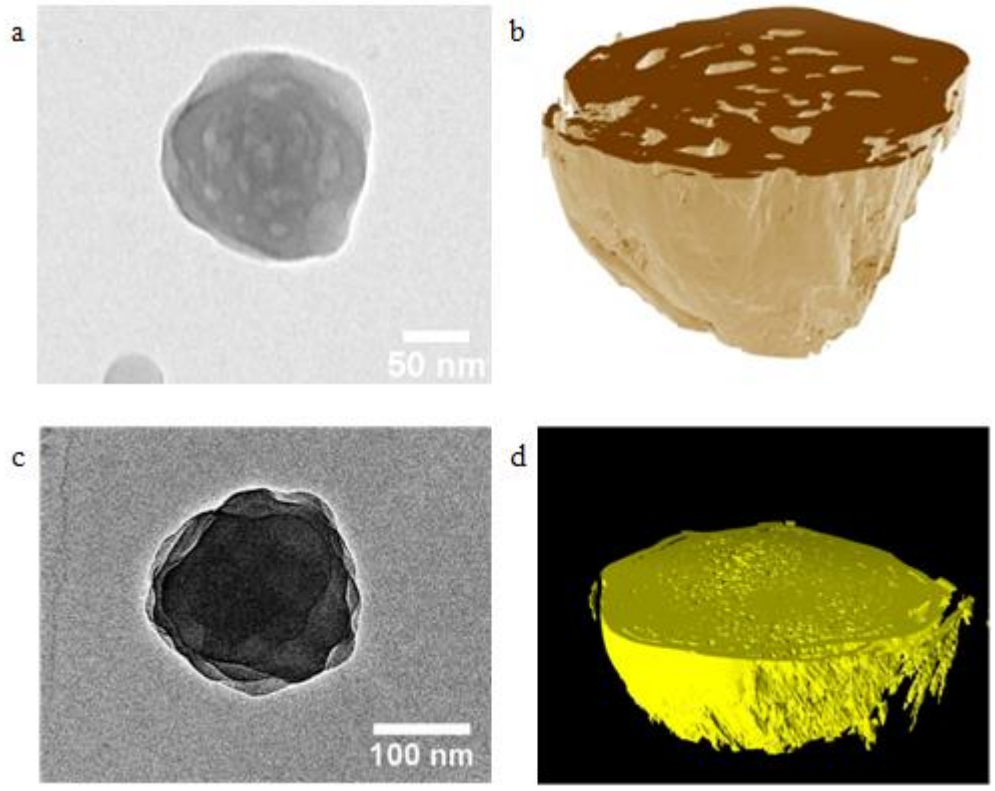

Figure 93. (a and c) bright field images for two multilamella structures formed from **4.05** and (b and d) their respective cross sections of the 3D reconstruction showing the bicontinuous internal structure. Note: the colour choices for (b and d) were chosen simply for aesthetics.

While specimen beam damage is obviously sample specific it should be noted that the ET was performed at 200 kV and data was collected over a period of > 1 hour, during which time no deterioration of the sample was observed.

4.2.11 Analysis of 4.05 by HAADF STEM on GO-TEM grids

Imaging polymeric particles without staining and in the dry state allows a wider range of analytical TEM techniques, such as those regularly used in hard material analysis, to be applied.

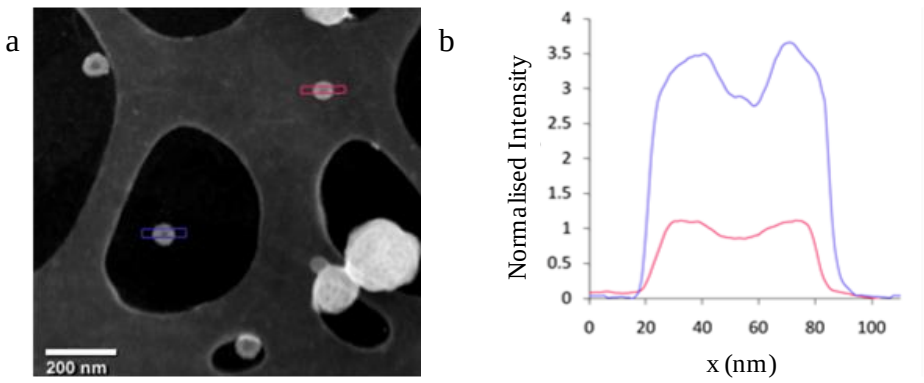

Figure 94. (a) HAADF image containing **4.05** polymersomes on GO (blue) and on the lacey carbon support (red) and (b) the plot profile along two polymersomes on different supports

For example, features observed in the images recorded from nanoscale polymer assemblies using conventional bright-field TEM, result from elastic scattering in the sample and interference effects due to the coherence of the electron beam. These phase contrast effects are highly sensitive to focus, even to the extent that the contrast can be reversed with focus, hence imaging is typically done at small defocus values. An alternative is to take images in the high angle annular dark field (HAADF) mode of STEM, which collects high-angle elastically scattered electrons. HAADF-STEM is an incoherent imaging technique where the image contrast depends on the atomic number of the scattering atoms, density of the sample, and its thickness (so called "mass-thickness" contrast). Therefore, when comparing materials with the same chemical composition image contrast is dominated by changes in density and thickness. **Figure 94a** shows a HAADF image of **4.05** polymersomes on the GO substrate which was previously used for bright field imaging. Using this method the membrane structure can be clearly resolved, however what is more significant is that the signal-to-noise ratio is significantly

greater for the polymersome on the GO support than for the polymersome on lacey carbon. The line profiles in **Figure 94b** demonstrate this increase in contrast by at least a factor of 3, and the corresponding improvement in the signal-to noise ratio.

4.2.12 Analysis of individual 4.05 nanoparticles by TEM, AFM and SEM on a GO-TEM grid

The TEM and AFM results for the **4.05** polymersomes were obtained using the same GO grids but from different, random areas of the grid. Using the GO grids, it is not only possible to compare the average results from these techniques but also, by using a 'finder' TEM grid, exactly the same area and sample can be examined by multiple techniques (TEM, AFM and SEM in this case). Finger grids have a macroscopic labelling system allowing specific areas of the grid to be repeatedly located. **Figure 95** (**a-c**) shows lower magnification images of the area where the TEM, AFM and SEM images of the same particles were recorded. **Figure 95** (**d-f**) shows TEM, AFM, and SEM images of **4.05** polymersomes on a GO support. To the author's knowledge this is the first time the same individual self-assembled polymeric structures have been imaged using multiple techniques. Imaging the exact same area of the grid further backs up the minimal damage caused when analysing these samples. The GO reduces charging in the SEM and while some contamination was observed during extended periods of beam irradiation, the particles could easily be imaged without the need for coatings, which are often used to protect soft materials.

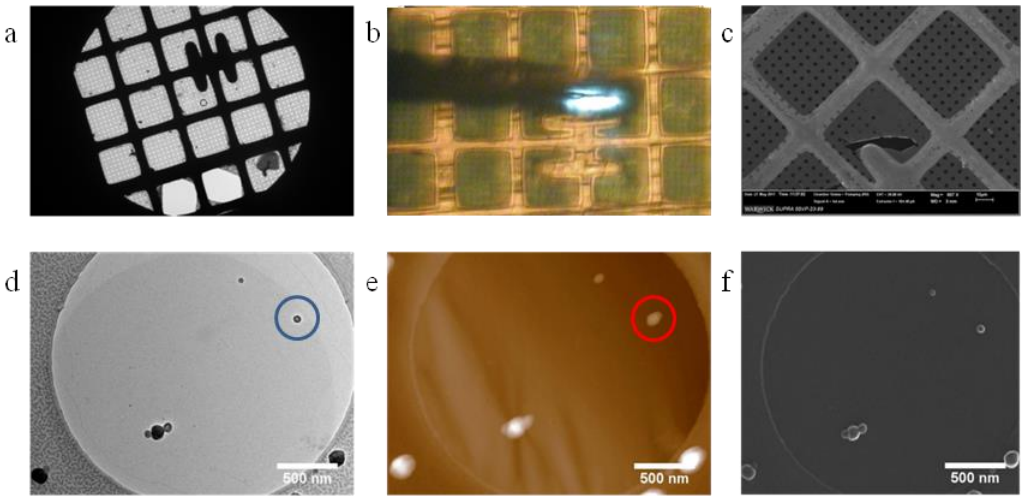

Figure 95. (a) Bright field TEM, low magnification, (b) light microscope image from the AFM and (c) SEM image at low magnification showing the 'H' marking on the finder TEM grid. (d) Bright field TEM, (e) AFM and (f) SEM images of exactly the same area of the GO grid.

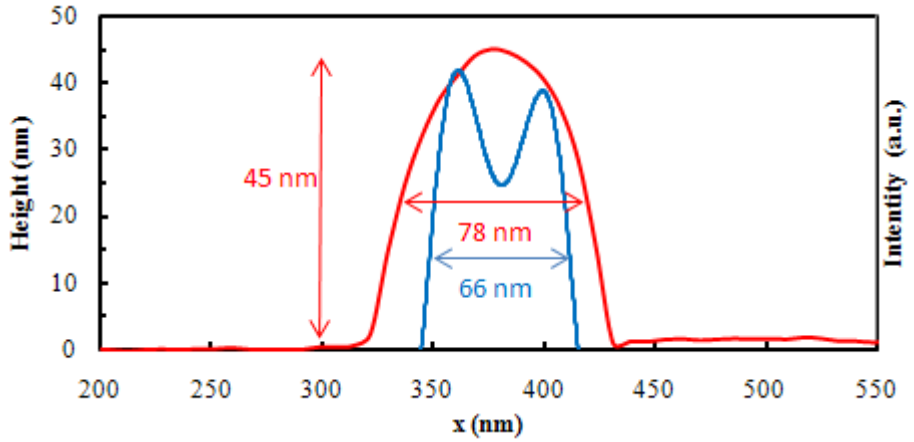

Figure 96. The plot profiles corresponding to the polymersome in **Figure 95** (circled in blue and red from the TEM and AFM images respectively). The TEM plot profile has been inverted for clarity.

The corresponding plot profiles from AFM and TEM (**Figure 96**) show the roughly spherical nature of the particle on the surface (AFM) and its hollow internal structure (TEM). The measured height (45 nm by AFM) and width (61 nm by TEM) show that it is not perfectly spherical, suggesting that drying may have distorted its

structure. It should be noted that the apparent width of the polymersome as measured by AFM is increased due to tip convolution effects.

4.2.13 Analysis of $PLLA_{40}$-*b*-PAA_{298} cylinders by TEM; drying induced reorganization

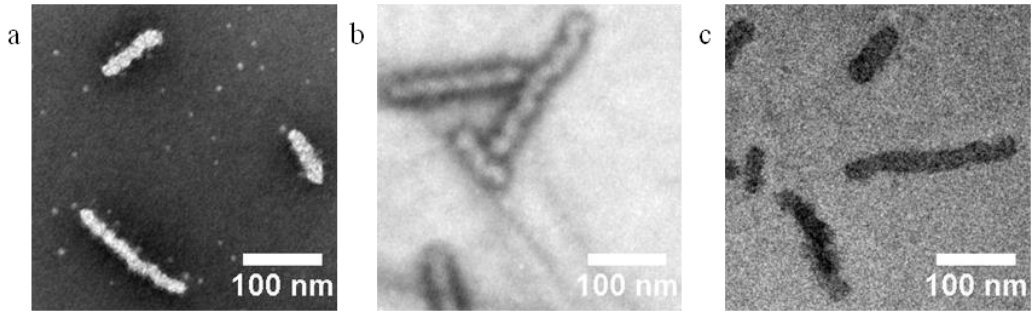

Figure 97. Representative TEM images of the $PLLA_{40}$-*b*-PAA_{298} cylinders using (a) a carbon formvar grid with PTA staining, (b) a GO-TEM grid and (c) cryo-TEM

As previously reported,[35] the crystallization behaviour of poly(L-lactic acid) (PLLA) can be exploited in order to drive the assembly of BCPs into cylindrical morphologies.[††] Previous studies focused on measuring the growth of the cylinders by TEM using conventional staining techniques and detailed solution characterisation by SANS and cryo-TEM confirmed that the cylinders have a core-shell structure.[36] **Figure 97** shows a comparison of representative TEM images of the same sample ($PLLA_{40}$-*b*-PAA_{286}) obtained using (**a**) a formvar carbon grid and phosphotungstic acid *(*PTA) staining, (**b**) a GO TEM-grid, (**c**) and cryo-TEM. All three images show similar cylindrical structures, however, on the GO support (**Figure 97b**) the particles have much lower contrast in the core compared to the

[††] PLA-*b*-PAA cylindrical nanoparticles were provided by Nikos Petzetakis

other techniques, giving the appearance of hollow nanotubes. Further investigation into the lower contrast core observed on the GO grids was necessary to fully understand this system.

Table 8. Summary of length and diameter measurements for $PLLA_{40}$-*b*-PAA_{298} cylinders the three different TEM techniques. 100 particles were counted for dry state imaging, 43 particles counted by cryo-TEM.

TEM Technique	L_{av} (TEM) / nm	D_{av} (TEM) / nm
PTA staining	111 (± 8)	26 (± 6)
GO	106 (± 6)	33 (± 5)
Cryo	103 (± 9)	32 (± 4)

Table 8 shows a summary of the length and diameter measurements made by each technique. It can be seen that the data is comparable for each measurement suggesting that the cylinders have not collapsed upon drying. As mentioned previously, these weak phase materials can be particularly sensitive to focus, to the point where contrast can be reversed with focus. **Figure 98** shows a focal series for the $PLLA_{40}$-*b*-PAA_{298} cylinders on GO. Image (**a**) was taken slightly under focus and shows the appearance of hollow nanotubes (analogous to **Figure 97b**), image (**b**) was taken slightly over focus and shows solid cylinders, and image (**c**) was taken with a large over focus value and shows a contrast reversal from the under focus image.

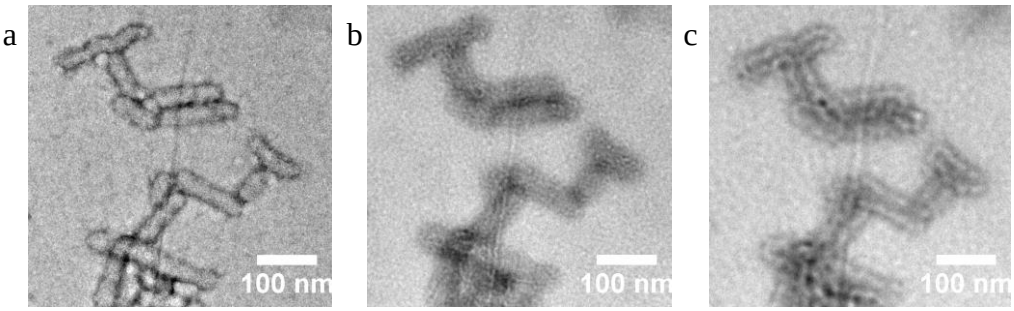

Figure 98. Focal series TEM images of the $PLLA_{40}$-*b*-PAA_{298} cylinders (a) under focus (ca. -500 nm), (b) slightly over focus (ca. 100 nm), (c) large over focus (ca. 500 nm).

In order to remove the effect of phase contrast the cylinders were imaged in the HAADF mode of STEM (mass-thickness contrast) (**Figure 99a**), which clearly shows a hollow core, proving that the appearance of nanotubes is not caused by a phase contrast effect. Both the bright field and HAADF images could still be misleading if the particles have been unintentionally stained when drying, (perhaps by an unknown salt impurity which binds to the acrylic acid). The cylinders were therefore imaged by energy filtered-TEM (EF-TEM) carbon mapping (**Figure 99b**). Here, only the electrons scattered by carbon atoms are detected, and the appearance of hollow nanotubes proves the particles have lower carbon content in the centre. **Figure 99c** shows a slightly under focus bright field TEM image for the cylinders prepared by method 3 (freeze-drying) and here the cylinders appear completely solid. This indicates that some re-arrangement occurs upon drying which can be prevented by this preparation method.

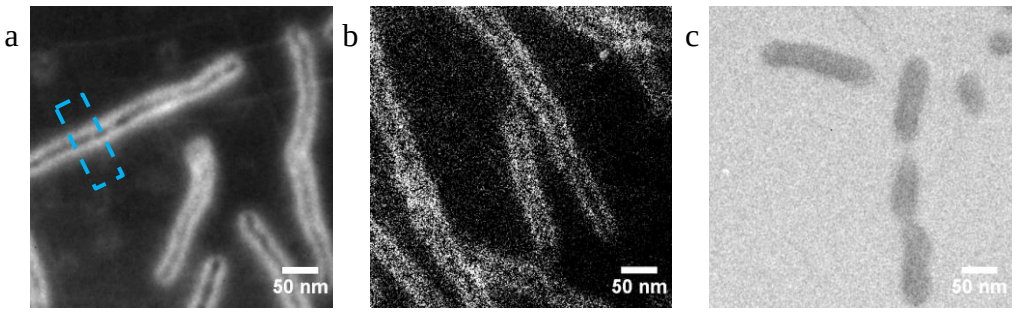

Figure 99. TEM images of hollow $P(AA)_{333}$-*b*-$P(L\text{-}LA)_{37}$ cylinders, (a) HADDF-STEM image of hollow $P(AA)_{333}$-*b*-$P(L\text{-}LA)_{37}$ cylinders, the blue dashed box shoes the area taken for the plot profile in **Figure 100** (b) EF-TEM carbon map of hollow PAA_{333}-*b*-$PLLA_{37}$ cylinders and (c) bright field TEM image of solid cylinders where the grid was prepared by method 3.

In order to get a better understanding of this re-arrangement upon drying, the same TEM grid used to record the images in **Figure 97b** was imaged using AFM. **Figure 100a** shows that not only have the cylinders retained their 3D shape, but also that their height (30 ± 4 nm) is roughly proportional to their width by GO or cryo-TEM (33 ± 5 nm and 32 ± 4 nm respectively), indicating that little distortion of the overall cylindrical structure occurs upon drying. In this case AFM was preferred to tomography as many particles (>50) could be imaged and analysed quickly. **Figure 100b** shows an overlay of the plot profiles from the HADDF-STEM image (blue, **Figure 99a**) and the AFM image (red, **Figure 100a**) which shows a comparable structure to the plot profiles from the polymersome in **Figure 96**, i.e. there is a spherical cross-section with a hollow interior. Importantly, all of the above mentioned techniques can be performed on the same GO-TEM grid giving consistency and confidence in the results, confirming that the cylinders are truly hollow nanotubes on the surface of the GO-TEM grid.

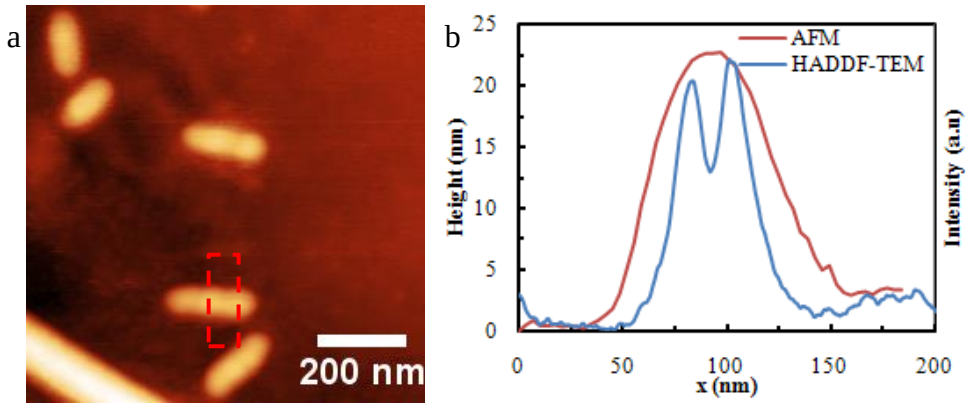

Figure 100. (a) AFM image of hollow PLLA-*b*-PAA cylinders, and (b) plot profiles from the HAADF-TEM image in **Figure 99a** and AFM image (a). The dashed red box indicates the area where the plot profile was taken.

Subsequently it has been shown that PLLA-PAA BCP cylinders spontaneously reorganise to form hollow nanostructures upon drying to GO-surfaces. It has been proposed that this reorganisation is due to complementary H-bonding between the protonated PAA units and the PLA carbonyls that occurs in the dry state. While surface functionalised hollow particles might prove useful for thin film studies,[37] it would be of great interest to those working with polymeric nanoparticles in solution if these structures could be harvested and used to produce hollow nanotubes in water. A 0.25 mg mL^{-1} solution of PLLA-*b*-PAA was dried in an eppendorf overnight, and then re-suspended in water at 5 mg mL^{-1}. **Figure 101a** shows a cryo-TEM image of the re-suspended solution which shows clear evidence of the hollow nanotubes, proving the hollow particles can be redispersed in solution. Imaging this solution after one month showed that ca. 95 % of the cylinders had re-equilibrated to form core-shell cylinders (**Figure 102**).

Figure 101b shows a schematic of the formation of hollow nanostructures in solution and indicates that re-equilibration can occur over time as water will

eventually break up the H-bonds. It has been shown that these hollow particles can be redispersed in solution and therefore drying and re-suspending these cylinders in water provides an extremely simple method for the creation of hollow nanotubes, which would not have been discovered by the use of dry state staining or cryo-TEM analysis alone. Furthermore, the re-equilibration of the hollow particles to form core-shell structures might allow for a controlled release of cargo in solution.

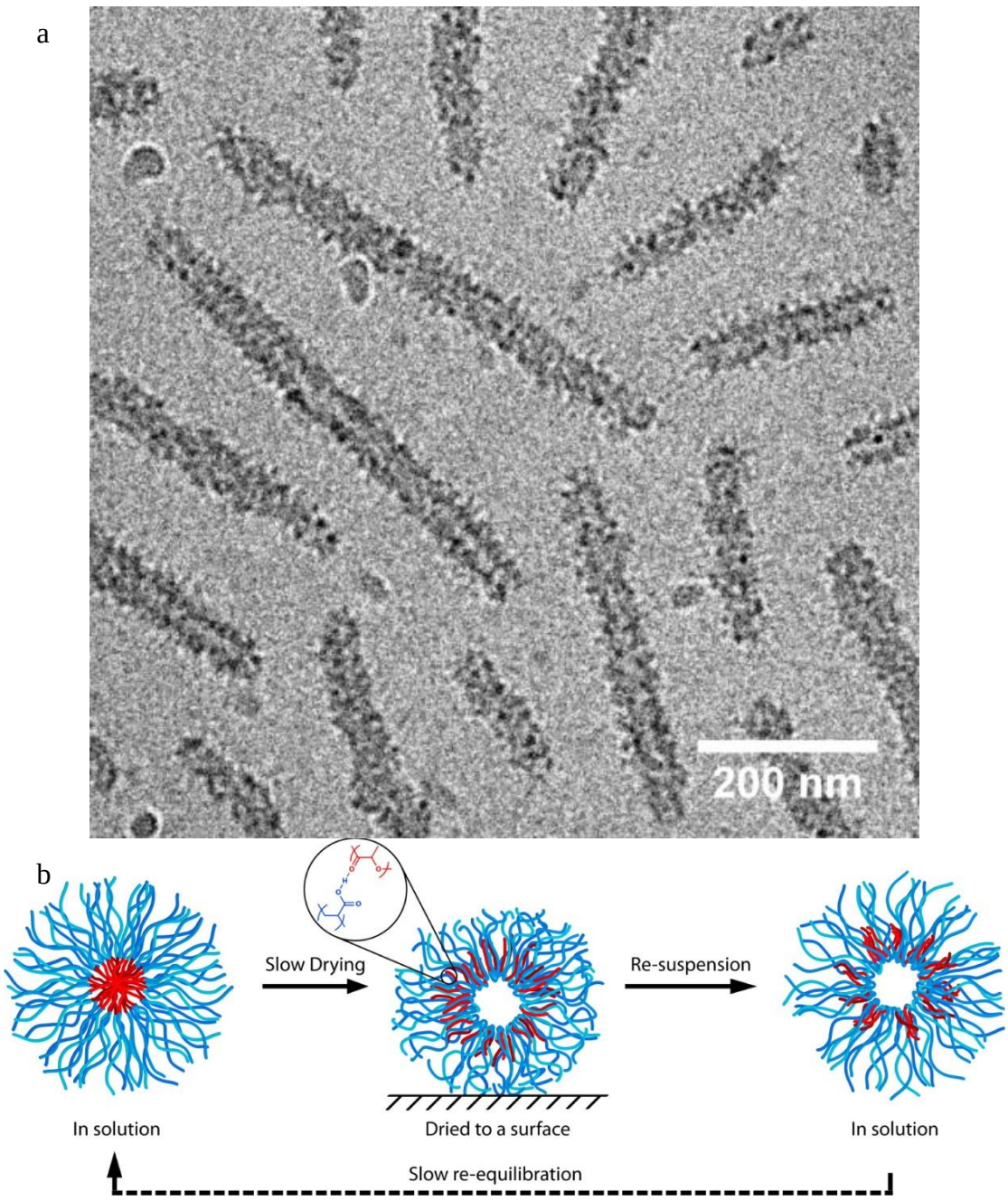

Figure 101. (a) cryo-TEM image of hollow $PAA)_{333}$-*b*-$PLLA_{37}$ cylinders and (b) schematic of the formation of hollow nanostructures in solution.

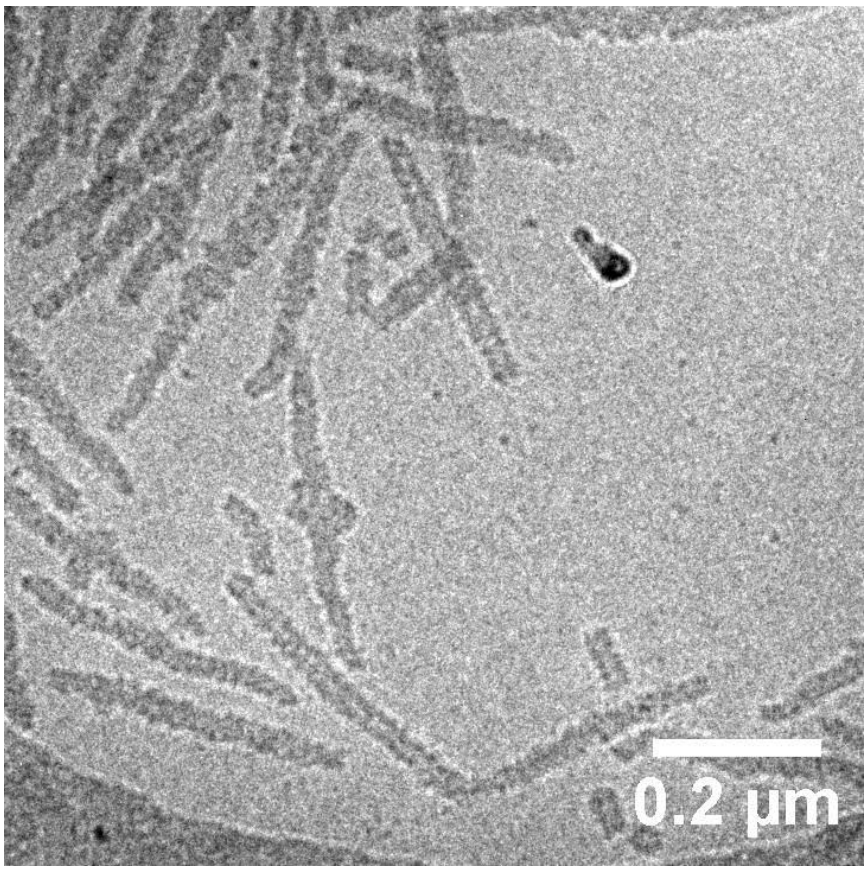

Figure 102. Cryo-TEM image of PAA_{333}-*b*-$PLLA_{37}$ cylinders one month after re-suspension.

4.2.14 Analysis of aggregates by TEM; exit wave reconstruction on GO-TEM grids[‡‡]

Thus far, analysis of polymer nanoparticles by TEM has focused on the particle macrostructure (e.g. size, shape, internal features). However, as discussed in Chapter 1, the resolution in TEM, where atomic structure is readily visible, is far greater than has been exploited for these types of materials. One problem for a lack of resolution using stained images is that the stains themselves generally have a resolution limit of

[‡‡] Adam Dyson wrote and applied all exit wave reconstruction software as well as constructed the figures for this section, including the determination of the contrast and wave transfer functions

> 2 nm.[30] For unstained images of soft materials (cryo-TEM or in the dry state) the lack of resolution is directly linked to their poor contrast. These small carbon structures can be considered weak phase objects,[38] meaning they affect the phase of the electron waves much more than the amplitude. Consequently images are typically taken under focus (as are most previous images in this thesis) to increase phase contrast making the particle more visible. The direct effect of imaging under focus however is that image resolution is sacrificed. **Figure 103** shows 3 images (**a-c**) of a **4.05** polymersome on GO taken at 3 different focus values (ca. -1 µm, -0.5 µm and on focus). Simple inspection of the images reveals that contrast decreases from **a-c**. **Figure 103b** appears to have more detail (higher resolution) than **Figure 103a**, however the contrast in **Figure 103c** is so poor that is appears to have less detail than **Figure 103**(**a** and **b**).

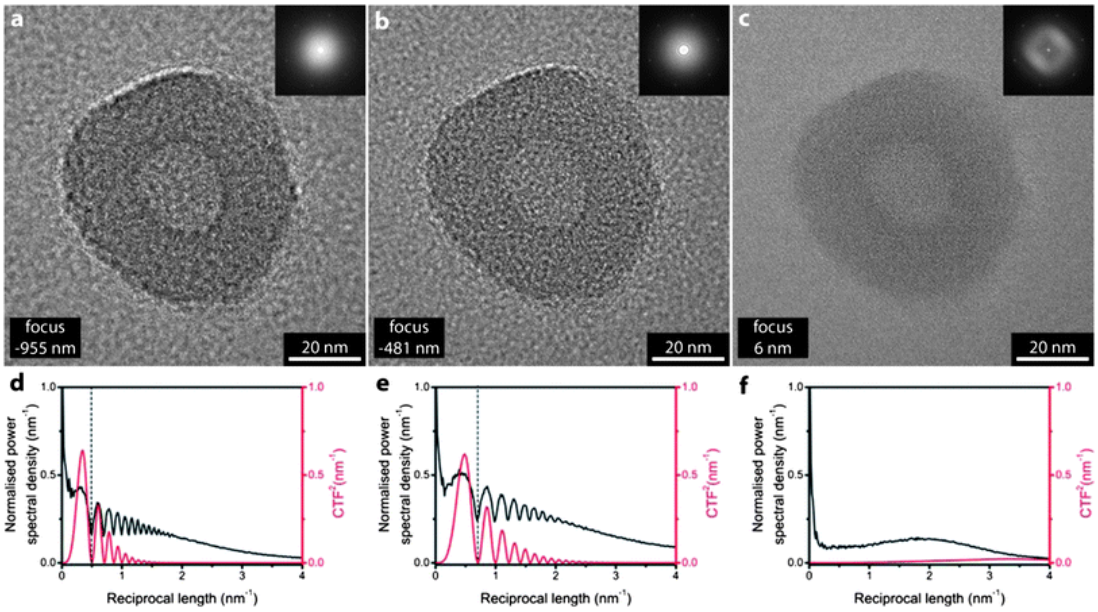

Figure 103. The effect of defocus on imaging. Bright field TEM images of a PAA-PS polymersome at (a) -955 nm focus, (b) -481 nm focus and (c) +6 nm focus. Inset are sections from their respective fast Fourier transforms. The normalised power spectral density (black) and square of the predicted contrast transfer function (red) for (a)–(c) are given in (d)–(f) respectively.[39]

This information is better represented by looking at the square of the contrast transfer function (CTF^2, **Figure 103d-f**). The CTF^2 is a function which describes how the information is transferred from the object to the image. The magnitude of the CTF^2 is related to contrast and decreases from **Figure 103d-f**. The first minimum in the CTF^2 is the point resolution of the image which occurs at higher reciprocal length (0.4, 0.7 and 4 nm^{-1}) when moving closer to focus (**d-f**). Therefore, a fundamental balance exists between contrast and resolution for a single image, and for the weak phase objects here this limits the resolution to a few nm. Exit wave reconstruction (EWR) can offer a solution to this problem. Here, a series of images are taken at different focus values (e.g. 40 images with 26 nm focal steps) and an algorithm is used to combine the images and reconstruct the phase of the wave function as it leaves the object under investigation. As the information from each image is combined, the missing information in each image (when the CFT^2 is zero) is obtained from another image where the CFT^2 has shifted (**Figure 103d-f**). **Figure 104a** shows the phase image from an exit wave reconstruction of a **4.05** polymersome. The image shows a comparable contrast to the under focus images in **Figure 103** (or the EWR amplitude image, **Figure 104b**), but much more detail can be seen in the structure. This is also evident from the square of the wave transfer function (WTF^2) where it can be seen that good contrast is obtained all the way out to 4 reciprocal nm (which indicates the image resolution is $\leq$ 0.25 nm). The wave transfer function is analogous to the CFT^2, but it is a function which describes how the information in the EWR is related to the object.

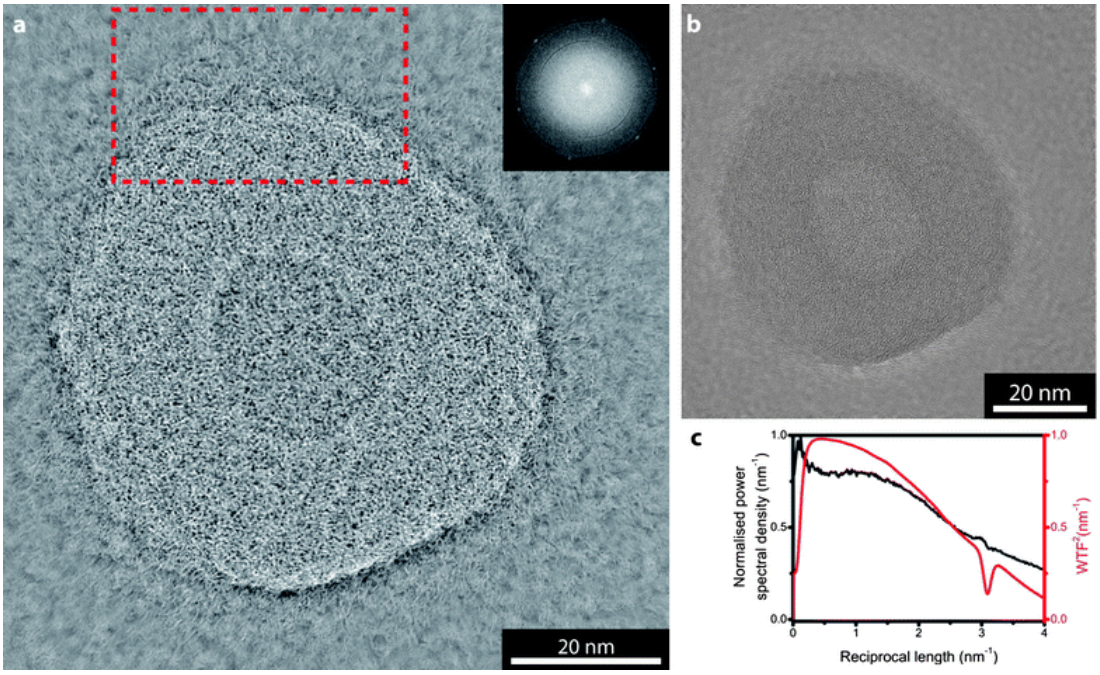

Figure 104. Exit wave reconstruction of the polymersome shown in Fig. 1. (a) phase image and (b) amplitude image. Inset in (a) is a section of its fast Fourier transform, the red dashed box indicates the region shown in **Figure 105**. In (c) the normalised power spectral density (black) for the phase image is compared with the square of the predicted wave transfer function (red).[39]

While resolution improvement is clearly beneficial, a nominal improvement in resolution may not provide greater insight into the object under investigation. **Figure 105b** shows an enlarged area of **Figure 104a**, near the edge of the polymersome where individual polymer chains can be identified. The polymersomes have three levels of structural detail: the nanostructure, the polymer chains and the monomers. EWR has not only improved the resolution significantly, but to the point where another level down in the polymersome hierarchy becomes observable (the polymer chains). Various control experiments were performed to prove that the observed structure in **Figure 104a** is not an artefact including performing EWR on non-consecutive sets of images and using commercially available EWR algorithms.[39]

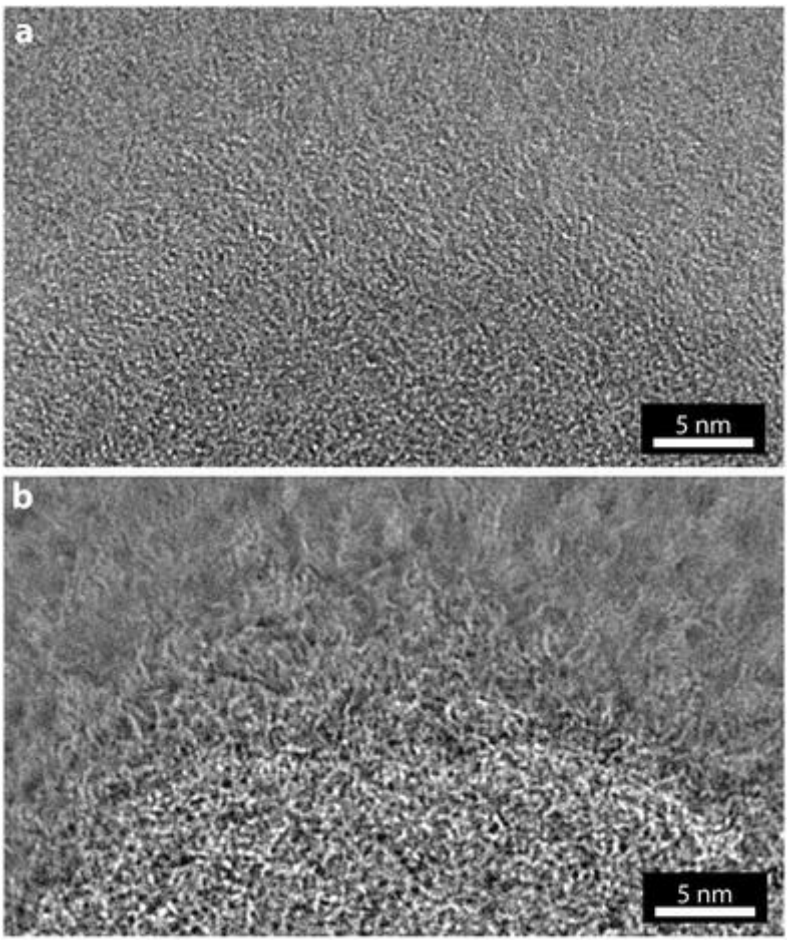

Figure 105. Comparison of conventional TEM imaging and EWR phase imaging. (a) Near focus TEM, and (b) EWR phase image, for the region of polymersome marked by the dashed box in **Figure 104**.[39]

Figure 105a shows the in focus image of the same area, showing that it is not impossible to observe this structure from a single image. To highlight the importance of using atomically thin supports EWR was performed on both a GO-TEM grid and a thin (6 nm) amorphous carbon TEM grid for the PLA-*b*-PAA cylinders. **Figure 106f** shows that EWR for PLLA-*b*-PAA cylinders on GO-TEM grids also results in the visualisation of polymer chain detail within the nanostructure, while the EWR on the thin carbon grids will bring out the detail in the amorphous background, which obscures the nanoparticle.

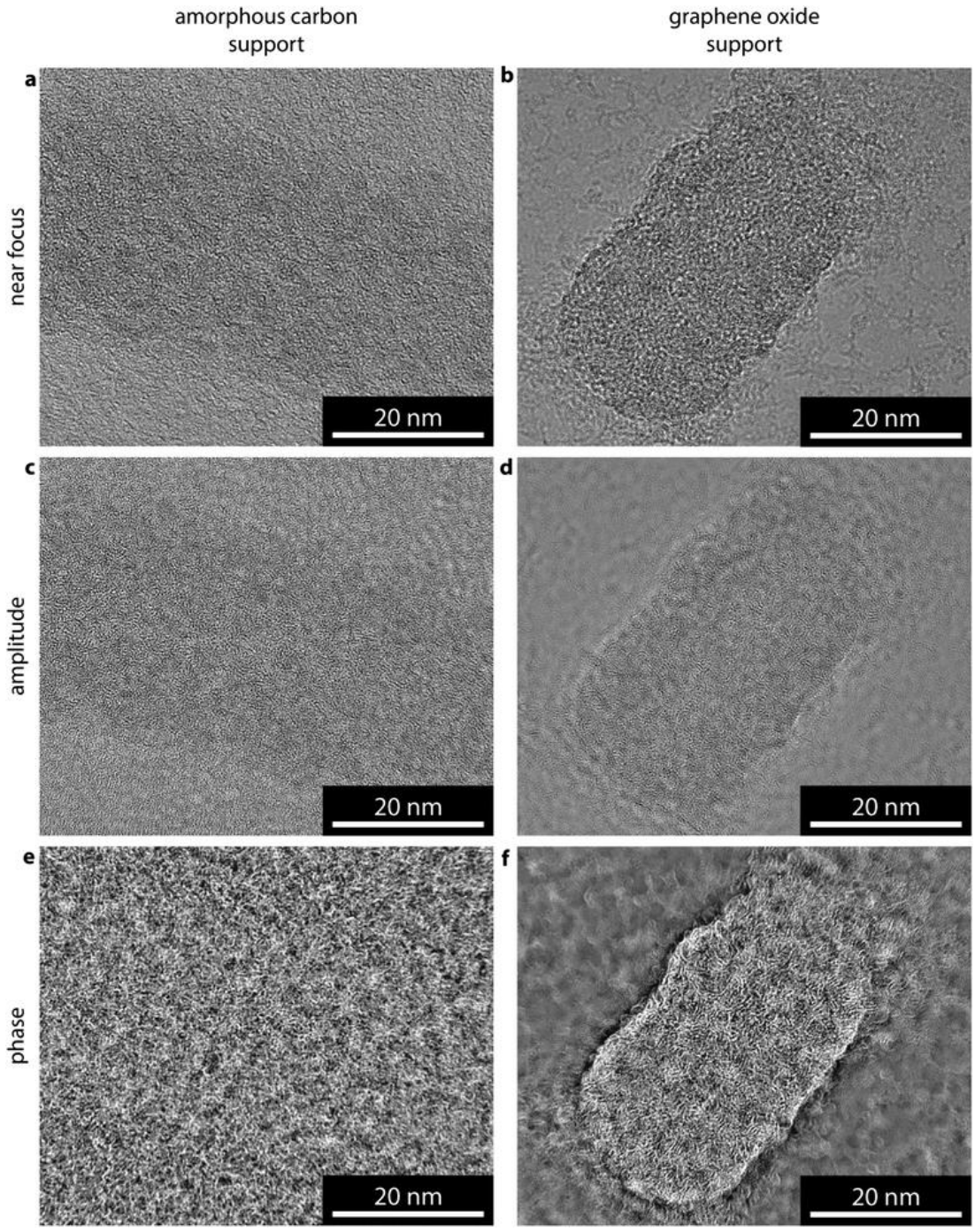

Figure 106. Comparison of EWR on amorphous carbon and graphene oxide supports. (a and d) Near focus, (b and e) EWR amplitude, and (c and f) EWR phase images of a PLA-*b*-PAA cylinder on amorphous carbon and graphene oxide supports respectively. The near focus images were taken with focus of −5 nm (a), and −30 nm (d).[39]

Figure 106f also shows that the chains at either end of the cylinder appear to pack differently from the chains at the side. As it has been reported that these cylinders grow via the crystallisation of PLA, these images can provide invaluable insight into the growth mechanism.[35, 40] Furthermore, **Figure 107a** (an enlargement of **Figure 106f)** shows an area of the cylinder where some vertically aligned parallel features can be seen, which could be related to the PLA crystalline domains. However, considering the ERW images were not taken with consideration of electron dose, it is likely that some of the polymer chain organisation had been distorted. These images highlight both the enormous potential for using EWR with self-assembled polymer systems and the need for making EWR compatible with low dose imaging. Performing EWR on just a GO substrate (with no particles) does not show these aligned parallel features, instead hexagonal like structures can be of seen which could be related to the repeating structure of the GO sheet (**Figure 107b**).

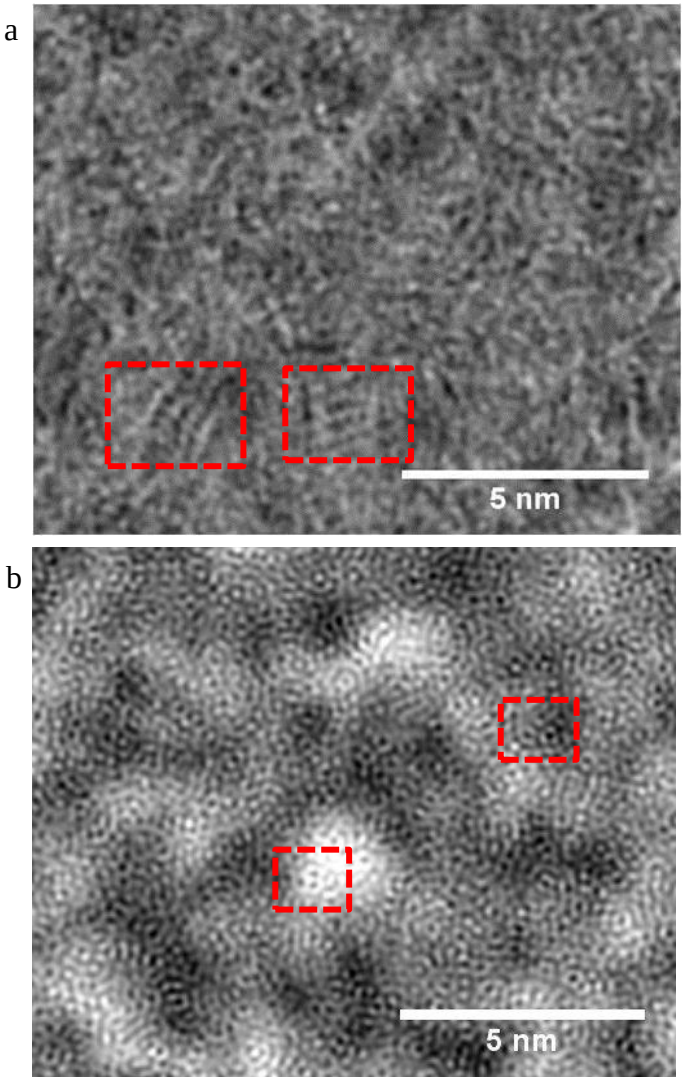

Figure 107. (a) an enlargement of **Figure 106f,** the red boxes indicate areas where parallel aligned features appear and (b) EWR of a single GO sheet, the red boxes indicated areas where hexagonal like structures can be seen.

4.3 Conclusions

Previous reports[7-10] have demonstrated the advantages of using GO as a substrate for TEM, such as the cheap, simple and robust preparation of both the GO and subsequent GO TEM grids. The good coverage of an almost electron transparent substrate gives ideal imaging conditions for low contrast specimens making analysis

far simpler than using staining methods or cryo-TEM. While GO is undoubtedly an excellent substrate for the analysis of soft materials by TEM, its compatibility with other techniques (AFM, SEM and STEM) not only open up this method to a greater number of researchers, but also allows and encourages the collection of data from multiple sources, both minimising misinterpretation and greatly improving analysis. It has been shown that GO-TEM grids can be easily prepared and that the coverage and thickness of GO can be tailored by altering GO-solution concentration and sonication times. The use of GO as a TEM substrate potentially negates the need to use stains for soft materials, reducing image artifacts and subjective interpretations, and simplifying TEM sample preparation. Although distortions due to drying will still be present, by combining TEM data with height information from AFM, these drying effects can be measured and better understood. GO has now become the standard substrate for dry state microscopy analysis in the O'Reilly group[40-46] and has been used by other groups to aid their analysis.[47-51] Specifically, the ability to image in the dry state without staining led to the discovery of a simple method for creating hollow particles in solution by exploiting a spontaneous drying induced reorganisation for PLA-*b*-PAA aggregates, where the multi-technique imaging capabilities of GO-TEM grids were vital for their characterisation in the dry state. With only one GO TEM-grid needed for analysis by TEM, SEM, and AFM, it is possible to analyse a sample quickly and consistently. It should be stressed that GO supports do not replace the need for complementary techniques that allow the native structures in solution to be assessed, such as cryo-TEM and scattering techniques (e.g. light scattering, X-ray and neutron diffraction) but they do offer a readily accessible alternative for routine analysis. In conclusion, the use of GO as a support

material for the characterisation of BCP assemblies allows high contrast images to be acquired without the use of stains, and opens the way for increased resolution structural determination and chemical analysis. One main issue arising from the work in this chapter is that non-rigid assemblies (e.g. polymer **2.10**), will collapse upon dehydration and therefore cannot be imaged in the dry state. Chapter 5 will address this issue.

4.4 Experimental

4.4.1 Materials

All chemicals were used as received from Aldrich, Fluka, or Acros unless otherwise stated. *t*-butyl acrylate and styrene monomers were distilled over CaH_2 prior to use and stored at 5°C. Azobisisobutyronitrile (AIBN) was recrystallized twice from methanol and stored in the dark at 5 °C. DDMAT [S-dodecyl-S'-(α',α'-dimethyl-α''-acetic acid)],[52] polylactide$_{40}$-*b*-polyacrylic acid$_{286}$ cylinders (**5**)[35] and solutions of graphene oxide[7] were synthesized as previously reported.[§§] Copper TEM grids were purchased from Agar, stained images were obtained on 300 mesh formvar/carbon grids, GO imaging was performed either on 400 mesh lacy carbon films or Quantifoil holey carbon grids with 200 mesh deposited with GO films and cryo-TEM images were on Quantifoil holey carbon grids with 200 mesh.

[§§] PLA-*b*-PAA materials were provided by Nikos Petzetakis

4.4.2 Instrumentation

^{1}H NMR spectra were recorded on a Bruker DPX-400 spectrometer in $CDCl_3$. Chemical shifts are given in ppm downfield from TMS. Size exclusion chromatography (SEC) measurements were conducted on a system comprised of a Varian 390-LC-Multi detector suite fitted with differential refractive index (DRI), light scattering (LS), and ultra-violet (UV) detectors equipped with a guard column (Varian Polymer Laboratories PLGel 5 µM, 50 × 7.5 mm) and two mixed D columns (Varian Polymer Laboratories PLGel 5 µM, 300 × 7.5 mm). The mobile phase was tetrahydrofuran with 5% triethylamine eluent at a flow rate of 1.0 mL min^{-1}, and samples were calibrated against Varian Polymer laboratories Easi-Vials linear poly(styrene) standards (162 - 2.4 × 10^5 $g.mol^{-1}$) using Cirrus v3.3 software. Infrared spectroscopy was recorded on a Perkin-Elmer, Spectrum 100 FT-IR spectrometer.

Cryogenic transmission electron microscopy (cryo-TEM) grids were imaged at 120 keV using a Tecnai G2 12 Twin TEM equipped with a Gatan CCD camera. The temperature of the cryo stage was maintained below -170 °C during imaging. GO and stained TEM images were recorded on either a JEOL 2000FX TEM or a JEOL 2100 equipped with Gatan Orius digital camera, both were operated at 200kV. Unless otherwise stated, images were acquired under conventional bright-field conditions. Tomography was carried out on a JEOL 2010F with a Gatan Ultrascan 4000 camera at 200 kV tilting from -42° to +42° in 2° increments. Images were acquired using Mr.T[53] software and reconstructed with a Simultaneous Iterative Reconstructive Technique (SIRT) algorithm, 30 iterations with a relaxation coefficient of 1. ImageJ[54] and TomoJ[55] were used for processing, and the surface

rendering after a manual segmentation process was undertaken using Amira software.

AFM images were taken in tapping mode on a Multimode AFM with Nanoscope IIIA controller with Quadrex, or an Asylum Research MFP3D-SA. Silicon AFM tips were used with nominal spring constant and resonance frequency of 3.5 Nm^{-1} and 75 kHz (MikroMasch NSC18).

A Zeiss Supra55VP was used to acquire the SEM images, operated at an accelerating voltage of 20 kV.

4.4.3 Methods

Synthesis of Graphene Oxide

H_2SO_4 (conc, 170 mL) was added to graphite (5 g) in a 250 mL round bottom flask on ice and stirred for 10 min. $KMnO_4$ (22.5 g) was added over 1 hour and the mixture was stirred for 2 hours on ice. The solution was allowed to warm to room temperature and stirred overnight. The viscous brown liquid was added to H_2SO_4 (5 wt%, 500 mL) with continuous stirring for 2 hours. An aqueous solution of H_20_2 (30 wt%, 15 g) was added and stirred for 2 hours. The viscous brown liquid was centrifuged and the supernatant discarded. An aqueous solution (500 mL) of H_2SO_4 (3 wt%) and H_2O_2 (0.5 wt%) was added to the precipitate and stirred for 1 min. The centrifugation and washing step was then repeated 5 times with the H_2SO_4 (3 wt%) and H_2O_2 (0.5 wt%) solution and 5 times with DI water. After a final centrifuge small portions of GO was stirred in water and freeze dried to obtain brown GO flakes. IR (ν_{max}/cm^{-1}): 3800-2400 (br), 1750, 1633, 1065.

Preparation of GO solutions

GO flakes were stirred in a nanopure water over night, sonicated for 30 seconds and left to stand. Any sediment was discarded after one day.

Preparation of GO-TEM grids

Quantifoil R2/2 TEM grids were plasma cleaned using an EMITECH K950X for 3 minutes at 20 mAmp and 0.8 mbar. The grids were immediately transferred to a piece of filter paper and one drop (from a 200 µL pipette) of GO solution was dropped from a height of 1 cm onto the TEM grids (allowing the filter paper to wick away most of the solution). The grids were left to dry in air for at least 30 minutes before use.

Application of Samples to GO-TEM grids

Samples were applied to GO-TEM grids by three methods:

Method 1: Apply a small volume (typically 4 µL) of sample to a GO-TEM grid held with a pair of tweezers (**Figure 78**), leave for a set time period (typically 2 min) to allow the structures to adsorb to the GO, wick the water away with a piece of filter paper.

Method 2: Apply a small volume (typically 4 µL) of sample to a GO-TEM grid held with a pair of tweezers (**Figure 78**) and leave until the water has completely evaporated.

Method 3: Apply a small volume (typically 4 µL) of sample to a GO-TEM grid held with a pair of tweezers (**Figure 78**),), leave for a set time period (typically 2 min) to

allow the structures to adsorb to the GO, submerge the grid in liquid nitrogen in order to freeze the sample, place the grid under vaccum in order to sublime water from the grid.

Application and Staining of Samples to Carbon Formvar TEM-grids

Carbon formvar TEM grids were plasma cleaned using an EMITECH K950X for 3 minutes at 20 mAmp and 0.8 mbar. A small volume (typically 4 µL) of sample was added to the TEM grid held with a pair of tweezers. The samples were left for a set time period (typically 2 min) to allow the structures to adsorb to the surface before the water was wicked away with a piece of filter paper. A small volume (typically 4 µL) of stain was then added to the grid and left for 2 minutes before being wicked away with a piece of filter paper. The grids were then left to dry in air for 30 minutes.

Preparation of Cryo-TEM samples

Samples were prepared at 25 °C using a FEI 110 Vitrobot to maintain a constant humidity environment. A droplet of 2-10 µL of sample solution was added to a holey carbon-coated copper grid, and the grid was blotted to remove excess solution. The grid was subsequently plunged into liquid ethane to vitrify the sample.

Synthesis of P^{t}BuA$_{11}$ (4.01)

DDMAT (0.14 g, 3.9 mmol), P^{t}BuA (1.0 g, 7.8 mmol), AIBN (6.4 mg, 0.39 mmol) and dioxane (1.14 mL) were added to a clean dry ampoule under N_2 and stirred until homogeneous. The solution was degassed *via* 3 freeze-pump-thaw cycles and placed under N_2. The solution was heated to 65 °C for 45 min and then quenched in liquid

N_2. The viscous solution was dissolved in the minimum amount of THF, and the polymer was precipitated into a mixture (by volume) of 7:1 cold MeOH:H_2O. The MeOH:H_2O solution was decanted, and the polymer was dissolved in THF and then dried over $MgSO_4$. The solution was filtered and the solvent removed *in vacuo* affording polymer **4.01**. M_n (^{1}H NMR) = 1.8 kDa, M_n (SEC) = 1.7 kDa, M_w/M_n (SEC) = 1.09. ^{1}H NMR ($CDCl_3$): δ (ppm) 3.33 (t, J = 7.4 Hz, 2H, SCSC*H*$_2$), 1.20-1.50 (br, $C(CH_3)_3$ polymer backbone), 1.30-2.30 (br, CH and CH_2 polymer backbone) 0.88 (t, J = 6.8 Hz, 3H, $(CH_2)_{11}CH_3$). IR (ν_{max}/cm^{-1}): 3095, 3090, 3027, 2929, 2858, 1955, 1872, 1803, 1733, 1601, 1593, 1493, 1451, 1370, 1181, 1154, 1069, 1028, 964, 906, 759, 698.

Chain extension of (4.01) with styrene to give P*t*BuA$_{11}$-*b*-PS$_{250}$ (4.03)

4.01 (0.027 g, 15 μmol) and styrene (0.70 ml, 6.1 mmol) were added to a clean dry ampoule under N_2 and stirred until homogeneous. The yellow solution was degassed *via* 4 freeze-pump-thaw-cycles and placed under N_2. The solution was then heated to 110 °C for 22 h and quenched with rapid cooling into liquid N_2. The viscous solution was dissolved in the minimum amount of THF, and the polymer was precipitated three times into cold MeOH. The polymer was filtered and dried *in vacuo*. M_n (^{1}H NMR) = 27.8 kDa, M_n (SEC) = 25.9 kDa, M_w/M_n (SEC) = 1.08. ^{1}H NMR ($CDCl_3$): δ (ppm) 6.25-7.25 (br, Ar-H polymer backbone), 3.33 (br, 2H, SCSC*H*$_2$), 1.20-1.50 (br, $C(CH_3)_3$ polymer backbone), 1.30-2.30 (br, CH and CH_2 polymer backbone) 0.88 (br, 3H, $(CH_2)_{11}CH_3$). IR (ν_{max}/cm^{-1}): 3095, 3090, 3027, 2929, 2858, 1955, 1872, 1803, 1733, 1601, 1593, 1493, 1451, 1370, 1181, 1154, 1069, 1028, 964, 906, 759, 698.

Conversion of P*t*BuA$_{11}$-*b*-PS$_{250}$ (4.03) to PAA$_{11}$-*b*-PS$_{250}$ (4.05)

4.03 (58.4 mg) was added to a small vial and dissolved in dichloromethane (3 mL). The solution was stirred at 0 °C for *ca.* 30 min and trifluoroacetic acid (1.0 mL) was added dropwise over *ca.* 10 min. The solution was stirred and allowed to warm to room temperature overnight. All volatiles were blown off with N_2. The remaining solid was dissolved in the minimum amount of THF, and the polymer was precipitated twice into cold MeOH. The polymer was filtered and dried *in vacuo*. ^{1}H NMR ($CDCl_3$): δ (ppm) 6.25-7.25 (br, Ar-H polymer backbone), 3.33 (br, 2H, SCSC*H*$_2$), 1.20-1.50 (br, C(CH_3)$_3$ polymer backbone), 1.30-2.30 (br, CH and CH_2 polymer backbone) 0.88 (br, 3H, (CH_2)$_{11}$C*H*$_3$). IR (ν_{max}/cm^{-1}): 3095, 3090, 3027, 2929, 2859, 1955, 1872, 1803, 1713 (br), 1601, 1593, 1493, 1451, 1370, 1181, 1154 (weak), 1069, 1028, 964, 906, 759, 698.

Conversion of P*t*BuA$_{100}$-*b*-PS$_{46}$ (4.04) to PAA$_{100}$-*b*-PS$_{46}$ (4.06)

4.04 (30 mg) was added to a small vial and dissolved in dichloromethane (3 mL). The solution was stirred at 0 °C for *ca.* 30 min and trifluoroacetic acid (2 mL) was added dropwise over *ca.* 10 min. The solution was stirred and allowed to warm to room temperature overnight. All volatiles were blown off with N_2. The remaining solid was dissolved in H_2O and dialysed against 2 L of DI water (with 7 changes) before being freeze dried. IR (ν_{max}/cm^{-1}): 3033, 2977, 2942, 2862, 1718, 1497, 1456, 1372, 1251, 1184, 1031, 811, 796, 699.

Self-Assembly of (4.05)

4.05 (8.0 mg) was added to a vial and dissolved in DMF (4.0 mL). The solution was stirred for *ca.* 30 min before the dropwise addition of nanopure water (4.0 mL) over *ca.* 60 min using a peristaltic pump. Then, the solution was dialyzed (using 3.5 kDa MWCO tubing) against 2 L of nanopure water with 3 water changes. The final polymer concentration in solution was 0.65 mg mL^{-1}.

Synthesis and Self-Assembly of PAA_{100}-*b*-PS_{46} (4.06)

4.06 was synthesized by an analogous method to **4.05** by varying the equivalents of *t*BuA and styrene. For self-assembly, **4.06** (4.0 mg) was added to a vial and dissolved in DMF (4.0 mL). The solution was stirred for *ca.* 2 h before the dropwise addition of nanopure water (4.0 mL) over *ca.* 60 min using a peristaltic pump. Then the solution was dialyzed (using 3.5 kDa MWCO tubing) against 2 L of nanopure water with 3 water changes. The final polymer concentration in solution was 0.3 mg mL^{-1}.

Production of hollow cylinders for cryo-TEM

Solutions of micellar assemblies (1 mL, 0.25 mg) were added to a 1.5 mL Eppendorf tube. The tube was placed in a desiccator (P_2O_5), at reduced pressure (10 mbar) for 16 h. Addition of a known quantity of nanopure water produced solutions of hollow nanoparticles at 5 mg mL^{-1}.

Recording of Focal Series for EWR

Focal series of 20 to 40 images were recorded via a custom EWR plugin for Digital Micrograph[***] with focal increments of approximately 20 to 30 nm between images. The aberration corrected JEOL JEM-ARM200F was operated at 80 kV with spherical aberration (Cs) tuned to approximately +1 mm and images were recorded on a Gatan SC-1000 Orius CCD camera. The JEOL JEM-2100 LaB6 was operated at 200 kV (estimated Cs ¼ 1 mm) and images were recorded on a Gatan SC-600 Orius CCD camera. For the EWR in **Figure 104** a focal series of 40 images with 26 nm focal steps were recorded. For the EWRs in **Figure 105** a focal series of 20 images with 26 nm focal steps were recorded

References

1. E. S. Read and S. P. Armes, *Chem. Commun.*, 2007, 3021-3035.
2. R. K. O'Reilly, C. J. Hawker and K. L. Wooley, *Chem. Soc. Rev.*, 2006, **35**, 1068-1083.
3. A. Blanazs, S. P. Armes and A. J. Ryan, *Macromol. Rapid Commun.*, 2009, **30**, 267-277.
4. K. T. Kim, S. A. Meeuwissen, R. J. M. Nolte and J. C. M. v. Hest, *Nanoscale*, 2010, **2**, 844-858.
5. G. L. M. Lazzari, S. Lecommandoux, *Block Copolymers in Nanoscience*, Wiley-VCH, 2006.

[***] Written by Adam Dyson

6. Y. Talmon, *J. Colloid Interface Sci.*, 1983, **93**, 366-382.

7. N. R. Wilson, P. A. Pandey, R. Beanland, R. J. Young, I. A. Kinloch, L. Gong, Z. Liu, K. Suenaga, J. P. Rourke, S. J. York and J. Sloan, *ACS Nano*, 2009, **3**, 2547-2556.

8. J. Sloan, Z. Liu, K. Suenaga, N. R. Wilson, P. A. Pandey, L. M. Perkins, J. P. Rourke and I. J. Shannon, *Nano Lett.*, 2010, **10**, 4600-4606.

9. R. S. Pantelic, J. C. Meyer, U. Kaiser, W. Baumeister and J. M. Plitzko, *J. Struct. Biol.*, 2010, **170**, 152-156.

10. N. R. Wilson, P. A. Pandey, R. Beanland, J. P. Rourke, U. Lupo, G. Rowlands and R. A. Roemer, *New. J. Phys.*, 2010, **12**, 125010.

11. W. S. Hummers and R. E. Offeman, *J. Am. Chem. Soc.*, 1958, **80**, 1339-1339.

12. J. P. Rourke, P. A. Pandey, J. J. Moore, M. Bates, I. A. Kinloch, R. J. Young and N. R. Wilson, *Angew. Chem. Int. Ed.*, 2011, **50**, 3173-3177.

13. J. Rafiee, M. A. Rafiee, Z.-Z. Yu and N. Koratkar, *Adv. Mater.*, 2010, **22**, 2151-2154.

14. E. G. Kelley, T. P. Smart, A. J. Jackson, M. O. Sullivan and T. H. Epps, *Soft Matter*, 2011, **7**, 7094-7102.

15. N. S. Cameron, M. K. Corbierre and A. Eisenberg, *Can. J. Chem*, 1999, **77**, 1311-1326.

16. L. F. Zhang and A. Eisenberg, *Science*, 1995, **268**, 1728-1731.

17. L. Zhang and A. Eisenberg, *Macromolecules*, 1996, **29**, 8805-8815.

18. L. F. Zhang and A. Eisenberg, *J. Am. Chem. Soc.*, 1996, **118**, 3168-3181.

19. L. Zhang and A. Eisenberg, *Macromolecules*, 1999, **32**, 2239-2249.

20. Q. G. Ma and K. L. Wooley, *J. Polym. Sci., Part A: Polym. Chem.*, 2000, **38**, 4805-4820.

21. A. O. Moughton and R. K. O'Reilly, *J. Am. Chem. Soc.*, 2008, **130**, 8714-8725.

22. A. Kawasaki, J. Furukawa, T. Tsuruta, G. Wasai and T. Makimoto, *Die Makromolekulare Chemie*, 1961, **49**, 76-111.

23. D. M. Vriezema, P. M. L. Garcia, O. N. Sancho, N. S. Hatzakis, S. M. Kuiper, R. J. M. Nolte, A. E. Rowan and J. C. M. van Hest, *Angew. Chem. Int. Ed.*, 2007, **46**, 7378-7382.

24. K. T. Kim, J. J. L. M. Cornelissen, R. J. M. Nolte and J. C. M. v. Hest, *Adv. Mater.*, 2009, **21**, 2787-2791.

25. Stijn F. M. van Dongen, M. Nallani, Jeroen J. L. M. Cornelissen, Roeland J. M. Nolte and Jan C. M. van Hest, *Chem. Eur. J*, 2009, **15**, 1107-1114.

26. P. J. Photos, L. Bacakova, B. Discher, F. S. Bates and D. E. Discher, *J. Control. Release*, 2003, **90**, 323-334.

27. J. P. Jain and N. Kumar, *Biomacromolecules*, 2010, **11**, 1027-1035.

28. J. Z. Du and R. K. O'Reilly, *Soft Matter*, 2009, **5**, 3544-3561.

29. O. Onaca, R. Enea, D. W. Hughes and W. Meier, *Macromol. Biosci.*, 2009, **9**, 129-139.

30. H. Friedrich, P. M. Frederik, G. de With and N. A. J. M. Sommerdijk, *Angew. Chem. Int. Ed.*, 2010, **49**, 7850-7858.

31. O. Terreau, C. Bartels and A. Eisenberg, *Langmuir*, 2003, **20**, 637-645.

32. A. O. Moughton, K. Stubenrauch and R. K. O'Reilly, *Soft Matter*, 2009, **5**, 2361-2370.

33. F. Nudelman, G. de With and N. A. J. M. Sommerdijk, *Soft Matter*, 2011, **7**, 17-24.

34. P. M. Frederik and N. Sommerdijk, *Curr. Opin. Colloid Interface Sci.*, 2005, **10**, 245-249.

35. N. Petzetakis, A. P. Dove and R. K. O'Reilly, *Chem. Sci.*, 2011, **2**, 955-960.

36. N. Petzetakis, M. P. Robin, J. P. Patterson, E. G. Kelley, P. Cotanda, P. H. H. Bomans, N. A. J. M. Sommerdijk, A. P. Dove, T. H. Epps and R. K. O'Reilly, *ACS Nano*, 2013.

37. J. Hong and H. Park, *Colloids Surf. A*, 2011, **381**, 7-12.

38. R. H. Wade, *Ultramicroscopy*, 1992, **46**, 145-156.

39. M. A. Dyson, A. M. Sanchez, J. P. Patterson, R. K. O'Reilly, J. Sloan and N. R. Wilson, *Soft Matter*, 2013, **9**, 3741

40. N. Petzetakis, D. Walker, A. P. Dove and R. K. O'Reilly, *Soft Matter*, 2012, **8**, 7408-7414.

41. A. Lu, P. Cotanda, J. P. Patterson, D. A. Longbottom and R. K. O'Reilly, *Chem. Commun.*, 2012, **48**, 9699-9701.

42. P. E. Williams, A. O. Moughton, J. P. Patterson, S. Khodabakhsh and R. K. O'Reilly, *Polym. Chem.*, 2011, **2**, 720-729.

43. R. McHale, J. P. Patterson, P. B. Zetterlund and R. K. O'Reilly, *Nature Chem*, 2012, **4**, 491-497.

44. P. Cotanda, A. Lu, J. P. Patterson, N. Petzetakis and R. K. O'Reilly, *Macromolecules*, 2012, **45**, 2377-2384.

45. R. J. Williams, R. K. O'Reilly and A. P. Dove, *Polym. Chem.*, 2012, **3**, 2156-2164.

46. C. F. Hansell and R. K. O'Reilly, *ACS Macro Letters*, 2012, **1**, 896-901.

47. T. O. McDonald, P. Martin, J. P. Patterson, D. Smith, M. Giardiello, M. Marcello, V. See, R. K. O'Reilly, A. Owen and S. Rannard, *Adv. Funct. Mater.*, 2012, **22**, 2469-2478.

48. B. L. Wilkinson, S. Day, R. Chapman, S. Perrier, V. Apostolopoulos and R. J. Payne, *Chem. Eur. J.*, 2012, **18**, 16540-16548.

49. M. Giardiello, T. O. McDonald, P. Martin, A. Owen and S. P. Rannard, *J. Mater. Chem.*, 2012, **22**, 24744-24752.

50. B. W. Greenland, M. B. Bird, S. Burattini, R. Cramer, R. K. O'Reilly, J. P. Patterson, W. Hayes, C. J. Cardin and H. M. Colquhoun, *Chem. Commun.*, 2013, **49**, 454-456.

51. K. L. Morris, L. Chen, J. Raeburn, O. R. Sellick, P. Cotanda, A. Paul, P. C. Griffiths, S. M. King, R. K. O'Reilly, L. C. Serpell and D. J. Adams, *Nature Commun*, 2013, **4**, 1480.

52. J. Skey and R. K. O'Reilly, *Chem. Commun.*, 2008, 4183-4185.

53. J. T. Chang, M. Marsh, F. Rixon and W. Chiu, *Microsc. Microanal.*, 2005, **11**, 308-309.

54. M. D. Abramoff, Magelhaes, P.J., Ram, S.J., *Biophotonics Int.*, 1997-2011, **11**, 36-42.

55. C. Messaoudil, T. Boudier, C. O. S. Sorzano and S. Marco, *Bmc Bioinformatics*, 2007, **8**, 288.

Chapter 5. Graphene oxide supported cryo-TEM: pushing the size limitations for imaging hydrated samples

5.1. Abstract

Cryo-TEM is one of the most powerful imaging techniques tools for the analysis of polymer aggregates in solution as particles can be imaged while hydrated, within a film of vitreous ice. However, this ice film thickness is limited by its mechanical stability and consequently there is a size limitation for observing particles. Such that particles that are much smaller than this thickness cannot be readily observed due to poor contrast within the ice film. Here it is shown that the use of GO as a physical support for the particles allows for reduced ice thickness resulting in the observation of smaller and more weakly scattering species at higher resolution.

5.2 Introduction

Cryo-TEM has become one of the most popular imaging methods for nanomaterials in solution due to its high spatial resolution, inference of internal structure (through cryo-electron tomography) and most importantly, the ability to image particles within a thin film of the vitrified solvent.[1-5] To this end cryo-TEM has proven invaluable for the study of DNA, proteins, viruses and synthetic soft nanomaterials.[6-9] A key limitation for imaging these soft structures is that relatively weak scattering elements (C, N, O, H) from which they are formed, can result in poor contrast against the vitrified solvent.[10] This becomes particularly important for smaller particles and to compensate for this, images are taken at large defocus values which reduces image resolution.[11] Thinner ice layers will scatter less and give better contrast for particles, however for cryo-TEM the thinnest obtainable ice layer is

determined by its mechanical and beam stability.[12] Consequently, there must be a size limitation for carbon based structures, where particles below this size are not observable due to the comparatively thick ice layer. **Figure 108** shows a cryo-TEM image of single chain nanoparticles reported by Meijer and co-workers.[13] Their small size, 3-5 nm, creates poor contrast and the images have probably been recorded at large defocus values to compensate. This results in the particles appearing as black dots, and the vitreous ice appearing textured. Typically, due to their small size, these types of nanoparticles are imaged by AFM,[14, 15] which has excellent height resolution. However as detailed in Chapter 1, AFM has extremely poor resolution in the x direction and cannot be used to infer internal structure.

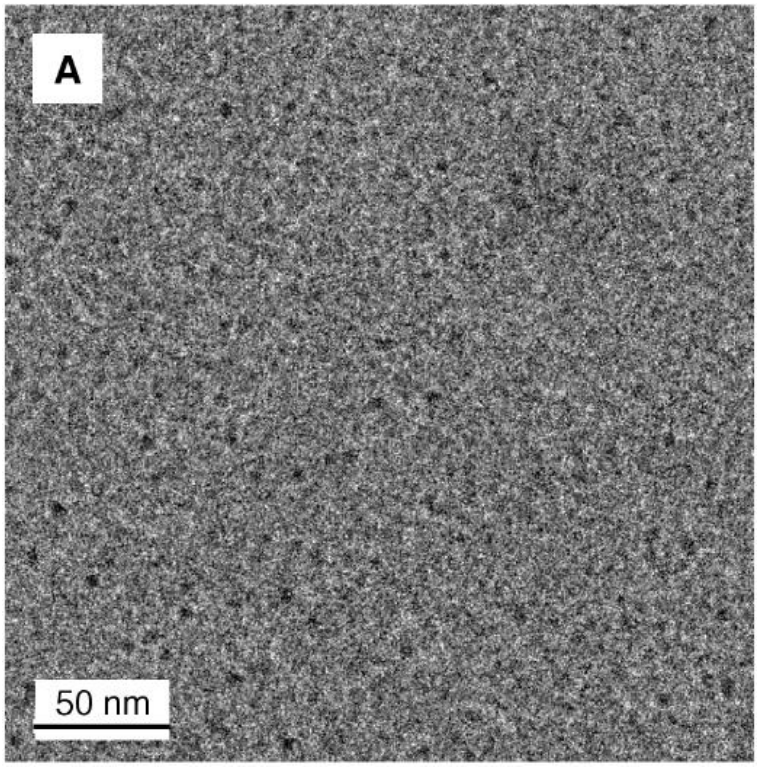

Figure 108. Cryo-TEM images of single chain nanoparticles formed from copolymers of a benzene-1,3,5-tricarboxamide-bearing methacrylate (BTAMA) and poly(ethylene glycol) methyl ether methacrylate (PEGMA). [13]

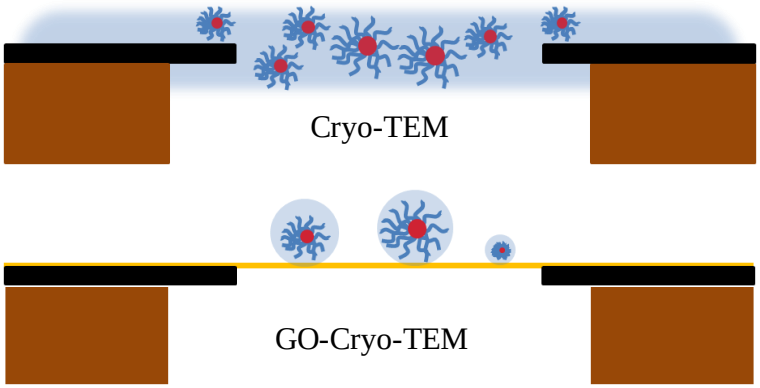

Figure 109. Schematic of a cryo-TEM and a GO-cryo-TEM grid.

In this chapter, GO-TEM grids are used to show that having a stable, electron transparent support allows for the removal of virtually all the water from the sample prior to vitrification and cryo-TEM imaging (**Figure 109**). This allows particles to be imaged in the minimum amount of water required for hydration, thereby minimising background scattering. The results are compared to those collected by conventional cryo-TEM and it is shown that by creating these super-thin ice layers much smaller particles (< 5 nm) become readily visible and sufficient contrast can be obtained closer to focus, increasing resolution.

Pantelic and co-workers have shown that graphene and graphene oxide supports are compatible with cryo-TEM, and can provide better contrast than thin amorphous carbon films, when samples are supported by either the GO or carbon layer.[16-18] This was demonstrated by analysis of a protein complex (20S proteasome, ca. 10 nm in diameter, **Figure 110**) and the tobacco mosaic virus. However, the

results were not compared to those obtained by cryo-TEM, and neither contrast nor resolution were compared in relation to ice thickness.

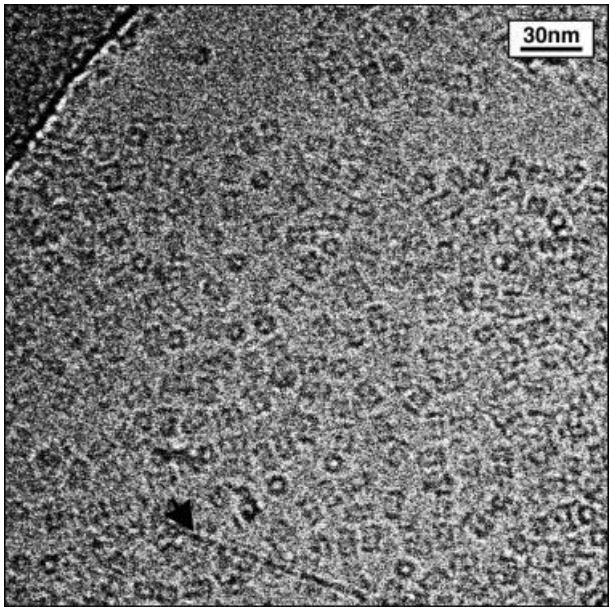

Figure 110. Cryo-TEM image of unstained 20S proteasome on graphene oxide.[18]

5.3 Results and discussion

5.3.1 Preparation of GO-Cryo-TEM grids

GO-cryo-TEM grids were prepared using a Vitrobot at 100 % humidity. The Vitrobot is a controlled environment vitrification system (CEVS) which is used for preparing cryo-TEM samples.[5] Holey carbon TEM grids, held by a pair of tweezers, are placed inside an environmentally controlled chamber where temperature and humidity can be pre-set. Typically 100 % humidity is used in order to avoid water evaporation from the sample during grid preparation, and the temperature can be adjusted depending on sample requirements. A small drop (typically 3 µL) is pipetted onto the carbon grid and an automatic blotting device is used to blot away

the majority of the solution creating thin layers of water covering the grid. The grid is subsequently plunged into liquid ethane in order to vitrify the sample, trapping the particles within thin ice layers.

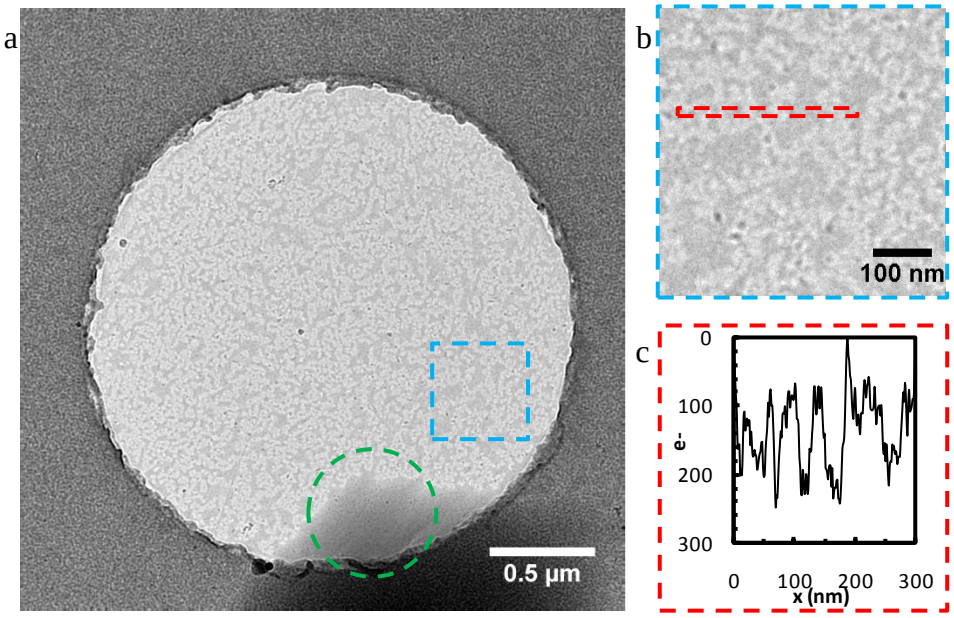

Figure 111. (a) GO-cryo-TEM image of a single sheet of GO covered by a super-thin non-continuous ice layer, (b) Enlarged area (from the area indicated by the blue square) showing the non-continuous ice layer and (c) a plot profile from the area indicated by the red box. The green circle indicates an area of thicker ice.

The pressure and timing (typically 3 seconds) of the automatic blotting device can be optimised in order to produce ice layers with differing thicknesses. Typically ice layers of 100 nm are targeted as they are thin enough to provide good contrast for most particles and thick enough to be mechanically stable and accommodate the particles under analysis.[3, 12] However there is always a distribution of ice layer thickness with some holes being empty and some holes containing ice which is too thick to obtain sufficient particle contrast. If the water layer is supported by GO it should be possible to create even thinner ice layers as GO should act as a physical

support and help with beam stability. In order to test this theory 3 µL of water was pipetted onto a GO-TEM grid and prepared for cryo-TEM using a Vitrobot. Increased blotting times (10 seconds) were used to remove as much of the water as possible from the grid. **Figure 111a** shows a layer of GO covered by a non-continuous film of ice or 'islands of ice'; probably due to dewetting of the GO when the water layer reaches a certain thickness. This is highlighted in **Figure 111b** and **c** which shows an enlarged area and a plot profile respectively indicating that these 'ice islands' can be extremely small (ca. 10 nm) in the x direction. With a suitable calibration, it should be possible to estimate the thickness of this ice by comparing the scattering to the number of electrons scattered by a single GO layer and work to determine this is ongoing.[19] However, considering the small size of these 'ice islands' in the x direction it is likely they are much thinner than those achievable by standard cryo-TEM and will subsequently be referred to as 'super-thin' ice layers.

As is highlighted by the green circle, thicker areas of continuous ice (more consistent with standard cryo-TEM ice thicknesses) are also present on the grid. The increase in contrast for this area provides further evidences that the non-continuous layer is much thinner. The distribution of ice layer thicknesses across the grid provides an ideal opportunity for directly measuring particle contrast in relation to ice thickness (discussed later) but it also presents a statistical problem when analysing samples by GO supported cryo-TEM. The best contrast will be achieved when imaging over a single sheet of GO *and* where these super-thin ice layers have formed. The current GO-TEM grid preparation allows for the coverage of, at best, ca. 30 % of the holes with single to triple layers of GO (see Chapter 4), therefore,

even if blotting conditions can be optimised to produce ca. 50 % of these holes being covered in super-thin layers, then the result is that only 15 % of the grid is useable. With the added problem that not all of *these* holes may be covered with an appropriate distribution of particles, this can make for difficult imaging conditions.

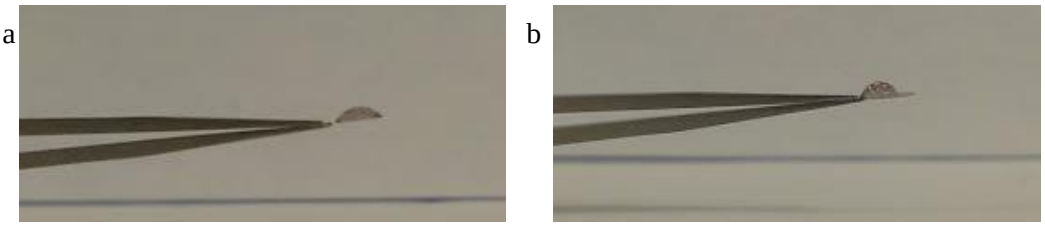

Figure 112. Photographs of a 2 µL drop of water pipetted onto GO-TEM grids prepared with 0.01 mg/mL and of GO and 5 minutes of sonication. (a) for a grid which had been prepared 30 minutes before and (b) for a grid prepared 24 hours before. The lower contact angle for the left grid clearly indicated its greater hydrophilicity.

As discussed in Chapter 4, the best contrast will be obtained for single to triple layers of GO, therefore in order to minimise the coverage of any thicker layers, it is recommended that low concentrations of GO (0.01 mg ml^{-1}) be used to prepare the GO-TEM grids. Another practical consideration when preparing GO-cryo-TEM grids is that while the GO-TEM grids are stable for many months, those with low coverage of GO will be largely hydrophobic. Typically, holey carbon TEM grids are glow discharged prior to vitrification for cryo-TEM to increase hydrophilicity and aid thin film formation. However, as glow discharging will destroy the thin layers of GO it is recommended that GO grids are prepared within 3 hours of sample application and vitrification. This method ensures the hydrophilicity imparted by glow discharging the grids prior to GO deposition is still present when applying the sample for GO-cryo-TEM preparation (**Figure 112**).

5.3.2 Imaging of $PLLA_{40}$-*b*-PAA_{298} cylinders by GO-cryo-TEM and cryo-TEM

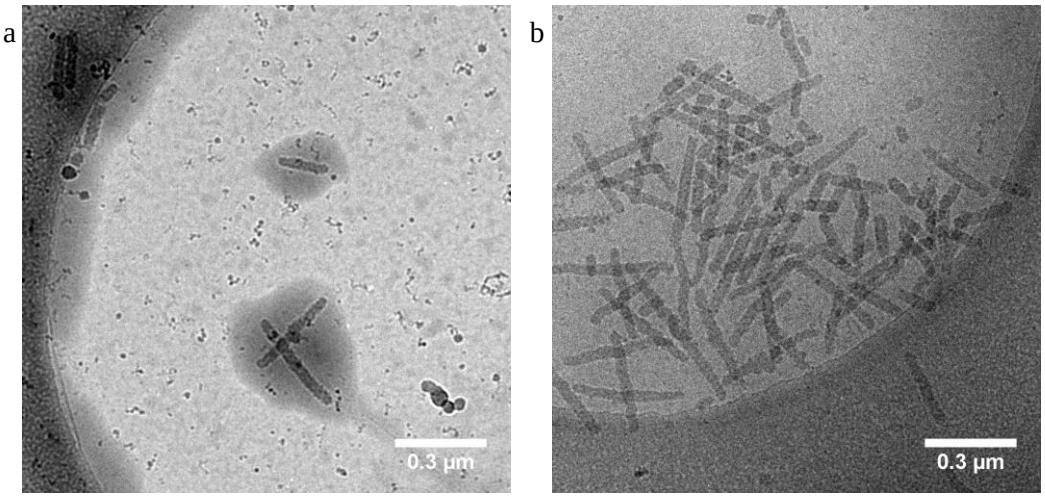

Figure 113. (a) GO-cryo-TEM and (b) cryo-TEM images of PLLA-*b*-PAA cylindrical micelles

Figure 113a shows that using GO-TEM grids in place of normal holey carbon TEM grids will allow covered GO holes to act as a support for the particles, where blotting has reduced the ice thickness to a normally unobtainable level. Providing the blotting and vitrification takes place at 100 % humidity it is impossible to completely remove water from aqueous samples, and particles will therefore remain hydrated. It can be seen in **Figure 113a**, that the PLA-*b*-PAA cylinders (discussed in Chapter 4) are still hydrated in a layer of ice but that the surrounding water layer has been almost completely removed (analogous to the schematic in **Figure 109**). This results in much better contrast than is typically achieved in cryo-TEM, as can be seen by a comparison between **Figure 113a** (GO-cryo-TEM) and **Figure 113b** (Cryo-TEM).

Note: both images were recorded under the same conditions (magnification, beam intensity and defocus). **Figure 113a** shows that the water layer surrounding the cylinders is quite large (ca. 50 nm) and it is therefore likely that this is related to the long PAA corona (DP = 298). This might provide information on the PAA corona stretching, despite the fact that PAA is not typically visible in cryo-TEM (discussed later). It can be also seen by comparing the images in **Figure 113** that there are more cylinders present on the cryo-TEM grid compared with the GO-cryo-TEM. Although particle distribution will never be consistent throughout the grid, removing more water from the grids will also result in the removal of more sample, thereby reducing particle concentration on the grid.

While the improvement in image contrast for the PLA-PAA cylinders is useful, due to their large size they are relatively easy to analyse by standard cryo-TEM in order to obtain information about their size and morphology. In order to realise the full potential of GO supported cryo-TEM smaller more weakly contrasting particles should be analysed. Small particles are particularly difficult to analyse by cryo-TEM, not only due to their weak contrast against the relatively thick ice layer but also because they cannot be seen in lower magnification images making it more difficult to locate the particles on the grid.

5.3.4 Imaging of silica nanoparticles

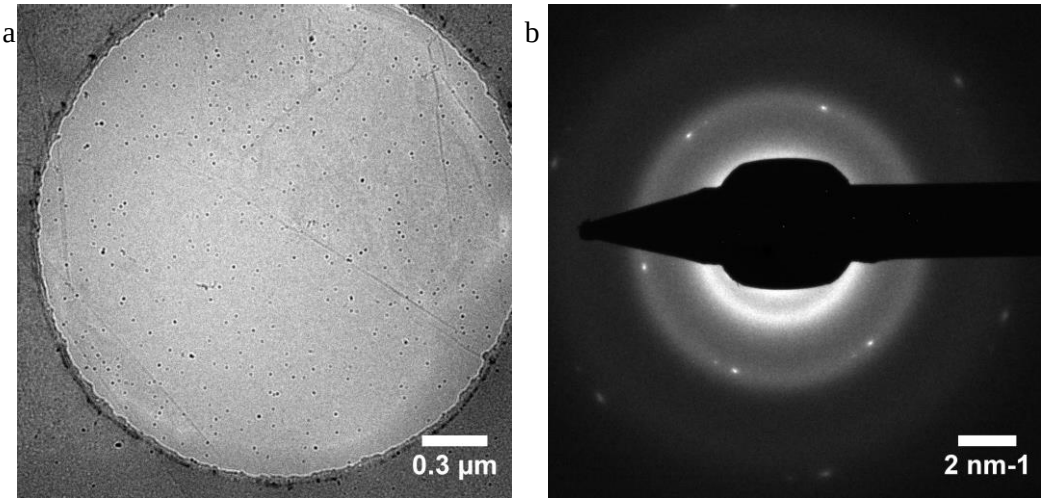

Figure 114. (a) GO-cryo-TEM image of silica nanoparticles on a predominantly single layer of GO covered by a super-thin ice layer and (b) SAED pattern showing a clear 6 fold diffraction pattern for a single layer of GO with a faint secondary 6 fold diffraction pattern indicating part of the hole is covered with a double layer.

In order to demonstrate the benefit of reduced background contrast, a solution of silica nanoparticles[†††] (diameters between 1-15 nm) were imaged; the distribution of sizes allows an easy assessment of how contrast varies with particle size and what the size limits are for imaging under these conditions. **Figure 114a** shows a GO-cryo-TEM image for a hole covered with predominantly single layered GO and super-thin ice layers. **Figure 114b** shows selected area electron diffraction (SAED) pattern proving this layer is predominantly single sheet. A close inspection of the diffraction pattern shows a faint secondary 6 fold diffraction pattern indicating part of the hole is covered with two layers. The diffuse ring present in **Figure 114b** is indicative of vitreous ice,[20] proving the particles are still hydrated and successful

[†††] Silica nanoparticles were synthesized and provided by Nico Sommerdijk and Camille Carcouet

vitrification occurred. **Figure 114a** shows that although the ice layer is non-continuous, there are many more areas of continuous ice than in **Figure 111**, where no sample was present.

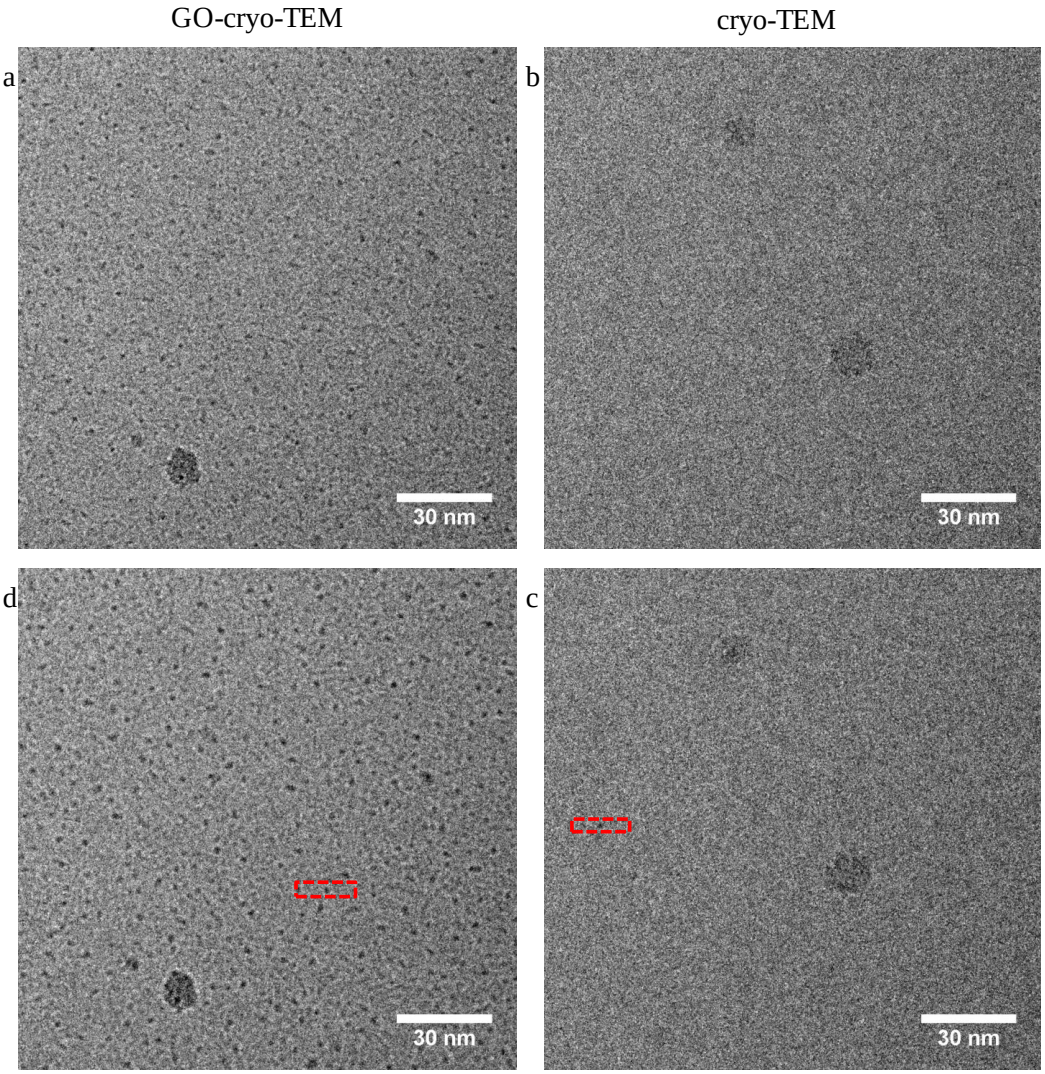

Figure 115. Images of silica nanoparticles recorded by (a) GO-Cryo-TEM at -0.5 µm, (b) Cryo-TEM at -0.5 µm (c) GO-Cryo-TEM at -1.0 µm and (d) Cryo-TEM at -1.0 µm. The red boxes indicate the areas where the plot profiles in **Figure 116** were taken.

This is probably due to the high concentration of particles on the surface which prevents de-wetting. Nevertheless as some discontinuity in the ice is present this area

should still be considered super-thin. **Figure 115** shows images of the super-thin areas created by GO-cryo-TEM (left) and standard cryo-TEM (right) at two defocus values, 0.5 µm (top) and 1.0 µm (bottom). In both cases the super-thin ice layers result in much better contrast for the particles.

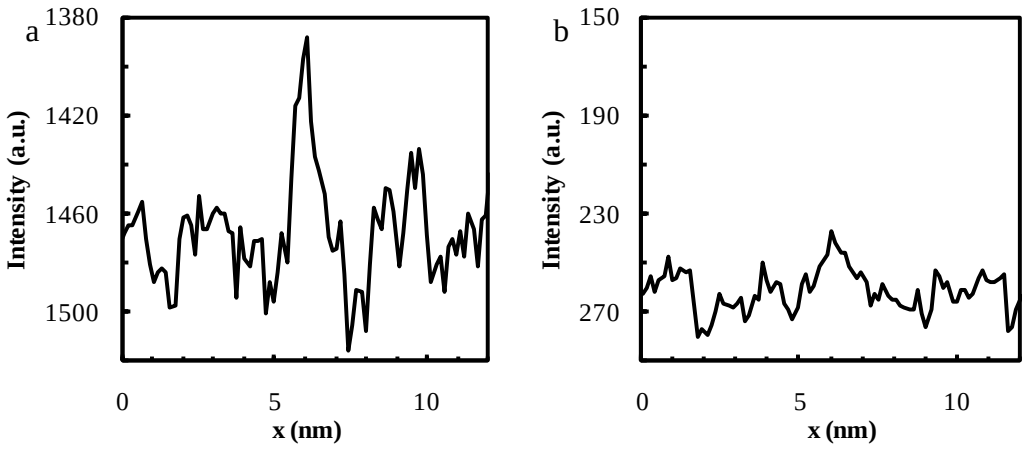

Figure 116. Plot profiles for the areas indicated by the red dashed boxes in **Figure 115** for (a) GO-cryo-TEM and (b) cryo-TEM.

For the standard cryo-TEM image the particles of ca. 10 nm in diameter are easily visible, but, while smaller particles (ca. 5 nm in diameter) are present these are much harder to distinguish. By comparison, particles of all sizes (down to ca. 1 nm in diameter) are easily visible in the GO-cryo-TEM image. This is better represented by taking plot profiles (**Figure 116**) for particles in both images (**Figure 115**, indicated by the dashed red boxes) which shows that much greater contrast is observed for particles of ca. 1.5 nm in diameter by GO-cryo-TEM (**Figure 116a**) than for particles of ca. 4 nm in diameter by cryo-TEM (**Figure 116b**).

It is likely then that particles < 4 nm are present in the cryo-TEM images (**Figure 115**, right) but that they are obscured by the relatively thick ice layers. To

test this theory, an area of the GO-cryo-TEM grid was imaged where a relatively thick (comparable to standard cryo-TEM) continuous film of water had formed over a sheet of GO. **Figure 117a** and **c** images were recorded under low dose conditions (ca. 2 $e^-/Å^2$) and **Figure 117c** is comparable to the standard cryo-TEM image in **Figure 115** (e.g. particles > 10 nm are easily visible, particles < 5 nm are not visible).

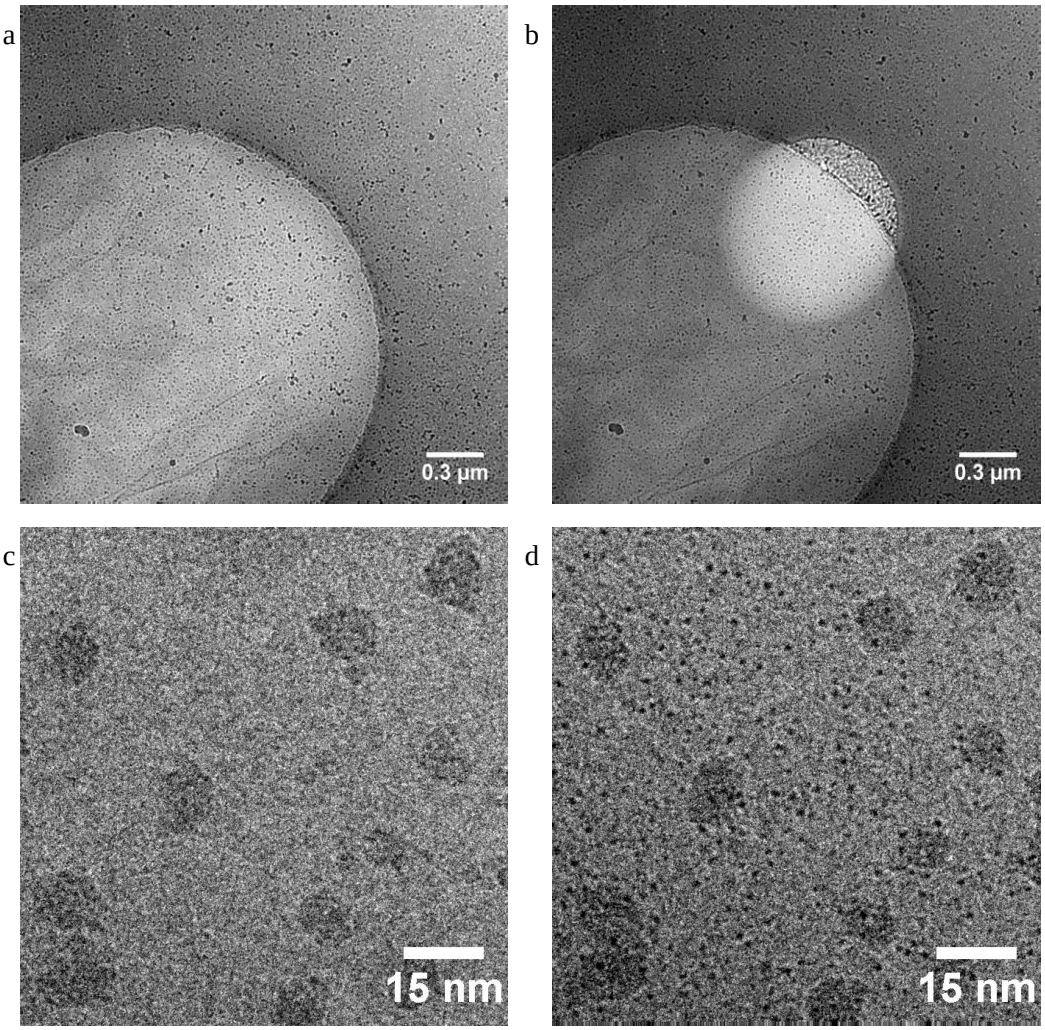

Figure 117. GO-cryo-TEM images of silica nanoparticles, (a) a low magnification image showing the thick ice layer, (b) the same area as (a) after being burnt by the beam, (c) higher magnification image under lose dose conditions showing poor contrast and that no <5 nm particles are observable, (d) shows the same area as (c) after the ice layer has been burnt away showing particles of ca. 1 nm in diameter are easily visible.

This area was then exposed to a high intensity beam for an extended period (ca. 124 $e^-/Å^2$) in order to reduce the thickness of the ice layer by sublimation, and then re-imaged **Figure 117b** and **d**. Although the higher intensity beam has probably damaged the particles, it is clear that not only has the contrast improved for all particles in the image, but that very small particles (ca. 1 nm in diameter), which were previously obscured, are now visible. This test proves that the super-thin ice layers are required to visualise these very small particles under low dose conditions, as in **Figure 115**. GO-cryo-TEM therefore provides an opportunity to image silica particles down to at least 1 nm which are not visible by standard cryo-TEM under these imaging conditions.

5.3.5 High magnification, near focus images by GO-cryo-TEM

As discussed in Chapter 4, having a lower contrast support not only produces better particle contrast but allows images to be recorded closer to focus with the consequence of higher resolution. The defocus values chosen in **Figure 115** (-1.0 µm and -0.5 µm) are not arbitrary; as discussed in Chapter 4, having good contrast at these defocus values might allow for the application of exit wave reconstruction (EWR) to cryo-TEM samples. With the remarkable increase in resolution demonstrated by this technique, being able to apply this to hydrated samples would undoubtedly be of interest to those working with cryo-TEM. **Figure 118** shows higher magnification images of 10 nm silica particles imaged by GO-cryo-TEM (left) and cryo-TEM (right), at 1.0 µm (top) and 0.5 µm (bottom) defocus values. Again the increase in contrast is made evident by comparing the two sets of images, but at higher magnification it is also observable that for the GO-cryo-TEM images

more detail is visible in the particle at -0.5 µm defocus than at -1.0 µm. For the cryo-TEM image this detail is not observable and in comparison to the analysis of the PLA-*b*-PAA cylinders imaged on an amorphous carbon grid (in Chapter 4), EWR is unlikely to bring out additional detail due to this poor contrast.

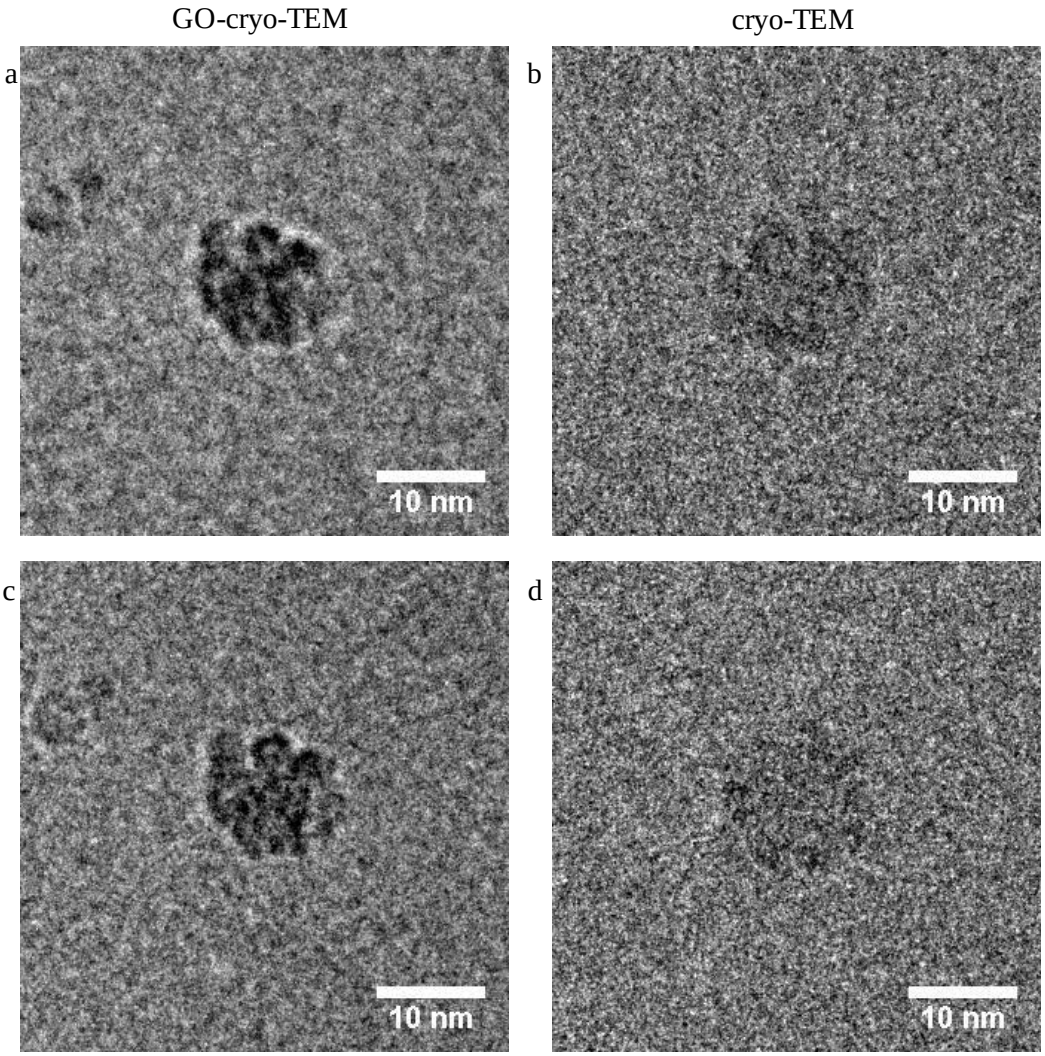

Figure 118. Images of silica nanoparticles recorded by (a) GO-cryo-TEM at -1.0 µm, (b) cryo-TEM -1.0 µm, (c) GO-cryo-TEM at -0.5 µm and (d) cryo-TEM -0.5 µm

Silicon is, of course, a higher Z element than carbon and therefore will scatter more electrons, providing better contrast. In order to evaluate the possibility of using EWR

in combination with GO-cryo-TEM for carbon based samples, PLA-*b*-PAA cylinders were imaged under the same conditions. **Figure 119** shows similar high magnification GO-cryo-TEM images for the PLLA-*b*-PAA cylinders taken at (a) -0.5 µm defocus and (b) at -1.0 µm defocus. These images show that good contrast can also be obtained for carbon based structures at high magnification and close to focus.

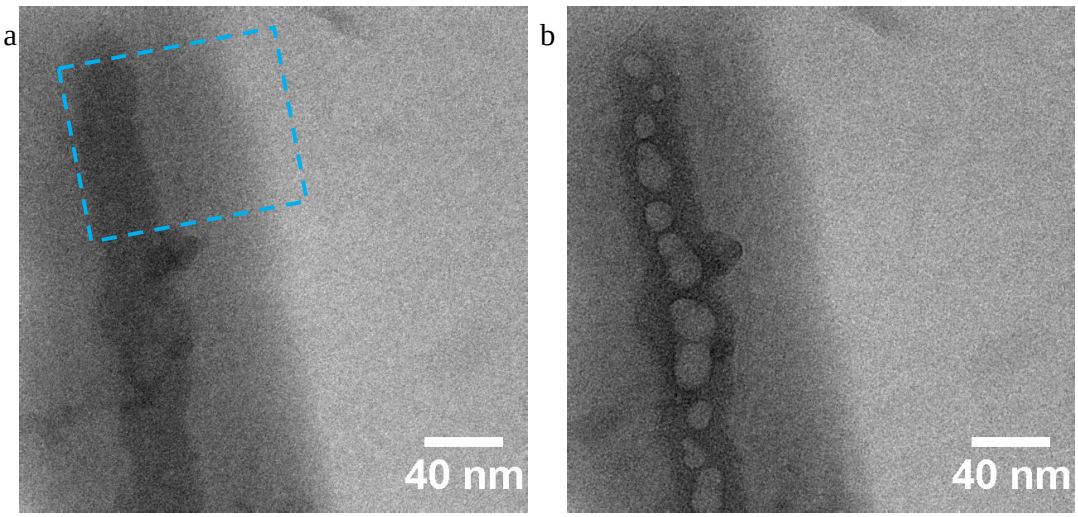

Figure 119. GO-cryo-TEM images of $PLLA_{40}$-*b*-PAA_{298} cylinders, (a) first image at -0.5 µm defocus and (b) second image at -1.0 µm defocus

However, **Figure 119b**, which was the second image to be taken, shows significant beam damage has occurred after the acquisition of just two images. This was not observed when acquiring the EWR images in Chapter 4 (20 images per reconstruction). However, it is difficult to compare beam damage directly across instruments if the exact electron counts were not measured (as in the EWR study in Chapter 4). It should be noted though, that for the EWR images in Chapter 4 a Field Emission Gun-TEM (FEG-TEM) was operated at 80 keV, while here a FEG-TEM

was operated at 300 keV. Of course lowering the keV will lower the image brightness giving poorer contrast and therefore some compromise between number of images, contrast obtained in each image and beam damage is likely to be needed to apply EWR to these samples. However these results are promising and further work is ongoing to optimise both the EWR image acquisitions and algorithms and the GO-cryo-TEM imaging method. **Figure 119a** also shows that there is a uniform water layer surrounding the hydrated cylinder and that the water layer appears to run parallel to the cylinder.

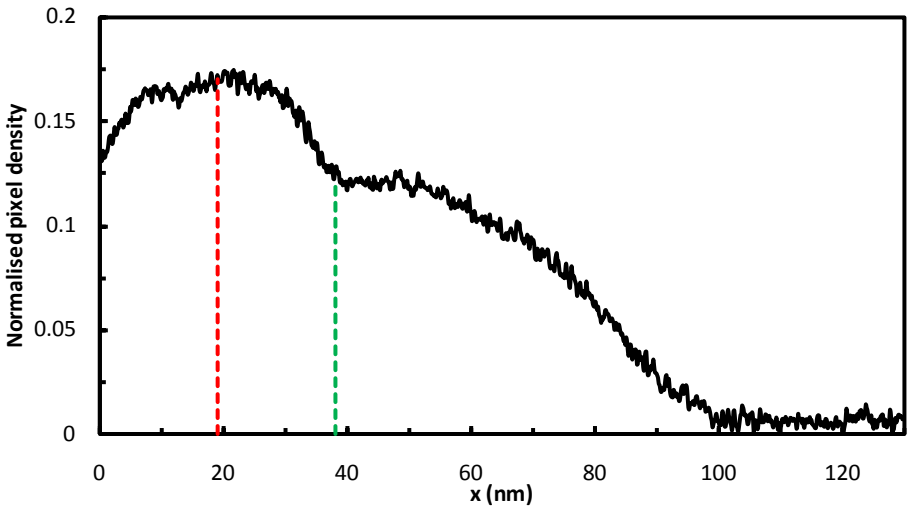

Figure 120. Plot profile for the area indicated by the dashed blue box in **Figure 119a**. The red and green dashed lines indicate the centre of the core and the core-corona interface respectively.

As previously mentioned this could be related to the length of the PAA corona, which could help with determination of the PAA stretching and obtaining a corona profile. **Figure 120** shows a plot profile for part of the cylinder in **Figure 119a** indicated by the blue dashed box. The profile shows a clear difference between core and corona, indicated by the dashed green line which reveals a core radius of 18 nm

and a corona length of 60 nm. This corresponds to a corona ω value of 0.8 which is within the range of PAA stretching values (0.4 – 0.9) measured by Colombani and co-workers,[21] as discussed in Chapter 1. This gives a strong indication that this is the minimum hydration level obtainable for these particles and that GO-cryo-TEM can be used to measure corona profiles for extremely hydrated polymers.

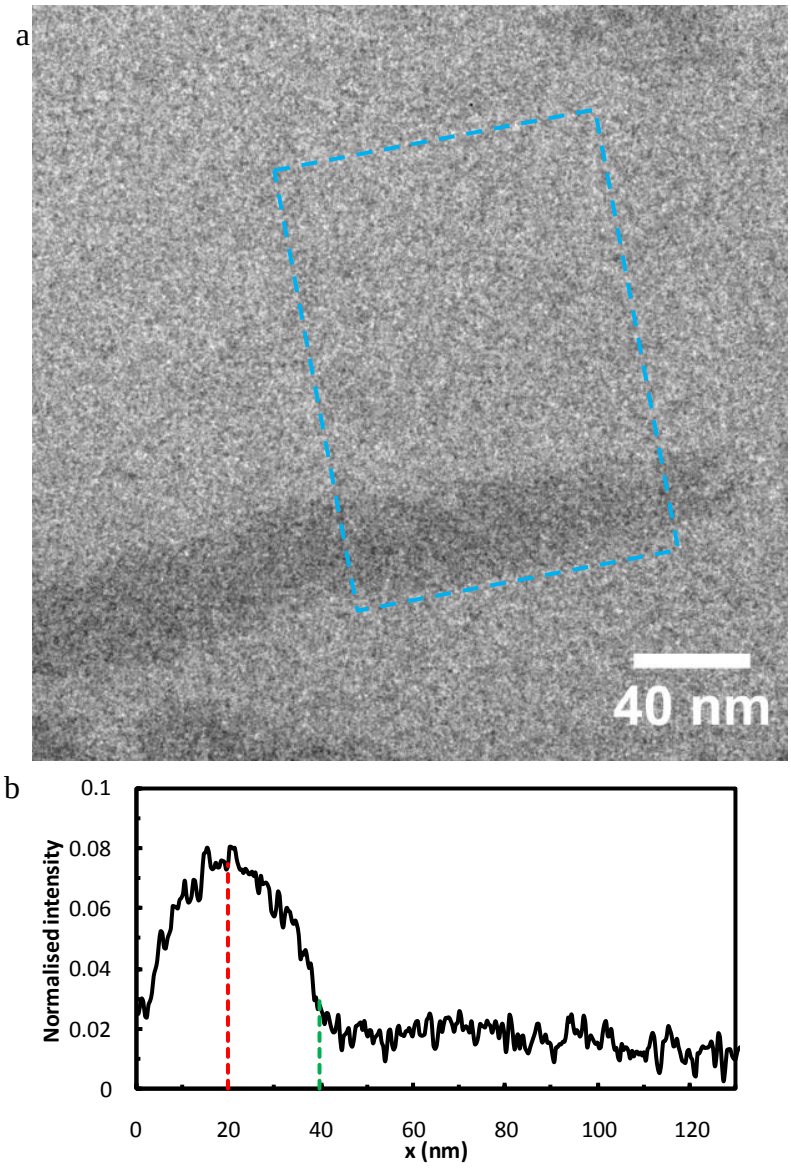

Figure 121. (a) cryo-TEM image of $PLLA_{40}$-*b*-PAA_{298} cylinders and (b) plot profile for the area indicated by the dashed blue box. The red and green dashed lines indicate the centre of the core the core-corona interface respectively.

Figure 121 shows a comparable image and plot profile for the PLLA-*b*-PAA cylinders taken by cryo-TEM. As expected there is much less contrast between particle and background compared to the GO-cryo-TEM image in **Figure 119**. The plot profile shows that the core is of a comparable size (20 nm radius) to the GO-cryo-TEM image, but that no information on the corona profile can be extracted due to its weak scattering against the relatively thick background.

5.3.6 Imaging of 2.10 by GO-cryo-TEM and cryo-TEM

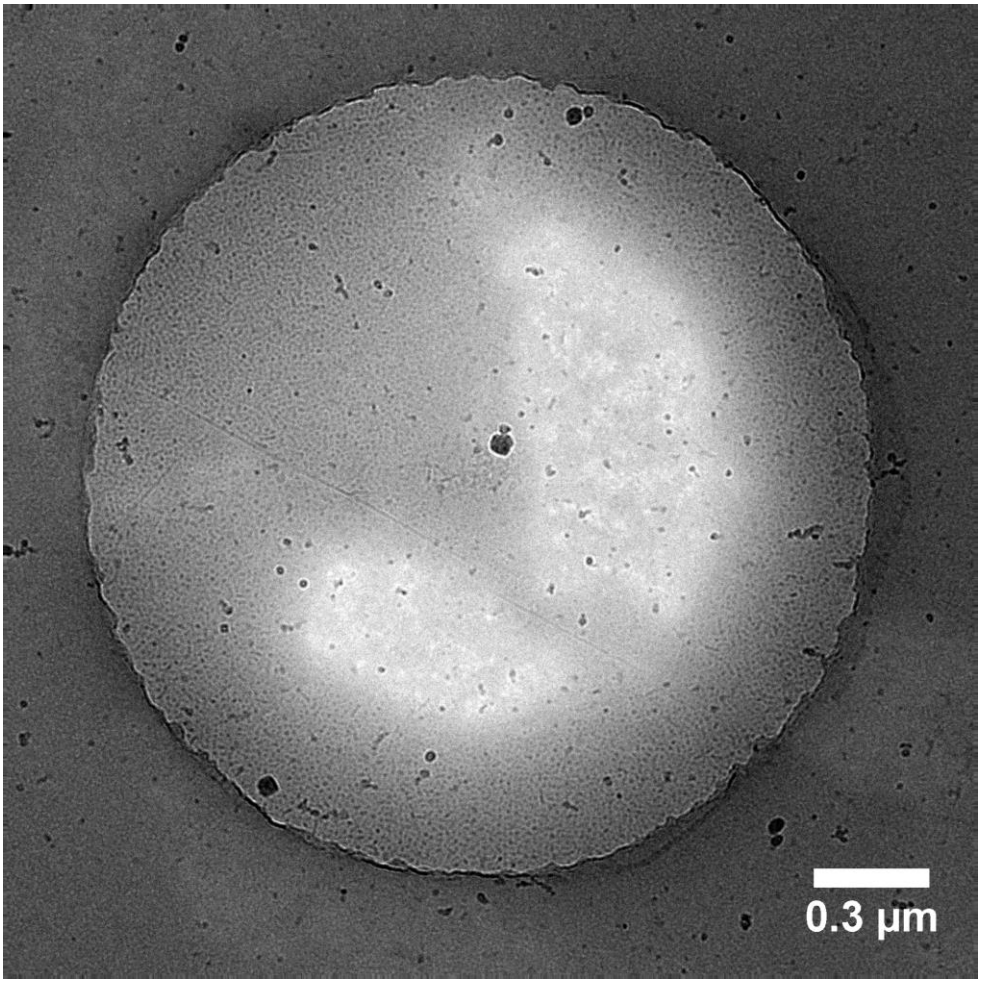

Figure 122. A GO-cryo-TEM grid hole covered with a layer of GO and both continuous (darker) and non-continuous (lighter) ice layers.

Chapters 2 and 4 illustrated the difficulty in analysing the non-pallidated SCS pincer PAA amphiphile assembly (**2.10**) by cryo-TEM, and in the dry state using GO-TEM grids, due to its weakly contrasting nature, and susceptibility of the assembled structures to fall apart upon dehydration. For these reasons **2.10** makes an ideal candidate for analysis by GO-cryo-TEM. **Figure 122** shows a hole which is covered with GO, some non-continuous super-thin ice and some continuous ice. While it is difficult to make out detail or sizes for the particles at this magnification it can be seen that the particles have a tendency to remain in the continuous layer.

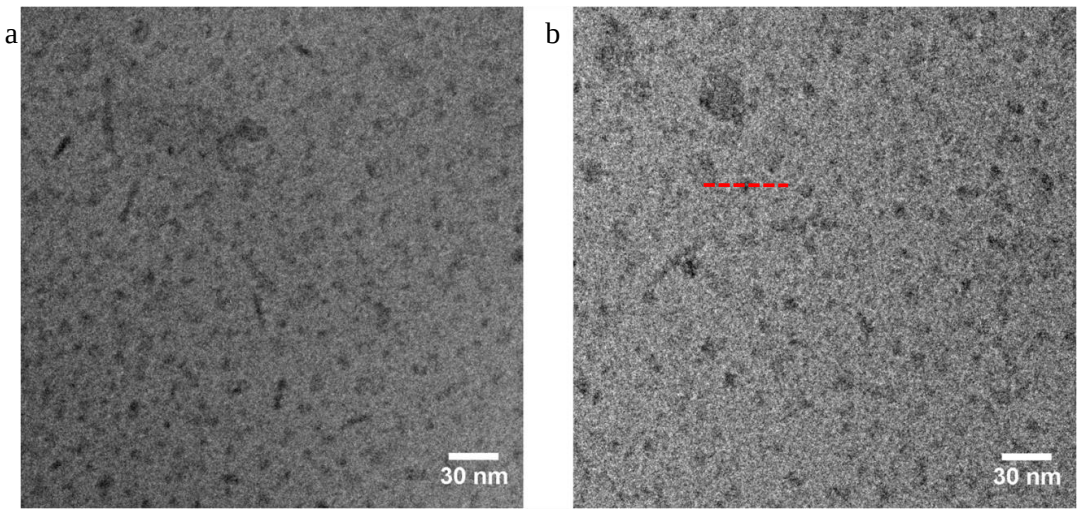

Figure 123. Images of **2.10** micelles recorded at -5 µm defocus by (a) GO-cryo-TEM and (b) cryo-TEM. The dashed red line indicates the area for the plot profile in **Figure 125b**.

This was noted throughout the grid, even in areas with a lower concentration of particles. This is possibly due to the fact that although the particle core is very small (a few nm) the PAA corona is comparatively large (DP = 50, L_{max} = 12.5 nm), therefore the minimum ice thickness obtainable in order for the particles to be hydrated is greater than the thickness of the super-thin layers, forcing the particles to

remain in the continuous layer. As such, higher magnification imaging in the non-continuous ice areas did not prove useful. **Figure 123** shows a comparison of images recorded by GO-cryo-TEM, in the continuous layer (a) and cryo-TEM (b). While the area for imaging in GO-cryo-TEM is not super-thin, the GO-cryo-TEM image clearly shows both spherical and cylindrical micelles with diameters of ca. 4 nm (consistent with previous SANS data) and there is a reasonable improvement over the standard cryo-TEM image. Furthermore the presence of the cylindrical micelles indicates that even with the increased blotting times and reduced ice thickness, this method is suitable for delicate samples.

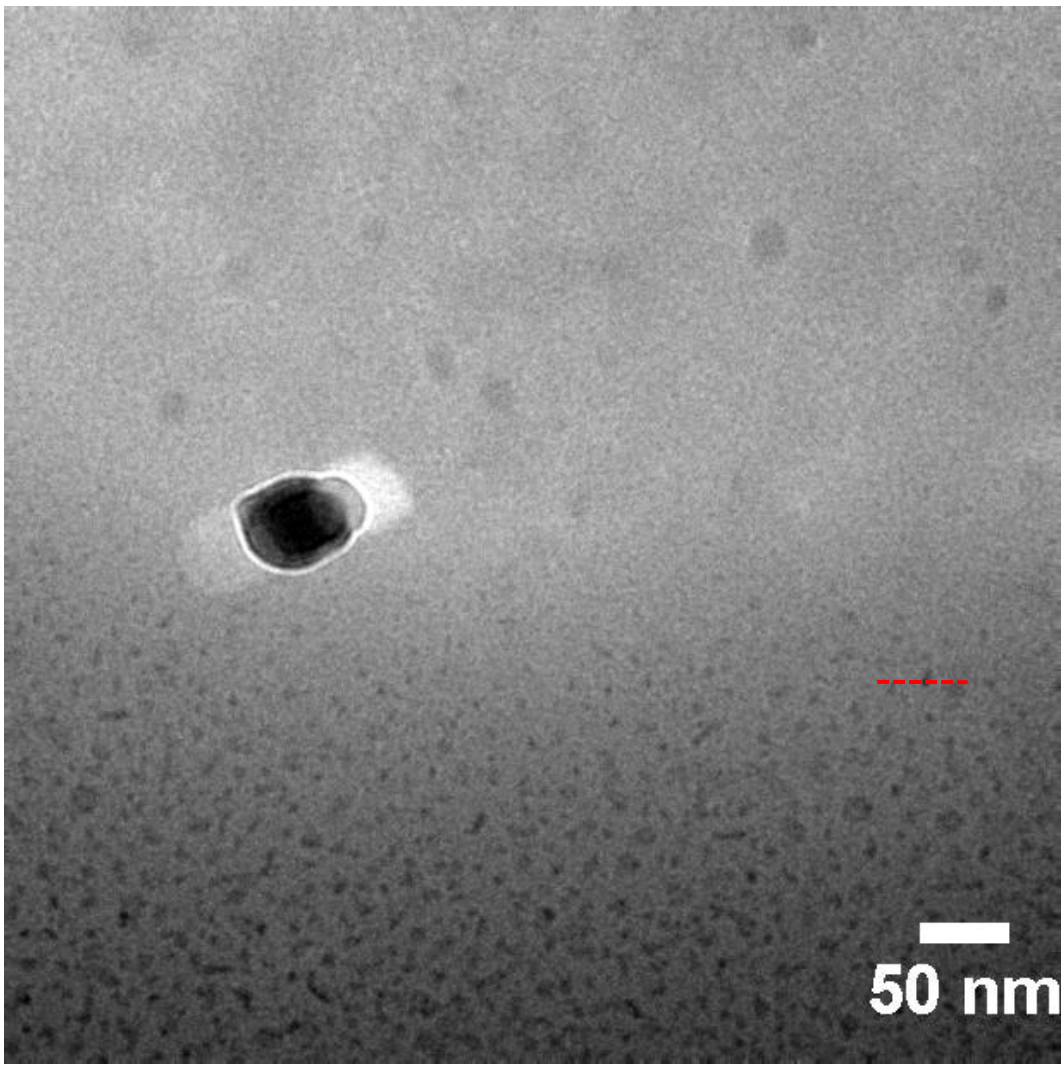

Figure 124. GO-cryo-TEM image of **2.10**. The dashed red line indicates the area for the line profile in **Figure 125**. The large dark feature in the image is crystalline ice formed after vitrification.

Figure 124 shows a GO-cryo-TEM image of **2.10** taken at the edge of one of the super-thin layers. The background contrast increases from the top of the image to the bottom as the ice thickness increases. Approximately half way down the image the particles begin to appear in the ice layer which indicates this is the minimum level of ice obtainable for these particles to remain hydrated. This is perhaps comparable to the size sorting effects that have been noted for cryo-TEM samples, where particles

tend to order themselves within the convex ice film, with smaller particles clustering in the thinner areas.[22]

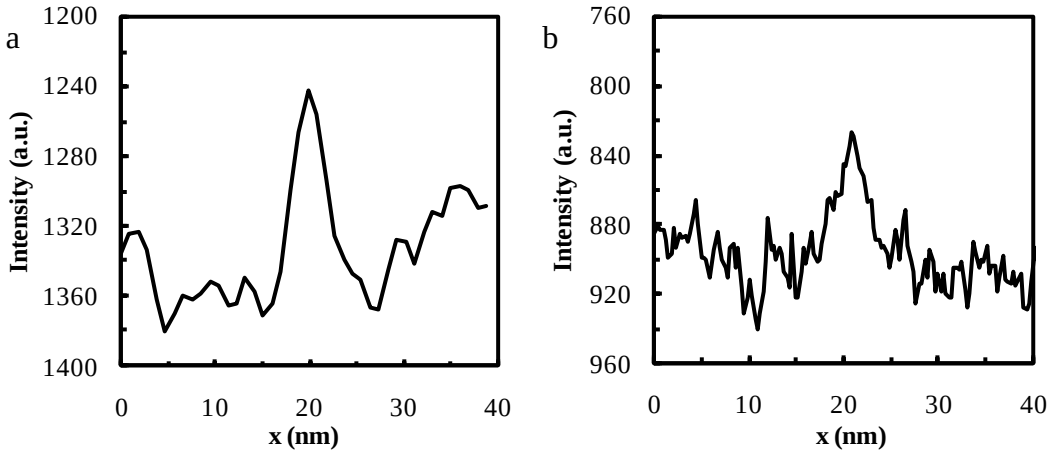

Figure 125. Line profiles for a **2.10** micelle, indicated by the dashed red line in **Figure 124**

It is likely then, because of the small core and relatively long corona (DP = 50), that this is the minimum ice thickness obtainable for these particles and therefore the best contrast obtainable by GO-cryo-TEM. **Figure 125a** and **b** show line profiles for the GO-cryo-TEM and cryo-TEM images in **Figure 124** and **Figure 123b** respectively (areas indicated by the dashed red lines). This data shows that despite their need for a thicker ice layer in order to remain hydrated, there is an improvement in contrast for the GO-cryo-TEM image over the cryo-TEM image. Furthermore, using GO-cryo-TEM allows for good contrast to be obtained for particles < 5 nm.

5.4 Conclusions

With the use of GO-TEM grids it is possible to vitrify and image aqueous solutions of carbon / silica based nanomaterials in the minimum amount of water necessary to

keep the particles hydrated. This is made possible by supporting the samples on atomically thin sheets of GO, which have a minimal contribution to the background scattering. It has been shown that imaging samples in super-thin ice layers results in increased contrast compared to standard cryo-TEM, allowing for images to be recorded closer to focus, resulting in better resolution. It has also been shown that extremely small particles and very hydrated polymers (e.g. PAA coronas) can be imaged which may not be visible under standard cryo-TEM conditions. GO-cryo-TEM is a powerful technique for imaging extremely small / weakly contrasting nanomaterials that test the boundaries of size for standard cryo-TEM.

5.5 Experimental

5.5.1 Materials

GO was synthesised as reported in Chapter 4, TEM grids used were Quantifoil R2/2, Quantifoil Micro Tools GmbH, Jena, Germany, PLLA-*b*-PAA cylinders[‡‡‡] were synthesised as previously reported.[23]

5.5.2 Instrumentation

Cryo-TEM images were taken at the Laboratory of Materials and Interface Chemistry of Eindhoven University of Technology. Sample preparation for cryo-TEM was carried out in an automated vitrification robot (FEI Vitrobot Mark III) using liquid ethane as cryogen. TEM grids (Quantifoil R2/2, Quantifoil Micro Tools

[‡‡‡] PLA-*b*-PAA cylinders were provided by Nikos Petzetakis

GmbH, Jena, Germany) were glow discharged prior to use in a Cressington 208 carbon coater for 40 s. CryoTEM samples were imaged with the TU/e CryoTitan (FEI,www.cryotem.nl). The CryoTitan is equipped with a field emission gun (FEG), a post column Gatan Energy Filter (GIF) and was operated at 300 kV. Images were recorded on a post-GIF 2k x 2k Gatan CCD camera using zero-loss energy filtering with a 20 eV energy window.

5.6 References

1. F. Nudelman, G. de With and N. A. J. M. Sommerdijk, *Soft Matter*, 2011, **7**, 17-24.
2. W. H. Massover, *Micron*, 2011, **42**, 141-151.
3. H. Friedrich, P. M. Frederik, G. de With and N. A. J. M. Sommerdijk, *Angew. Chem. Int. Ed.*, 2010, **49**, 7850-7858.
4. S. Zhong and D. J. Pochan, *Polym. Rev.*, 2010, **50**, 287-320.
5. J. R. Bellare, H. T. Davis, L. E. Scriven and Y. Talmon, *J. Electron Microsc.*, 1988, **10**, 87-111.
6. X.-c. Bai, T. G. Martin, S. H. W. Scheres and H. Dietz, *PNAS*, 2012, **109**, 20012-20017.
7. T. Kato, R. P. Goodman, C. M. Erben, A. J. Turberfield and K. Namba, *Nano Lett.*, 2009, **9**, 2747-2750.
8. A. Laschewsky, J.-N. Marsat, K. Skrabania, H. v. Berlepsch and C. Böttcher, *Macromol. Chem. Phys.*, 2010, **211**, 215-221.
9. K. Mitsuoka, *Micron*, 2011, **42**, 100-106.

10. R. H. Wade, *Ultramicroscopy*, 1992, **46**, 145-156.

11. D. B. Williams and C. B. Carter, *Transmission Electron Microscopy —A textbook for Materials Science*, Plenum Press, New York, 1996.

12. H. Cui, T. K. Hodgdon, E. W. Kaler, L. Abezgauz, D. Danino, M. Lubovsky, Y. Talmon and D. J. Pochan, *Soft Matter*, 2007, **3**, 945-955.

13. T. Terashima, T. Mes, T. F. A. De Greef, M. A. J. Gillissen, P. Besenius, A. R. A. Palmans and E. W. Meijer, *J. Am. Chem. Soc.*, 2011, **133**, 4742-4745.

14. P. Wang, H. Pu and M. Jin, *J. Polym. Sci. Part A: Polym. Chem.*, 2011, **49**, 5133-5141.

15. C. T. Adkins, H. Muchalski and E. Harth, *Macromolecules*, 2009, **42**, 5786-5792.

16. R. S. Pantelic, J. C. Meyer, U. Kaiser and H. Stahlberg, *Solid State Commun.*, 2012, **152**, 1375-1382.

17. R. S. Pantelic, J. W. Suk, Y. Hao, R. S. Ruoff and H. Stahlberg, *Nano Lett.*, 2011, **11**, 4319-4323.

18. R. S. Pantelic, J. C. Meyer, U. Kaiser, W. Baumeister and J. M. Plitzko, *J. Struct. Biol.*, 2010, **170**, 152-156.

19. B. Feja and U. Aebi, *Journal of Microscopy*, 1999, **193**, 15-19.

20. J. Dubochet, M. Adrian, J.-J. Chang, J.-C. Homo, J. Lepault, A. W. McDowall and P. Schultz, *Q. Rev. Biophys.*, 1988, **21**, 129-228.

21. O. Colombani, M. Ruppel, M. Burkhardt, M. Drechsler, M. Schumacher, M. Gradzielski, R. Schweins and A. H. E. Müller, *Macromolecules*, 2007, **40**, 4351-4362.

22. I. Harwigsson, O. Soederman and O. Regev, *Langmuir*, 1994, **10**, 4731-4734.

23. N. Petzetakis, A. P. Dove and R. K. O'Reilly, *Chem. Sci.*, 2011, **2**, 955-960.

Chapter 6. Conclusions and future work

This thesis has dealt with two separate but related issues in the field of polymer self-assembly. In Chapter 2 it was shown that the incorporation of SCS pincer complexes into amphiphilic homopolymers provides a relatively simple route to functional nanoreactors. It was also demonstrated that increase reaction rates can lead to significantly reduced catalyst loadings due to the 'concentrator effect'. The remaining chapters focused on analysing polymer aggregates in solution. Chapter 3 showed how the combination of multiple analysis techniques, based on both scattering (LLS and SANS) and microscopy (cryo-TEM), can be used to analyse polymer aggregates in solution. Of particular interest was the agreement between SANS and cryo-TEM in determining the corona profile. Chapter 3 demonstrated that using GO as a substrate for multiple dry state microscopy techniques (TEM, STEM, AFM and SEM) allows for the unambiguous determination of size and morphology for polymer aggregates. Furthermore with the application of EWR it was shown that individual polymer chains can be observed within the aggregate, giving access to a level of detail which has not been previously available. In Chapter 6 GO was used as a substrate for cryo-TEM where it was demonstrated that, with the aid of a nearly electron transparent support, particles could be imaged within super thin ice layers, resulting in much better particle contrast and allowing the observation of smaller and more weakly contrasting particles than is possible by conventional cryo-TEM.

Future work to further this research should focus on the optimisation of the catalysis in Chapter 2 to further decrease the catalyst loadings. This could be done by either increasing the hydrophobic domain in order to stabilise the particles at lower nanoreactor concentrations, or by altering the polymer architecture in order to

produce a mixed micelle system, resulting in the ability to decrease loadings at a constant nanoreactor concentration. Perhaps the most exciting future project would involve the combination of the work in Chapter 3-5. The combination of EWR with tomography on GO-TEM grids could provide access to 3D images where individual polymer chains can be followed throughout the aggregate. Furthermore if these methods could be made compatible with low dose imaging, their use in combination with GO-cryo-TEM, might result in the 3D reconstruction of polymer aggregates in solution at unprecedented resolutions. Finally, if applied to the aggregates in Chapter 2 the 3D structures could be used to generate corona profiles for comparison with the SANS data in order to valid the reconstructions.

In summary it has been demonstrated that self-assembly of amphiphilic polymers be used to reduce the catalysts loadings of precious materials. While the analysis of these aggregates can be difficult, through the use of multiple analysis techniques, based on scattering and microscopy, and particularly through the use of GO as a substrate for microscopy, this analysis can be in depth and readily performed.